HOMOGENEOUSLY ALLOYED CADMIUM SULFOSELENIDE NANOCRYSTALS

by

Laura Anderson Swafford

Dissertation

Submitted to the Faculty of the

Graduate School of Vanderbilt University

in partial fulfillment of the requirements

for the degree of

DOCTOR OF PHILOSOPHY

in

Chemistry

December, 2006

Nashville, Tennessee

Approved:

Sandra J. Rosenthal

Norman H. Tolk

David E. Cliffel

Charles. M. Lukehart

Leonard C. Feldman

Dedicated

to

The memory of my father, Michael Scott Swafford, Ph.D.

ACKNOWLEDGEMENTS

I would like to thank the following people, who were instrumental in the completion of this work:

My advisor, Professor Sandra J. Rosenthal, for providing me with the opportunity to work on this project, and for guidance throughout the years.

Professor Leonard C. Feldman, for the idea of alloy nanocrystals, for allowing me to use the Rutherford backscattering experiment, and for asking the hard questions.

Professor Norman H. Tolk, for allowing me to work on the SHG and IPE projects, and for providing much additional guidance and discussion.

Professors Charles Lukehart and David Cliffel, for additional help and support.

Dr. John Kozub (W. M. Keck Free Electron Laser Center) and Mike Crumb (Quantronix), for help with the Quantronix laser systems.

Professor Anthony B. Hmelo, Dr. Sarit Dhar, and Sriram Dixit, for training and help with the Rutherford backscattering experiment.

Members of the Tolk research group, especially Drs. Zsuzsanna Marka, J. Keith Miller, Robert Pasternak, and Ying Xu, for help with the SHG and IPE experiments, and for being good friends.

Members of the Rosenthal research group, especially Dr. Andreas Kadavanich, Dr. Ian Tomlinson, Dr. Meg Erwin, Dr. Tadd Kippeny, Rachel Ward, Dr. James McBride, Mike Bowers, M. Danielle Garrett, Tony Watt, and Lauren Weigand, for help of all kinds, and for sharing the insanity.

Funding for this work was provided by several Teaching Assistantships from Vanderbilt University, two GAANN Fellowships, a VINSE Fellowship, and a University Graduate Fellowship, as well as grants from the National Renewable Energy Laboratory (AAD91866811), the Department of Energy (DEFG0202ER45957), and

the National Institutes of Health (RO1 EB003728).

TABLE OF CONTENTS

LIST OF TABLES

LIST OF FIGURES

CHAPTER I

INTRODUCTION

1.1 Overview

Semiconductor nanocrystals, or quantum dots, are crystalline semiconductors whose largest dimension is on the nanometer scale (1-1000 nm). They are of primary interest to several fields of research because of their unique size-dependent optical and electronic properties (Figure 1.1). Applications include photovoltaics,[1–6] light-emitting diodes,[7–9] photocatalysis,[10–13] bioassays,[14–20] and electronics.[21–23] Specific applications, however, require multiple characteristics in a single system. For example, very small nanocrystals are desirable for *in vivo* imaging,[14] yet multiplexing experiments require a range of sizes in order to achieve a range of fluorescence colors. Size also plays a role when nanocrystals must be incorporated into larger superstructures such as mesoporous materials in photovoltaics (e.g., Appendix D).[4,24] One solution to the problem of dual requirements is to employ alloy nanocrystals. Since the optical properties of alloys vary with composition, it is possible to tune the spectrum while maintaining a small size. Thus, by varying composition, we gain a second tool for altering physical and optical properties. Both size and composition may be tuned to select multiple desirable qualities simultaneously (Figure 1.2).

To date, research into pseudobinary (AB_xC_{1-x}) semiconductor alloy nanocrystals has been limited.[25–33] In some cases, alloys have been the unintentional result of an attempt to synthesize a different crystal structure.[25,26] They have also been successfully employed as shell materials for binary nanocrystals;[26–28] a shell that combines the core semiconductor with a higher band gap semiconductor generates increased fluorescence due to confinement of the electron and hole to the core while simultaneously ameliorating undesirable interface effects, such as lattice mismatch

Figure 1.1: Size-dependence of the optical properties of CdSe nanocrystals. (Top) light absorption by nanocrystals ranging from small (left) to large (right). (Bottom) the same nanocrystals, illuminated by ultraviolet light, displaying size-dependent light emission. Courtesy of Michael Bowers of the Rosenthal group.

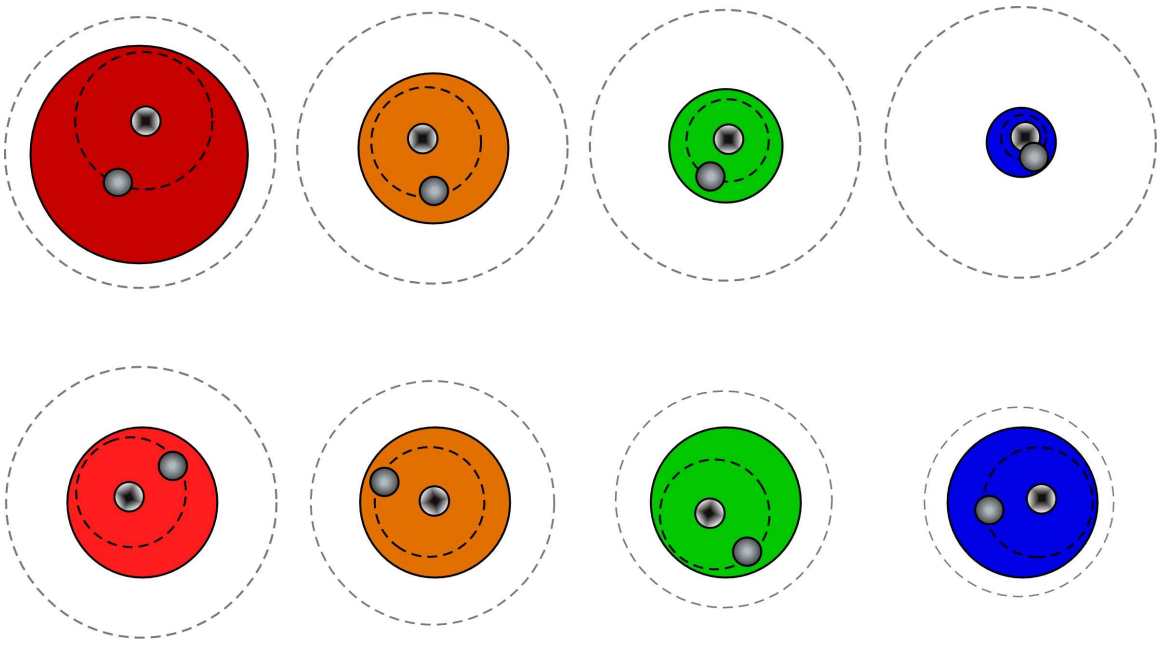

Figure 1.2: Size- and composition-dependence of color in nanocrystals. This cartoon demonstrates how the band gap of semiconductor nanocrystals may be tuned by size (top) or by composition (bottom). The dashed circles represent the Bohr exciton diameter, which can change with composition.

leading to incomplete shell growth.[26] A number of studies have examined the optical properties of alloy nanocrystals, but either the alloys are shown to have a gradient structure,[25,29] in which the composition of the alloy is different in different parts of the nanocrystal, or no analysis into the homogeneity of the alloy is provided.[30,31] The distinction between a gradient alloy and a homogeneous one is critical because, as we and others show, gradient alloy nanocrystals show optical properties that are significantly different than homogeneous alloys.[32,34] Kuno and coworkers' study of HgS_xSe_{1-x} nanocrystals presents a highly detailed examination of the optical properties of homogeneous nanocrystals, but only for a single size.[33] To our knowledge, only Bailey and Nie's study of $CdSe_xTe_{1-x}$ nanocrystals has explored the effect of alloy composition on the optical properties of homogeneous nanocrystals of several different sizes.[32]

Much of the difficulty in alloy nanocrystal research lies in devising a synthetic scheme to produce the desired alloy structure, be it homogeneous or gradient. To achieve homogeneity, the growth rates of the two constituent materials must be equal,[29,32] and the conditions necessary for the growth of one constituent cannot impede the growth of the other. In addition, the structure and bonding of the two materials must be sufficiently similar to allow their facile mixing; otherwise, the formation of segregated structures such as core/shells or two different binary nanocrystals may result. In this work we report the synthesis of homogeneous CdS_xSe_{1-x} nanocrystals over the range $x = 0$ to $x = 1$ using a single synthetic method. The nanocrystals are characterized with respect to structure, composition, size, and optical band gap, and on the basis of these, the dependence of band gap on size and composition is extracted. In addition, by varying the concentration of one of the ligands in the synthesis, we show that we can alter the morphology of the nanocrystals from homogeneous nanocrystals to highly fluorescent, gradient nanocrystals to nanorods with a strong gradient occurring in a single direction, which could be very useful for unidi-

rectional charge transport in nanoelectronic devices. To understand the underlying physics of the alloy nanocrystals, we begin with a general discussion on the physics of nanocrystals and alloys separately.

1.2 Semiconductor nanocrystals

The characteristics of any crystal change as it moves from the bulk to the nanometer size regime. Surface-to-volume ratio increases, surface strain and reconstruction increase as facets become smaller and edges move closer together, and the number of bulk crystal defects decreases. As a result of these differences, many of the physical properties are likewise altered,[35] including melting and phase transition temperatures,[36,37] magnetic properties,[38] mechanical properties, chemical reactivity,[10] and even interatomic distances.[37] In addition to these structurally induced changes, as the crystal becomes very small, typically on the order of 10 nm or smaller, quantum confinement begins to play a critical role in the electronic properties of the nanocrystal, including the dielectric constant,[39] oscillator strength,[40,41] optical susceptibilities,[42] energy band structure,[39,43] all of which become size-dependent. These properties can change dramatically, particularly in the strong confinement regime, defined as when a nanocrystal has a radius of less than or equal to the Bohr exciton radius of the bulk material. As this work concerns the optoelectronic behavior of semiconductor nanocrystals, this section presents a simple overview of the effects of confinement on some of these properties, beginning with electronic structure.

1.2.1 Electronic structure

Semiconductor nanocrystals are crystals whose electronic structure is intermediate between molecular and bulk semiconductor in nature. In a molecule, the electronic structure is characterized by a series of discrete molecular orbitals of different energies. Of these, the highest occupied molecular orbital (HOMO) and the

lowest unoccupied molecular orbital (LUMO) are significant in that the lowest-energy electronic transition in a molecule in the ground state occurs when an electron is promoted from the HOMO to the LUMO. In contrast, in a bulk material the electronic structure is characterized by a series of energy bands centered about the molecular orbitals, with the width of each band related to the strength of the nearest-neighbor interactions.[44] Bulk semiconductors contain energy bands that in the ground state are either completely occupied (valence bands, VB) or completely unoccupied (conduction bands, CB), and the lowest-energy electronic transition occurs when an electron is promoted across a band gap from the valence band maximum (VBM) to the conduction band minimum (CBM). Nanocrystals, containing only $\sim 10^1 - 10^5$ atoms, are not large enough to display the full band structure of a bulk material. Instead, as nanocrystal size increases, the bands grow outward from the central molecular orbital.[44] Nanocrystals are thus characterized by energy 'bands' that are truly bandlike in the center but also have discrete energy states towards the edges of each band. These concepts are depicted in Figure 1.3.

This explanation of the band structure of nanocrystals has two significant consequences. First, the lowest-energy electronic transitions in nanocrystals occur between discrete states in the VB and the CB, so that absorption spectra show a series of distinct peaks corresponding to discrete transitions at low energies and a bandlike continuum at higher energies (Figure 1.4). Second, since the center of each band develops first, smaller nanocrystals have valence band maxima and conduction band minima that are closer in energy to the molecular HOMO and LUMO, respectively, than larger nanocrystals. Consequently, the lowest-energy transition, corresponding to the optical band gap, is more energetic in smaller nanocrystals than in larger ones. It is noted that because the lowest energy transition, corresponding to the HOMO-to-LUMO transition, is between disctrete energy levels, the band gap energy is typically measured at the center of the lowest-energy peak in the absorption spectrum. This

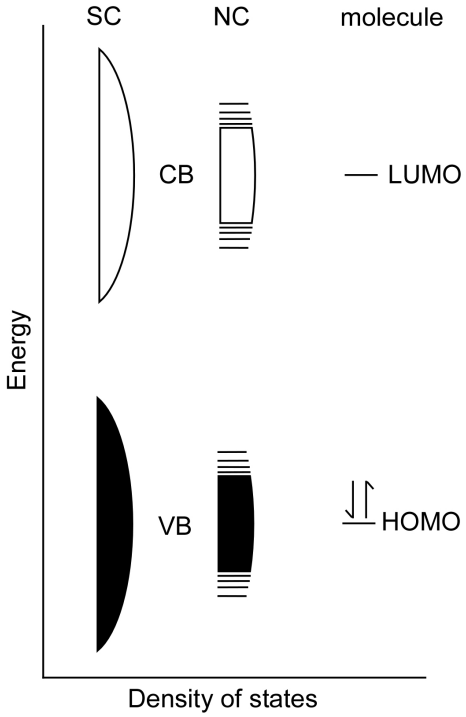

Figure 1.3: Electronic structures of bulk semiconductors (SC), semiconductor nanocrystals (NC), and molecules.

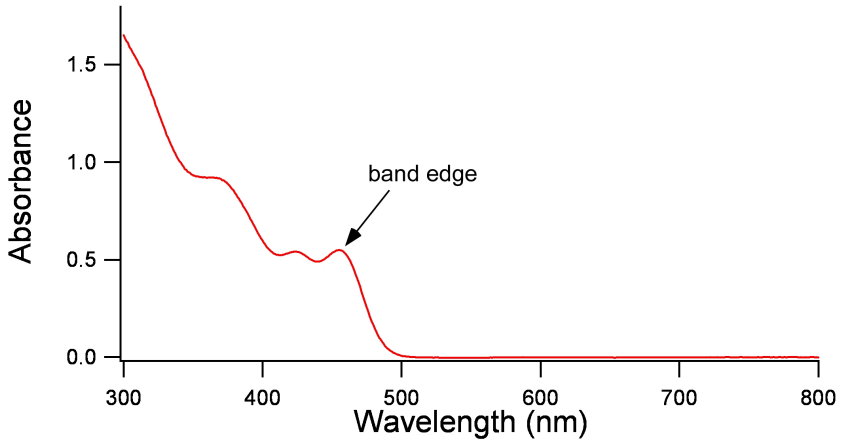

Figure 1.4: Absorption spectrum of 35 Å diameter $CdS_{0.6}Se_{0.4}$ nanocrystals. The peaks at 450 nm, 420 nm, and 360 nm correspond to electronic transitions between discrete energy levels in the nanocrystals, while the growing absorption continuum at wavelengths below 360 nm results from electronic transitions between the truly continual portion of the valence and/or conduction bands.

method is more consistent with molecular transitions, and contrasts to measuring the band gaps of bulk semiconductors as the onset of absorption.

Because of the orbital structure of crystalline materials, size actually dominates the behavior of nanocrystals. In a crystal, orbitals are delocalized over the crystal lattice. Bulk semiconductors appear infinitely large to electrons in the CB and holes in the VB; they can move freely through the lattice, and their behavior is not bound by the size of the crystal. When a crystal becomes small enough, however, the surface of the crystal begins to impact the orbital structure by imposing boundary conditions. This has two major consequences. First, in contrast to bulk semiconductors, photogenerated electrons and holes are forced into close contact, resulting in predominantly excitonic behavior. Second, quantum mechanically charge carriers transition from free particle behavior in bulk to particle-in-a-box behavior in nanocrystals.[45] These phenomena are discussed below.

1.2.2 Excitons

As a result of the spatial constraints imposed by the small size of nanocrystals, optically excited electrons and holes exhibit somewhat different behavior than in the bulk. Notably, because they are forced to remain physically close to each other, they often form excitons, or bound electron-hole pairs. To better understand this behavior, we first consider the behavior of optically excited electrons and holes in bulk semiconductors.

In a bulk semiconductor, a free electron and hole are created when a photon is absorbed with sufficient energy to promote an electron from the valence band to the conduction band. In this case the energy $\hbar\omega$ of the photon is converted into the potential energy V required to raise the electron into the conduction band of the material ($V \geq E_g$, where E_g is the band gap energy of the material), the kinetic energies of the electron, T_e, and hole, T_h, any Coulomb attraction E_{Coul} between the

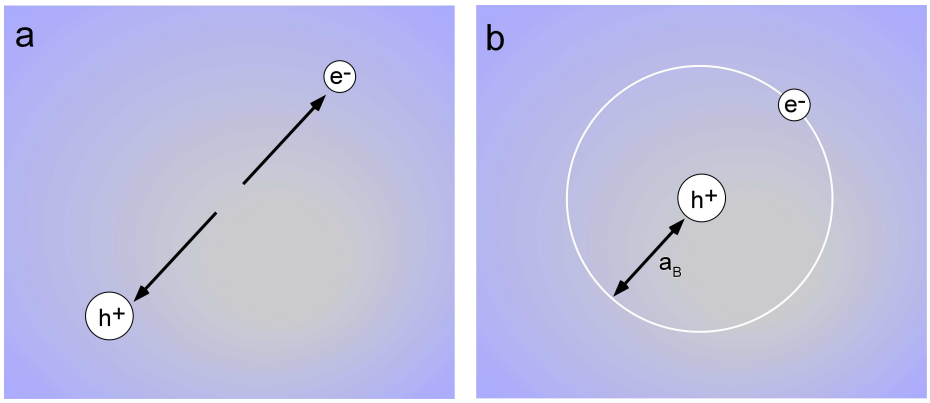

Figure 1.5: Photogeneration of charges in bulk semiconductors. Generally, if a photon is absorbed with energy greater than the band gap, a free electron and hole are created (a). If a photon is absorbed with energy slightly less than the band gap (b), an exciton forms.

electron and hole, as well as the energies required to generate any other phenomena (i.e. phonons) associated with the absorption event:

$$\hbar\omega = V + T_e + T_h + E_{Coul} + \ldots \tag{1.1}$$

This occurs such that both the energy and momentum of the original photon are conserved. Almost invariably when $\hbar\omega \geq E_g$, the result is that the Coulombic attraction between the electron and hole is insufficient to overcome their momenta; the electron and hole separate into independently moving ('free') particles (Figure 1.5a), and the Coulomb attraction disappears as the electron-hole distance increases.

Occasionally, when the kinetic energies of the particles are sufficiently small, the Coulomb attraction between the two charges results in a metastable bound state in which the faster-moving electron orbits the slower hole, forming an exciton (Figure 1.5b). Because Coulombic attraction lowers the total energy of the system, bulk semiconductors can also absorb photons with energies that are slightly less than the band gap. These absorption events exclusively generate excitons, because the only negative energy contribution to the right side of Equation 1.1 is the Coulomb attraction, which essentially disappears for non-excitonic systems. When the absorbed

photon has less energy than the band gap, the resultant electron and hole exist in excitonic states within the band gap - the electron in a virtual state slightly below the conduction band minimum, and the hole in a virtual state slightly above the valence band maximum. These states do not exist within the semiconductor itself, but rather are created as a result of the energy-lowering Coulomb attraction between the electron and hole.

As we shall see in Section 1.2.3, excitons behave similarly to hydrogen atoms, substituting a hole for the proton that forms the nucleus of the hydrogen atom. Like the hydrogen atom, excitons have a potential energy well and can exist in many quantized electronic states (excitonic states) within that well (e.g., Figure 1.6). The average distance between the electron and hole is the bulk Bohr exciton radius, a_B, whose value is characteristic of the semiconductor; this distance turns out to be critical in quantum confinement.

Excitons have finite lifetimes. They may decay through electron-hole recombination or through interactions with other phenomena within the semiconductor. Traps, scattering centers, free charges, phonons, and photons can all disrupt excitons; moreover, excitons whose electrons and holes are within the conduction and valence bands of the semiconductor may also decay by releasing energy and momentum, for example by emitting a phonon, and moving to lower energy states within the bands as free charge carriers. Since most of the exciton-disrupting phenomena are more prevalent at higher temperatures and since most photogenerated electrons and holes never form excitons at all, excitons are very rare in bulk semiconductors under normal conditions.

In stark contrast, excitons play a critical role in the optoelectronic behavior of nanocrystals. In nanocrystals, when a photon is absorbed, an electron and hole are generated, just as in bulk materials. However, except for surface effects and tunneling, which we shall ignore for this qualitative discussion, the electron and hole

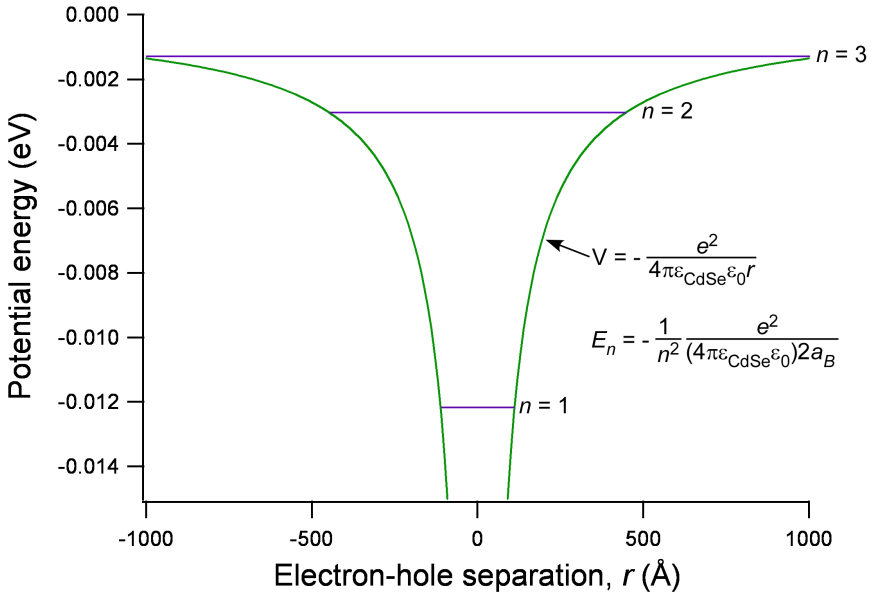

Figure 1.6: Potential energy well for excitons in bulk CdSe. The equation for potential energy, V, is analogous to that for the hydrogen atom, with the addition of the dielectric constant of CdSe, $\epsilon_{CdSe} = 10.6$.[46] The electronic contribution of the n^{th} electronic state, E_n, to the total energy of the exciton is also analogous to the electronic energy of the hydrogen atom, with the addition of the dielectric constant of CdSe and the substitution of the bulk Bohr exciton radius of CdSe, $a_B = 56$ Å,[43] for the Bohr radius of the hydrogen atom.

are confined to the very small volume of the nanocrystal. Unlike bulk semiconductors, in which the majority of optically generated electrons and holes quickly separate, in nanocrystals Coulomb attraction is always present and is a major contributor to the overall energy of the system. How much it contributes depends on the size of the nanocrystal.

If the electron and hole cannot be separated, then they behave energetically as an exciton, in that Coulomb attraction affects the wavefunction of the system. Thus the minimum-energy separation between the electron and hole is the Bohr exciton radius. However, the nanocrystal may have a radius smaller than a_B, so that the electron and hole are forced closer together than desirable. In this case, quantum confinement dictates that the kinetic energy of the two charges is greater than the Coulomb attraction. Although charge carriers in nanocrystals always behave somewhat differently than in bulk semiconductors, when electrons and holes are confined to a separation on the order of or less than a_B, the electronic properties become strongly size-dependent and are quite different from those of the bulk.

Researchers have defined two size regimes for nanocrystals: the weak confinement regime, in which nanocrystals have radii of greater than a_B, and the strong confinement regime, in which nanocrystals have radii of less than a_B (Figure 1.7).[47] In the weak confinement regime, the electron-hole pair behave primarily as bulk excitons, with a small perturbation imposed by the limited space. In the strong confinement regime, rather than behaving as an electron orbiting a hole, the two charges behave more as two independent particles trapped in a confined space (the nanocrystal), with a significant perturbation to the simplistic particle-in-a-box model due to the Coulomb attraction between the two particles.

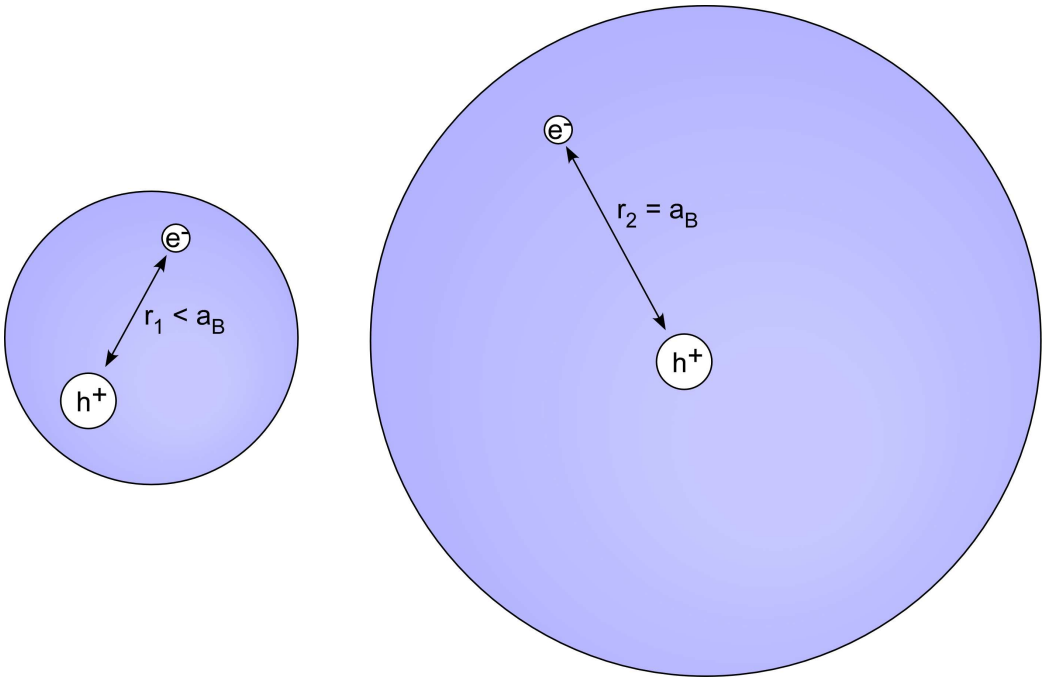

Figure 1.7: Confinement of charges in semiconductor nanocrystals. In nanocrystals, photogenerated electrons and holes are forced into contact by the physical confinement of the nanocrystal, resulting in an induced excitonic state. The degree of confinement is dictated by the size of the nanocrystal; in the strong confinement regime (left), excitons are constrained to an average distance r_1 of less than the Bohr exciton radius, while in the weak confinement regime (right), excitons can achieve the optimal electron-hole separation r_2 of a_B.

1.2.3 Band gap

The most immediately visible evidence of quantum confinement in semiconductor nanocrystals, and the focus of this work, is the shift in the optical absorption and emission spectra with size. An absorption event promotes an electron from the valence band to the conduction band, leaving a hole behind in the valence band. The resultant bound electron-hole pair is an excellent real-world example of the particle-in-a-box model in quantum mechanics,[48] and a basic model for the behavior of this system was developed by Brus.[45,49] In order to understand the behavior of the electron and hole in this system, Brus' model makes the following approximations about the system:

1. The nanocrystal is spherical, with a radius of R.

2. The interior of the nanocrystal is a uniform medium - there are no point charges or occupied spaces other than the excited electron and hole (i.e., nuclei or bound electrons).

3. The potential energy outside the nanocrystal is infinite; thus the electron and hole are always found within the nanocrystal (i.e., the surface of the nanocrystal defines the walls of the 'box').

4. The basic physical and electronic properties of the nanocrystal (i.e., dielectric constant, band gap, etc.) are the same as in the bulk material.

The Hamiltonian for a free point charge in a nanocrystal with radius R is

$$\hat{H} = -\frac{\hbar^2}{2m_q}\nabla_e^2 + \hat{V}; \qquad \hat{V} = \begin{cases} 0 & r \leq R \\ \infty & r \geq R \end{cases} \tag{1.2}$$

where m_q is the effective mass of the charge carrier ($q = e$ for electrons and h for holes) and r is the distance from the center of the nanocrystal. The solution to

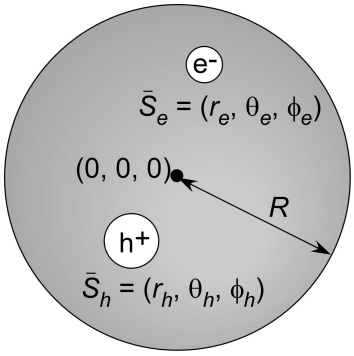

Figure 1.8: Positional terms for the particle-in-a-box model of a nanocrystal. R is the radius of the nanocrystal, and $\bar{s}_e$ and $\bar{s}_h$ are the positions of the electron and hole, respectively.

the Schrödinger equation in this case is the familiar particle-in-a-box solution to the Schrödinger equation, modified for the case of a sphere:

$$\psi_n(r) = \frac{1}{r\sqrt{2\pi R}} sin\left(\frac{n\pi r}{R}\right) \tag{1.3}$$

$$E_n = \frac{\pi^2\hbar^2 n^2}{2m_q R^2}; \qquad n \in \mathbb{N} \tag{1.4}$$

Qualitatively, (1.4) illustrates the particle-in-a-box behavior of nanocrystals. As the size of the nanocrystal increases, the potential energy of the free charge carrier decreases.

In reality, creation of an exciton in a nanocrystal involves two charges, the electron and the hole. In the case of an electron-hole pair, the Hamiltonian is

$$\hat{H} = -\frac{\hbar^2}{2m_e}\nabla_e^2 - \frac{\hbar^2}{2m_h}\nabla_h^2 + \hat{V}\left(\bar{s}_e, \bar{s}_h\right) \tag{1.5}$$

where $\bar{s}_e$ and $\bar{s}_h$ are the positions of the electron and hole, respectively, within the nanocrystal. As before, the potential energy is assumed infinite for $r > R$. For $r < R$ there are two contributions to potential energy: Coulomb attraction between the negatively charged electron and the positively charged hole, and polarization energy of the lattice surrounding the charges. The Coulomb attraction is given by

$$\hat{V}_{Coul}\left(\bar{s}_e, \bar{s}_h\right) = -\frac{e^2}{4\pi\epsilon_{nc}\epsilon_0|\bar{s}_e - \bar{s}_h|} \tag{1.6}$$

where ϵ_{nc} is the dielectric constant for the bulk semiconductor and ϵ_0 is the vacuum permittivity. The polarization energy is a solvation effect. Essentially, the electron cloud near a point charge inside a nanocrystal polarizes to better accommodate the free charge. This polarization in turn influences the energy of the second charge. The polarization term is given by

$$\hat{V}_{pol}\left(\bar{s}_e, \bar{s}_h\right) = \frac{e^2}{2}\sum_{k=1}^{\infty}\left[\alpha_k \frac{s_e^{2k} + s_h^{2k}}{R^{2k+1}}\right] \tag{1.7}$$

where

$$\alpha_k = \frac{(\epsilon - 1)(k+1)}{4\pi\epsilon_{nc}\epsilon_0(\epsilon k + k + 1)}; \qquad \epsilon = \frac{\epsilon_{nc}}{\epsilon_{ext}} \tag{1.8}$$

and ϵ_{ext} is the dielectric constant of the medium surrounding the nanocrystal. Combining Equations 1.5 - 1.8, the total Hamiltonian for the electron-hole system in a nanocrystal is

$$\hat{H} = -\frac{\hbar^2}{2m_e}\nabla_e^2 - \frac{\hbar^2}{2m_h}\nabla_h^2 - \frac{e^2}{4\pi\epsilon_{nc}\epsilon_0|\bar{s}_e - \bar{s}_h|} + \frac{e^2}{R}\sum_{k=1}^{\infty}\left[\frac{(\epsilon-1)(k+1)}{4\pi\epsilon_{nc}\epsilon_0(\epsilon k + k + 1)}\left(\frac{\bar{s}}{R}\right)^{2k}\right] \tag{1.9}$$

It is noted that as the electron and hole are confined to the same space, the s_e and s_h terms in the polarization potential of Equation 1.9 are equivalent and therefore collapsible into a single positional term, $\bar{s}$. It is further noted that from this equation, it is clear that as $R \to \infty$, the polarization term $\hat{V}_{pol} \to 0$, and the Hamiltonian in (1.9) becomes the hydrogen-like Wannier exciton Hamiltonian of the bulk.[49]

In order to evaluate the lowest energy of the electron-hole system, it is first necessary to determine the wave function for the system. This wave function must be some function of the lowest-energy wave functions of the individual charges within the nanocrystal, $\psi\left(\bar{s}_e\right)$ and $\psi\left(\bar{s}_h\right)$, as in Equation 1.3. As a first order approximation we use the uncorrelated wave function

$$\Phi_{exc}\left(\bar{s}_e, \bar{s}_h\right) = \psi_1\left(\bar{s}_e\right)\psi_1\left(\bar{s}_h\right) \tag{1.10}$$

Applying this wave function to the Hamiltonian in (1.9) and solving the Schrödinger equation, the calculated internal energy of the exciton is

$$E_{exc} = \frac{\pi^2\hbar^2}{2R^2}\left(\frac{1}{m_e}+\frac{1}{m_h}\right) - \frac{1.8e^2}{4\pi\epsilon_{nc}\epsilon_0 R} + \frac{e^2}{R}\overline{\sum_{k=1}^{\infty}\left[\alpha_k\left(\frac{s}{R}\right)^{2k}\right]} \tag{1.11}$$

Here $\langle|\bar{s}_e - \bar{s}_h|\rangle = \frac{R}{1.8}$ is the average separation of the two charges,[49,50] the first term is the kinetic energy, T, the second term is the Coulomb attraction, V_{Coul}, and the third term is the polarization energy, V_{pol}. The bar over the polarization energy term denotes the average over the wave function $\psi_1(\bar{s})$:

$$\begin{aligned} V_{pol} &= \frac{e^2}{R}\overline{\sum_{k=1}^{\infty}\left[\alpha_k\left(\frac{s}{R}\right)^{2k}\right]} \\ &= \frac{e^2(\epsilon-1)}{2\pi R\epsilon_{nc}\epsilon_0}\int_{r=0}^{R}\left[sin^2\left(\frac{\pi r}{R}\right)\sum_{k=1}^{\infty}\left[\frac{k+1}{(\epsilon+1)k+1}\left(\frac{r}{R}\right)^{2k}\right]\right]\frac{dr}{R} \end{aligned} \tag{1.12}$$

In its series-expanded form, the integral can be reduced to

$$\begin{aligned} X(\epsilon) = \int_0^1 \frac{2x^2\sin^2(\pi x)}{\epsilon+2}\Bigg[{}_2F_1\left(\left[1,\frac{\epsilon+2}{\epsilon+1}\right],\frac{2\epsilon+3}{\epsilon+1},x^2\right) + \\ + \frac{\frac{x^2}{2}\frac{\epsilon+2}{\epsilon+1}\Gamma\left(\frac{\epsilon+2}{\epsilon+1}\right)\Gamma\left(\frac{2\epsilon+3}{\epsilon+1}\right){}_2F_1\left(\left[2,\frac{2\epsilon+3}{\epsilon+1}\right],\frac{3\epsilon+4}{\epsilon+1},x^2\right)}{\frac{2\epsilon+3}{\epsilon+1}\Gamma\left(\frac{\epsilon+2}{\epsilon+1}\right)\Gamma\left(\frac{2\epsilon+3}{\epsilon+1}\right)}\Bigg]dx \end{aligned} \tag{1.13}$$

where $x = r/R$, ${}_2F_1([a,b],c,z)$ is the Gaussian hypergeometric function, given by

$$\begin{aligned} {}_2F_1([a,b],c,z) = 1 + \frac{ab}{1!c}z + \frac{a(a+1)b(b+1)}{2!c(c+1)}z^2 + \\ + \frac{a(a+1)(a+2)b(b+1)(b+2)}{3!c(c+1)(c+2)}z^3 + \ldots \end{aligned} \tag{1.14}$$

and $\Gamma(z)$ is the gamma function, defined by

$$\Gamma(z) \equiv \int_0^\infty t^{z-1}e^{-t}dt \tag{1.15}$$

The integral $X(\epsilon)$ can be solved numerically using standard mathematical evaluation programs such as Maple™ and Mathematica™. Figure 1.9 shows the dependence of $X(\epsilon)$ on ϵ. Empirically, $X(\epsilon)$ fits well to a double exponential:

$$X(\epsilon) = 0.027031 + 0.13680e^{-0.23624\epsilon} + 0.11368e^{-1.0766\epsilon} \tag{1.16}$$

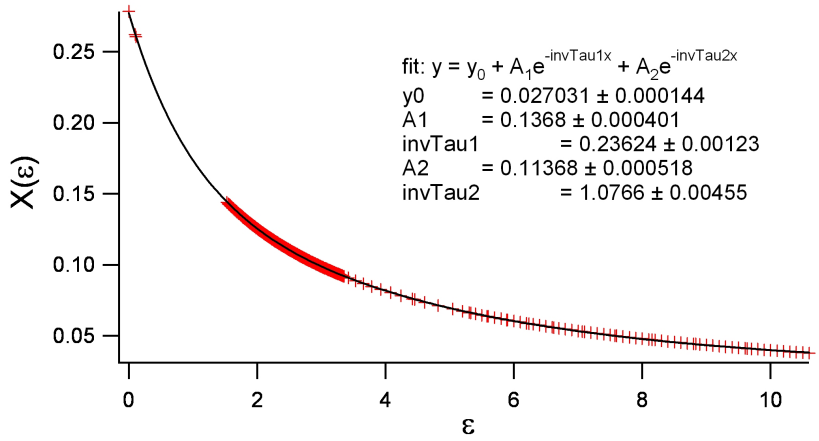

Figure 1.9: $X(\epsilon)$ as a function of ϵ, from Equation 1.13. Red markers indicate calculated values for $X(\epsilon)$, while the black line is a double exponential fit to the data.

The optical band gap, E_{opt}, can be used to compare the theoretical energy with experiment:

$$E_{opt} = E_g(\infty) + \frac{\pi^2\hbar^2}{2R^2}\left(\frac{1}{m_e} + \frac{1}{m_h}\right) - \frac{1.8e^2}{4\pi\epsilon_{nc}\epsilon_0 R} + \frac{e^2\,(\epsilon - 1)}{2\pi R\epsilon_{nc}\epsilon_0}X(\epsilon) \tag{1.17}$$

where the first term, $E_g(\infty)$, is the band gap of the bulk semiconductor; the second term is the kinetic energy of the electron and hole, T; the third term is the Coulomb attraction, V_{Coul}; and the final term is the polarization energy, V_{pol}. $E_g(\infty)$ is included because this is the potential energy required to promote an electron from the valence band to the conduction band. Figure 1.10 compares optical band gaps for CdSe nanocrystals in a low-dielectric solvent (n-decane, $\epsilon_{ext} = 1.99$) and in a high-dielectric solvent (aniline, $\epsilon_{ext} = 6.89$) calculated using Brus' model with those determined through experiment.[40,51–54] Two features of the calculated energies are notable. First, although n-decane and aniline have very different dielectric constants, the difference in the optical band gaps of the nanocrystals in the two solvents is negligible. This is because in this model the dielectric constant of the solvent only affects the polarization energy, which is the smallest term in Equation 1.17. Given the other

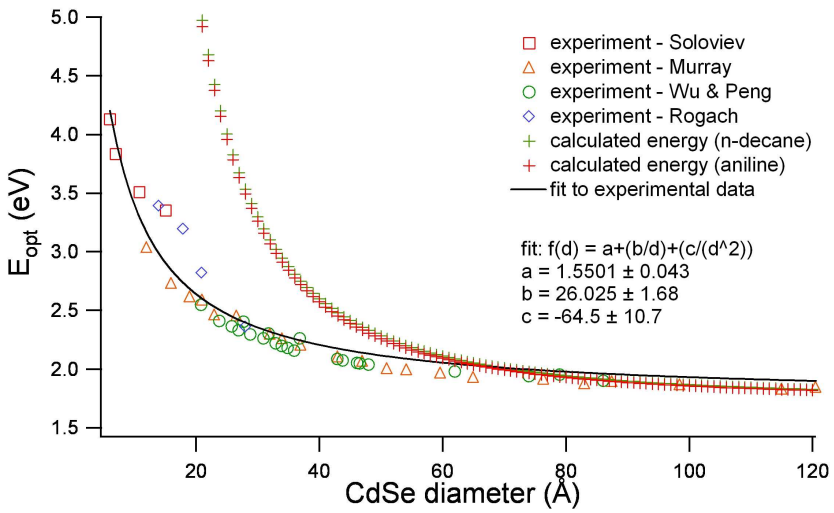

Figure 1.10: Calculated and experimental optical band gap energies of CdSe nanocrystals as a function of nanocrystal size. Band gaps were calculated according to Equation 1.17 with $E_g = 1.751$ eV, $m_e = 0.11m_0$, and $m_h = 0.45m_0$ for nanocrystals in a low-dielectric solvent (n-decane, $\epsilon_{ext} = 1.99$) and in a high-dielectric solvent (aniline, $\epsilon_{ext} = 6.89$).[46] Experimental data was extracted from Yu *et al.*,[40] Soloviev *et al.*,[51] Murray *et al.*,[52] Peng *et al.*,[53] and Rogach *et al.*[54] The experimental data are empirically fit to a simplified form of Equation 1.17 for purposes of comparison.

approximations in the model, it is sufficient to ignore the dielectric constant of the solvent and to use a standard dielectric constant for the outer medium (e.g., $\epsilon_{ext} = 1$), or to neglect the polarization energy altogether. Second, while the calculated energies match experimental results closely for large R, they deviate tremendously at small R, largely due to excessive kinetic energy (see Table 1.1). Brus attributes the failure of this model largely to the failure of the effective mass approximation above kinetic energies of about 0.5 eV.[49] Since only the kinetic energy involves effective mass, this failure certainly explains the large overestimation of kinetic energy in small nanocrystals. Other sources of error include the treatment of the exterior medium as a medium with infinite potential energy,[49] so that the wave function stops at the nanocrystal surface, the treatment of the nanocrystal as spherical with a uniform medium,[39] and the neglect of surface effects.[49] Appendix A details more accurate models that account for some of the sources of error in Brus' model; nevertheless, the model presented

Table 1.1: Calculated energetic contributions (in eV) to optical band gaps, E_{opt} (calc.), of CdSe nanocrystals. Band gaps were calculated according to Equation 1.17. At large nanocrystal diameters, the calculated energy closely matches the experimental value. As the diameter decreases, the calculated kinetic energy becomes falsely large, resulting in band gaps that are much greater than the true value, E_{opt} (expt.).

Diameter (Å)	T	V_{Coul}	V_{pol}	E_{opt} (calc.)	E_{opt} (expt.)
120	0.104	-0.041	0.013	1.83	1.84[52]
60	0.414	-0.080	0.026	2.10	1.98[40]
30	1.657	-0.163	0.052	3.30	2.26[40]
15	6.627	-0.326	0.104	8.16	3.35[51]

here provides an excellent qualitative understanding of the behavior of lowest-energy excitons using basic quantum mechanical principles.

The ultimate goal of this work is to establish a relationship between size, composition, and band gap in nanocrystals. The need for a mathematical description of the dependence of band gap on size is implicit. Clearly Brus' model is insufficient, particularly since the majority of nanocrystals in the study are in the strong confinement regime where the failure of the effective mass approximation is most prevalent. However, the model provides the form for a mathematical description. The optical band gap energy is a sum of the band gap of the bulk material, which is independent of nanocrystal diameter, the kinetic energy, which is proportional to $1/R^2$, and the potential energies (Coulomb and polarization), which are proportional to $1/R$. By allowing the proportionality constants for the $1/R$ and $1/R^2$ terms to float, a reasonably good fit to experimental data can be obtained for both CdS and CdSe (e.g., see the fit to experimental data given in Figure 1.10). Therefore, we write the dependence of band gap on size as

$$E_g(d) = E_g(\infty) + \frac{a}{d} + \frac{c}{d^2} \tag{1.18}$$

where d is the diameter of the nanocrystal. It is noted that unlike Brus' model, the parameters a and c have no physical meaning; they are empirical, allowing a

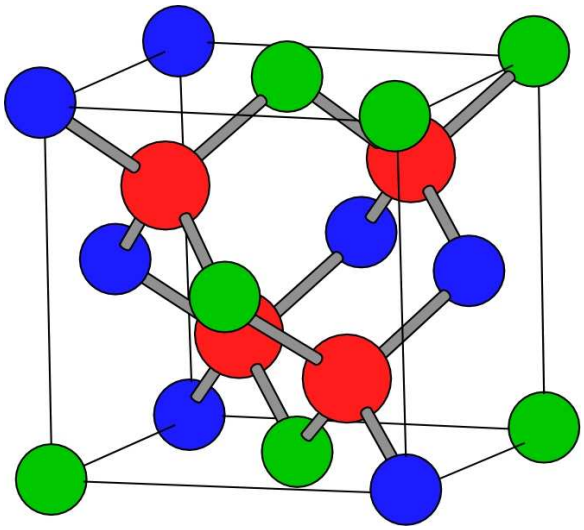

Figure 1.11: Unit cell of zinc-blende CdS_xSe_{1-x}. Cadmium atoms (red) occupy the cationic lattice sites, while the homologous sulfur (green) and selenium (blue) atoms randomly occupy the anionic lattice sites.

description of the observed behavior of the system. With a mathematical relationship between size and band gap established, we now consider the relationship between composition and band gap.

1.3 Alloys

Alloys are liquid or solid solutions of two or more metals, semiconductors, or insulators. As opposed to pure materials, alloys can exhibit a range of chemical formulae, given the same base elements. For example, brass alloys have the formula Cu_xZn_{1-x}, where x can vary, while the mineral pyrite, which is not an alloy, has the distinct formula FeS_2. Also unlike pure materials, crystalline alloys need not exhibit regular placement of the individual elements. The CdS_xSe_{1-x} studied here displays a zinc-blende lattice structure, with cadmium atoms occupying the cationic lattice sites, and sulfur and selenium randomly occupying the anionic sites (Figure 1.11). This type of alloy is known as pseudobinary because it is composed of two compound semiconductors, CdS and CdSe, even though it contains three elements, like a ternary

alloy.

As might be expected, the physical, optical, and electronic properties of alloys vary (usually continuously) with the elemental composition of the alloy. Prior to the advent of ready access to nanomaterials, whose characteristics are tunable with size, changing alloy composition was the only means of precisely tuning the desired properties of a material. In ancient times, bronze and brass were harder and more durable than pure copper. More recently, alloys have been employed in the semiconductor industry for use in photovoltaics,[55–58] light-emitting diodes,[59,60] lasing media,[61,62] and high-k dielectrics.[63,64]

Just as the properties of nanomaterials vary predictably with size, so do those of alloys. CdS_xSe_{1-x}, like most alloys, demonstrates a lattice constant, a, that changes linearly with composition:[65]

$$a(x) = xa_{CdS} + (1-x)a_{CdSe} \tag{1.19}$$

Other properties, however, do not vary linearly. In the case of band gap energies, isovalent alloys such as CdS_xSe_{1-x} generally form no new states (except when there is a large size or electronegativity mismatch between homologous atoms, such as GaP:N or GaP:Bi).[66,67] Instead, the band edges move continuously with composition according to[66]

$$E_g(CdS_xSe_{1-x}) = xE_g(CdS) + (1-x)E_g(CdSe) - bx(1-x) \tag{1.20}$$

Here the band gap is expressed as the sum of a linear combination of the band gaps of the two pure materials and a quadratic 'bowing' contribution, $\Delta E_g = bx(1-x)$, characterized by the bowing constant, b. This relationship is empirical, and in actuality alloys deviate slightly from (1.20) due to localized compositional fluctuations;[68–72] these deviations are small, however, so we base further discussions of compositional dependence of band gap on the expression in (1.20).

Bowing is caused by chemical and structural differences when an alloying atom replaces its homologous counterpart, generating a change in the overall lattice energy:[66,73]

$$\Delta E_g = \Delta E_g^{chem} + \Delta E_g^{struct} \tag{1.21}$$

The chemical contribution is due to the different electronegativities, *en*, and hybridizations, *pd*, of the homologous atoms:

$$\Delta E_g^{chem} = \Delta E_g^{en} + \Delta E_g^{pd} \tag{1.22}$$

while the structural contribution is induced by the different bond lengths, μ, and tetragonal bond angles, η, generated when placing atoms of different size in the cationic or anionic lattice sites:

$$\Delta E_g^{struct} = \Delta E_g^{\mu} + \Delta E_g^{\eta} \tag{1.23}$$

It is thus evident that the bowing effect is enhanced when homologous atoms have large differences in radii, electronegativities, or hybridizations. Indeed, bowing can be so strong that the minimum (or maximum) band gap of an alloy lies outside the range defined by its constituent materials.[32,66,73] In the majority of alloys, bowing acts to decrease the band gap below its linear value (i.e., $b > 0$), though the reverse has also been observed.[73] In CdS_xSe_{1-x}, sulfur and selenium have similar radii and electronegativities, so the bulk bowing constant, 0.3,[68,74,75] is small.

1.4 Concluding remarks

In this chapter, we have established mathematical relationships for the dependence of band gap on size in nanocrystals and the dependence of band gap on composition in bulk alloys. The question remains how these relationships combine in alloy nanocrystals. In the following chapters, we detail the synthesis of CdS_xSe_{1-x} nanocrystals. The nanocrystals are analyzed using transmission electron microscopy,

UV-visible absorption spectroscopy, Rutherford backscattering spectrometry, and X-ray diffractrometry to confirm their homogeneity and to determine size, composition, and band gap. With this information, we establish for the first time the relationship between size, composition, and band gap in alloy nanocrystals.

CHAPTER II

EXPERIMENTAL

2.1 Nanocrystal synthesis

CdSe nanocrystals were prepared by four different methods. Initially, CdSe nanocrystals were synthesized by the pyrolysis of organometallic precursors according to the method of Murray *et al.*,[52] as modified by Peng *et al.*[53] This method relied on an unknown impurity (UI) in the trioctylphosphine oxide (TOPO) solvent to produce nanocrystals with narrow size distributions; hence it is referred to as the TOPO/UI synthesis.

In 2001, the commercial synthesis of technical-grade (90%) TOPO was altered. Nanocrystals synthesized in the new TOPO no longer had the narrow size distribution that made the TOPO/UI synthesis so useful. Consequently, a new synthesis was devised by Tadd Kippeny of the Rosenthal group.[76,77] Based partly on the syntheses of Hines and Guyot-Sionnest[78] and Peng *et al.*,[79] the synthesis includes hexadecylamine (HDA) and dodecylphosphonic acid (DPA) in the solvent mixture. HDA passivates the nanocrystal surface more completely than TOPO,[78] leading to a decreased growth rate and permanent size focusing,[80,81] while DPA binds well to the Cd precursor, again slowing growth and thus promoting narrow size distributions.[79,80] The use of dodecylphosphonic acid instead of hexylphosphonic acid is unique to Kippeny's synthesis. Nanocrystals produced by this method showed excellent shape and size control, being nearly monodisperse.

The third synthesis is a modification of the TOPO/HDA/DPA method. Developed by Mike Bowers of the Rosenthal group,[8] the CdO/TOPO synthesis uses cadmium oxide as the cadmium precursor and octadecene (ODE) as a cosolvent. The octadecene serves to provide additional thermal volume to the reaction, to stabilize

the tributylphosphine used in the reaction and is thought to remove excess phosphonic acid from the reaction solution. Nanocrystals produced by this reaction were of the same quality as those produced by the TOPO/HDA/DPA method, but the reaction was slower, allowing the production of sizes that ranged from 15 - 100 Å.

The final synthesis is a modification of Peng's cadmium oxide/oleic acid (OA) synthesis.[82] The CdO/OA synthesis employs ODE rather than TOPO as a primary, noncoordinating solvent; nanocrystals produced by this method are coated with oleic acid (OA) instead of TOPO. Although this reaction proceeds much faster than the CdO/TOPO synthesis and produces lower-quality CdSe nanocrystals (less shape control, larger size distribution), it can be used to produce CdS and CdS_xSe_{1-x} nanocrystals as well as CdSe nanocrystals. Consequently, this was the primary synthesis used in the alloy experiments.[34]

2.1.1 TOPO/UI method

Syntheses were performed in a Vacuum Atmospheres dri-box under nitrogen atmosphere in order to prevent adverse reactions of the organometallic precursors with oxygen or water, as well as to minimize oxide formation on the nanocrystal surface. Tributylphosphine (TBP, 93%), TOPO (90%), and selenium powder were purchased from Aldrich. Dimethylcadmium ($CdMe_2$, 99%) was obtained from Strem Chemicals and vacuum distilled at approximately 10^{-6} Torr. Solvents were obtained from Fisher Scientific and dried and made O_2-free by refluxing in stills containing CaH_2, potassium metal, sodium metal, or NaK.

A standard synthesis follows: a 0.12 M Se precursor solution was prepared by complexing 0.096 g Se powder with 10 mL TBP by mixing. This solution was stable in nitrogen and could be stored for months without degradation. Just prior to nanocrystal synthesis the Se:TBP solution was mixed with 166 μL $CdMe_2$ to form the reaction solution. Unlike the Se precursor, the reaction solution degraded within

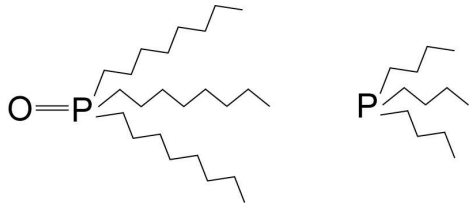

Figure 2.1: (Left) trioctylphosphine oxide and (right) tributylphosphine.

hours of preparation and had to be used quickly. 12 g TOPO were heated in the reaction vessel (Figure 2.2) to a crystal nucleation temperature of 360 °C. 6 mL of the reaction solution were quickly injected via a large-bore syringe into the heated TOPO while stirring, and the temperature was immediately reduced to 300 °C. At this temperature existing crystals continued to grow, but no new crystals nucleated, promoting a narrow size distribution. The crystals were allowed grow until the desired size was achieved, as measured by UV-visible absorption spectroscopy. The solution was then allowed to cool to room temperature (often about 25 minutes).

Different sizes of nanocrystals were synthesized by varying the reaction conditions. Larger sizes were obtained by additional injections of reaction solution at various concentrations during the growth phase of the reaction. Smaller sizes were synthesized by decreasing the concentration of the initial reaction solution or by rapidly cooling the reaction following the injection of the reaction solution.

Following synthesis, nanocrystals were isolated by methanol washing. Methanol was added to the reaction vessel until the solid nanocrystal solution had completely dissolved and nanocrystals flocculated out of solution. The mixture was then centrifuged until all nanocrystals were packed at the bottom of the vial. The liquid solution was then decanted, leaving only the nanocrystal pellet. Samples were washed three times, which has been shown to remove all excess reactants.[83] After washing, the packed nanocrystals were exposed to the atmosphere of the dri-box until dry. The vials were then sealed and stored in the dri-box.

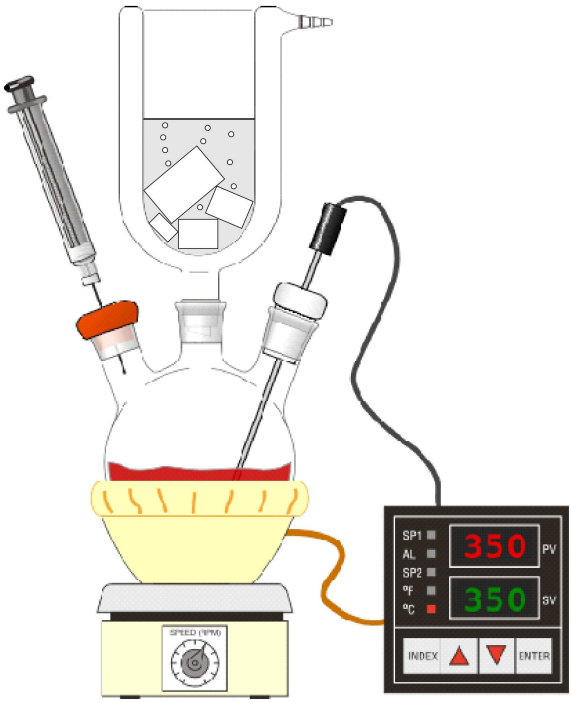

Figure 2.2: Reaction setup for CdSe nanocrystal synthesis inside the dri-box. The reaction vessel was a three-necked flask seated inside a heating mantle atop a stir plate. A stir bar inside the flask rapidly stirred the solution to help maintain a uniform concentration of reactants, thus promoting a narrow size distribution. A thermocouple, inserted through a custom-built Teflon adaptor attached to a digital temperature controller, which in turn provided power to the heating mantle, allowed precise control of the temperature within the reaction vessel. A rubber septum on the left neck allowed the introduction of the reaction solution via syringe. A condenser set in the center neck provided reflux conditions and limited the release of phosphines and organics into the dri-box atmosphere. The condenser was cooled by a mixture of tetrahydrofuran and dry ice and vented to the dri-box. Glass joints and the Teflon adapter were wrapped with Teflon tape to further reduce phosphine release into the atmosphere.

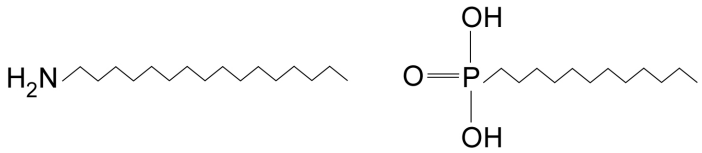

Figure 2.3: (Left) hexadecylamine and (right) dodecylphosphonic acid.

2.1.2 TOPO/HDA/DPA method

In the TOPO/HDA/DPA synthesis, the Se precursor solution was identical to that used in the TOPO/UI method - 0.096 g (0.0012 mol) Se powder dissolved in 10 mL TBP. 125 μL (0.0017 mol) of $CdMe_2$ was added to this precursor solution to form the reaction solution, which was then stored at 0 °C. It is noted that eventually the reaction solution turned green, indicating the growth of small nanocrystals, but this did not appear to affect the quality of the resultant nanocrystals. If large nanocrystals were desired, a concentrated growth solution was made by dissolving 0.96 g (0.012 mol) Se powder in 10 mL TBP, then adding 1.25 mL (0.017 mol) $CdMe_2$. The Se precursor, reaction solution, and growth solution were prepared in the dri-box. Just prior to synthesis, 6 mL of the reaction solution was drawn into a large syringe with a 12-gauge needle, primed, and placed into the dri-box antechamber to await injection conditions. The reaction medium, the primary difference between this reaction and the TOPO/UI reaction, was composed of 8.64 g TOPO, 3.57 g HDA (Aldrich, 90% Tech grade), and 0.171 g DPA, synthesized on-site by the Arbuzov reaction.[80,84]

The glassware setup is depicted in Figure 2.4. The synthesis was conducted outside the dri-box, primarily because of the phosphine contamination of the dri-box atmosphere that occurred during synthesis in the box. To prevent O_2 and water contamination during the reaction, the glassware was heated to 200°C in an oven and then assembled hot, including the addition of the reaction medium (TOPO/HDA/DPA) during the assembly. The glassware was then allowed to cool to room temperature under a steady argon gas flow.

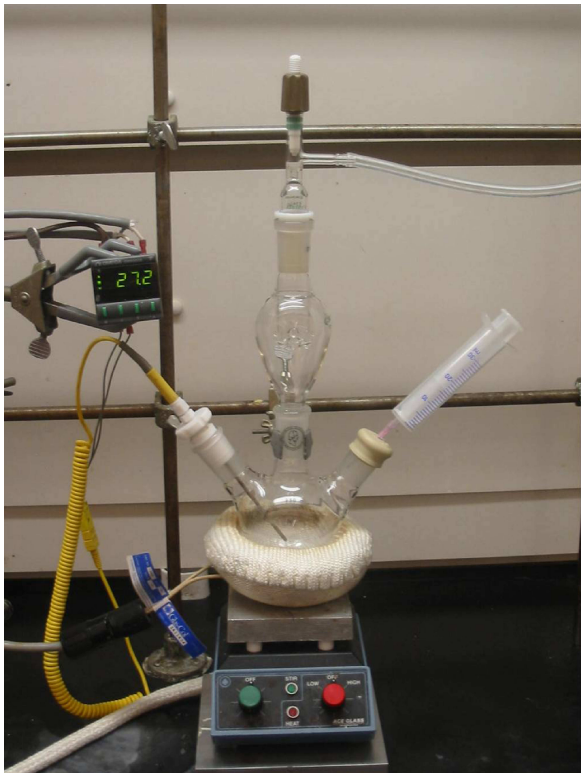

Figure 2.4: Reaction setup for CdSe nanocrystal synthesis outside the dri-box. The reaction vessel was a three-necked flask seated inside a heating mantle atop a stir plate. A stir bar inside the flask rapidly stirred the solution to help maintain a uniform concentration of reactants during the reaction and thus a narrow nanocrystal size distribution. A thermocouple, inserted through a custom-built Teflon adaptor attached to a digital temperature controller, which in turn provided power to the heating mantle, allowed precise control of the temperature within the reaction vessel. A rubber septum on the left neck allowed the introduction of the reaction solution via syringe. A rotovap bump trap attached to an argon bubbler and set in the center neck provided additional gas volume to accommodate sudden temperature changes and allowed the reaction to occur in an oxygen- and water-free environment. Teflon adapters prevented the glass joints from freezing while maintaining the argon environment.

Once the glassware had cooled, a 12-gauge needle was inserted into the septum, and the flask was heated to 150 °C over a period of 5 minutes. This heating allowed oxygen, water, and other undesirables to purge from the assembly, leaving an argon atmosphere. At 150 °C, the needle was removed and the flask was heated to a crystal nucleation temperature of 330 °C. The syringe containing the reaction solution was then withdrawn from the antechamber and injected into the reaction medium. The temperature was quickly lowered to 265 °C, and the nanocrystals were allowed to grow to the desired size, as measured by UV-visible spectroscopy. As DPA sublimes at 160 °C,[80] the heating, injection, and temperature reduction were accomplished as rapidly as possible to prevent too much DPA loss. If large nanocrystals were desired, growth solution was added gradually using a syringe pump. When the desired size was attained, the reaction was cooled to room temperature by applying compressed air to the exterior of the reaction vessel.

Following synthesis, the nanocrystals were washed three times: first in methanol, then in octanol, and finally in methanol again. The methanol washes dissolved everything except the nanocrystals and any excess HDA, which remained as a solid pellet after centrifugation. During the octanol wash, the nanocrystals solubilized, while the HDA precipitated out of solution. Therefore, following centrifugation during the second wash, the supernate was saved and the precipitate discarded. Methanol was then added directly to the octanol/nanocrystal solution to isolate the nanocrystals. Cleaned nanocrystals were stored in the dri-box until use.

It is noted that as a result of the HDA and DPA, nanocrystals grew much more slowly in this reaction than in the TOPO/UI reaction, leading to higher quality nanocrystal batches. Because of greater control provided by the HDA and the DPA, nanocrystals were more uniform in both shape and size.[76,77]

2.1.3 CdO/TOPO method

A concentrated (1.2 M) Se precursor solution was prepared by dissolving 0.96 g Se powder in 10 mL TBP in the dri-box. This solution was then diluted to 0.12 M with 90 mL octadecene (ODE; Aldrich, 90% Tech) outside the dri-box. As the phosphines in this injection solution were dilute, it was stable at room temperature in air for up to two months.

Growth reagent was prepared from a unit quantity of DPA, cadmium oxide powder (CdO; Strem, 99.999%), ODE, and 1.2 M Se solution (0.496 g, 0.128 g, 5 mL and 0.6 mL, respectively) and was scaled as needed. These reagents, less the Se solution, were heated to 250 °C under argon with vigorous stirring until the red color of the CdO disappeared, indicating the formation of cadmium phosphonate. The solution was allowed to cool to room temperature with continued stirring, followed by addition of the 1.2 M Se solution. This reagent remained as a suspension and was stable for several days at 0 °C.

The reaction medium was also mixed from a unit quantity of TOPO and HDA (7.2 g and 2.97 g, respectively), along with 0.128 g of CdO and 0.496 g of DPA, and could be scaled as necessary. These contents were heated in a glassware setup identical to that of the TOPO/HDA/DPA method (Figure 2.4) to a nucleation temperature of 330 °C. The synthesis was conducted outside the dri-box, as CdO and the Se precursor are stable in air, and as the reaction is much less violent than the $CdMe_2$ reactions. A needle was placed in the septum to allow for an argon purge until the reaction solution reached 150 °C, at which point the reaction vessel was considered water- and oxygen-free. Upon reaching 330 °C, 5 mL of the 0.12 M Se solution were swiftly injected. The temperature was immediately reduced to 265 °C. The reaction progress was followed via UV-visible spectroscopy on aliquots pulled from the reaction flask, and size was determined from the first excitonic peak. Once the growth had slowed (less than 2 nm change in the band edge in 5 - 7 minutes), growth reagent

was loaded into a syringe and added via syringe pump at a rate of $\sim$ 0.45 mL/min. For large nanocrystals, growth reagent was added until the nanocrystals achieved the desired size. To achieve very small nanocrystals (less than 20 Å), a small amount of toluene was added to the injection solution to speed the temperature reduction of the reaction mixture through evaporative cooling. For extremely small sizes (less than 17 Å), in addition to the addition of toluene to the injection, a second syringe of toluene or butanol was used to reduce the reaction temperature to less than 150 °C within 2 - 10 seconds after injection (depending on the desired size).

Synthesized nanocrystals were generally stored in the solidified reaction medium until needed. Nanocrystals were isolated by solvating the reaction mixture in a mixture of butanol and ethanol, followed by centrifugation. The resulting pellet was solvated by a small amount of octanol and centrifuged again to remove excess HDA. The supernate was reserved, and ethyl acetate and methanol (approximately 5/95 by volume) were added to precipitate the nanocrystals, which were then isolated again by centrifugation. The liquid was decanted and the vials allowed to stand inverted to remove any excess solvent. The resulting nanocrystals were then solvated in the non-polar organic solvent of choice (usually toluene or hexanes).

2.1.4 CdO/OA method

A concentrated (4 M) Se precursor solution was prepared by dissolving 0.96 g Se powder in 2.5 mL TBP in the dri-box. The vial containing the solution was sealed, sonicated using a Branson 3210 sonicator until the Se had completely dissolved, and then brought back into the dri-box and stored until use.

Injection solutions were prepared by mixing dilute (0.1 M) solutions of selenium and sulfur. The 0.1 M Se solution was prepared by adding 2.5 mL of the 4 M Se precursor solution to 97.5 mL of ODE. The sulfur solution was prepared by adding 0.321 g (0.1 mol) sulfur powder (Fisher, reagent grade) to 100 mL ODE and heating

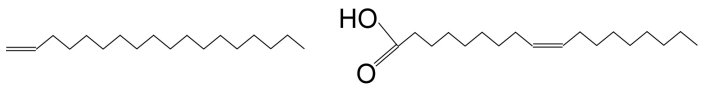

Figure 2.5: (Left) octadecene and (right) oleic acid.

to 50 - 100 °C for several hours until the sulfur had completely dissolved. Both anion solutions were stable in air at room temperature. To produce alloys of composition CdS_xSe_{1-x}, $15x$ mL of S solution and $15(1-x)$ mL of Se solution were mixed in a 25 mL Erlenmeyer flask shortly before use. 10 mL of the mixed injection solution were then drawn into a 30 mL disposable syringe with a 12-gauge needle in preparation for injection.

Without the addition of growth solution, nanocrystals were limited to less than 40 Å in diameter; thus, use of a growth solution was frequently necessary. Growth solution was prepared using sulfur powder, the 4 M Se precursor, and a cadmium oleate (Cd:OA) precursor solution. The Cd:OA solution was prepared by first mixing 3.04 g CdO powder, 24 mL OA, and 100 mL ODE in a 250 mL three-necked round-bottom flask. The flask was then incorporated into the setup shown in Figure 2.4. Initially, a 12-gauge needle was inserted into the septum, so that the system could purge. The mixture was then heated to 290 °C while stirring. When the temperature reached 140 °C, the purge needle was removed. At 275 - 280 °C, the CdO reacted with the OA to form cadmium oleate; this was visible as a disappearance of the rust-colored CdO to form a transparent, colorless solution. Residual CdO stuck to the walls of the flask was removed by loosening the clamps holding the reaction apparatus and shaking the entire apparatus back and forth. Once all CdO had disappeared, the solution was cooled to room temperature. This solution could be stored in room atmosphere and temperature for months. Over time, the Cd:OA slowly solidified to a white solid, but could be melted by heating slightly. Shortly before use, the growth solution was prepared by first mixing 31 mL (0.005 mol) Cd:OA solution and $0.16x$

g of sulfur powder and heating to 50 - 100 °C until the sulfur dissolved. The solution was removed from heat, and $1.25(1-x)$ mL of concentrated (4 M) Se precursor was added to form the final growth solution. The growth solution was then loaded into a syringe for use with the syringe pump.

To synthesize the nanocrystals, a reaction solution was prepared by mixing 256 mg (0.002 mol) CdO, 2.4 mL OA, and 10 mL ODE in a 250 mL three-necked round-bottom flask. The flask was then incorporated into the setup shown in Figure 2.4. As before, a purge needle was inserted into the septum, and the setup was allowed to purge until 140 °C, at which time the needle was removed. As in the synthesis of the growth solution, the CdO and OA reacted at roughly 275 °C, turning the solution colorless, and the setup was shaken to remove any remaining CdO from the walls. The reaction solution was then heated to an injection temperature of 310 °C.

Because of the speed of the reaction and the relatively low heat capacity of ODE, once the temperature of the reaction solution reached 310 °C, the set point on the temperature controller was lowered to 270 °C, followed by immediate injection of the injection solution. The nanocrystals were allowed to grow until approximately the desired size was reached; due to the speed of the reaction, the reaction could not be monitored by UV-visible spectroscopy, so the nanocrystals' size could only be approximated by visually observing the color of the reaction. Without the addition of growth solution, the nanocrystals stopped growing within three minutes of injection. To terminate the reaction, the heating mantle was removed, and compressed air was applied to the reaction vessel to cool the reaction solution to less than 100 °C. Alternately, a butanol injection of up to 30 mL could be used to evaporatively cool the solution when small nanocrystals were required.

Samples were washed within several hour of synthesis to avoid an adverse reaction by the unreacted precursor. Nanocrystals were washed by the addition of butanol (Sigma, reagent grade, 99.9%) and ethanol (Aaper, 200 proof) to the nano-

crystal solution. The nanocrystals precipitated out of solution, and were collected by centrifugation, discarding the supernate. The pelleted nanocrystals were then resuspended in hexanes. This procedure was repeated eight times, as excess ODE and OA adhere quite well to the precipitating nanocrystals.

The amount of butanol and ethanol required depended both on the size of the nanocrystals and on how many washings had already been completed. OA-coated nanocrystals are slightly soluble in butanol, with smaller nanocrystals being more soluble. They are insoluble in ethanol; however, oleic acid is also slightly insoluble in ethanol. Using too much butanol kept the nanocrystals from pelleting out of solution in the centrifuge, while too much ethanol caused the nanocrystals and oleic acid to form a thick oil. Generally, butanol was added to the suspended nanocrystals until just after entire solution became opaque, then ethanol was added until the nanocrystals began to flocculate or until the top of the centrifuge vial was reached (whichever came first). With small nanocrystals, a few milliliters of butanol were added (the solution did not necessarily turn opaque), then ethanol was added as before.

The CdO/OA method can be used to produce nanocrystals of any size; however, previous studies have shown that the ratio of cadmium to selenium strongly influences the focus size and final growth size of nanocrystals in CdO-based reactions.[85] Nevertheless, the ratio of Cd:anion was typically maintained at 2:1 (1:1 in the growth solution). However, we found that when making larger batches of nanocrystals, or when making particularly large or small nanocrystals, the Cd:anion ratio became more important. For large nanocrystals, the ratio of Cd:anion was increased up to 5:1, while for very small nanocrystals, the ratio was reduced to 1.2:1; further reduction of the ratio caused poor size distributions. The amount of oleic acid used scaled directly with the amount of cadmium.

White-light nanocrystals, or equivalently sized alloy nanocrystals, are cur-

rently of particular interest, and so we detail their synthesis specifically here. The reaction solution consisted of 307 mg CdO, 12 mL ODE, and 2.88 mL OA; the injection solution consisted of 20 mL of 0.1 M Se precursor. Prior to injection, the reaction solution was heated to 315 °C, and a syringe containing 30 mL of a mixture of butanol and ethanol (1:3 by volume) was placed in the septum, in preparation for injection. Once the reaction solution reached 315 °C, the heating mantle was removed, and the Se solution was injected. As soon as the Se injection was complete, the alcohol was injected, which cooled the temperature to 110 - 130 °C; simultaneously, compressed air was applied to cool the temperature of the solution to less than 70 °C. Addition of ethanol either caused precipitation of the nanocrystals, or caused a bilayer to form. If the nanocrystals precipitated, then washing proceeded normally. If a bilayer formed, then the nanocrystal layer (pale yellow) was separated from the ethanol layer using a separation funnel, and washing proceeded normally.

Once nanocrystals had been synthesized, they were characterized according to at least three analytical techniques. UV-visible absorption spectroscopy (Section 2.2) was used to determine the band gap energy. Transmission electron microscopy (Section 2.3) was use to determine average size and size distribution. Rutherford backscattering spectrometry (Section 2.4) was used to determine the elemental composition. In addition, two additional techniques, X-ray diffraction spectroscopy and fluorometry (Section 2.5) were sometimes used to provide additional insight into crystallinity and optical properties.

2.2 UV-visible absorption spectroscopy

Due to the effects of quantum confinement in nanocrystals, UV-visible absorption spectroscopy is an extremely useful tool in monitoring the growth and optical properties of nanocrystals. All absorption spectra in the experiments detailed in this thesis were obtained with a Cary 50 UV-visible spectrometer with a 1-cm path length,

liquid sample holder. Sample cuvettes were of glass or quartz as needed. Generally spectra were taken in the range 300 - 800 nm.

In order to take absorption spectra, samples were dissolved in toluene or hexanes. Before each spectrum was taken, a blank spectrum of the solvent was taken in the same cuvette. This spectrum was automatically subtracted from the spectrum of the nanocrystal solution by the Cary 50 software to obtain the nanocrystals' true spectrum.

2.2.1 Monitoring nanocrystal growth

To monitor the growth and size distribution of nanocrystals during synthesis, a small aliquot of the reaction solution was removed from the reaction vessel at periodic intervals and placed in a cuvette. Hexane or toluene was added to the cuvette both to cool the nanocrystal solution, preventing further nanocrystal growth in the cuvette, and to provide sufficient volume to obtain a spectrum. A spectrum was taken, and the nanocrystals were discarded. While it is time-consuming to use absorption spectra to obtain quantitative information about the size distribution of nanocrystals in the sample, spectra provide an excellent indication of the quality of samples - the sharper and better defined the features of the spectra are, the narrower the size distribution are likely to be (Figure 2.6).[76]

2.2.2 Nanocrystal sizing

Absorption spectra were also used to find the average diameter of nanocrystals. Since quantum confinement causes the wavelength of the first absorption feature to shift with nanocrystal size, this feature is a measure of nanocrystal diameter. Previous experiment has yielded calibration curves for CdSe and CdS that relate the wavelengths of the first absorption features to nanocrystal diameter (Figures 2.7 and 2.8). The data were semiempirically fit according to Equation 1.18 to obtain the

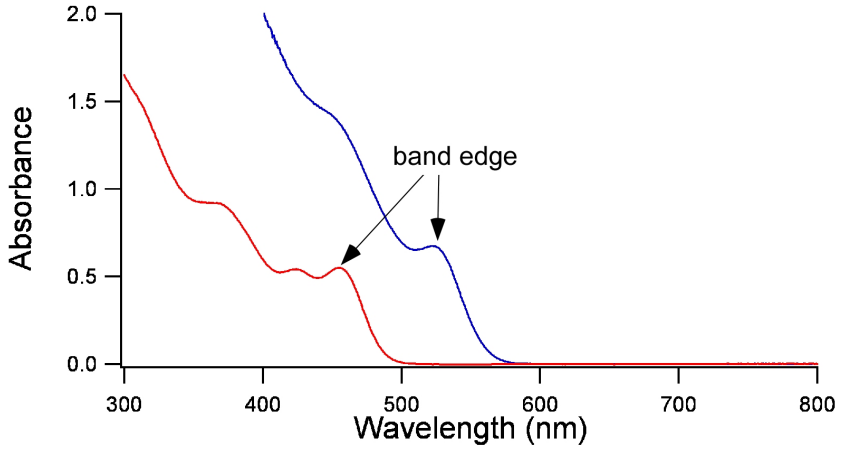

Figure 2.6: Spectra of $CdS_{0.6}Se_{0.4}$ with good (red) and poor (blue) size distributions. Nanocrystals with good uniformity of size and shape typically display a number of peaks beyond the band edge peak, while those with poor size distributions or poor shape control show fewer peaks.

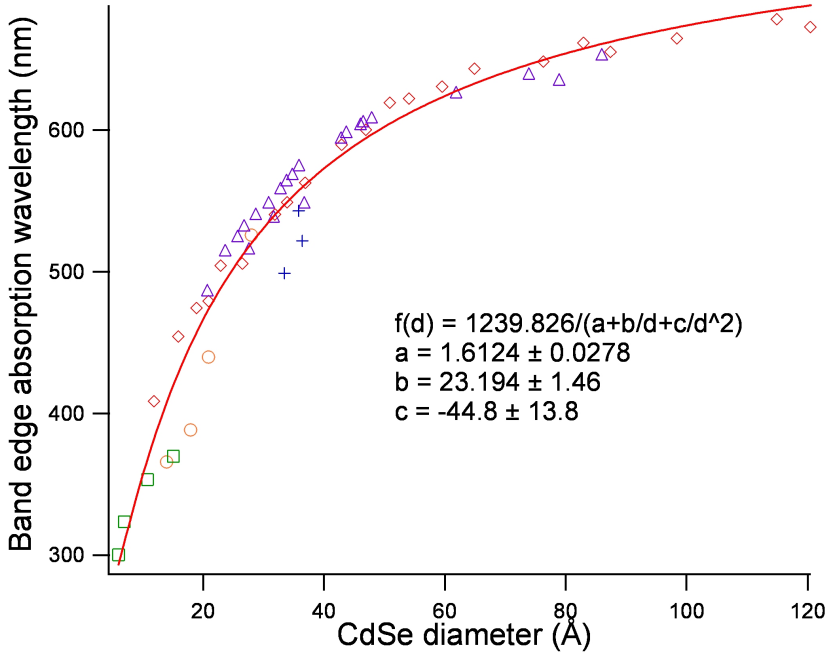

Figure 2.7: Band edge absorption of CdSe nanocrystals as a function of nanocrystal diameter. All markers are experimentally determined values: red diamonds from Murray *et al.*,[52] orange circles from Rogach *et al.*,[54] green squares from Soloviev *et al.*,[51] blue crosses from Swafford *et al.*,[34] and purple triangles from Peng *et al.*[53] and Yu *et al.*[40]

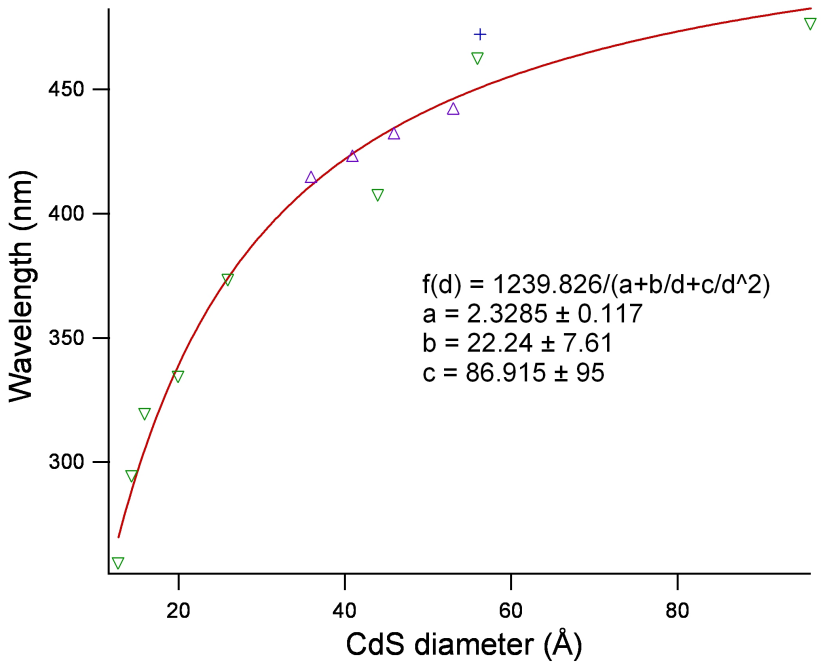

Figure 2.8: Band edge absorption of CdS nanocrystals as a function of nanocrystal diameter. Experimental values from Yu *et al.*[40] (purple triangles), Swafford *et al.*[34] (blue crosses), and Vossmeyer *et al.*[86] (green inverted triangles).

relationships

$$\lambda = \frac{1240}{1.6 + \frac{23}{d} - \frac{45}{d^2}} \tag{2.1}$$

for CdSe and

$$\lambda = \frac{1240}{2.3 + \frac{22}{d} + \frac{87}{d^2}} \tag{2.2}$$

for CdS. By using these relationships, it is possible to determine the average size of nanocrystals in a sample from the wavelength of the band edge absorption feature. It is noted that because the relationship between size and band gap was not known for the alloy nanocrystals, the alloys could not be sized based upon their spectra; instead, transmission electron microscopy was necessary (Section 2.3).

2.2.3 Size distributions

Absorption spectra can also be used to determine the standard deviation, σ_d, or size distribution of the diameters of nanocrystals in a sample. According to Klimov,[87] the inhomogeneous broadening (Γ = FWHM) of the band edge peak of nanocrystals with average diameter d is proportional to the shift in the energy of this peak, $E_g(d)$, with respect to the bulk band gap energy, $E_g(\infty)$, by

$$\Gamma = \frac{4\sigma_d}{d}\left[E_g(d) - E_g(\infty)\right] \tag{2.3}$$

In an absorption spectrum of nanocrystals, however, the high-energy side of the band edge peak overlaps peaks from higher-energy transitions. In order to obtain σ_d, we define λ_d as the wavelength of maximum absorbance (A) in the band edge peak and λ_{HWHM} as the wavelength on the low-energy side of the band edge peak at which $A_{\lambda_{HWHM}} = \frac{1}{2}A_{\lambda_d}$. In terms of wavelength, then, Equation 2.3 can be rearranged to

$$\sigma_d = \frac{d\left(\frac{1}{\lambda_d} - \frac{1}{\lambda_{HWHM}}\right)}{2\left(\frac{1}{\lambda_d} - \frac{1}{\lambda_\infty}\right)} \tag{2.4}$$

where λ_∞ = 710 nm for CdSe and 490 nm for CdS.[46] As with using absorption spectra to determine average diameter, this method of determining size distribution

relies on prior knowledge of the bulk band gap. Since there is some discrepancy in these values for bulk CdS_xSe_{1-x}, and since using transmission electron microscopy was necessary to determine average diameters for the alloy nanocrystals, it was also used to determine size distributions for these samples.

2.3 Transmission electron microscopy

High-resolution transmission electron microscopy (HR-TEM) was used to assess the quality of a batch of nanocrystals by allowing the user to examine the shape and crystallinity of the nanocrystals, as well as to determine the average size and size distribution more accurately than the absorption methods outlined above.

TEM samples were prepared as follows. CdSe nanocrystals were suspended in hexanes to a concentration yielding an absorbance of $0.05 - 0.2$ at the band edge. A drop of solution was deposited onto a 01822-F formvar-on-graphite TEM grid (Ted Pella, Inc.) held with anticapillary tweezers to prevent transfer of the nanocrystals to the tweezers. The excess liquid was then wicked off using a Kimwipe™, leaving less than a monolayer of nanocrystals on the grid ready for imaging.

HR-TEMs were performed using a Phillips CM20 200 kV TEM with a LaB_6 emission source and an optimal resolution of 2.4 Å. A complete procedure for the use of this TEM is provided by McBride.[88] A television camera was available for viewing the sample, but photographic film was used to capture images. Images were captured at 400 kx or 540 kx resolution. The higher magnification yielded clearer fringe patterns, but the TEM was calibrated at 400 kx (see below), so images taken at this resolution could be measured accurately. Alternately, lattice fringes from the CdSe nanocrystals could be used to find the measurements of various features in the images taken. It is noted that while earlier nanocrystal images were obtained by the author, images of the alloy nanocrystals were taken by James McBride of the Rosenthal group.

Nanocrystal imaging through TEM was the definitive test for whether samples were of sufficient quality for further experimentation. Although UV-visible spectroscopy is a good indicator of uniformity of size and shape, it does not yield insight into the exact shape of the nanocrystals, nor degree nor type of crystallinity. TEM clearly shows the shape of the nanocrystals, and as a coherent imaging technique, it shows coherent patterns, or 'fringes', within the nanocrystals only when there is a high degree of crystallinity. Each sample used in the experiments detailed in this work was first screened by TEM for roughly spherical shape, good size distribution, and good crystallinity.

2.3.1 Nanocrystal sizing

Once a sample appeared to be of sufficient quality, prints of TEM images taken at 400 kx were used to determine the average diameter and size distribution. The prints were scanned into Canvas 9™, a technical drawing program, and the image contrast was heightened using the 'levels' option as necessary. By measuring some feature on the scanned image, generally one of the numbers printed on the image, and comparing it to the length of the same feature on the original negative, the scaling between image and negative was determined. This scalar was then multiplied by the magnification of the negative to obtain the scale of the scanned features to the real features imaged by the TEM. Next, $200 - 300$ nanocrystals per sample were measured along the long axis using Canvas 9's measuring tool. To avoid biasing the sample, all nanocrystals in a given area of each print were sized, without regard to the clarity of individual nanocrystals. Since smaller nanocrystals show less contrast, measuring only nanocrystals with good contrast might result in an erroneously large measured average diameter. To avoid measuring the same nanocrystal more than once, a number was placed over each nanocrystal as it was measured. Figure 2.9 shows an example of measured nanocrystals.

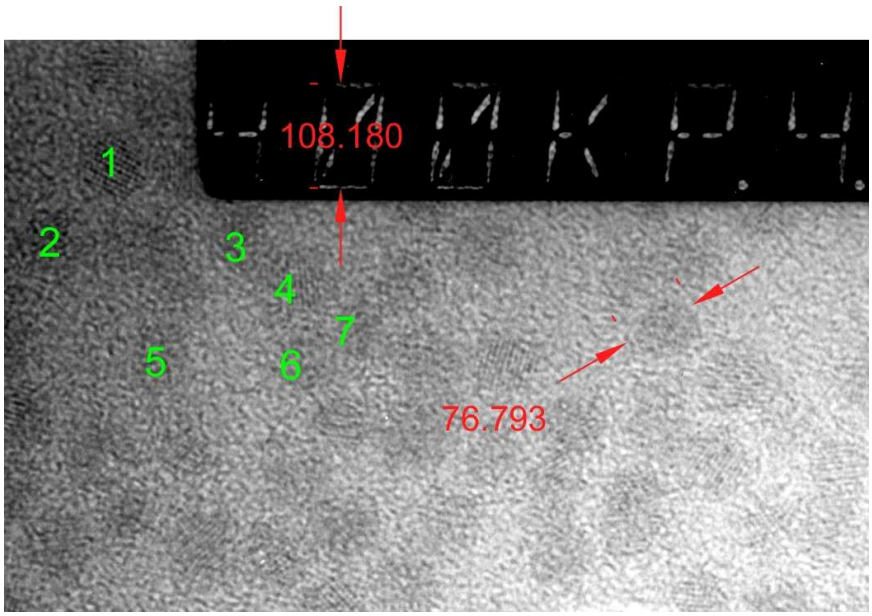

Figure 2.9: Nanocrystal sizing using calibrated images. In this case, a "0" in the scanned image measured 10.7 mm, while the corresponding length on the negative was 2.72 mm, giving an image-to-negative scale of 0.254 and an image-to-true feature scale of 102,000 at a TEM magnification of 400 kx. As each nanocrystal was measured, it was numbered to prevent multiple measurements. The lengths shown in the image have units of Ångstroms.

Once sufficient nanocrystals had been measured, the measured image diameters were imported into Igor Pro™, a data analysis program, as a data 'wave' (column). The image diameters were then divided by the magnification scalar determined above to obtain the true nanocrystal diameters. The extrema of the diameters were identified, and the diameters were histogrammed into a new wave. The range of the new wave was set at least 5 Å greater than the maximum diameter and less than the minimum diameter. The bin size was set to 0.5 Å. Finally, the histogram of the diameters was fit to a Gaussian to obtain the average and standard deviation of the diameters.

This method of sizing nanocrystals is more time consuming than sizing using UV-visible absorption spectra (Section 2.2.2), but it is a more accurate method because it directly measures the nanocrystals. In addition, it does not rely on the presence of fringes, as does sizing through counting fringes (detailed below), so the quality of the image need not be quite as good.

2.3.2 TEM calibration

The nanocrystal sizing technique described above relies on an accurate calibration of the TEM magnification. To verify that the 400 kx magnification setting on the TEM was correct, three samples of CdSe nanocrystals were sized assuming a magnification of 400 kx. The measured sizes were then compared to the CdSe calibration curve given in Figure 2.7 and were found to be significantly different than the literature-predicted values. As a result, the true magnification was determined using the spacing of fringes in CdSe nanocrystal images.

TEM is a coherent imaging technique; properly oriented crystalline lattices create interference patterns in the transmitted electrons, generating periodic light and dark patterns in the images, or lattice fringes. These fringes have a characteristic spacing that depends on the type and orientation of the crystal. In wurtzite

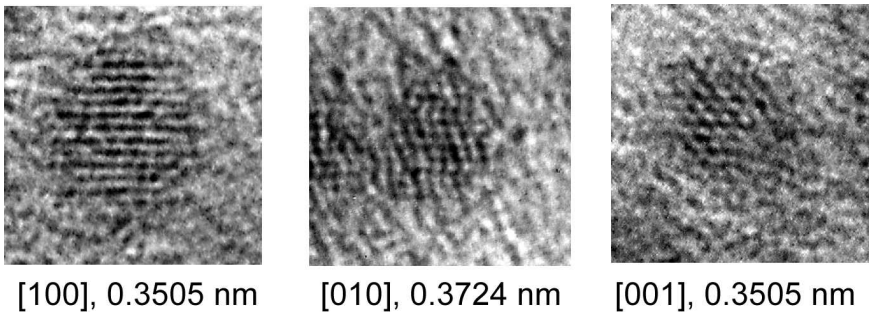

Figure 2.10: Three orientations of wurtzite CdSe nanocrystals in TEMs. The spacing between nearest-neighbor fringes is listed beside each orientation. Spacings were obtained from Kadavanich.[89]

CdSe nanocrystals, which are produced by the TOPO/UI, TOPO/HDA/DPA, and CdO/TOPO syntheses, the three most common orientations observed are the [100], [010], and [001] faces (Figure 2.10). The [100] orientation shows parallel lines orientated perpendicular to the C_3 axis; the spacing between these lines is 3.505 Å. The [010] orientation shows individual spots organized in rows perpendicular to the C_3 axis, and zig-zagging parallel to the C_3 axis; the spacing between a spot on one horizontal row and its nearest neighbor on an adjacent row is 3.724 Å. The [001] orientation shows a hexagonal array of spots perpendicular to the C_3 axis; the spacing between adjacent spots is 3.505 Å. Zinc-blende CdSe, the product of the CdO/OA synthesis, commonly shows only the [100] orientation, with a fringe spacing of 3.505 Å. (It is noted that the wurtzite and zinc-blende conformations are both close-packed crystal structures that differ only in the stacking order; the distance between atoms remains constant, resulting in identical fringe spacings in the [100] orientation.)

To determine the true TEM magnification, Canvas 9™ was used as before to measure the distance between n fringes in a CdSe nanocrystal in the [100] orientation. Because the spacing between successive fringes is known to be 3.505 Å, the true distance measured was $3.505n$ Å. As before, by measuring some feature on the scanned image and comparing it to the length of the same feature on the original negative, the scaling between image and negative was determined. The true distance between

fringes was then divided by the image-to-negative scalar to obtain the magnification of the TEM. This process was repeated for 200 nanocrystals, and the calculated TEM magnifications from each measurement were averaged to obtain a calibrated TEM magnification of 414 kx. Although this value is only 3.5% greater than the stated magnification, it profoundly altered the bowing constant determined in this work, and so was a critical step in sizing the nanocrystals.

It is noted that counting fringes can also be used to size nanocrystals. By counting the number of fringes across a nanocrystal, it is possible to determine directly the diameter of the nanocrystal.[89] In some respects, this method of nanocrystal sizing is the most accurate. Lattice constants are largely independent of size,[52,90] and counting fringes does not rely upon the accuracy of the TEM's calibration. However, in any TEM image, the majority of nanocrystals lie on the substrate at an angle inconducive to generating clear fringes; moreover, nanocrystals actually begin to move off-axis when subjected to bombardment by the electron beam for very long, so that fringing may be lost.[88] Therefore, this method of sizing is more difficult than measuring calibrated images. In addition, it has been found that often the surface of the nanocrystals has a thick layer of disorganized material (oxide or disordered semiconductor), preventing fringing near the surface.[76,91] The lattice constants of the alloy nanocrystals depend on composition (e.g., Equation 1.19 in Section 1.3), so that an error in the experimentally determined composition would necessarily impact the measured diameters. Finally, TEM images of the alloy nanocrystals often evinced a less coherent fringe pattern than in wurtzite CdSe, due to a different nanocrystal shape or defects in the crystals. As a result, this manner of nanocrystal sizing was rejected in favor of the sizing technique discussed in Section 2.3.1.

2.4 Rutherford backscattering spectrometry

Rutherford backscattering spectrometry (RBS) is a technique in which the energies of light ions scattered inelastically off nuclei in a sample are used to determine the quantity and placement of different elements in the sample (see Feldman and Mayer[92] for a detailed description). The technique is extremely sensitive, and can detect the presence of atoms in picomolar quantities[93] or the presence of films as thin as 20 Å.[94] In the experiments presented here, RBS was used both to quantify the chemical composition of nanocrystals and to quantify the thicknesses of the nanocrystal layers in SHG samples (Appendix G).

2.4.1 Sample preparation

Samples upon which SHG had previously been run, such as Si/CdSe or Si/SiO_2, were used as made. Otherwise, samples were prepared by depositing nanocrystals on a conductive substrate: pyrolytic graphite (Carbone of America) or Si wafers (University Wafer) cut to approximately 1 cm^2. The choice of substrate was dictated by the qualities of the nanocrystal sample. Generally, graphite was the substrate of choice because carbon is a lighter element than silicon, which allowed the identification and quantification of elements heavier than carbon without resorting to channeling experiments (see Feldman and Mayer[92] for a description of channeling). However, the graphite had a far rougher surface than mirror-finish Si, so Si was used when sample roughness using graphite yielded poor quality spectra. In addition, a Si substrate was employed when attempting to quantify the amount of carbon in a sample, or when the solvent needed to dissolve the sample material was incompatible with graphite. For example, TiO_2 nanocrystals generally dissolve only in polar solvents, such as water, which cannot wet a nonpolar graphite surface. The native SiO_2 on the surface of Si normally accepts polar solvents, and treatment with HF to remove the SiO_2 layer, as in Appendix G, yields a hydrogen-passivated surface that accepts nonpolar solvents.

Only well washed nanocrystals could be analyzed by RBS. Excess surfactant leaves an insulating coating on the substrate, which causes peak broadening and can change the energy signatures of the different elements,[94] while excess starting material causes the experimentally determined areal densities of Cd, Se, S, etc., to be non-representative of the nanocrystals in the sample. Taylor *et al.* established that three washes are sufficient to remove any undesirables from TOPO-capped nanocrystals, without washing so many ligands from the surface of the nanocrystals that solubility becomes problematic.[95] Our own experiments established that at least six washings were required for OA-capped nanocrystals.

To prepare RBS samples, clean nanocrystals were diluted to an optical density of 0.6 - 0.8 in a volatile solvent, usually hexanes, that also wet the substrate (without beading). Next, a few drops of the solution were placed on the substrate - just enough to completely wet the surface. The solvent was wicked off by touching the corner of the substrate with a Kimwipe™, leaving a uniform coating of nanocrystals on the substrate without the formation of drying marks (indicative of surface roughness).

It is noted that because RBS results in the implantation of ions in the sample and the disruption of crystalline structures, samples could not be used in further experiments following elemental analysis.

2.4.2 Data collection

RBS was performed using a custom setup. A 2.0 MeV Van de Graaf generator (set to E_{lab} = 1800 keV for these experiments) ionized and energized a gas source, usually ^{4}He. The resultant ion beam was directed with magnets down a beam line, through a 1 mm aperture to the sample. A current of around 10 nA on the Faraday cup, which measured the current carried by the beam, was sufficient for characterization of both thin film and nanocrystal samples. Backscattered ions were collected at an angle of $\theta = 176^\circ$ with a solid state detector. Experiments were carried out

in high vacuum, ($< 10^{-6}$ Torr). The RBS experiment was controlled by a data collection program written in Igor Pro™ by members of the Feldman research group in the Department of Physics and Astronomy. A spectrum of a bismuth standard with an areal density of bismuth of 4.77×10^{15} cm^{-2} was always taken at the beginning of each day, both to make sure that the RBS experiment was working properly (since the spectrum of this standard was known), and to calculate the detector solid angle, a parameter necessary for later calculations.

Since the experiment recorded backscattered ions at all energies simultaneously, data collection was controlled by setting a limit on the total charge accumulated on the sample. This limit was defined by the user, and could be changed during the scan as needed. Unless the experimental setup changed somehow during the course of the scan (e.g., if the detector heated up), the recorded spectrum was the same at all times, save that the signal-to-noise ratio improved with increasing time. The detector counted the number of backscattered ions ('counts') as a function of backscatter energy ('channel'); thus, the experiment displayed Poisson counting statistics, so that the error in the number of counts was the square root of the number of counts.[96] Because the calculated areal density of an element in a sample is proportional to the number of counts, to obtain an error of $< 5\%$ in the areal density at least 1000 counts were needed for each of the elements of interest. Generally, scans were begun with the total charge limit set at its default value of 2.000 μC and increased periodically by the user during the scan until the requisite counts had been accumulated (generally $2 - 50$ μC).

2.4.3 Data analysis

RBS yields a spectrum of the number of backscattered ions as a function of channel number, which is directly proportional to the energy of the backscattered ions. This spectrum can be translated into the areal densities of different atoms in a sample. The densities can be found in two ways. The first way is to use the areas

under the peaks in a spectrum and the mathematic principles of RBS to calculate the densities by hand. This method is the most accurate, but it requires that the spectrum be very clean and that the layer(s) being analyzed be fairly thin - less than several hundred Ångstroms. The second method is to use a modeling program. Modeling is not quite as accurate as first-principles calculations, but it can be used on a much wider range of spectra. In this work we occasionally used the modeling program SIMNRA. The reader is referred to the SIMNRA manual[97] for a discussion on the program; the remainder of this section is devoted to the phenomenological calculations.

Figure 2.11 shows four spectra representative of the range of RBS spectra obtained during this work. Spectrum (a) shows an ideal spectrum of CdS_xSe_{1-x} nanocrystals on a graphite substrate. Peaks are separated and roughly Gaussian in shape, indicating that the nanocrystal film is thin and relatively smooth. In this case, the areas under the peaks are representative of the true areal densities of the atoms in the sample, and hand calculations could accurately calculate areal density. Spectrum (b) is of a SHG sample, 1.9 layers (as determined by RBS) of 80 Å CdSe nanocrystals on Si. The peaks appear nearly Gaussian, but with large low-energy tails, indicating a thin sample, but one with surface contamination or roughness. Because of the tails, the peaks overlap to an extent, making a determination of the areas under the peaks, and therefore the areal densities, difficult; this spectrum would best be analyzed using a modeling program. Spectrum (c) is of a commercial sample of a 300 Å SiO_2 layer on *p*-doped Si. The SiO_2 layer is very smooth, as evidenced by the lack of tailing, but it is thick enough that the O peak appears as a plateau rather than a Gaussian peak. The leading edge of the Si peak is Si from the SiO_2 layer, while a second edge near channel 210 shows the beginning of backscattering from Si in the substrate. It is noted that the dopant in the substrate, phosphorus, is not present in quantities sufficient to register by RBS. To accurately determine the areal density of oxygen in

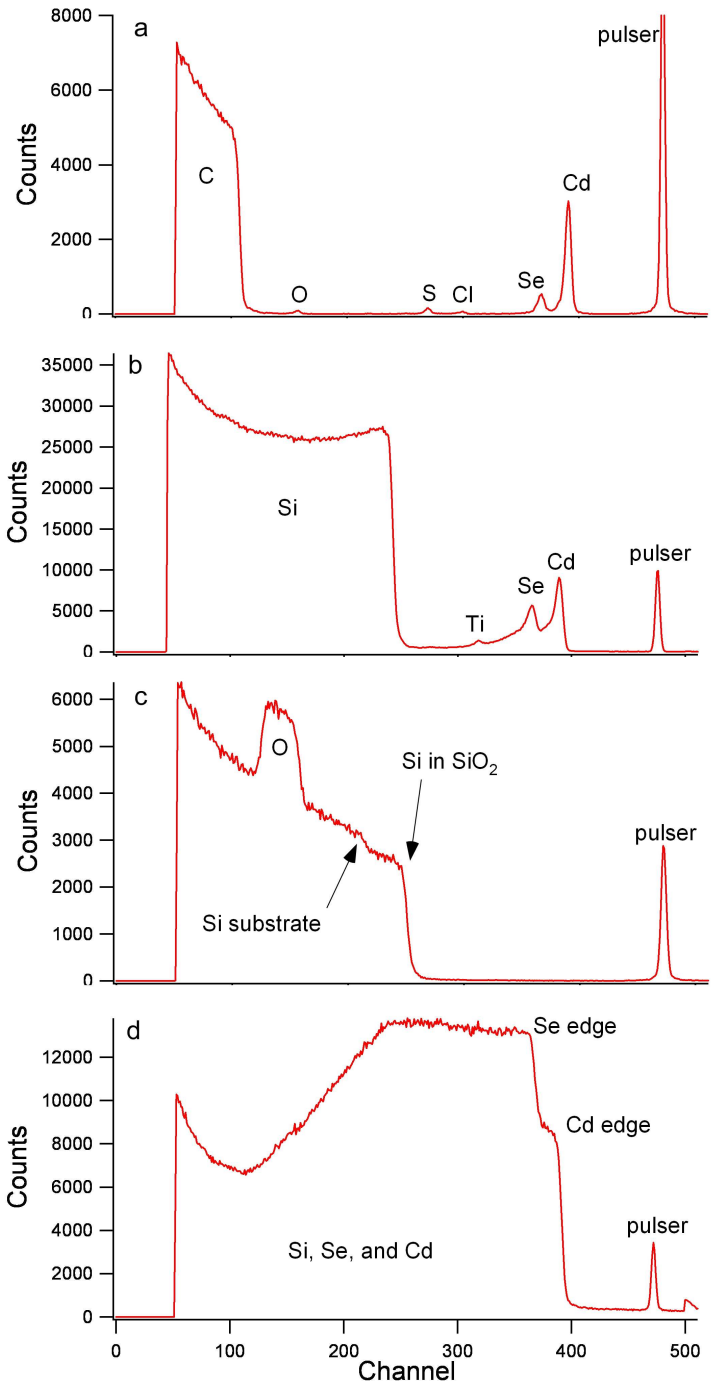

Figure 2.11: Typical RBS spectra. The bottom axis, channel number, is proportional to the energy of the backscattered ions.

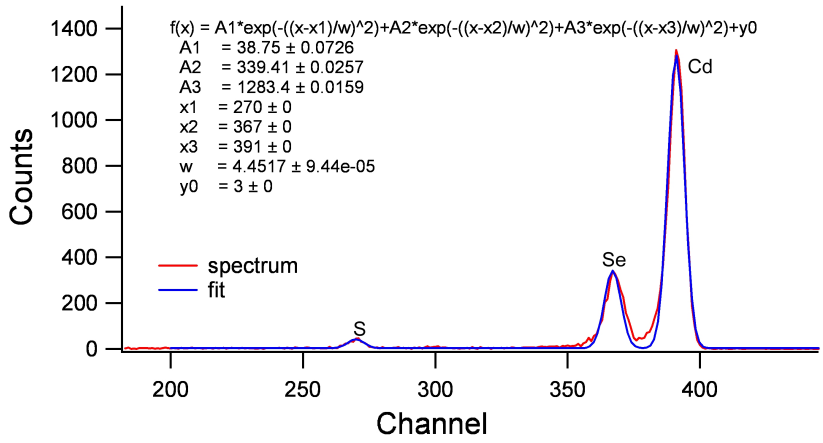

Figure 2.12: RBS spectrum of $CdSe_{0.67}S_{0.33}$ alloy nanocrystals fit to a sum of Gaussians. In this case, because of the small number counts in the S peak, it was necessary to fix the background noise. Nanocrystals were synthesized by Lauren Weigand of the Rosenthal group.

this sample, a modeling program would be needed. Spectrum (d) is of a thick layer of CdSe nanocrystals on Si. In this case, the layer of nanocrystals is thick enough that the Cd and Se peaks are plateaus rather than Gaussian in shape and blend into the Si plateau. As with spectrum (c), this spectrum needed to be fit using a modeling program.

Areal density

If an RBS spectrum contained peaks that were mostly Gaussian in shape, then the area of each peak was found using Igor Pro™, either by using the 'AreaXY' feature, which directly calculated the area under each peak, or by fitting the peaks to a sum of Gaussians (Figure 2.12). The latter approach was generally employed when two peaks (usually Cd and Se) overlapped.

Once the area of each peak of interest was known, the areal density, N_x (atoms·cm^{-2}), of element x in the thin film, was found by:[94]

$$N_x = \frac{(A_x)\,(DTR)\,(C_{Bi})\,(e)}{(Q)\,(\Omega)\left(\frac{\sigma}{\sigma_R}\right)_x(\sigma_x)} \tag{2.5}$$

Here e is the fundamental charge of an electron; A_x is the area of the peak ; DTR is the dead time ratio, calculated by dividing the 'true time' by the 'live time', both of which are listed in the history panel of the data file (DTR > 1); C_{Bi} is the bismuth correction factor, assumed to be 1; Ω is the detector solid angle in steradians, determined each time RBS was performed using the bismuth standard; Q is the integrated charge in Coulombs, listed in the history panel of the data file; $\left(\frac{\sigma}{\sigma_R}\right)_x$ is the non-Rutherford correction factor, determined by

$$\left(\frac{\sigma}{\sigma_R}\right)_x = 1 - \frac{0.049 Z_{ion} Z_x^{\frac{4}{3}}}{E_{lab}} \tag{2.6}$$

where Z_{ion} and Z_x are the atomic numbers of the backscattered ion and target element x, respectively, and E_{lab} is the energy of the ion beam in keV (E_{lab} = 1800 keV in the experiments detailed here); and σ_x is the Rutherford cross-section for element x, calculated by

$$\sigma_x = \frac{(\sigma_R)_x}{E_{lab}^2} \times 10^{-24} \tag{2.7}$$

where $(\sigma_R)_x$ is the Rutherford cross-section, given by[94]

$$(\sigma_R)_x = \left[\left(\frac{Z_{ion} Z_x e^2}{4E_{lab}}\right)^2\right] \frac{4\left[\sqrt{m_x^2 - m_{ion}^2 \sin^2\theta} + m_x \cos\theta\right]^2}{m_x \sin^4\theta \sqrt{m_x^2 - m_{ion}^2 \sin^2\theta}} \tag{2.8}$$

where m_{ion} and m_x are the masses of the backscattered ion and target element, respectively, and θ is the backscatter angle (176° in the experiments presented here). Tabulated Rutherford cross-sections can also be found in the *Handbook of Modern Ion Beam Materials Analysis*.[94]

The bismuth standard used in these experiments had an areal density of $N_{Bi} = 4.77 \times 10^{15}$ atoms·cm^{-2}. Thus, between the experimental values determined by taking an RBS spectrum of the standard and the tabulated values, Equation 2.5 could be rearranged to solve for the detector solid angle. Since Ω remained the same as long as the ion beam was not moved, once Ω was calculated using the bismuth standard, it could be used to calculate areal densities from RBS spectra taken of any sample the same day.

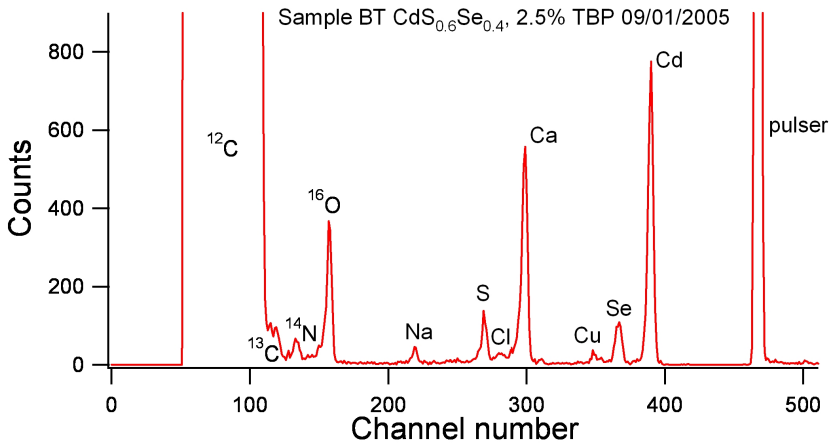

Figure 2.13: Impurities in RBS scan of $CdS_{0.6}Se_{0.4}$ nanocrystals. In this sample, numerous metal impurities were unexpectedly detected by RBS. The metals were identified using Equations 2.10 - 2.11, which allowed them to be traced to the butanol used to clean the nanocrystals. As a result of this scan, the type of butanol used in the cleaning process was changed to one that had fewer contaminants.

Of course, Equations 2.5 - 2.8 rely on physical properties (m_x and Z_x) specific to the element of interest, so it was necessary to identify correctly each peak in the spectrum. The x-axis in RBS spectra corresponds linearly to the energy of the backscattered ions. Since ions scattering off heavier nuclei have greater energy than those scattering off lighter nuclei, the elements in an RBS spectrum appear from left to right in increasing atomic mass. Thus, except for the 'pulser' peak, which is always the rightmost peak and does not correspond to any element, cadmium always appeared as the rightmost elemental peak in any nanocrystal sample, followed by Se, and so on, because Cd was the heaviest element, and Se the next heaviest. Most of the time, *a priori* knowledge of the sample composition was sufficient to identify different elements in the spectrum without resorting to calculations.

Identification of unknown elements

Occasionally, an unanticipated impurity showed up in a spectrum and needed to be identified (e.g., Figure 2.13). To identify the element, the channel numbers had

to be converted to an energy scale. First, the channel numbers for two known peaks, preferably far apart in the spectrum, were identified (e.g., Cd and the leading edge of C in a sample of CdSe on graphite). Next, the kinematic factor was calculated for each of the known elements by

$$K_x = \left[\frac{\left(m_x^2 - m_{ion}^2 \sin^2\theta\right)^{\frac{1}{2}} + m_{ion}\cos\theta}{m_x + m_{ion}} \right]^2 \tag{2.9}$$

It is noted that tabulated values for K_x are also available.[94] Since K_x is also defined as

$$K_x \equiv \frac{E_x}{E_{lab}} \tag{2.10}$$

where E_x is the energy of the ions backscattered from element x, the kinetic factors were then used to calculate the backscatter energies corresponding to the channel numbers of the known elements. Once these energies were determined, a line equation of the form

$$E = mN_{ch} + b \tag{2.11}$$

was used to convert channel number (N_{ch}) to energy for all peaks in the spectrum. Next, the energies of the unknown peaks and Equation 2.10 were used to calculate the kinematic factors for the unknown element. Finally, the masses of the unknown elements were calculated by Equation 2.9, providing a means of identifying the elements; alternately, the elements were identified by matching K_x to the tabulated values.

Nanocrystal composition from RBS

Once the areal densities of each of the elements of interest had been determined, it was possible to calculate a number of compositional parameters. In the alloy experiments, RBS was used primarily to determine the relative amounts of cadmium, selenium, and sulfur in the nanocrystals. These elements were unique to the nanocrystals themselves; they were not present in the ligands or as impurities in the

solvents used in cleaning or solvating the samples. RBS analysis of the waste material further verified that six washes were sufficient to remove any unreacted precursors, so the areal densities of cadmium, selenium, and sulfur detected by RBS were reflective of the relative amounts of cadmium, selenium, and sulfur in the nanocrystals. The concentrations of the three component elements were found by dividing the areal densities of each of the elements by the sum of the areal densities of sulfur and selenium.

Provided that there is at least one unique element, other quantifications are also possible. In particular, equations were developed to calculate the surface coverage of a nanocrystal by a specific ligand and to calculate the thickness of an inorganic coating, or shell, in core-shell nanocrystals. Results based on these equations first appeared in Rosenthal *et al.*,[18] and have been used since in a variety of other publications by the Rosenthal group. These calculations are detailed in Appendix B.

2.5 Fluorometry and X-ray diffractrometry

UV-visible absorption spectroscopy, transmission electron microscopy, and Rutherford backscattering spectrometry were the three key analytical techniques used in the alloy experiments, because they yielded the band gaps, diameters, and compositions of the alloy samples, respectively. Consequently, these techniques were performed on every sample. Two additional techniques, fluorometry and X-ray diffractrometry (XRD) were also performed on a more limited basis to provide additional insight into the behavior of the alloy nanocrystal. Fluorometry revealed the static emission spectra of the nanocrystal samples, which are of interest for potential light-emitting applications (LEDs, fluorescent labels). XRD yielded the crystallinity of the nanocrystals, as well as their lattice constants.

Fluorometry was performed on an ISS PC1 photon counting spectrofluorometer. Sample preparation was identical to that for absorption spectra. Both photoluminescence (PL) and photoluminescent excitation (PLE) spectra were performed.

PL spectra were obtained with an excitation wavelength of 400 nm and an emission range of $425 - 800$ nm. PLE spectra were obtained with an emission wavelength set to the maximum of the band edge emission as measured by PL and an excitation range of 300 nm through the emission wavelength.

X-ray diffraction (XRD) scans were obtained using a Scintag X_1 $\theta/2\theta$ automated powder X-ray diffractometer with a Cu target ($\lambda = 1.54056$ Å), a Peltier-cooled solid-state detector, and a zero-background, Si(510) sample support. Nanocrystals were precipitated out of solution and were spread on the support while still wet. XRD scans were taken in the range $2\theta = 20^\circ - 70^\circ$ over a period of four hours. All XRD was performed by Tony Watt of the Rosenthal group.

CHAPTER III

RESULTS AND DISCUSSION

3.1 On achieving homogeneity

(*It is noted that the initial work into developing the alloy synthesis was performed by Lauren Weigand and Michael Bowers of the Rosenthal group. However, because it is not published elsewhere and is pertinent to the project, it is summarized here.*)

In order to synthesize homogeneous CdS_xSe_{1-x} nanocrystals, sulfur and selenium must be added at the same rate to the growing nanocrystals. While the exact mechanisms of nanocrystal nucleation and growth are not known,[85,98–100] and the kinetics are debated,[82,99] it is reasonable to assume that the reactivities of cadmium monomer toward the two anions on the nanocrystal surface should not be markedly different, given that sulfur and selenium are isoelectronic and have very similar Lewis basicities. If the reactivities were very different, it is likely that a homogeneous alloy would be difficult if not impossible to achieve. Assuming that the rate of addition of cadmium to the growing nanocrystal is largely independent of the anion species to which it binds, and assuming that the rates of addition of sulfur and selenium obey first-order kinetics with respect to anion concentration, then the ratio of these rates is proportional to the ratio of the concentrations of sulfur and selenium:

$$\frac{\frac{d[\text{AS-S}]}{dt}}{\frac{d[\text{AS-Se}]}{dt}} = \frac{k_1\,[\text{AS}]\,[\text{S}]}{k_2\,[\text{AS}]\,[\text{Se}]} = \frac{k_1}{k_2}\frac{[\text{S}]}{[\text{Se}]} \tag{3.1}$$

Here AS is an available site for anion bonding, and k_1 and k_2 are rate constants. This model of growth kinetics suggests two means of balancing these rates. For the rates to remain identical throughout nanocrystal growth, either the concentrations of sulfur and selenium must not change significantly during growth, or k_1 and k_2 must

be identical.

Initially, a cadmium-limiting synthesis was attempted, because it was thought that manipulating the concentrations of the primary reactants (S, Se, and Cd) was easier than manipulating a host of other reaction conditions. This approach had previously been used successfully to produce $CdSe_xTe_{1-x}$ nanocrystals, using an eight-fold excess of anion to cadmium.[32] Using the TOPO/HDA/DPA synthesis detailed in Section 2.1.2, CdSe nanocrystals were synthesized, varying both the ratio of cadmium to selenium and the ratio of DPA to cadmium. The original synthesis had molar ratios of 1.42:1 Cd:Se and 0.67:1 DPA:Cd and produced high-quality nanocrystals that were nearly uniform in size and shape. However, when the Cd:Se ratio was dropped to 0.25:1, i.e., the reaction was made cadmium-limiting, the reaction either failed to progress when the DPA:Cd ratio was small (0:1) or displayed uncontrolled growth when the DPA:Cd ratio was larger (1:1 and 3.8:1). These results are summarized in Figure 3.1.

The disparate behaviors of the reaction with DPA concentrations underscores the importance of this molecule in controlling the nucleation and growth of CdSe nanocrystals. With a high DPA:Cd ratio (3.8:1), small nanocrystals nucleated with an acceptably narrow size distribution. However, they soon began to grow rapidly and uncontrollably, as evidenced by the rapid red-shifting of the absorption onset and pronounced broadening of the absorption peak with growth time (Figure 3.1b). Omitting DPA produced nanocrystals whose initial absorption spectra indicated similar nucleation, but as time passed they exhibited little growth (Figure 3.1d), suggesting that DPA promotes nanocrystal growth.[98] The 1:1 DPA:Cd synthesis created superior small nanocrystals compared with synthesis without DPA, but again produced uncontrolled growth and large size distributions at larger sizes (Figure 3.1c). Clearly the presence of DPA led to a sharper size distribution during the nucleation step. Since the nanocrystals sampled at two minutes absorbed well to the blue of those

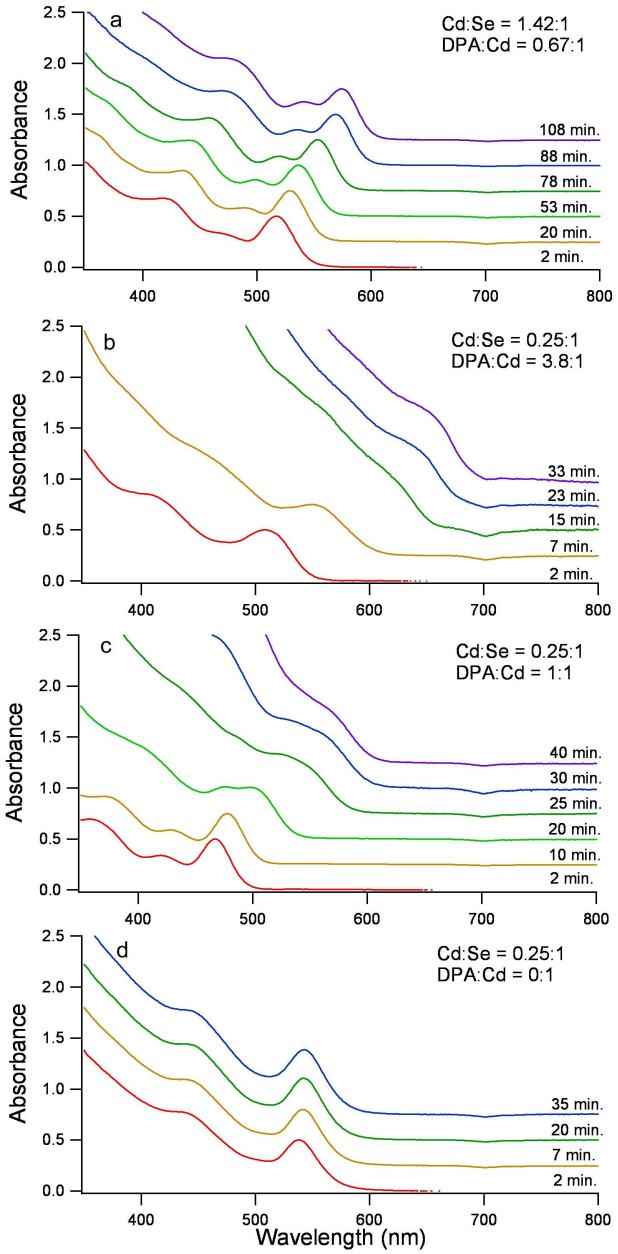

Figure 3.1: Absorption spectra of CdSe nanocrystals grown using the TOPO/HDA/DPA synthesis (Section 2.1.2), varying the Cd:Se and DPA:Cd ratios. Times indicated are growth times. (a) The original cadmium-rich synthesis produced slowly growing, fairly uniform nanocrystals, as evidenced by the sharp features in the absorption spectra. (b) Nanocrystals synthesized with a Cd:Se ratio of 0.25:1 and a DPA:Cd ratio of 3.8:1 grew uncontrollably, as evidenced by the loss of features in the spectra. (c) When the DPA:Cd ratio was reduced to 1:1, the nanocrystals produced initially grew slowly and uniformly, but lost their size coherency as they grew larger. (d) When DPA was eliminated from the synthesis, nanocrystals nucleated but failed to grow. Nanocrystals were synthesized by Lauren Weigand of the Rosenthal group.[101]

grown without DPA after the same elapsed time and were therefore smaller, DPA seems to slow nucleation and early growth.[99]

Although the TOPO/HDA/DPA synthesis did not adapt well to cadmium-limiting conditions, it was hoped that it could nonetheless be used by tuning the reactivities of the CdS and CdSe reaction conditions. To that end, the synthesis was adapted for sulfur first by substituting elemental sulfur for elemental selenium, then by substituting hexamethyldisilathiane (TMS_2S, Aldrich),[102] each in a 1:1 molar ratio to the selenium in the original synthesis. Both resulted in uncontrolled growth and poor size distributions; in addition, elemental cadmium was observed to plate out on the walls of the reaction vessel in the reaction involving elemental sulfur. Given that sulfur dissolves readily into TBP, we attribute the plated cadmium to a strong bonding between sulfur and TBP. If the TBP does not readily release sulfur under the reaction conditions, then nanocrystals cannot form easily, and the free cadmium metal in solution begins to plate out as a side reaction. Nanocrystals synthesized by these reactions are shown in Figures 3.2a and b.

Because the TOPO/HDA/DPA synthesis did not work well under cadmium-limiting conditions or with sulfur as one of the reactants, an alternate synthesis developed by Yu *et al.*[82] was employed, using CdO as a precursor, ODE as a noncoordinating solvent, and OA as the coordinating ligand (Section 2.1.4). In the CdS version of this synthesis, sulfur is simply dissolved in ODE, and no TBP is present to irreversibly bind it. The result is a controlled synthesis yielding nanocrystals with low size- and shape dispersity. The CdSe version of this synthesis, which still uses selenium complexed to TBP, is less controlled than the CdS synthesis, but the resultant nanocrystals are nonetheless close enough in size and shape that the synthesis could be used in further experiments. CdS and CdSe nanocrystals synthesized by the CdO/OA preparation are shown in Figures 3.2c and d.

Having found analogous synthetic schemes for the two types of nanocrystals, it

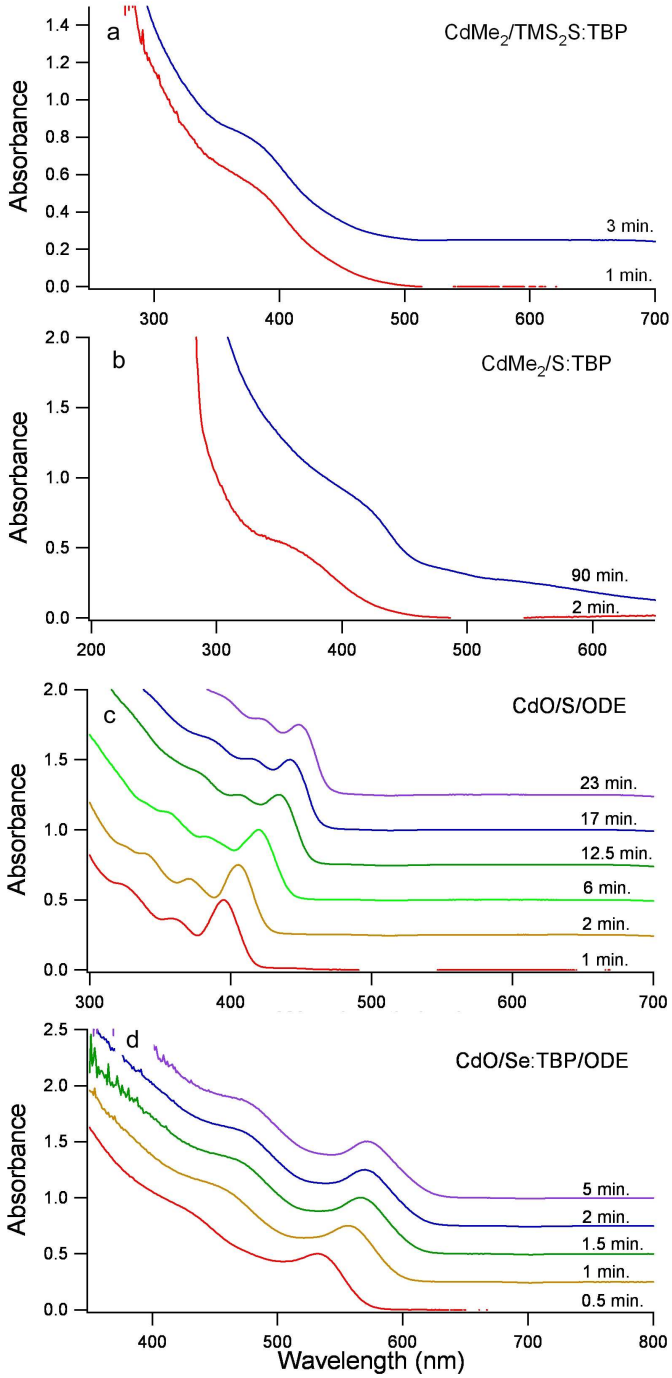

Figure 3.2: Absorption spectra of CdS and CdSe nanocrystals grown varying the cadmium and anion precursors. Dimethylcadmium synthesis (Section 2.1.2) using TMS_2S/TBP (a) or S:TBP (b) produced uncontrolled growth and poor size distributions. When the CdO/OA synthesis was used, resultant CdS nanocrystals showed excellent shape- and size control (c); CdSe nanocrystals, while not as well controlled as in the TOPO/HDA/DPA synthesis (Figure 3.1a), nonetheless showed reasonably good shape- and size control (d). Nanocrystals were synthesized by Lauren Weigand of the Rosenthal group.[101]

remained to be seen whether the schemes could be integrated to produce homogenous alloys. Of particular concern was the inhibitory effect of TBP on CdS synthesis. To assess the composition and homogeneity of alloy nanocrystals, batches of CdS_xSe_{1-x} nanocrystals were made with precursor S:Se ratios of 4:1, 3:2, 2:3, and 1:4. During the synthesis of each batch, 4 mL aliquots of the nanocrystal solution were withdrawn at timed intervals to monitor nanocrystal growth. These aliquots were isolated and characterized using UV-vis spectroscopy, RBS, and TEM. TEM and UV-vis spectroscopy were used to verify that nanocrystals were growing uniformly and that nanocrystals of only one type were present. RBS was used to determine the composition of nanocrystals in each aliquot.

To explore the effect of TBP on the reaction, experiments were performed using Se precursor solutions that were 2.5%, 3%, and 8.3% by volume TBP in ODE (1:1, 1.2:1, and 3.3:1 molar ratio TBP:Se). Figure 3.3 shows the composition of alloy nanocrystals with a precursor sulfur fraction of 0.4 as a function of growth time. The same trends were seen for all compositions. Nanocrystals made with 2.5% TBP precursor were spherical and had a sulfur concentration that was nearly constant throughout their growth, an indication of homogeneous alloying. Nanocrystals produced using 3.0% TBP precursor remained spherical, but the sulfur concentration increased slightly with time, indicating a gradient structure. We explain the increasing sulfur concentration on the basis of the excess TBP. Prior to injection, the sulfur and selenium precursors were mixed, allowing any TBP not bound to selenium to bind to sulfur instead. When injected into the reaction vessel, the bound sulfur reacted much slower than selenium or unbound sulfur, causing initial sulfur concentrations that were lower than might be expected. Then, as available selenium depleted, sulfur was increasingly the only anion available for nanocrystal growth, causing the sulfur concentration on the exterior of the nanocrystal to increase, resulting in the observed gradient structure. The optical behavior of these nanocrystals also differed from

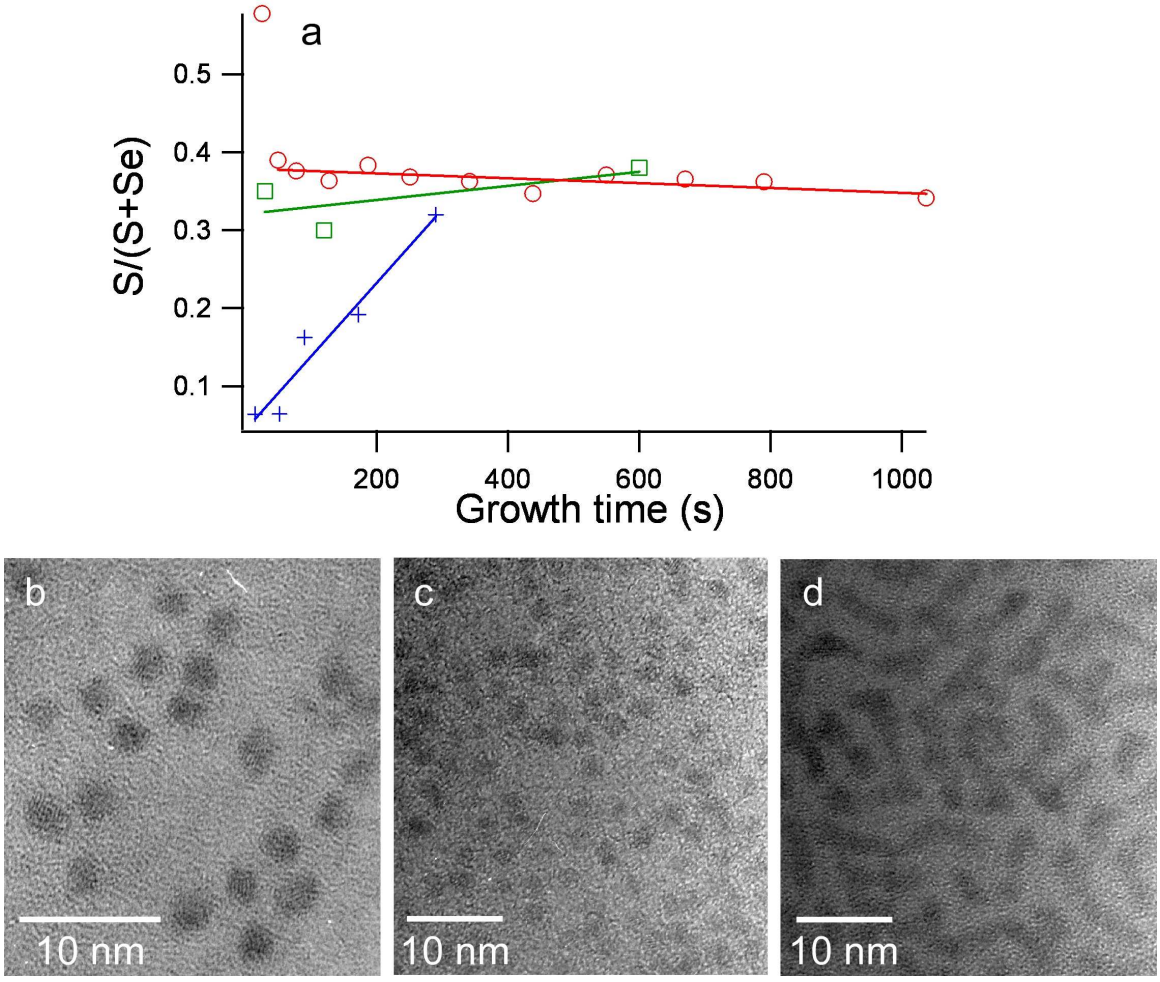

Figure 3.3: (top) Alloy composition as a function of growth time for $CdS_{0.4}Se_{0.6}$ grown using Se precursor solutions that were 2.5% (red circles), 3.0% (green squares), and 8.3% (blue crosses) TBP by volume. The 8.3% precursor shows a strong increase in sulfur with growth, indicating the formation of gradient alloys. The 3.0% precursor shows a slight increase in sulfur, and the 2.5% precursor a slight decrease. It is noted that the nanocrystals produced using the 2.5% TBP precursor were synthesized with the use of growth solution, unlike the 3.0% and 8.3% nanocrystals; the 2.5% nanocrystals are therefore much larger. (bottom) TEM images of nanocrystals synthesized using 2.5% (b), 3.0% (c), and 8.3% (d) TBP solutions. Lower amounts of TBP produce spherical nanocrystals, while higher amounts produce irregularly shaped nanorods.[34]

those produced by the 2.5% precursor. Fluorescent quantum yields for the 3.0% TBP nanocrystals were higher, on the order of 0.30, as compared to yields of < 0.01 for the 2.5% TBP nanocrystals and for pure CdS and CdSe. This is easily explained by the gradient structure; if the exterior had a higher concentration of sulfur, then electrons and holes in excited nanocrystals would be energetically confined to the center of the nanocrystal, enhancing fluorescence in the same manner as a core/shell structure. Moreover, a limited study on the band gaps of these nanocrystals yielded a bowing constant of 0.37 ± 0.23, which, as we shall see, is larger than the bowing constant of the 2.5% TBP nanocrystals. This increase would be consistent with the 3.0% TBP nanocrystals behaving like homogeneous nanocrystals that were slightly smaller and slightly more selenium-rich, as could be expected from a gradient structure.

To explore further the effect of TBP on alloy growth, the TBP concentration was increased to 8.3%. With TBP in such excess, the gradient effect was greatly enhanced; the concentration of sulfur in the nanocrystals was initially almost nonexistent and increased dramatically with growth time. TEM images show that nanocrystals produced by this route were rod-like, suggesting that free TBP promotes growth along the *c*-axis, possibly by effectively increasing the Cd:anion ratio. Since they preferentially grew in a single direction, and since previous work has shown that nanocrystals grow almost exclusively from the unpassivated anion-terminated face,[76,98] the gradient also likely propagated solely in this direction; certainly the quantum yield of these nanocrystals was no greater than the 3.0% TBP nanocrystals, indicating that the selenium-rich portion of these nanocrystals is no more shielded from the exterior than the 3.0% TBP nanocrystals. Although the 8.3% TBP nanocrystals were the wrong structure and composition for this study and were therefore quickly abandoned, they nonetheless remain an intriguing structure with potential applications in nanoelectronic devices. The one-dimensional gradient may generate gradient energy bands that could funnel charges unidirectionally; similar structures can be found in

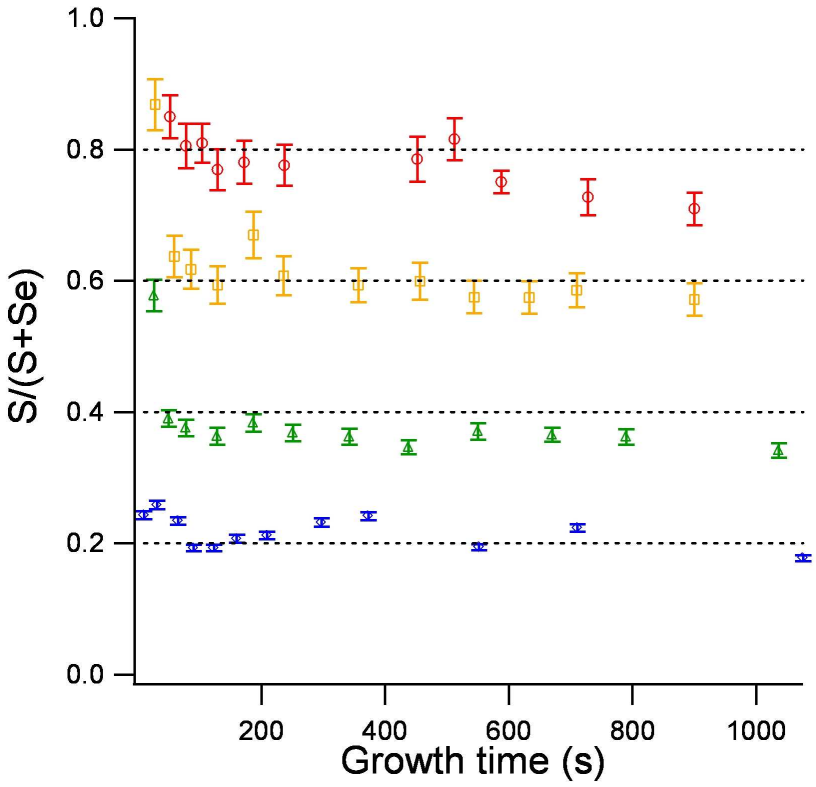

Figure 3.4: Alloy composition as a function of growth time for $CdS_{0.8}Se_{0.2}$ (red circles), $CdS_{0.6}Se_{0.4}$ (orange squares), $CdS_{0.4}Se_{0.6}$ (green triangles), and $CdS_{0.2}Se_{0.8}$ (blue diamonds). RBS analysis of aliquots of nanocrystals pulled from single batches of nanocrystals during growth reveals that the composition of the nanocrystals remains reasonably constant over the growth period, an indication of alloy homogeneity.[34]

bulk semiconductor devices. Thus, simply by altering the amount of TBP in the reaction it is possible to create homogeneous alloys, highly fluorescent gradient alloys, and unidirectionally gradient alloys. On the basis of these experiments, it was decided that the 2.5% TBP Se precursor produced the most homogeneous alloy structure.

3.2 Homogeneity and structure

Having determined a synthetic scheme for producing homogeneous alloys, the alloys were thoroughly characterized with respect to homogeneity and structure. Figure 3.4 shows the alloy composition as a function of growth time for all the different starting compositions of 2.5% TBP alloys. Except very early in nanocrystal growth,

the composition remained nearly constant over the growth period, indicating that the alloys were homogeneous, rather than gradient or core/shell in nature. It should be noted that at the very smallest sizes, all nanocrystals were shown to be sulfur-rich by RBS. There are two possible explanations for this observation. The first is simply that it is very difficult to clean the smallest nanocrystals, so RBS may have detected unreacted sulfur precursor. The second explanation is that the kinetics of nucleation are different than the kinetics of growth, resulting in sulfur enrichment at the smallest sizes. Indeed, the smallest sizes are most likely magic-number nanocrystals, composed of only a few atoms.[8,85,103–106] CdSe nanocrystals halted at the same stage of growth displayed the same absorption and emission characteristics as magic-number nanocrystals produced previously by a different synthesis (Figure 3.5).[8] If it is true that the nucleation kinetics in this reaction favor the formation of sulfur-rich seeds, these seeds are very small. As seen in Figure 3.4, the nanocrystals achieve the expected composition within 30 s, suggesting that the sulfur-rich seeds are so small that they constitute a nearly negligible portion of the nanocrystal. As we shall see later, the sulfur-rich seeds do not seem to affect the dependence of band gap on size and composition; therefore, we consider the nanocrystals to be essentially homogeneous.

This conclusion is supported by XRD scans of the nanocrystals (Figure 3.6), which show a linear change in lattice spacing as composition changes from CdS to CdSe (Figure 3.7). If the nanocrystals were a mixture of CdS nanocrystals and CdSe nanocrystals instead of alloys, the resultant XRD diffraction scans would exhibit a superposition of the scans of pure CdS and pure CdSe. It is noted that core/shell nanocrystals also show scans that are intermediate between the scans of the core and the shell.[102,109] However, since the RBS data show little change in composition with size, core/shell structures are unlikely; to maintain a core/shell structure throughout nanocrystal growth would necessitate constant rearrangement of interior atoms, which is highly unlikely. The scans also show a zinc-blende conformation throughout the

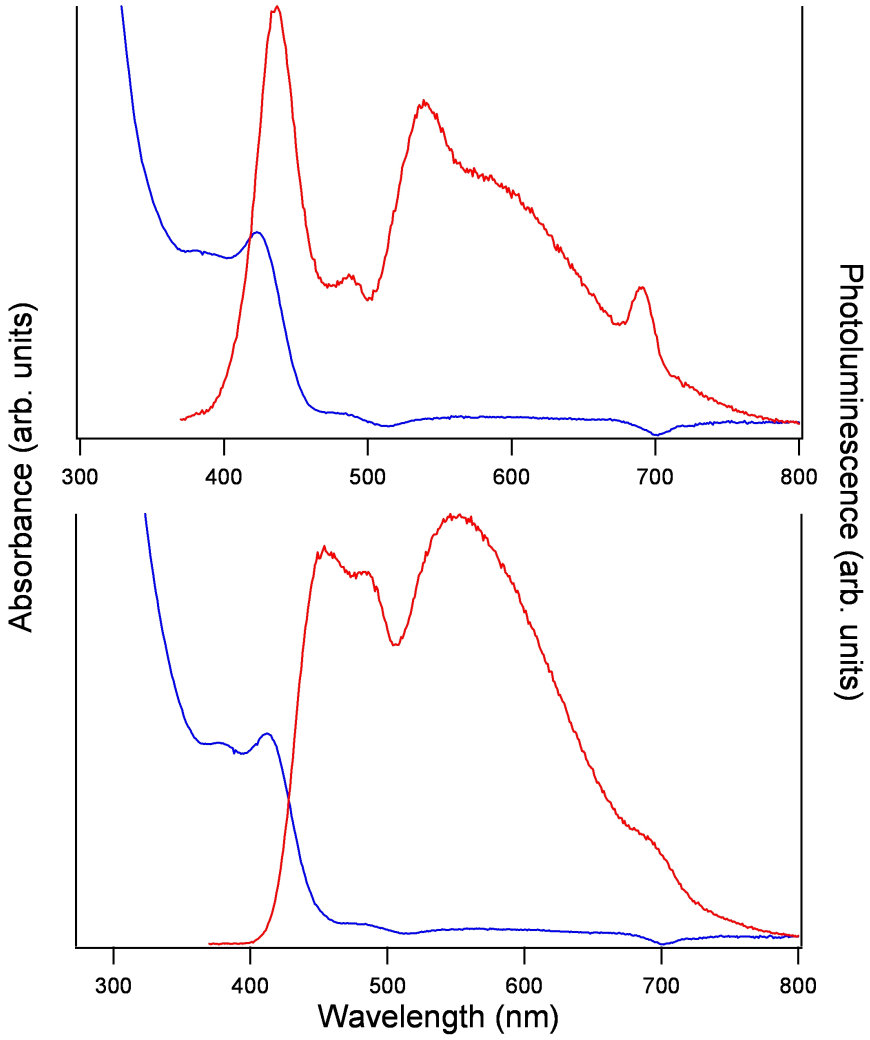

Figure 3.5: Absorption (blue) and emission (red) spectra of magic-number CdSe nanocrystals synthesized using the alloy synthetic prep (top), as compared to those synthesized using the method of Bowers *et al.*[8] (bottom). The absorption spectra for the two preps are similar, indicting that the nanocrystals are the same size. While the PL spectra are dissimilar, differences in the spectra are largely a matter of the relative intensities of the individual features. The exception is the highest-energy feature, which is blue-shifted in the alloy prep relative to the Bowers prep. It is possible that the relative intensities are dictated by the different ligands of the surfaces of the nanocrystals. The features at 700 nm are instrument artifacts. Nanocrystals synthesized by the Bowers method were synthesized by Michael Bowers of the Rosenthal group.

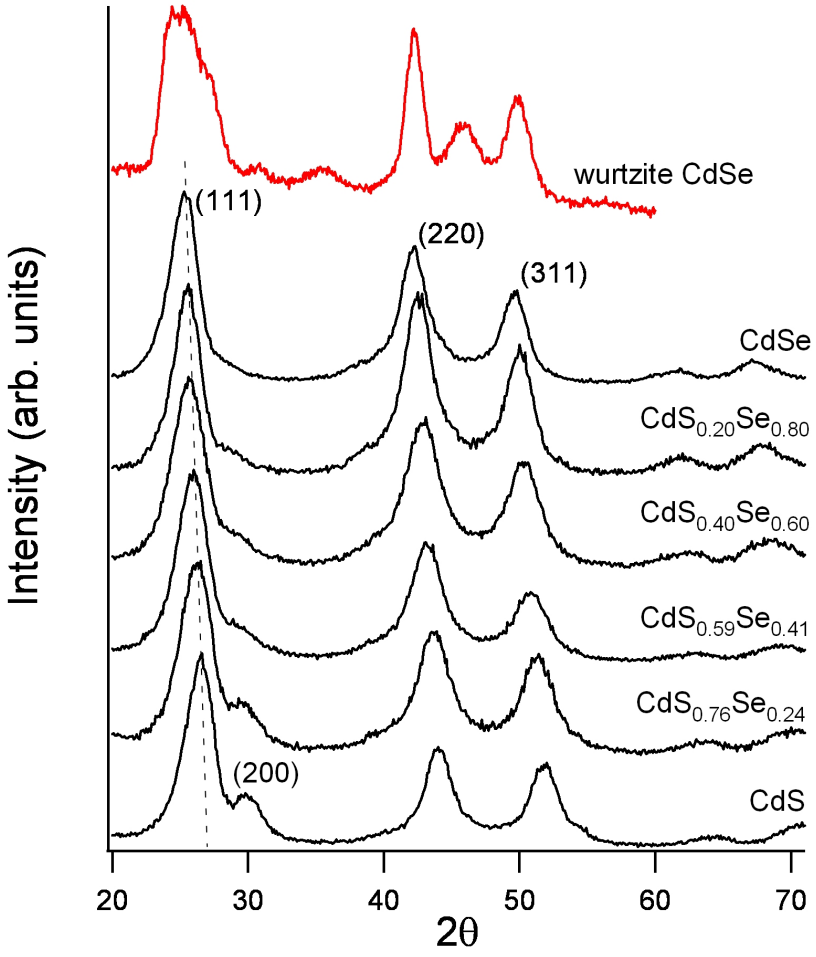

Figure 3.6: X-ray diffraction scans of CdS_xSe_{1-x} nanocrystals (black). Scans have been normalized to the height of the (111) peak and offset vertically. The scans characterize a zinc-blende structure,[107,108] with a linear change in lattice spacing from $x = 0$ to $x = 1$ (e.g., see dashed line) and a gradual subsidence of the (200) peak, indicating the formation of alloy nanocrystals rather than a mixture of CdS and CdSe particles.[34] A scan of wurtzite CdSe nanocrystals (red) is provided for comparison. Scans were obtained by Tony Watt, and wurtzite nanocrystals were synthesized by Michael Bowers, both of the Rosenthal group.

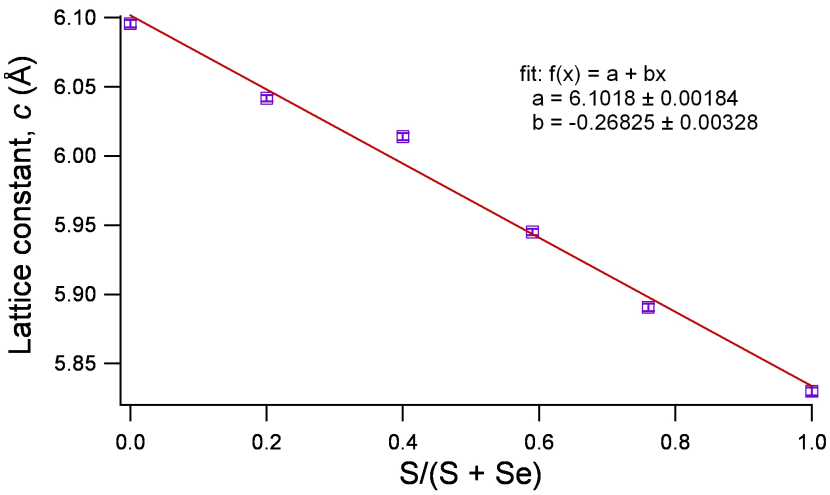

Figure 3.7: Lattice constant as a function of alloy composition, showing the linear relationship predicted by Végard's law. Constants were determined from the data in Figure 3.6 in the following manner. First, the (111) peak of each scan was fit to a Gaussian to find the value of 2θ corresponding to the peak maximum. This value was then substituted into Bragg's law, $2d\sin\theta = n\lambda$, with $n = 1$ and $\lambda = 1.54056$ Å, to yield the distance between successive (111) planes, $d_{(111)}$. Finally, this distance was converted to the lattice constant, c, by $c = 3^{1/2}d_{(111)}$.

range of compositions, in contrast to Yu and Peng's synthesis,[82] which shows a mix of zinc-blende and wurtzite structures. The zinc-blende structure is likely due to the surfactant system used;[108,110,111] that there are fewer wurtzite stacking faults may reflect the higher temperatures at which the synthesis was conducted or the lower amount of tributylphosphine used (1:1 Se:TBP molar ratio).

High resolution TEM images confirm the zinc-blende structure and show nanocrystals that appear spherical with a few aberrant pyramids (Figure 3.8). An indication of the narrow size distribution is that these nanocrystals readily form arrays on the carbon film support.[112] The average size distribution of the samples was measured using TEM images was 11.5% (standard deviation); this number is likely slightly larger than the true distribution due to the method of measuring.

Although no systematic study was performed, James McBride of the Rosenthal group performed atomic number contrast scanning transmission electron microscopy

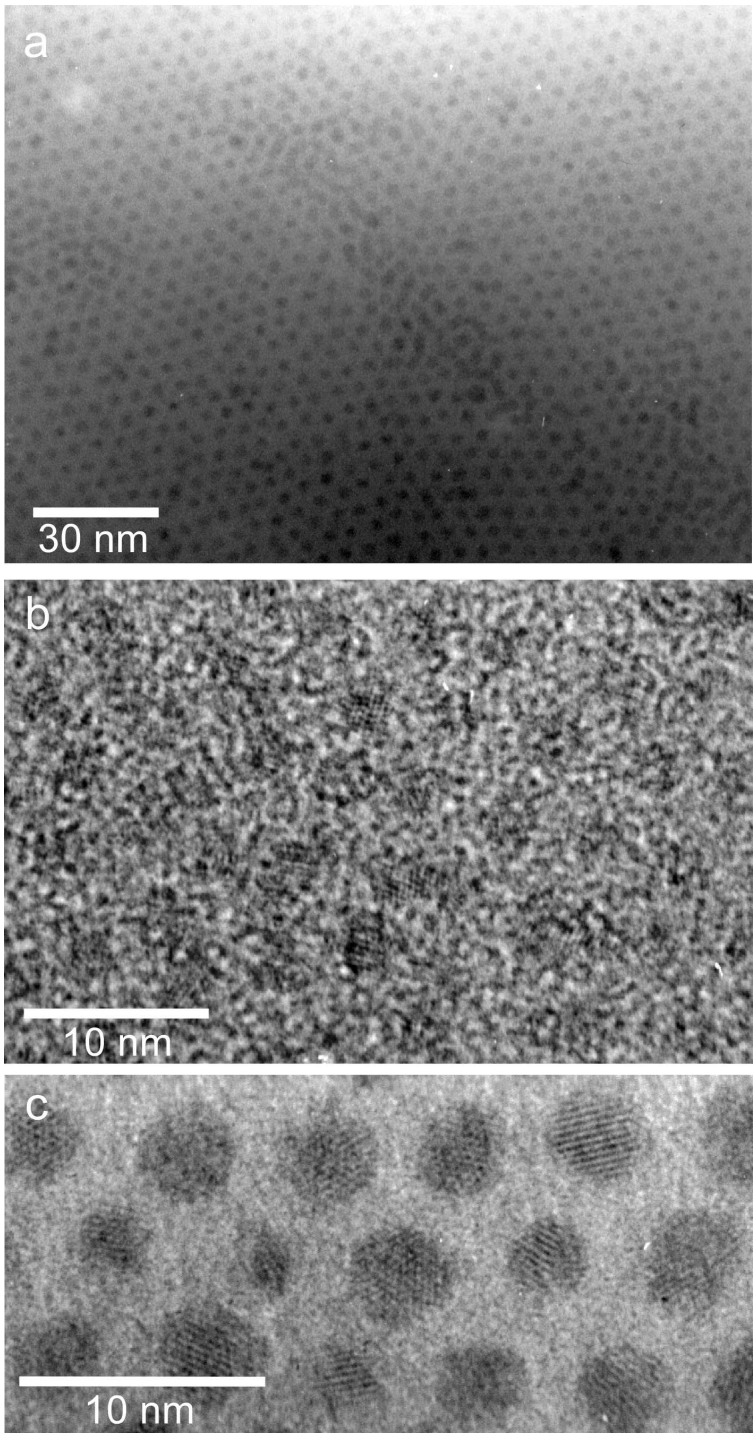

Figure 3.8: TEM images of $CdS_{0.8}Se_{0.2}$ (a), $CdS_{0.4}Se_{0.6}$ (b), and $CdS_{0.2}Se_{0.8}$ (c) show a highly crystalline, spherical, primarily zinc-blende structure with a few wurtzite stacking faults. Size dispersity is low, allowing the nanocrystals to array on the TEM grid.[34] Images were obtained by James McBride of the Rosenthal group.

(Z-STEM) on select alloy samples using a VG microscopes model HB603U STEM operating at 300 kV and fitted with a C_s corrector from Nion at the Oak Ridge National Laboratories. As an incoherent imaging technique, Z-STEM yields highly resolved shape and facet detail, as well as mass contrast, allowing a more detailed analysis than TEM can provide. Recently, this technique was successfully used by McBride and coworkers to observe the differences in CdSe nanocrystals synthesized by two different methods[76] and to study the morphology of different shell materials grown on CdSe nanocrystals.[26] In particular, the mass contrast that Z-STEM provides allowed McBride to easily distinguish between the core and shell materials in the latter study, a feat that TEM could not achieve. In the same manner, Z-STEM was performed on the alloy nanocrystals to determine whether the selenium and sulfur atoms within the alloy nanocrystals were segregated (i.e., whether the nanocrystals were inhomogeneous) or not.

Figures 3.9 and 3.10 show bright field and dark field Z-STEM of $CdS_{0.4}Se_{0.6}$ nanocrystals. The bright field image shows that, unlike the uniform crystallinity of the CdSe nanocrystals produced by the TOPO/HDA/DPA method,[76] the alloy nanocrystals often show multiple crystalline domains, and sometimes amorphous regions as well. This is likely the result of lattice strain induced by the different sizes and electronegativities of the anions. These differences could cause the nanocrystal to grow in different crystalline orientations from different facets of the seed, and nanocrystal growth, while occurring at high temperature, happens so rapidly that the nanocrystal does not anneal to a single-crystal structure. The dark field image contains the mass contrast that makes Z-STEM particularly useful. Though the bright field image shows different domains, which might indicate segregation of CdS and CdSe within each crystal, the dark field image shows no evidence of segregation. The intensity is uniform throughout each nanocrystal, in contrast to core/shell or other segregated structures, in which the segregation is obvious.[26] Thus, Z-STEM

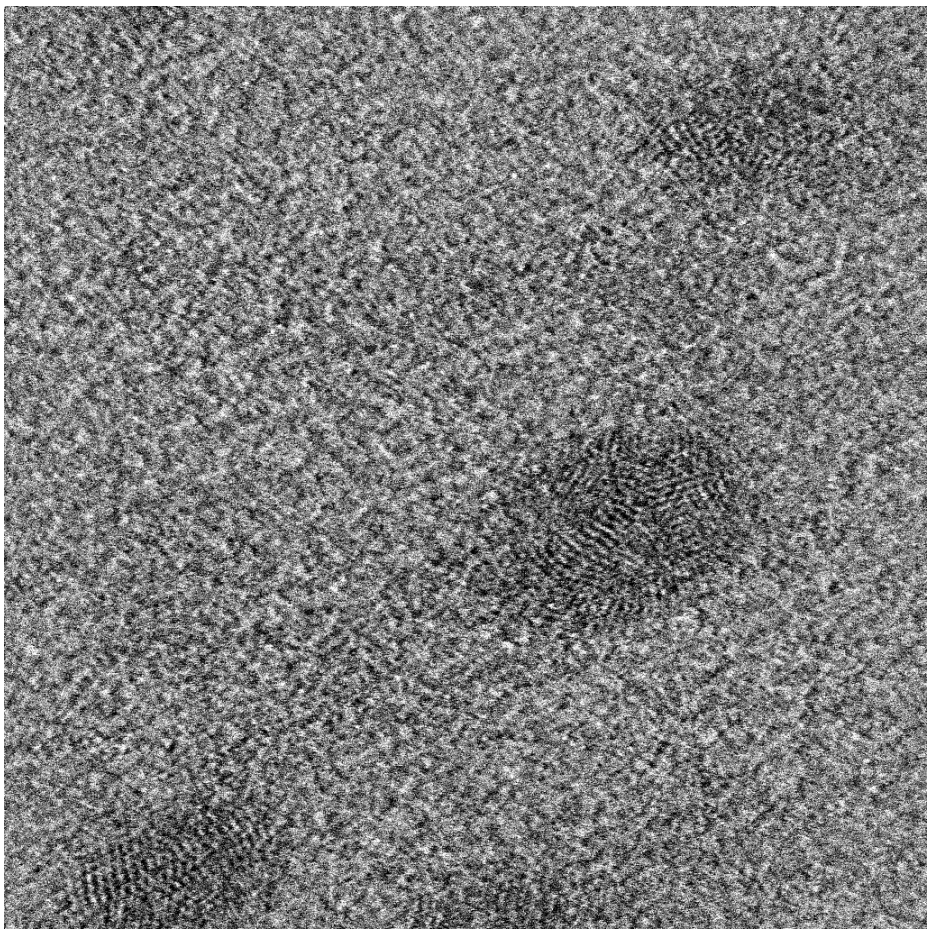

Figure 3.9: Bright field Z-STEM of $CdS_{0.4}Se_{0.6}$ nanocrystals. The nanocrystals in this image show the different crystalline domains present in the nanocrystals. Image obtained by James McBride of the Rosenthal group.

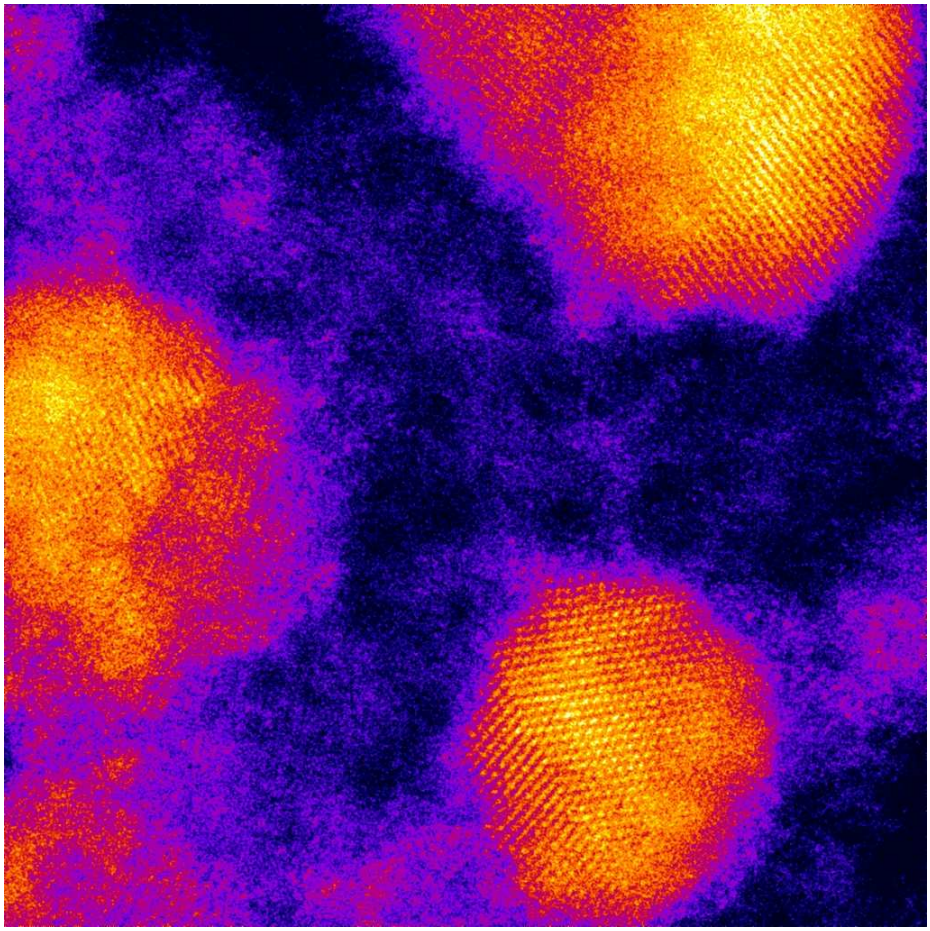

Figure 3.10: Dark field Z-STEM of $CdS_{0.4}Se_{0.6}$ nanocrystals. Dark field images show mass contrast; however, images of the alloy nanocrystals fail to show segregation of the sulfur and selenium atoms (core/shell structure, different domains within the nanocrystal, etc.), leading to the conclusion that the nanocrystals are homogeneous. Image obtained by James McBride of the Rosenthal group.

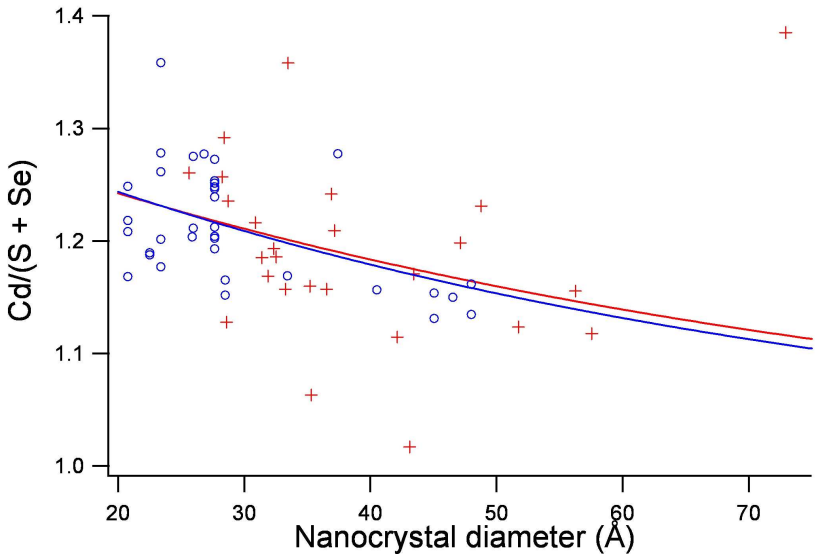

Figure 3.11: Cadmium-to-anion ratios for oleic acid-coated (red crosses) alloy nanocrystals and tri-*n*-octylphosphine oxide-coated (blue circles) CdSe nanocrystals as a function of nanocrystal diameter. Values for TOPO-coated nanocrystals were obtained from Taylor *et al.*[95] Both synthetic schemes produced approximately the same excess of cadmium, as indicated by the trend lines.

demonstrates that the nanocrystals are of uniform composition, but contain many crystalline domains per nanocrystal.

In addition to the characterization of the alloy homogeneity, crystallinity, and shape, RBS was used to characterize the surface of the nanocrystals. Figure 3.11 shows the cadmium-to-anion ratios for the alloy nanocrystals and for TOPO-coated CdSe nanocrystals from Taylor *et al.*[95] as a function of nanocrystal diameter. Both sets of nanocrystals displayed excess cadmium, and greater excess cadmium was associated with smaller nanocrystals. As indicated by the trend lines, the dependence of the cadmium-to-anion ratio on diameter was approximately identical for both sets of nanocrystals. No difference in the ratios was noted for nanocrystals of similar size but different composition. As did Taylor *et al.*, we attribute the excess cadmium to the surface. Like TOPO, oleic acid binds exclusively to cadmium; therefore, it passivates otherwise unbonded cadmium orbitals at the surface. Unbonded surface anion orbitals

cannot be passivated by these ligands, so a surface with excess, passivated cadmium is more energetically favorable than one with an equal amount or excess of unpassivated anion orbitals. It is noted that nanocrystals synthesized by the TOPO/HDA/DPA method have both TOPO and HDA, which passivates both cadmium and selenium, as surface ligands; because both elements can be passivated, these nanocrystals contain cadmium and selenium in equal quantities.[76,80] On the basis of the alloys' similarity to TOPO-coated nanocrystals, dissimilarity to TOPO/HDA-coated nanocrystals, and insensitivity to alloy composition, we conclude that the excess cadmium is localized on the surface, and that the effect is ligand-specific rather than an effect of composition.

3.3 Optical properties and bowing constant

Figure 3.12 shows typical UV-vis absorption and PL spectra for the alloy nanocrystals. The spectra appear similar to CdS and CdSe nanocrystals. Absorption spectra are characterized by several peaks, an indication of good size distribution. The spacing and intensity of these features show some variation (e.g., see Figure 3.13b); the reason for this is unknown at this time, though PLE spectra of the nanocrystals confirm that the cause is not inhomogeneity in the samples (e.g., Figure 3.12b). PL spectra are typically characterized by two peaks: a higher-energy, narrow (30 - 38 nm FWHM) peak assigned to band edge emission, and a lower-energy, broad peak assigned to 'deep trap' emission, caused by trapping of the photoexcited hole to unpassivated surface anion orbitals.[113–115] The band edge emission is red-shifted from the band edge absorption peak by 5 - 30 nm, with smaller nanocrystals showing larger shifts. Likewise, the relative intensity of deep trap emission varies from none in large nanocrystals to a peak intensity on the order of the intensity of the band edge emission for small nanocrystals; this behavior is similar to CdSe nanocrystals synthesized in TOPO.[113] Some of the smaller nanocrystals begin to display the second

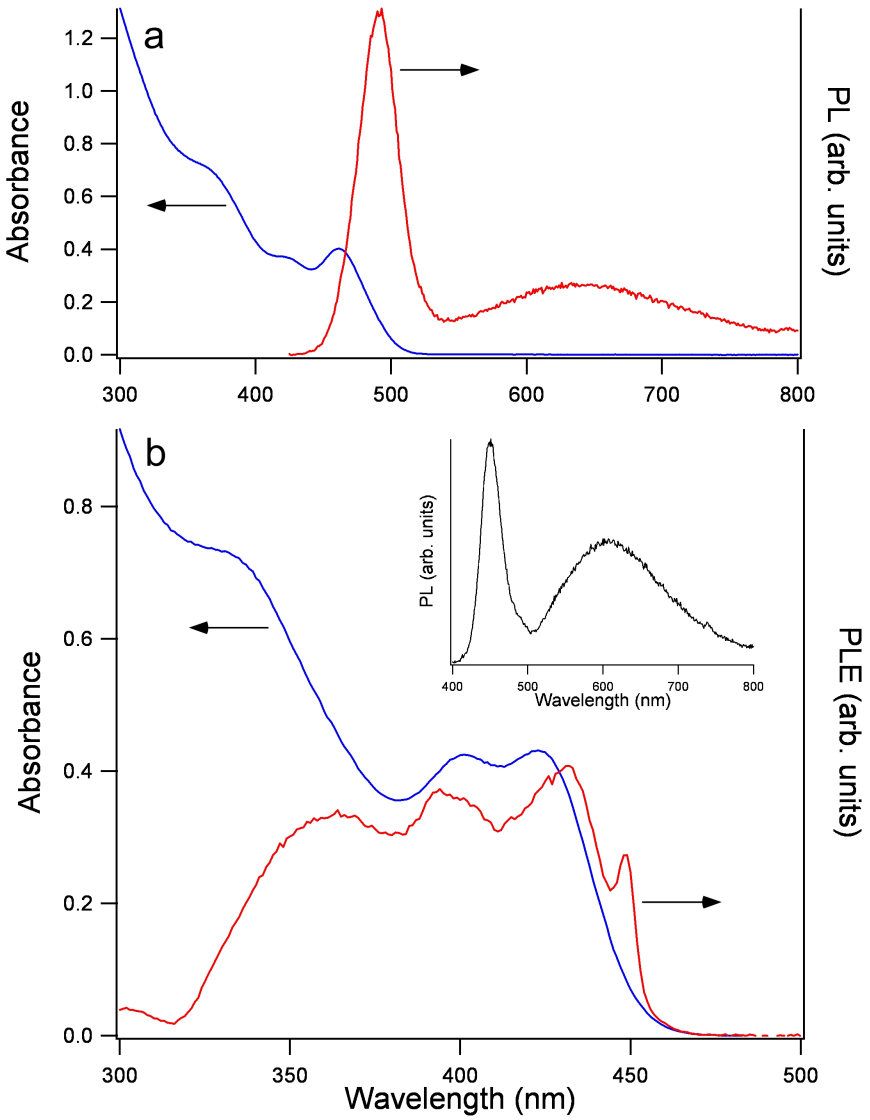

Figure 3.12: a) Absorption and photoluminescence spectra of 35 Å $CdS_{0.53}Se_{0.47}$ nanocrystals. These spectra typify the optical properties of the alloy nanocrystals. b) Absorption and photoluminescent excitation spectra of 24 Å $CdS_{0.70}Se_{0.30}$ nanocrystals. The absorption spectrum is unlike typical CdS and CdSe spectra in that the two lowest-energy features are of equal intensity. This pattern was often seen in the sulfur-rich alloys, raising the possibility of a bimodal size distribution. However, the PLE spectrum, taken at the maximum of the band edge emission (450 nm), agrees closely with the absorption spectrum close to the band edge, an indication that the sample is uniform. The feature at 450 nm in the PLE spectrum is an instrument artifact. The inset shows the PL spectrum for this sample. The PL spectra in (a) and (b) were taken with an excitation wavelength of 367 nm.[34]

band edge-like emission feature seen in magic-number nanocrystals (Figure 3.5).

As discussed in Section 1.3, the band gaps of alloys often vary nonlinearly with composition as

$$E_g\left(\mathrm{CdS}_x\mathrm{Se}_{1-x}\right) = xE_g\left(\mathrm{CdS}\right) + (1-x)\,E_g\left(\mathrm{CdSe}\right) - bx(1-x) \tag{3.2}$$

where the bowing constant, b, describes the extent of nonlinearity.[66] In the case of nanocrystals of any given composition, quantum confinement also dictates a size dependence (Section 1.2.3):

$$E_g(d) = E_g(\infty) + \frac{a}{d} + \frac{c}{d^2} \tag{3.3}$$

where d is the nanocrystal diameter and a and c are empirical fit parameters. The dependence of band gap on size and on composition are demonstrated in Figure 3.13. Substituting (3.3) into (3.2), we find that the dependence of band gap on size and composition is given by

$$E_g\left(x,d\right) = x\left[E_g(\mathrm{CdS},\infty) + \frac{a_1}{d} + \frac{c_1}{d^2}\right] + (1-x)\left[E_g(\mathrm{CdSe},\infty) + \frac{a_2}{d} + \frac{c_2}{d^2}\right] - b_d x(1-x) \tag{3.4}$$

In this expression, the bowing constant is expressed as a function of the nanocrystal diameter. The size dependence is included for a number of reasons. First, lattice spacing is known to decrease slightly with decreasing nanocrystal diameter, a function of surface tension.[37] Second, surface reconstruction can affect cation-anion bond lengths as well as electron distribution.[116–118] Third, ligand effects can also alter cation-anion bond lengths and charge distribution.[117] Combined, these effects could significantly impact the bowing constant, particularly at small diameters. It is noted that in Equation 3.4, any nonlinearity in the change in the parameters a and c between their CdS and CdSe values is contained within the bowing constant; if these values vary with composition in a manner different than the bulk band gap ($E_g(\mathrm{CdS},\infty)$ and $E_g(\mathrm{CdSe},\infty)$), then the bowing constant should depend on size.

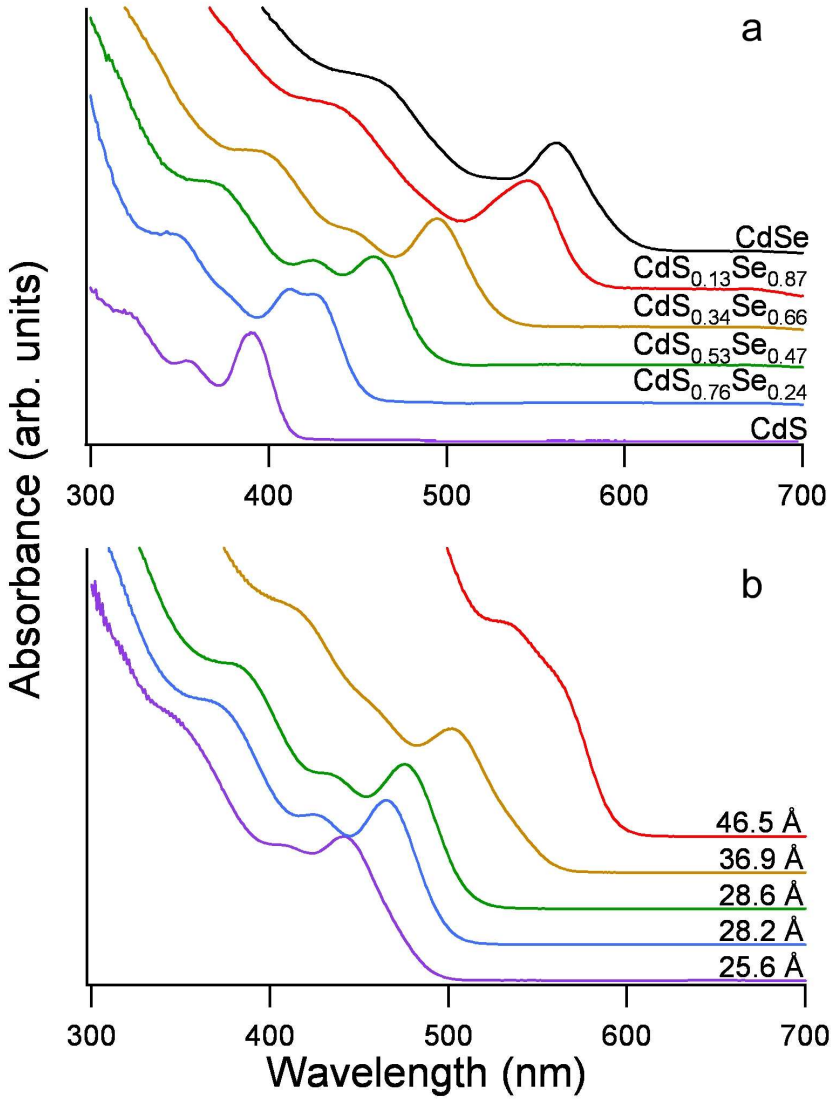

Figure 3.13: UV-visible absorption spectra demonstrating dependence of band gap on size and composition: (a) composition dependence of ∼30 Å nanocrystals; (b) size dependence of ∼$CdS_{0.4}Se_{0.6}$ nanocrystals.[34]

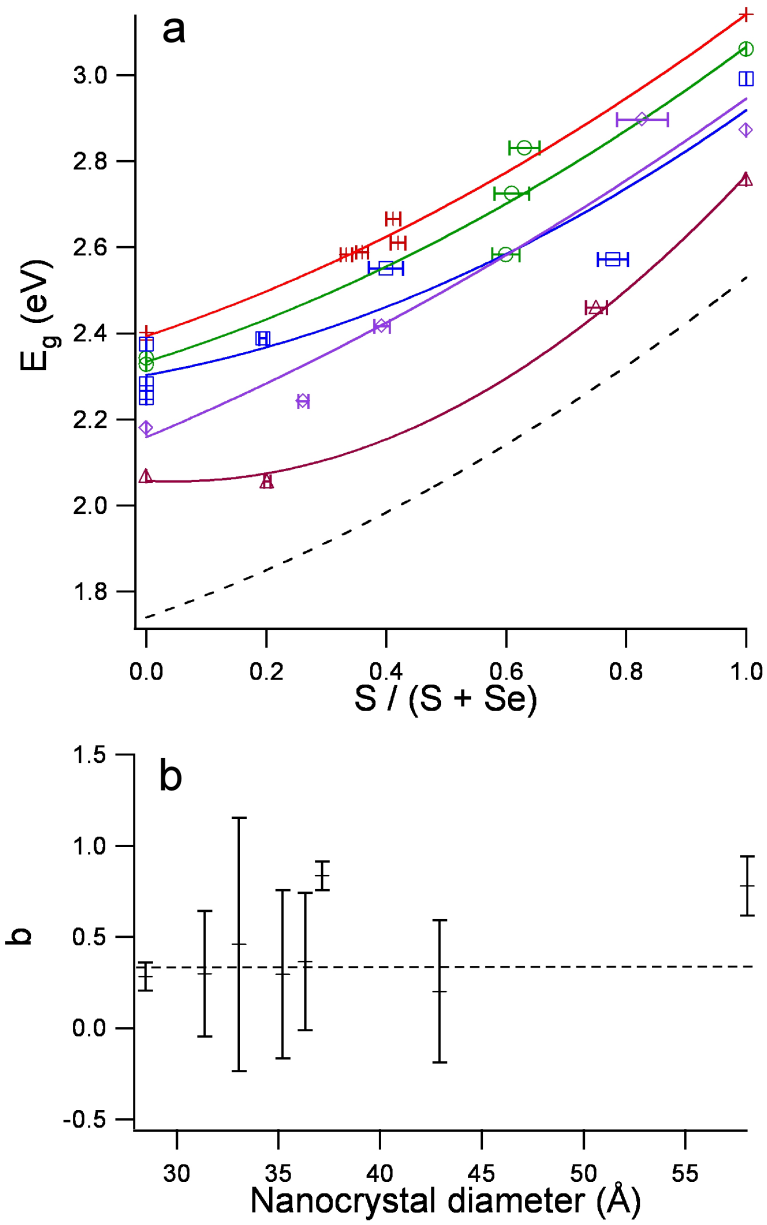

Figure 3.14: Bowing vs. size for CdS_xSe_{1-x} nanocrystals. a) Band gap as a function of composition for 28 Å (red crosses), 31 Å (green circles), 36 Å (blue squares), 43 Å (purple diamonds), and 58 Å (brown triangles) nanocrystals. Curves show the bowing, which remains relatively constant and closely follows the bulk bowing behavior (dashed line from Equation 3.2; $E_g(\mathrm{CdS}, \infty) = 2.53$ eV,[46] $E_g(\mathrm{CdSe}, \infty) = 1.74$ eV,[46] $b = 0.3$[68,74,75]). Values for CdS and CdSe nanocrystals were either measured in this work, extrapolated from Yu *et al.*,[40] or calculated from a fit to the data of Yu *et al.* (CdS: $E_g(\infty) = 2.53$ eV, $a = 9.3$ eV-Å, $c = 231$ eV-Å^2; CdSe: $E_g(\infty) = 1.74$ eV, $a = 19.6$ eV-Å, $c = -28.8$ eV-Å^2). For clarity, only five sizes are shown. b) Bowing constant as a function of nanocrystal diameter. Dashed line indicates the bowing constant, 0.29, obtained by fitting all data to Equation 3.4. From this graph, it is evident that the bowing constant is independent of size (within the uncertainty of the data) over the range of the experiment.[34]

Figure 3.14 shows the dependence of bowing constant on size. Results show that within the uncertainty and range of this work, the bowing constant is in fact insensitive to diameter, in agreement with previous work on $CdSe_xTe_{1-x}$.[32] This suggests that the small change in lattice constant with size is not enough to significantly impact the band structure. More intriguingly, it suggests that the surface and surrounding environment (ligands and solvent), which are known to impact strongly the optical and electronic behavior of nanocrystals,[39,49,80,119–122] do not affect nanocrystal band gap bowing beyond their effects on the size dependence of the band gap. As size decreases and the surface-to-volume ratio increases, surface effects play an increasingly important role in nanocrystal behavior, distorting bonding and electronic structure, which might affect bowing for the reasons mentioned above. Finally, the fact that the bowing in these nanocrystals is identical to bulk values suggests that any structural anomalies and compositional fluctuations, both of which are known to contribute to the bowing phenomenon,[66,68,123] are not severe enough to affect the optoelectronic behavior of the nanocrystals, so that they can indeed be considered homogeneous.

With this information, the band gaps, compositions, and diameters of 35 alloy samples ranging in diameter from 20 Å to 80 Å (Table 3.1) were combined with band gap and size data for CdS and CdSe extrapolated from Yu *et al.*[40] (Table 3.2) and fit to Equation 3.4 in two ways, summarized in Table 3.3. First, all data for CdS and CdSe were fit to Equation 3.3 to obtain a and c for the two materials. These values for a and c were then substituted into (3.4) along with the bulk band gaps, yielding a bowing constant of 0.31 ± 0.10. Next, the fit was repeated, but a and c were allowed to float, yielding a bowing constant of 0.29 ± 0.16. (The experimental values as well as the floated fit values are graphed in Figure 3.15.) These values are in good agreement; moreover, they agree well with the bulk bowing constant, which has been reported as 0.3.[68,74,75] Others have reported values less than 0,[123–125] presumably due

Table 3.1: Diameters, compositions, and band gaps of alloy nanocrystals.

diameter Å	x	band gap (eV)	diameter Å	x	band gap (eV)
24.1 ± 3.3	0.699 ± 0.025	2.93	35.8 ± 5.2	0 ± 0	2.28
25.6 ± 3.8	0.462 ± 0.013	2.81	36.1 ± 2.3	0.777 ± 0.025	2.57
28.2 ± 2.9	0.411 ± 0.012	2.67	36.4 ± 5.2	0 ± 0	2.38
28.4 ± 2.8	0.333 ± 0.010	2.58	36.5 ± 4.5	0.194 ± 0.006	2.39
28.6 ± 2.9	0.420 ± 0.012	2.61	36.9 ± 3.1	0.399 ± 0.029	2.55
28.7 ± 4.4	0.359 ± 0.010	2.59	37.2 ± 3.8	0.774 ± 0.032	2.67
30.9 ± 3.4	0.609 ± 0.029	2.72	37.3 ± 4.0	0.670 ± 0.035	2.55
31.4 ± 4.5	0.630 ± 0.025	2.83	42.1 ± 3.0	0.393 ± 0.013	2.30
31.9 ± 3.7	0.599 ± 0.023	2.58	43.1 ± 4.9	0.827 ± 0.042	2.90
32.3 ± 3.6	0.589 ± 0.021	2.38	43.4 ± 4.9	0.261 ± 0.009	2.42
32.5 ± 4.1	0.382 ± 0.010	2.46	47.1 ± 4.3	0.783 ± 0.022	2.47
33.3 ± 5.1	0.361 ± 0.013	2.54	48.8 ± 5.2	0.764 ± 0.026	2.49
33.5 ± 4.1	0 ± 0	2.48	51.7 ± 5.4	0.193 ± 0.004	2.13
33.5 ± 3.1	0.665 ± 0.023	3.07	56.3 ± 6.9	1 ± 0	2.63
34.5 ± 3.9	0.591 ± 0.024	2.76	57.6 ± 5.9	0.202 ± 0.006	2.06
35.1 ± 5.1	0.209 ± 0.010	2.38	58.5 ± 5.5	0.751 ± 0.017	2.46
35.2 ± 3.8	0.556 ± 0.015	2.47	72.9 ± 12.6	0.727 ± 0.027	2.36
35.3 ± 2.6	0.533 ± 0.020	2.69			

Table 3.2: Diameters and energies for CdSe and CdS extrapolated from Yu *et al.*[40]

CdSe diameter (Å)	CdSe band gap (eV)	CdSe diameter (Å)	CdSe band gap (eV)	CdS diameter (Å)	CdS band gap (eV)
6.0	4.13	34.9	2.18	12.9	4.79
7.0	3.83	35.9	2.16	14.4	4.21
10.8	3.51	36.8	2.26	16.0	3.89
12.0	3.04	37.0	2.20	18.7	3.71
14.0	3.39	42.9	2.09	23.2	3.32
15.1	3.35	43.0	2.10	36.0	2.99
16.0	2.73	43.8	2.07	38.9	3.04
17.9	3.19	46.1	2.05	41.0	2.93
19.0	2.62	46.6	2.05	46.0	2.87
20.8	2.55	47.0	2.07	53.1	2.80
20.9	2.82	48.0	2.04	55.9	2.68
21.0	2.59	51.0	2.00		
23.0	2.46	54.2	1.99		
23.8	2.41	59.7	1.97		
25.8	2.36	62.0	1.98		
26.6	2.45	65.0	1.93		
26.9	2.33	74.0	1.94		
27.7	2.40	76.4	1.91		
28.0	2.36	79.0	1.95		
28.8	2.29	83.0	1.88		
30.9	2.26	86.1	1.90		
31.8	2.30	87.5	1.89		
32.0	2.30	98.5	1.87		
32.9	2.22	115.0	1.83		
33.9	2.20	120.5	1.84		
34.0	2.26				

Table 3.3: Fitting parameters for calculation of bowing constant.
[a] a and c are calculated by fitting CdS and CdSe data from Yu *et al.*[40] as well as our data to Equation 3.3, with $E_g(\infty)$ fixed at 2.53 eV[46] and 1.74 eV,[46] respectively. These values were then substituted into Equation 3.4 to obtain the bowing constant.
[b] The bulk band gaps of 2.53 eV[46] and 1.74 eV[46] for CdS and CdSe, respectively, were substituted into Equation 3.4 to obtain the bowing constant as well as a and c.

	a_{CdS} (eV-Å)	c_{CdS} (eV-Å^2)	a_{CdSe} (eV-Å)	c_{CdSe} (eV-Å^2)	b
fixed[a]	8.4 ± 2.1	245 ± 34	19.6 ± 0.8	-28.8 ± 7.5	0.31 ± 0.10
floated[b]	7.9 ± 2.7	252 ± 44	19.5 ± 0.8	-28.0 ± 7.0	0.29 ± 0.16

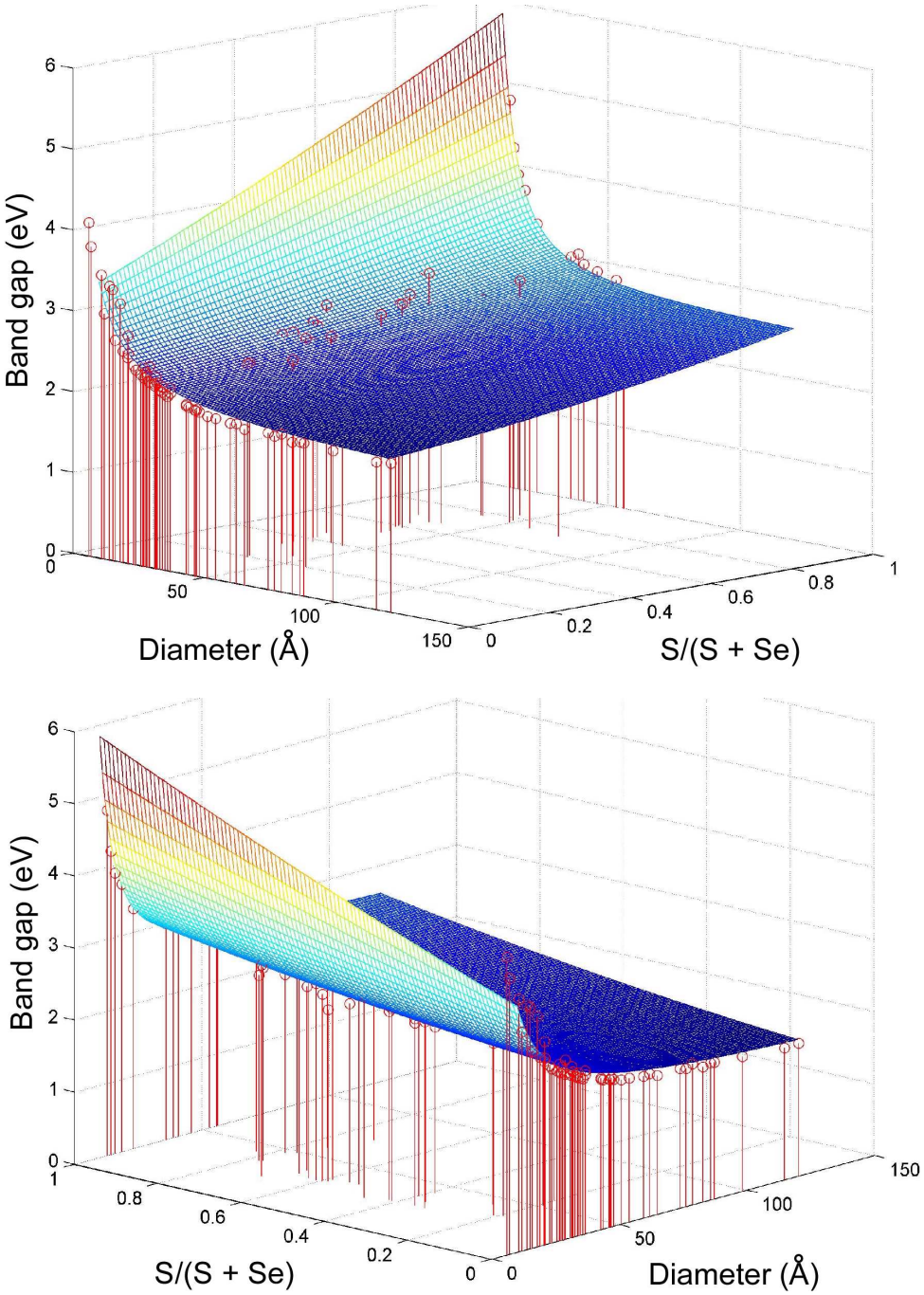

Figure 3.15: Dependence of band gap on size and composition. Experimentally determined values are represented by red circles, while the colored surface shows the fit obtained by allowing the values for a and c to float (Table 3.3). Two different views of the same data are shown for clarity.

to differences in synthetic and analytical techniques; however, it has been suggested that the work showing negative bowing constants was performed on thin films whose actual composition and homogeneity may be suspect.[74] In addition, the values for a and c obtained from Equation 3.4 when they were allowed to float agree well with their values from fits to pure CdS and CdSe.

That the observed bowing constant in the nanocrystals agrees with the bulk value, and that the bowing constant, a, and c were approximately identical regardless of how the data were fit, suggests that a and c are linear combinations of the binary constituents. Consequently we may simplify Equation 3.4 to

$$E_g(x,d) = E_g(x,\infty) + \frac{a_x}{d} + \frac{c_x}{d^2} \tag{3.5}$$

where $E_g(x,\infty)$ is given by Equation 3.2, and a_x and c_x are the linear combinations

$$\begin{aligned} a_x &= x a_{CdS} + (1-x) a_{CdSe} \\ c_x &= x c_{CdS} + (1-x) c_{CdSe} \end{aligned} \tag{3.6}$$

Equation 3.5 is a more elegant form of Equation 3.4, because it shows the traditional dependence of band gap on size for nanocrystals (e.g., Equation 3.3); moreover, it demonstrates that the bowing constant is independent of both size and the empirical parameters, a and c.

Although a and c are strictly empirical parameters, if we relate them back to Brus' original equation for the size dependence of the band gap (Equation 1.17), the behavior of the alloy nanocrystals has some interesting implications for other physical properties of the alloys. Comparing Equations 1.17 and 1.18, we find that

$$a \propto \frac{1}{\epsilon_{nc}} \tag{3.7}$$

and

$$c \propto \left(\frac{1}{m_e^*} + \frac{1}{m_h^*} \right) = \frac{1}{\mu} \tag{3.8}$$

(It is noted that these relationships show how empirical a and c truly are - Equation 1.17 dictates that $a < 0$ and $c > 0$, yet in the cadmium sulphoselenide nanocrystals, $a > 0$ and $c < 0$ for selenium-rich nanocrystals.) If the relationships in Equations 3.7 and 3.8 were accurate, it would imply that since a and c also vary linearly with alloy composition, the dielectric constant and reduced mass of excitons, μ, vary inversely with nanocrystal composition. This contrasts evidence from other bulk alloys, which show dielectric constants and reduced masses that display linear or quadratic dependence on composition.[126,127] There are a number of possible reasons for this discrepancy. First is the fact that a and c are empirical; therefore they may not accurately detail the behavior of the dielectric constant and the effective masses of the charge carriers. Second, a quadratic relationship may appear similar to an inverse relationship over a limited range, depending on the extent of the bowing. It is possible that the true dependence is quadratic, but that the change is small enough that it appears inverse. Third, these parameters are size-dependent;[39,49] the size-dependence may mask or alter the composition dependence found in bulk semiconductors. In order to distinguish which of these possibilities might be correct, further experimentation is necessary. Both examinations of the size/composition/band gap of alternate semiconductor nanocrystals and direct determination of the dielectric constants and effective masses in alloy nanocrystals are indicated.

CHAPTER IV

CONCLUSION

Increasing demand for nanomaterials with multiple, precisely tuned properties has prompted efforts to synthesize alloy nanocrystals. These nanocrystals have the advantage that their optical and electronic properties are tunable both by size and by composition, allowing researchers to select more than one property (e.g., size and color) for specific applications. The focus of this work was on the synthesis of homogeneously alloyed cadmium sulfoselenide nanocrystals. The nanocrystals were characterized with respect to size, composition, and band gap, resulting in the formulation of a quantitative relationship between these properties.

To synthesize the nanocrystals, compatible syntheses for CdS and CdSe first had to be identified. Next, the syntheses needed to be integrated in such a way as to produce homogeneous nanocrystals. Using Rutherford backscattering spectrometry to analyze the elemental composition during growth and X-ray diffractrometry to ensure that the nanocrystals were not simply a mixture of pure CdS and pure CdSe, two synthetic strategies were attempted to produce homogeneity. The first, limiting the amount of cadmium in the reaction mixture, was unsuccessful. The second, tuning reaction conditions other than the amounts of the cadmium, sulfur, and selenium precursors, proved to be the key to the synthesis of homogeneous nanocrystals in all proportions. Specifically, we discovered that by varying the amount of tri-*n*-butylphosphine in the selenium precursor solution, we could produce nanocrystals that ranged from unidirectionally gradient nanorods to spherical, homogeneous nanocrystals.

That the alloy nanocrystals display different morphologies, different quantum yields, and gradient or homogeneous structures depending on the amount of TBP

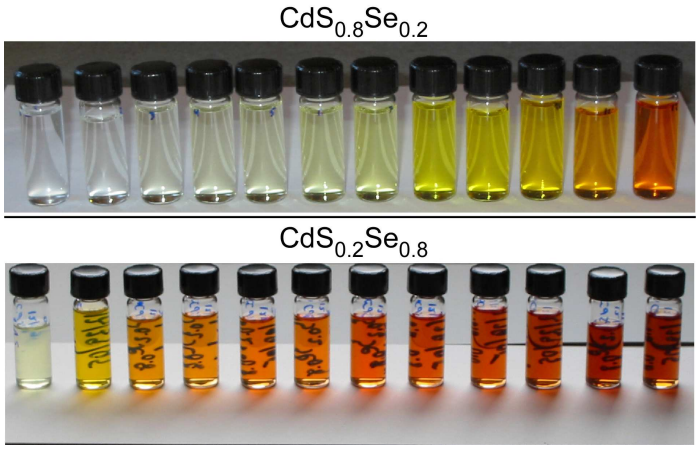

Figure 4.1: Size range of $CdS_{0.8}Se_{0.2}$ (top) and $CdS_{0.2}Se_{0.8}$ (bottom) nanocrystals, demonstrating the alloy nanocrystals' band gap dependence on size and composition. Nanocrystals range from <20 Å (left) to >100 Å (right). $CdS_{0.2}Se_{0.8}$ nanocrystals of a given size absorb to the ref of their $CdS_{0.8}Se_{0.2}$ counterparts because the $CdS_{0.2}Se_{0.8}$ nanocrystals contain more selenium.

used during synthesis underscores the need for thorough materials characterization. Many researchers simply assume that their syntheses behave ideally. In the synthesis of core/shell nanocrystals, it is often assumed that all shell precursor material reacts (100% yield) to form shell, and that the shell is of uniform thickness on every facet of the core, yet it has been demonstrated not only that do shells grow preferentially off specific facets,[26,35] but that shell precursor often forms new nanocrystals rather than adhering to cores.[26] With respect to the alloy nanocrystals, we and others have shown that simply adding together the necessary precursors does not ensure that a homogeneous alloy of the same composition results.[32–34] In order to fully characterize the CdS_xSe_{1-x} nanocrystals' structure and composition, we applied a combination of RBS, XRD, TEM, and Z-STEM, which allowed us to conclude that the nanocrystals were indeed homogeneous. Without these tools, such a conclusion would be no more than speculation.

As a complement to the synthesis, we sought to quantify the relationship between size, composition, and band gap. The dependence of band gap on composition

in bulk semiconductors is well known,[65] as is the dependence of band gap on size in nanocrystals.[40,49] Surprisingly, research into alloy nanocrystals had not previously included any detailed study into how these dependencies interact, although Bailey and Nie noted that the bowing of the band gap in $CdSe_xTe_{1-x}$ nanocrystals of the same size appeared to be identical to the bowing of bulk $CdSe_xTe_{1-x}$.[32]

Despite the evidence of Bailey and Nie, we initially believed that the degree of bowing should depend on nanocrystal diameter. Bowing is caused both by differences in the chemical properties of the constituent elements and by structural changes in the bond lengths and angles.[66] While the chemical properties of the constituent elements are the same regardless of nanocrystal diameter, bond lengths contract slightly with decreasing diameter,[37] and the large surface-to-volume ratio in smaller nanocrystals may make the lattice more accommodating to strain; moreover, the nanocrystal surface and surface ligands could have unknown effects on the bowing. However, when the diameters, compositions, and band gaps of a number of alloy samples were compared, we found that the bowing constant was insensitive to size, with a value, 0.29 ± 0.16, equal to the bulk value, 0.3.[68,74,75] We can only conclude that the effects of size on the crystalline structure are not significant enough to impact the band gap.

The fact that bowing is insensitive to nanocrystal size opens up new possibilities for novel nanomaterial design. Since the bowing is known for many bulk alloys, we now have a means of predicting the behavior of the corresponding nanocrystals, allowing us to more accurately choose which structures to synthesize to obtain desired characteristics. In addition, regardless of the degree of bowing, these experiments demonstrate that, by varying the composition of the nanocrystals, we have introduced an additional means of tuning their properties. Multiple wavelengths can be generated by a single size, which could be useful when size requirements are specific, such as in biological imaging, where small nanocrystals are desirable. In addition, by using alloys, we can easily achieve band gaps (and other properties) which otherwise

would be difficult to achieve. For example, in the case of CdS and CdSe, making nanocrystals with a band gap of 2.6 eV (480 nm) is normally difficult; CdS nanocrystals would need to be very large (>100 Å), often resulting in a large size dispersity, while CdSe nanocrystals would conversely be very small (21 Å), difficult to synthesize accurately due to the speed of most reactions, difficult to image by TEM, and less stable than medium and large nanocrystals. $CdS_{0.8}Se_{0.2}$, however, produces the same band gap with a nanocrystal diameter of 32 Å, which is an ideal size from the standpoint of synthesis, imaging, and stability. We anticipate that for these and other reasons, alloys will play an increasingly important role in nanoengineering.

APPENDIX A

ADDITIONAL MODELS FOR QUANTUM CONFINEMENT IN NANOCRYSTALS

Section 1.2.3 presented a simple model of the dependence of the optical band gap on nanocrystal size. This model agreed well with experiment in the weak confinement regime but not in the strong confinement regime due to a series of assumptions made to simplify the model. In this appendix we present two additional models that are more complex yet more accurate.

A.1 Particle in a finite spherical potential well

One of the major questions at the core of the behavior of CdSe nanocrystals is how the electron and hole in a nanocrystal interact with the environment surrounding the nanocrystal. In Section 1.2.3, we modeled the wave function of a free charge as a particle in an infinite potential well; however, in reality the environment surrounding the nanocrystal has a finite potential energy. Indeed, research has clearly shown that the medium immediately surrounding the nanocrystal plays a significant role in the optoelectronic behavior of photogenerated charges within CdSe. Changing the surface ligand has been shown to shift the absorption and emission spectra,[50,77,120,128,129] to increase or decrease the fluorescent quantum yield,[50,77,87,120,128,130,131] and even to eliminate specific charge recombination pathways.[77,120,128,132,133] These effects have been attributed both to changing the nature of surface states and to movement of the charges off the nanocrystal to the surrounding medium. As a result, researchers often resort to coating nanocrystals in a thin layer of a higher-band gap semiconductor to produce core-shell nanocrystals. These nanocrystals exhibit greatly enhanced fluorescent quantum yields over the original core nanocrystals because the greater band gap of the shell passivates surface traps, as well as confining the electron and hole to

the core so that they are more likely to recombine radiatively at the band edge.

Recently, Tadd Kippeny of the Rosenthal group at Vanderbilt University noted anomalous behavior in CdSe/ZnSe core-shell nanocrystals.[77] Larger nanocrystals behaved as expected; upon shelling, the absorption spectrum remained largely unchanged, while the fluorescent quantum yield. However, as nanocrystals smaller than ∼33 Å in diameter were shelled, the absorption and emission spectra initially red-shifted without a significant rise in quantum yield. Then, once the core-shell reached 33 Å in diameter, any further shell material had the normal effect; quantum yield increased, and the absorption spectrum did not change. Kippeny attributed this behavior to the change in band offsets between CdSe and ZnSe as the CdSe core grew, combined with a tunneling effect that allowed charges limited access to the higher-energy material. Clearly in this case, a simple model assuming infinite potential outside the core CdSe is insufficient to explain the observed behavior.

In the current work on CdS_xSe_{1-x}, tunneling can also explain why a small core of sulfur-rich alloy does not appear to impact the light absorption properties of the nanocrystals. If the core is sufficiently small, and if the band energies are not much different in the core than in the surrounding alloy (for example, the difference in band gap energy between bulk $CdS_{0.8}Se_{0.2}$ and $CdS_{0.6}Se_{0.4}$ is only 0.182 eV), then the effect on electrons and holes is minimal, and they behave approximately as though the medium is uniform.

To explore the effects of tunneling on band gap energies, the model presented in Section 1.2.3 can be modified to model a 'particle in a spherical finite potential well'. This model, based on the work of Brus,[45] Flügge,[134] and Schooss,[135] still fails for small nanocrystals due to the effective mass approximation, yet it gives a good qualitative explanation of the phenomena that cannot be explained using an infinite potential well model.

We begin by defining the potential energy of the system using the exterior

medium, or 'solvent', as the reference potential:

$$V(r) = \begin{cases} -V_0 & r \leq R \\ 0 & r \geq R \end{cases} \tag{A.1}$$

We further define the following abbreviations:

$$\varkappa^2 = \frac{2m_0 \left|E'\right|}{\hbar^2} \tag{A.2}$$

$$k^2 = \frac{2m_q \left(V_0 - \left|E'\right|\right)}{\hbar^2} \tag{A.3}$$

$$\chi_0^2 = \frac{2m_0 V_0 R^2}{\hbar^2} \tag{A.4}$$

where E' is the energy and m_q the effective mass of particle q, m_0 is the electron rest mass, and R is the nanocrystal radius. It is noted that although we initially define the energy E' of the particle with respect to the solvent potential, by the end of this derivation we solve for the energy E of the particle above the bottom of the potential well:

$$E = V_0 - \left|E'\right| \tag{A.5}$$

It is also noted that χ_0 can be thought of as the 'well size'; because it is proportional both to the potential energy required to overcome the well height and produce a free particle (V_0) and to the radius of the well (R), the magnitude of χ_0 is a measure of how confined the particle is to the well. Finally, we define the term

$$\xi = \sqrt{\beta \frac{V_0 - \left|E'\right|}{V_0}} \tag{A.6}$$

where

$$\beta = \frac{m_q}{m_0} \tag{A.7}$$

We note that χ_0 and ξ are mathematical constructs, defined such that

$$\chi_0 \xi = kR \tag{A.8}$$

and

$$\varkappa R = \chi_0 \sqrt{1 - \frac{\xi^2}{\beta}} \tag{A.9}$$

Having defined the mathematical basis for the derivation, we begin by considering the case where $E' \leq 0$. In this case, the ground state wave function has the general form[134]

$$\psi(r) = \begin{cases} \frac{A}{r}\sin(kr) & r \leq R \\ \frac{C}{r}e^{-\varkappa r} & r \geq R \end{cases} \tag{A.10}$$

Since the wave function must be continuous, $\psi_{nc}(R) = \psi_0(R)$, where $\psi_{nc}(r)$ is the wave function when $r \leq R$ and $\psi_0(r)$ is the wave function when $r \geq R$. This implies that

$$C = A\sin(kR)\, e^{\varkappa R} \tag{A.11}$$

Normalizing, we find that

$$A = \frac{1}{\sqrt{\pi}}\left[R - \frac{1}{k}\sin(kR)\cos(kR) + \frac{1}{\varkappa}\sin^2(kR)\right]^{-1/2} \tag{A.12}$$

To solve for E, we use the fact that the flux of charges across the nanocrystal/solvent interface must be equal in both directions. According to BenDaniel and Duke,[136] at the junction of two finite potentials, the flux of charge across the interface must be equal, so that

$$\left.\frac{1}{m_q}\frac{\partial\psi_{nc}}{\partial r}\right|_{r=R} = \left.\frac{1}{m_0}\frac{\partial\psi_0}{\partial r}\right|_{r=R} \tag{A.13}$$

Using this equality and Equations A.8 and A.9, we establish the relationship

$$\tan(\chi_0\xi) = \frac{\chi_0\xi}{1-\beta-\beta\chi_0\sqrt{1-\frac{\xi^2}{\beta}}} \tag{A.14}$$

Graphing $\tan(\chi_0\xi)$ and $\chi_0\xi\left[1-\beta-\beta\chi_0\sqrt{1-\frac{\xi^2}{\beta}}\right]^{-1}$ versus ξ in the range $0 < \xi < \sqrt{\beta}$, the points at which the two functions intersect yield the values of ξ for which the equation is satisfied. There may be several of these points. Figure A.1 shows graphs of the left and right sides of Equation A.14 with respect to ξ for well sizes of 20 (top) and 90 (bottom) when $\beta = 0.11$ (the value for an electron in CdSe). When $\chi_0 = 20$, the two functions intersect twice, so that there are two ξ_n that satisfy Equation A.14, while when $\chi_0 = 90$, the functions intersect nine times, giving nine

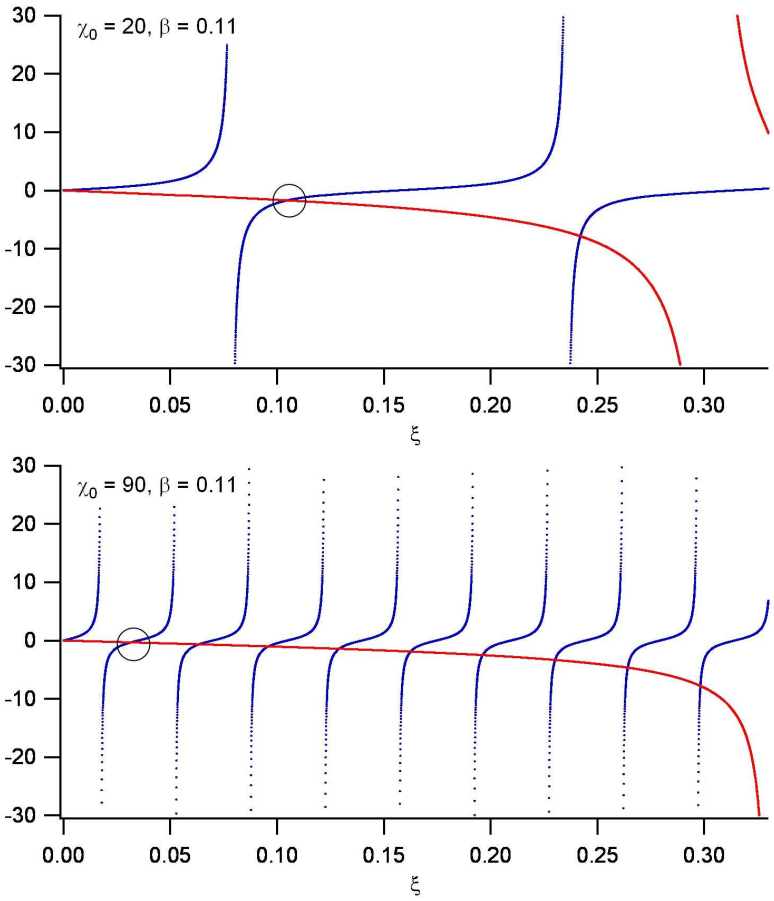

Figure A.1: Graphical solutions to (A.14) for well sizes of 20 (top) and 90 (bottom) when $\beta = 0.11$. The blue line is the function $f(x) = \tan(\chi_0 \xi)$, while the red line is the function $g(x) = \chi_0 \xi \left[1 - \beta - \beta\chi_0 \sqrt{1 - \frac{\xi^2}{\beta}}\right]^{-1}$; points of intersection indicate solutions to Equation A.14. The ground state solution (ξ_1) for each well size is circled. It is noted that $g(x)$ is soluble only in the range shown, so that the intersections shown are the only ones possible.

possible eigenvalues for ξ_n. Phenomenologically this makes sense - larger well sizes indicate wells of greater length or more potential energy, either of which would result in more energy levels available in larger wells than in smaller ones. In general, each ξ_n yields a wave function for a particle whose kinetic energy above the bottom of the well is[45]

$$E_n = \frac{\hbar^2 \chi_0^2 \xi_n^2}{2 m_q R^2} \tag{A.15}$$

The smallest of these, ξ_1, yields the ground-state energy (E_1).

Using the above equations, energies and wave functions were generated for electrons and holes in CdSe nanocrystals of radius 1 - 120 Å in toluene. Since the valence band maximum (VBM) and conduction band minimum (CBM) for CdSe are not known, the CBM was assumed to be that calculated by Wang and Zunger, –3.523 eV.[39] The VBM was taken to be CBM - 1.751 eV = 5.274 eV.[46] The effective masses of the electron and hole were taken to be $0.112m_0$ and $0.45m_0$,[46] respectively, inside the nanocrystal and m_0 outside the nanocrystal, in the manner of Schooss.[135] The electron affinity and ionization potential of toluene were assumed to be -1.19 eV and 8.9276 eV,[137,138] yielding potential energy wells for the electron and hole of 4.713 eV and 3.5536 eV, respectively.

Figure A.2 shows a selection of these calculated wave functions superimposed on the potential wells in which they were generated, highlighting the important trends in the wave functions. In each case, the wave functions are vertically offset from the bottom of the well by E_1, the energy of the wave function (dashed lines). Notably, as the nanocrystal decreases in size, the energy of the ground state (E_1) increases. (a) - (c) show wave functions of electrons in nanocrystals of diameters 15 Å (a), 30 Å (b), and 60 Å (c). As the diameter decreases from 60 Å to 15 Å, the ground state energy rises from 0.22 eV to 1.37 eV. A similar trend is evident in the hole energies in (d) and (f). As well as increasing energy, the probability $|\psi|^2$ of finding the charge outside the nanocrystal increases with decreasing diameter. In (c), the probability of finding the

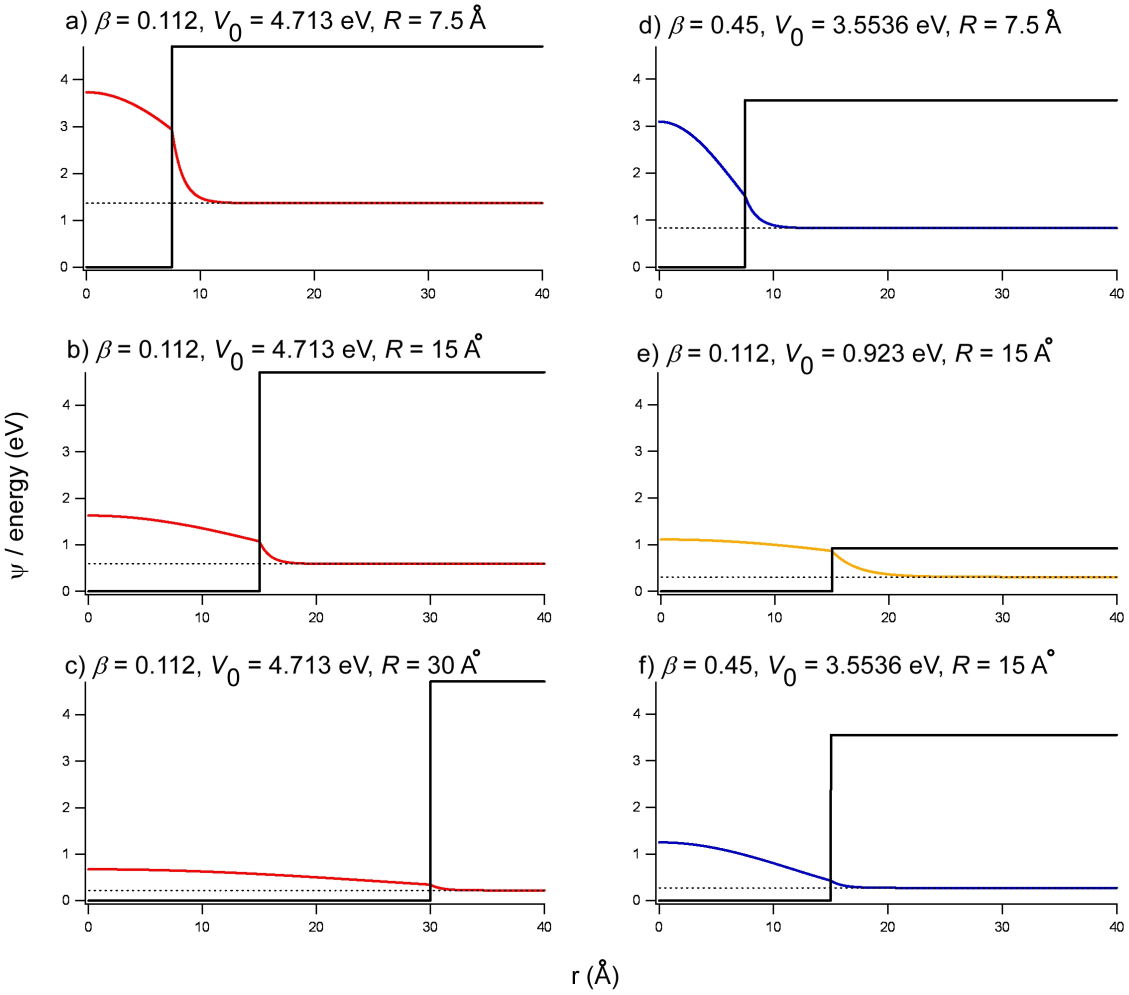

Figure A.2: wave functions generated using the 'particle in a finite spherical potential well' model.

electron outside the nanocrystal is 1.1%, whereas in (a) the probability is 12.9%. The probability of finding the hole outside the nanocrystal is slightly less: 0.2% in a 60 Å nanocrystal (f) versus 6.2% in a 15 Å nanocrystal (d). These values are somewhat inflated because they do not account for the Coulomb attraction between the electron and hole and because of the failure of the effective mass approximation in the 15 Å nanocrystals; nevertheless, they clearly demonstrate that the charge carriers spend a significant portion of time outside the core nanocrystal, and that the proportion of time increases as the nanocrystal diameter decreases.

To explore further the effect of band offsets on the wave function, (b) and (e) compare the wave functions of an electron in a 30 Å nanocrystal in a deep potential well (b) and in a shallow potential well (e). These might correspond to a nanocrystal in an organic solvent with a much larger band gap and one with an inorganic shell of only moderately larger band gap. As expected, the wave function of the electron in the shallow well extends much further into the surrounding medium; in this case, the electron is in the surrounding medium 15.3% of the time, compared to 4.4% outside the deeper well. This demonstrates that in a core-shell material such as Kippeny's CdSe/ZnSe system, the electron and hole can spend a significant portion of time in the shell material, even if band alignment dictates that the electron and/or hole be preferentially confined to the core. As this effect is more prominent in smaller nanocrystals, this accounts for the greater red-shift observed in smaller nanocrystals upon shelling. Likewise, it suggests that a small sulfur-rich core in the alloy nanocrystals does not greatly impact the band gap, since the band offset between the 'core' and 'shell' is small.

We now consider the case when $E' > 0$. In this case, the energy of the particle is greater than the potential of the solvent. In this case the wave function is given by

$$\psi(r) = \begin{cases} \frac{A}{r}\sin(k'r) & r \leq R \\ \frac{B}{r}\sin(\varkappa r) + \frac{C}{r}cos(\varkappa r) & r \geq R \end{cases} \tag{A.16}$$

where

$$k'^2 = \frac{2m_q\left(|E'| - V_0\right)}{\hbar^2} \tag{A.17}$$

Again, by using the continuity requirement and Equation A.13, we can relate A, B, and C:

$$\begin{aligned} A &= \frac{1}{\sin\left(k'R\right)}\left[B\sin\left(\varkappa R\right) + C\cos\left(\varkappa R\right)\right] \\ B &= \frac{\cos\left(\varkappa R\right) + \beta\tan\left(k'R\right)\sin\left(\varkappa R\right)}{\beta\tan\left(k'R\right)\cos\left(\varkappa R\right) - \sin\left(\varkappa R\right)}C \end{aligned} \tag{A.18}$$

Notably, when $E > V_0$, $\psi(r)$ does not vanish as $r \to \infty$. This has several important consequences. First, we have proven mathematically what is intuitively obvious - that when the energy of the particle is greater than the potential of the solvent, the particle is unbound. Once generated, it freely passes off the nanocrystal into the solvent and does not return. Second, the wave function cannot be normalized. Third, and most importantly, energy above the solvent potential is not quantized; instead, a particle with any energy greater than V_0 behaves as a wave, with a deBroglie wavelength of $\frac{2\pi}{k'}$ inside the nanocrystal and $\frac{2\pi}{\varkappa}$ outside the nanocrystal.[139] It is noted that the wave function undergoes a phase shift and an amplitude shift at the interface. The lack of quantization for $E > V_0$ has fundamental consequences for the ground state energy of a particle in a finite spherical potential well - namely, that V_0 is the upper limit for the ground state kinetic energy.

A.2 Computational models

To quantitatively model the dependence of band gap on size, it is necessary to provide a more accurate description of the nanocrystal by including the prolate, elliptical shape of the nanocrystal; by taking into account the effect of the wurtzite crystal structure on the valence band energy; by considering the size-dependence of such physical properties as dielectric constants and electron and hole effective masses; and by using a quantum mechanical exchange interaction between the electron and

Table A.1: Parameters used in calculating optical band gaps according to Wang and Zunger.[39] Band gaps were calculated by E_g = CBM − VBM. Dielectric constants were calculated using Equations 2 and 7 of the aforementioned reference.

nanocrystal diameter, d (Å)	VBM (eV)	CBM (eV)	$\beta(d)$	$E_g(d)$ (eV)	$\epsilon_{nc}(d)$
12.79	-6.273	-2.174	0.139	4.099	4.6942
20.64	-5.829	-2.807	0.212	3.022	5.4885
29.25	-5.617	-3.091	0.282	2.526	6.0219
38.46	-5.489	-3.236	0.348	2.253	6.4224
∞	-5.241	-3.523	1	1.718	9.7

hole.[39,140] Such calculations are too complex to solve by any but computational methods, which is beyond the scope of this work; however, as an example of the results attainable by such methods, we consider the optical band gaps calculated by Wang and Zunger.[39] Using mesoscopic pseudopotential methods, Wang and Zunger calculated the VBM, CBM, and the ionic contribution to exciton screening (β) for four sizes of CdSe nanocrystals as well as the bulk values. These values were then used to calculate the electronic band gaps (E_g) and the relative dielectric constants for the four sizes and the bulk. These results are summarized in Table A.1. The electronic band gaps and dielectric constants were then empirically fit to a double exponential to obtain the size dependence:

$$E_g(d) = (1.178\text{ eV}) + (2.305\text{ eV})e^{-3.8665d} + (8.0862\text{ eV})e^{-0.16538d} \tag{A.19}$$

$$\epsilon_{CdSe}(d) = 9.7 - 4.7771e^{-0.010168d} - 3.3662e^{-0.11125d} \tag{A.20}$$

(The coefficients in the exponents of both equations have units of Å^{-1}.) Finally, Equation 3 of Wang and Zunger was used to calculate the size dependence of the optical band gap of the nanocrystals:[39]

$$E_{opt}(d) = E_g(d) - \frac{3.572\text{ eV}\cdot\text{Å}}{d\cdot\epsilon_{CdSe}(d)} \tag{A.21}$$

Figure A.3 compares optical band gaps calculated using Brus' model with those calculated using Wang and Zunger's equation. Although Wang and Zunger's calcu-

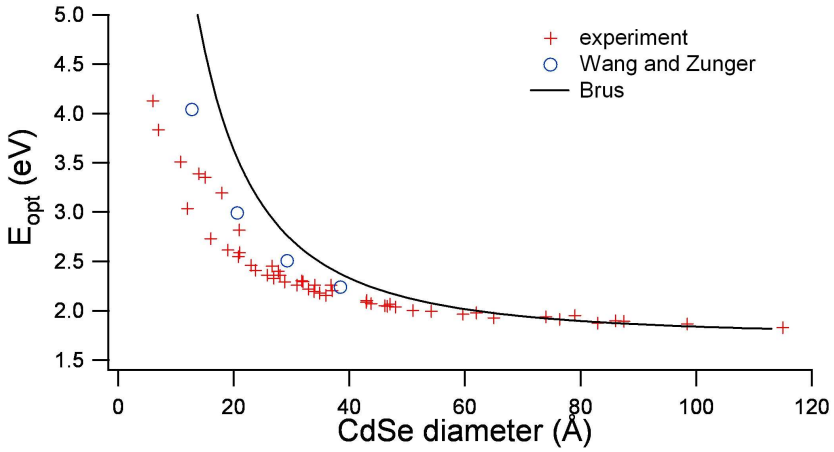

Figure A.3: Optical band gaps of CdSe nanocrystals calculated according to Brus' model[49] and according to Wang and Zunger's model.[39] The experimental data from Figure 1.10 is also provided for purposes of comparison.

lated values still err on the side of high energy, particularly for smaller nanocrystals, they are much closer to the true values than Brus' model, a reflection of the greater accuracy of the model.

APPENDIX B

ADDITIONAL RBS ANALYSIS

This appendix details three sets of equations, used to quantify nanocrystal surface coverage by ligands, core-shell thickness, and SHG sample thicknesses based on RBS analysis, that were derived during the course of this work but do not pertain to the alloy nanocrystal project. Results based on these equations first appeared in Rosenthal *et al.*,[18] and have been used since in a variety of other publications by the Rosenthal group.

B.1 Nanocrystal surface coverage by ligands

The percent coverage of nanocrystal surface by a particular ligand was calculated from RBS spectra in the following manner. First, the areal densities of Cd and Se were calculated. Because CdSe nanocrystals often have excess Cd on the surface,[95] the ratio of Cd to Se was set equal to $1 + x$:

$$\frac{N_{Cd}}{N_{Se}} = 1 + x \tag{B.1}$$

Next, the molecular weight of a CdSe 'diatom' was calculated by

$$w_{Cd_{1+x}Se_1} = (1 + x)(112.41 \text{ g·mol}^{-1}) + 78.96 \text{ g·mol}^{-1} \tag{B.2}$$

Assuming a spherical nanocrystal, the approximate volume, $V(d)$, of one nanocrystal was determined from its diameter, d, which could be found using HR-TEM or UV-visible spectroscopy:

$$V(d) = \frac{1}{6}\pi d^3 \tag{B.3}$$

The volume, density of wurtzite CdSe ($D_{CdSe} = 5.81$ g·mL^{-1}[141]), and diatomic molecular weight (from Equation B.2) were used to calculate the number of Se atoms in

one nanocrystal:

$$n_{Se}(d) = N_A \cdot \frac{1}{w_{Cd_{1+x}Se_1}} \cdot D_{CdSe} \cdot V(d) \qquad (N_A = \text{Avogadro's number}) \qquad \text{(B.4)}$$

and using Equation B.1, the number of Cd atoms per nanocrystal was determined.

That all excess Cd atoms are located on the nanocrystal surface[95] complicates the determination of the number of surface Cd and Se atoms. To account for the excess Cd, the volume and diameter of the nanocrystal without excess Cd were calculated. This volume, $V(d')$, was calculated by a rearrangement of Equation B.4, using a diatom molecular weight corresponding to $x = 0$ and the number of Se atoms found previously. The number of surface atoms of each type was then calculated by first finding the number of interior atoms. By definition, any atom that is one diatomic layer, $a = 3.505$ Å, away from the surface must be an interior atom. Therefore, the diameter of the interior of the nanocrystal is $d' - 2a$. The number of interior Se atoms, $n_{Se}(d' - 2a)$, was then calculated using Equations B.3 and B.4, with the stoichiometric diatomic weight $w_{Cd_1Se_1}$. The number of interior Cd atoms is the same as the number of interior Se atoms. Finally, the number of exterior Se atoms was calculated by

$$n_{Se}(ext) = (1 - x)n_{Se}(d) - n_{Se}(d' - 2a) \qquad \text{(B.5)}$$

while the number of exterior Cd atoms was calculated by

$$n_{Cd}(ext) = n_{Cd}(d) - n_{Cd}(d' - 2a) \qquad \text{(B.6)}$$

It is noted that the term $1 - x$ in Equation B.5 accounts for the excess surface Cd atoms; on average, one Cd atom passivates one Se atom, and the number of excess Cd atoms is $xn_{Se}(d)$. The extra Cd atoms are already included in the term $n_{Cd}(d)$ in Equation B.6.

The number of surface Cd and Se atoms were then related to the number of ligands per nanocrystal. The number of ligands per nanocrystal was determined by

finding the areal density of an atom unique to the ligand (e.g., phosphorus in TOPO) and relating that density to the density of Cd:

$$n_{lig} = \frac{N_{lig}}{N_{Cd}} n_{Cd}(d) \tag{B.7}$$

Having found the number of ligands per nanocrystal, the percent coverage is simply the ratio of the number of ligands per nanocrystal to the number of exterior Cd or Se atoms per nanocrystal, depending onto which atom the ligand binds.

It is noted that this method of calculating the percent coverage is accurate only if the nanocrystal sample was thoroughly cleaned before RBS analysis, and if the ligand did not get pulled off the nanocrystal surface by the 10^{-6} Torr conditions of the RBS beam line. The first could be verified by taking RBS spectra of the nanocrystal wash waste to verify that the last wash was ligand-free.[95] To deal with the second is more difficult. Experience has shown that phosphines, phosphine oxides, and sulfides bind well to the nanocrystal surface, but that amines do not. One sign that ligands have been removed by the vacuum conditions is that the percent coverage by *all* ligands in a sample is much less than the number of surface atoms that can bind the ligands. If this is found to be the case, a different technique should be used, such as NMR.

B.2 Shell thickness in core-shell nanocrystals

RBS was also used to calculate the thickness of shells in core-shell nanocrystals (e.g., see Rosenthal *et al.*[18]). First, Equations B.1 - B.4 were used to calculate the core volume, V_c, and the number of Cd and Se atoms per core. Then the number per core-shell of each shell atom was determined using Equation B.7. As with the core material, the empirical formula and the 'diatom' molecular weight of the shell material were determined using Equations B.1 and B.2. Next, these values and the density of the shell material were used in Equation B.4 to calculate the volume of the shell material, V_s.

Sometimes the core and shell had one type of atom in common (for example, Se in CdSe/ZnSe). In such a case, the areal density of the common atom needed to be separated into core and shell densities before the different volumes could be determined. Ideally, a sample of cores was saved during the core-shell synthesis; RBS on the cores would yield the correct ratio of Cd to Se in the cores. From this ratio, the core and shell areal densities of the common atom could be calculated in the core-shell sample. If a sample of cores was not available, Cd and Se were simply assumed to be stoichiometric in the core.

Once the volumes of the core and shell were known, then the volume of the total core-shell was simply the sum of the individual parts. Again assuming a spherical core-shell, then the diameter of the core-shell, d_{cs}, was

$$d_{cs} = \left[\frac{6}{\pi}\left(V_c + V_s\right)\right]^{\frac{1}{3}} \tag{B.8}$$

Since the diameter of the core was known from UV-vis spectroscopy or TEM, the thickness of the shell was simply

$$r_s = \frac{1}{2}\left(d_{cs} - d_c\right) \tag{B.9}$$

As with the calculation of surface ligand coverage, this calculation depends on having a clean sample. In addition, while vacuum cannot remove shell material, the shell precursors sometimes form nanocrystals composed solely of the shell material. There is no way for RBS to distinguish between shell material in core-shells and shell material in shell-only nanocrystals. TEM often detects the presence of shell-only nanocrystals; if a significant number of these are detected, then the shell thicknesses calculated by RBS are grossly inaccurate. The only way to determine shell thickness accurately is then atomic number contrast scanning transmission electron microscopy (Z-STEM).[88]

B.3 SHG sample thickness

One of the important questions that needed to be answered in determining experimental protocol, as well as in analyzing SHG data was the determination of how many layers of nanocrystals were on the Si surface in Si/CdSe samples. Additionally, it was occasionally necessary to obtain the thicknesses of a variety of thin films.

To determine thin film thickness, the areal density, N_t, of an element unique to the thin film (e.g., oxygen in a sample of Si/SiO_2) was simply divided by the density of the thin film material, D_{tf}:

$$t_{tf} = \frac{N_t}{D_{tf}} \tag{B.10}$$

If no element was unique to the thin film, then SIMNRA was used to determine film thickness.

To find the number of layers of CdSe nanocrystals on the Si surface in SHG samples, the number of Se atoms per nanocrystal, n_{Se}, was first determined according to Equations B.1 - B.4. Next, the areal density of nanocrystals, N_{CdSe} was determined by

$$N_{CdSe} = \frac{N_{Se}}{n_{Se}} \tag{B.11}$$

The number of nanocrystal layers was determined in the same manner as in Equation B.10:

$$n_{CdSe} = \frac{N_{CdSe}}{D_{pack}} \tag{B.12}$$

where D_{pack}, the packing density, is defined as the fraction of occupied space in the nanocrystal layer. Unfortunately, the packing density of the nanocrystals is not known. To estimate the packing density, we began by making the assumption that the packing was some form of close packing (i.e., that there were no holes in the layer large enough to accommodate an entire nanocrystal).[112] Under this assumption, the packing density of spheres lies somewhere between the densities of random close packing and hexagonal close packing: $D_{pack} \approx 0.64 - 0.74$.[142–145] However, nanocrystals are not spherical; the packing of ellipsoids is more efficient: $D_{pack} \approx 0.68 - 0.76$,[146–148] and the

packing of identical Wurtzite nanocrystals should be more efficient yet. Because real samples of nanocrystals are non-uniform, Wurtzite ensembles that have only gravity to force them into a close-packed arrangement, we estimated that $D_{pack} \approx 0.70$.

Finally, if the actual thickness of the nanocrystal layer was desired, the average areal density of Cd and Se atoms was found by

$$N_{avg} = \frac{N_{Cd} + N_{Se}}{2} \tag{B.13}$$

The thickness was then calculated from the average areal density by

$$t_{CdSe} = \frac{N_{avg}}{d_{CdSe} D_{pack}} \tag{B.14}$$

APPENDIX C

NANOMATERIAL-BASED PHOTOVOLTAICS

Currently the majority of world energy demands are met through the use of nonrenewable or nuclear resources. However, as demand for energy increases, we are quickly exhausting our nonrenewable energy reserves.[149,150] In contrast, renewable energy resources such as sun, wind, water, biomass, and the earth itself can provide more than enough energy to meet demand. In addition, most of these produce clean energy with no polluting by-products. Of these energy sources, solar energy offers the greatest potential source of energy accessible by current technology. Though solar cells have been commercially available for several decades, high production costs and low power conversion efficiencies have kept them from occupying a large portion of the energy market. Commercial wafer-based crystalline silicon solar cells, which comprise more than 80% of the current solar energy market, have power conversion efficiencies of only $12-17\%$ and produce electricity at a cost of 25-50c/kWh, five times the cost of fossil fuel-generated electricity.[151,152]

The efficiencies of photovoltaics can be improved through the use of light-concentrating optics, alternate semiconductors such as GaAs, heterojunction structures involving more than one type of semiconductor, or complex structures designed to maximize light absorption within the photoactive region. Unfortunately, the efficiency of any photovoltaic based on traditional semiconductors is ultimately limited by several factors. First, the energy of incident photons in excess of the band gap is wasted as heat. Second, the output voltage is always less than the maximum possible voltage due to interface and other effects. Third, electrons and holes generated outside the active region of the device (the depletion region) do not contribute to device output. Fourth, many additional photogenerated electrons and holes are lost through

additional loss mechanisms, including charge recombination and carrier trapping at defects. As an example, the ideal efficiency of a *pn* junction silicon photovoltaic is only 26% at 1 sun intensity under AM 1.5 lighting conditions (see Appendix E for a description of lighting conditions).[153] A working limit for bulk semiconductor photovoltaics based on heterojunction structures seems to be 15% efficiency; while higher efficiencies can be achieved, they are achieved at the expense of ease of production, cost of production, or environmental impact.[151]

In contrast, nature provides an excellent example of a highly efficient solar cell. Photosynthesis, the process used by plants to harvest light and store its energy in the form of carbohydrates, has a power conversion efficiency of 50% at wavelengths at which chlorophyll absorbs, and an internal photon-to-electron quantum yield of 99%.[154] In photosynthesis, a series of organic molecules are used first to harvest light, then to transport the resultant charge carriers through separate molecules to the chemical reaction centers which use them. By funneling charges through separate media, charge carrier recombination is essentially eliminated. In many ways, photosynthesis represents the ideal in photovoltaic technology: the system is highly efficient, and obviously is both inexpensive to produce and environmentally friendly.

It would be extremely difficult for humanity to design a photovoltaic system as complex and efficient as chlorophyll and photosynthesis; however, we can access some of the desirable features of the photosynthetic system to improve on current photovoltaics by incorporating nanomaterials in photovoltaic design. Nanomaterial-based photovoltaics are photovoltaics whose charge generating and transporting materials are discrete molecules or nanoparticles rather than bulk semiconductors. These nanomaterials vary widely, and include organic and inorganic dyes, semiconducting oligomers and polymers, electrolytes, buckminsterfullerene derivatives, and semiconductor nanocrystals and nanorods. The physical properties of nanomaterials are as varied as the nanomaterials themselves; the only thing these materials share in com-

mon is their small size: 1 Å − 100 nm in the longest dimension. Nanomaterials can be assembled in combination and in a variety of architectures to form photodiodes or heterojunction photovoltaics.

In this appendix we review different examples of molecular and nanomaterial-based photovoltaics (NBPs) and discuss the physics of these devices. In order to illustrate the differences between these devices and bulk semiconductor solar cells, we first review the physics of the *pn* junction solar cell and other photovoltaic designs based on bulk semiconductors. We also describe nature's solar energy converter, the photosystem of plants, which has many of the properties desired in NBPs. Finally, we discuss a CdSe nanocrystal-based photovoltaic proposed by the Rosenthal group in the context of these photovoltaics.

C.1 Conventional photovoltaics

C.1.1 pn junction photovoltaics

Historically silicon was the first material used to make solar cells, and it is still the most widely used semiconductor for solar cells, although other materials, such as GaAs and $CuInSe_2$, are also being explored. Today's commercial solar cells typically consist of polycrystalline silicon and have efficiencies ranging from $12 - 17\%$.[151,155] High-purity, monocrystalline Si cells show a power conversion efficiency as high as 24.4% in laboratory experiments,[156] only slightly less than their ideal efficiency, 26% (see Appendix E for a mathematical description of power conversion efficiencies and other photovoltaic terminology).[153] The ideal limit comes about for three reasons. First, the energy of incident photons in excess of the band gap is wasted as heat. Second, the output voltage is always less than the maximum possible voltage due to interface and other effects. Real devices do not realize the ideal efficiency due to additional loss mechanisms resulting from the width of the depletion region, charge recombination, and carrier trapping at defects. Third, Si does not absorb the full solar

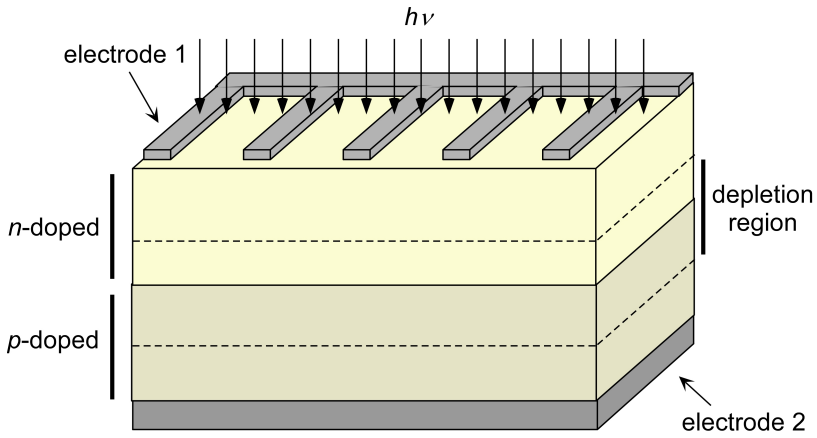

Figure C.1: A *pn* junction photovoltaic. Sunlight enters through the fingered electrode at the top of the device. Light which is absorbed within the depletion region generates free electrons and holes, which then travel to opposite electrodes, generating current. Not shown to scale.

spectrum; light with energy below silicon's optical band gap does not contribute to charge carrier generation. We detail a *pn* junction device and these loss mechanisms below, as it is exactly these mechanisms that NBPs may overcome.

The prototypical *pn* junction device is a semiconductor that is *p*-doped in one region and *n*-doped through the remainder of the material (Figure C.1). Electrodes attached to the *p*- and *n*-doped regions collect photogenerated charge carriers. The photoactive region of the device is the depletion layer - the area at the junction of the *p*- and *n*-doped regions which, under dark conditions, is depleted of free charges. The depletion layer is photoactive because it has an intrinsic electric field, which acts to separate electron-hole pairs generated within the depletion layer, accelerating electrons towards the *n*-doped region and holes towards the *p*-doped region. Only electrons and holes generated in this region contribute to photocurrent; outside the depletion layer, there is no electric field to separate the photogenerated charges, so they are lost to recombination. Since those areas of the semiconductor not in the depletion layer do not contribute to charge generation, yet do contribute to current loss through resistance and trapping mechanisms, the most efficient *pn* junction solar

cells are those whose depletion layers extend the full width of the semiconductor.

To understand the physics of the depletion layer and how a *pn* junction photovoltaic works, we follow Sze's treatment of *pn* junctions.[157] We consider first the hypothetical situation in which the *p*- and *n*-doped regions are separate (Figure C.2a). Because of the doping in the two semiconductors, the *p*-doped region has a certain concentration, N_a, of acceptor sites, which donate free holes to the semiconductor. The doping levels in *pn* junction devices is much higher than the free electron and hole populations in an intrinsic semiconductor. Therefore, the number of acceptor sites is approximately the same as the number of free holes in the *p*-doped semiconductor: $p \approx N_a$, where p is the concentration of free holes in the semiconductor; the number of free electrons is virtually nonexistent. Likewise, the *n*-doped region has a concentration, N_d, of donor sites, which is equal to the concentration of free electrons, n, in the semiconductor, and virtually no holes are present. To form the junction, the two regions are brought together. Once in contact, holes from the *p*-doped region and electrons from the *n*-doped region diffuse across the interface (Figure C.2b). As they intermingle, they mutually annihilate, leaving the area surrounding the interface devoid of free charges: the depletion layer. However, the positively charged donor and negatively charged acceptor sites are still present. Consequently, an electric field is generated across the depletion region (Figure C.2c); elsewhere in the semiconductor there is no electric field, because the concentration of free charges is equal to the concentration of donors or acceptors.

Using the depletion approximation, we can calculate the physical characteristics of the depletion layer. The depletion approximation states in a formal way what we have already assumed: that minority carrier concentrations on each side of the depletion layer are so small that they can be treated as nonexistent; that the free (majority) carrier concentration outside the depletion layer is equal to the donor or acceptor density; and that free carrier concentration within the depletion layer is

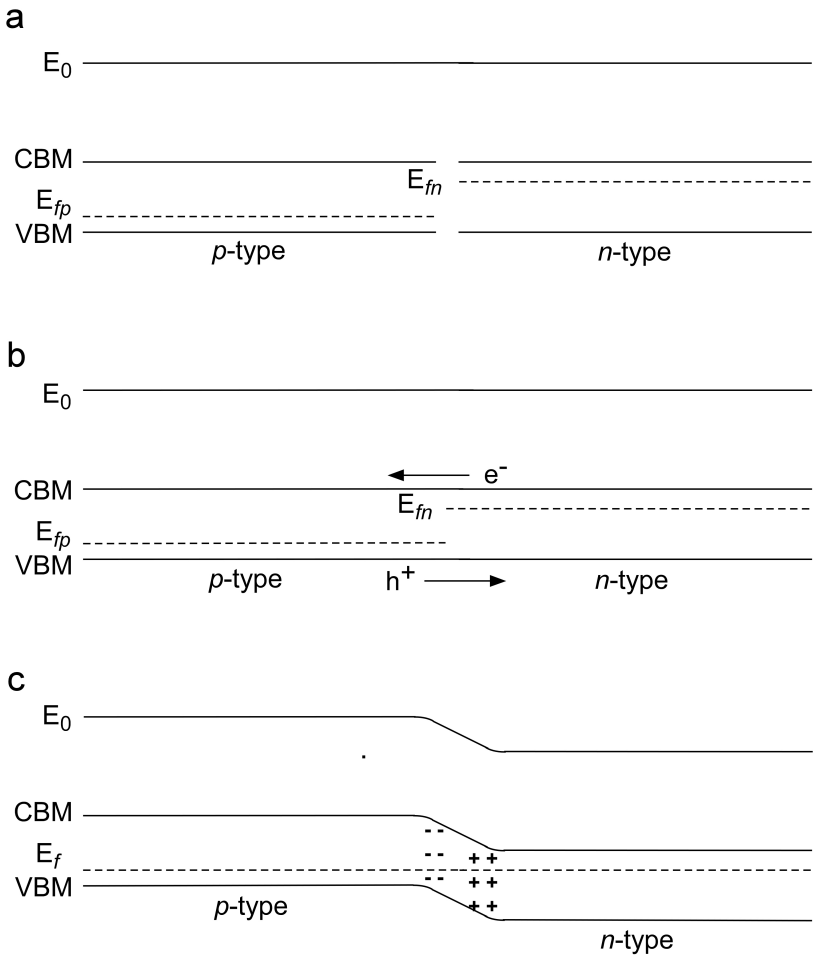

Figure C.2: Formation of the depletion layer in a *pn* junction. The vacuum level energy, E_0, is given as reference.

much less than the donor or acceptor density. We define the width of the depletion layer as

$$x_d = x_n + x_p \tag{C.1}$$

where x_p and x_n are the widths of the depletion region in the p- and n-doped regions, respectively. We also define the point $x = 0$ as the point of interface between the two regions. Under the assumptions of the depletion approximation, the electric field within the device is

$$\varepsilon(x) = \begin{cases} -\frac{qN_a}{\epsilon_s}(x + x_p) & -x_p < x < 0 \\ -\frac{qN_d}{\epsilon_s}(x_n - x) & 0 < x < x_n \\ 0 & x < -x_p, x > x_n \end{cases} \tag{C.2}$$

where ϵ_s is the dielectric constant of the semiconductor and q is the elementary charge.

The behavior of the Fermi level in the depletion layer warrants particular attention, as it is the difference in Fermi levels that determines the potential drop across the interface and the width of the depletion layer. The Fermi levels of the separated regions can be calculated from the doping levels by

$$E_{fn} = E_i + k_B T \ln\left(\frac{N_d}{n_i}\right) \quad (n\text{-doped}) \tag{C.3}$$

$$E_{fp} = E_i - k_B T \ln\left(\frac{N_a}{n_i}\right) \quad (p\text{-doped}) \tag{C.4}$$

where E_i is the intrinsic Fermi level energy (the Fermi level of the semiconductor if undoped), n_i is the intrinsic free electron concentration, T is the temperature, and k_B is Boltzman's constant. When the depletion layer is established, there cannot be a discontinuity in the Fermi level of the joined materials. Under ideal conditions, the Fermi levels of the two regions align, generating a potential drop across the interface of

$$\phi_i - V_a = \frac{k_B T}{q} \ln \frac{N_d N_a}{n_i^2} \tag{C.5}$$

where ϕ_i is the built-in potential and V_a is the applied bias, if present.

The width of the depletion region depends on the potential drop across the interface by

$$x_d = \left[\frac{2\epsilon_s}{q} (\phi_i - V_a) \left(\frac{1}{N_a} + \frac{1}{N_d} \right) \right]^{1/2} \tag{C.6}$$

Once the photogenerated electrons and holes have moved out of the depletion layer, they have a potential difference of

$$V_{max} = \mathrm{CBM}_n - \mathrm{VBM}_p = E_g - (\phi_i - V_a) \tag{C.7}$$

where E_g is the band gap of the semiconductor and CBM_n and VBM_p are the conduction band minimum (CBM) and valence band maximum (VBM) of the n- and p-regions, respectively. Because electrons and holes cannot transfer to electrodes that are higher in energy than CB_n and VB_p, the potential given in Equation C.7 represents the maximum possible voltage in the pn junction device under a given bias.

This simple description of the physics of the pn junction device illustrates two important limitations to this design. First, the photoactive region is limited to the depletion layer. As seen in Equation C.5, the width of the depletion layer depends on the doping levels of the p- and n-regions and on the potential drop across the interface. The width can be increased by decreasing the doping levels in the semiconductor. From Equation C.7, this also increases V_{max}; however, the electric field across the depletion layer decreases. Charges travel through the device more slowly, and charge recombination becomes more likely. The width can also be increased by applying a bias to decrease the voltage drop across the interface; again, the electric field across the interface decreases and charge recombination increases.

The second limitation lies in the fact that light harvesting and charge transport occur in the same medium. As seen above, increasing the width of the depletion layer in pn junction devices diminishes the electric field, leading to more charge recombination within the depletion layer. In addition, the resistivity of any semiconductor

increases with decreasing doping;[157] in increasing the width of the depletion layer by decreasing doping levels, charge recombination *outside* the depletion layer also increases. Moreover, any charges generated outside the depletion layer are lost to charge recombination.

In light of these loss mechanisms, some intrinsic design parameters for NBPs are apparent. First, the entire volume of the device should be photoactive. This can be accomplished by utilizing thin film or bulk heterojunction geometries, and by incorporating nanomaterials that have larger absorption cross-sections than their bulk counterparts. Second, electrons and holes should be transported through separate media with a minimal interface region in order to minimize recombination. Additionally, this naturally implies light harvesting and charge transport should be carried out by separate components.

C.1.2 Alternative bulk semiconductor photovoltaics

Although silicon and other single-material *pn* junction photovoltaics are certainly the most common bulk semiconductor photovoltaics, there are a wide variety of alternative architectures also based on bulk semiconductors. The simplest of these is the *pn* heterojunction photovoltaic. The *pn* heterojunction is essentially the same structure as the single-material *pn* junction, save that the *p*- and *n*-type semiconductors are of different materials. The physics presented in Section C.1.1 apply also to heterojunction photovoltaics. At the interface the vacuum energy levels of the two materials align; then, as in single-material photovoltaics, the energy bands of the materials bend so that outside the depletion region the Fermi levels align. Because the materials are not identical, the alignment of the vacuum energy levels at the interface may result in one or more Schottky barriers at the interface (Figure C.3).

The advantages to using different semiconductors for the *p*- and *n*-type materials are twofold: a better control of interface properties, and the ability to manipulate

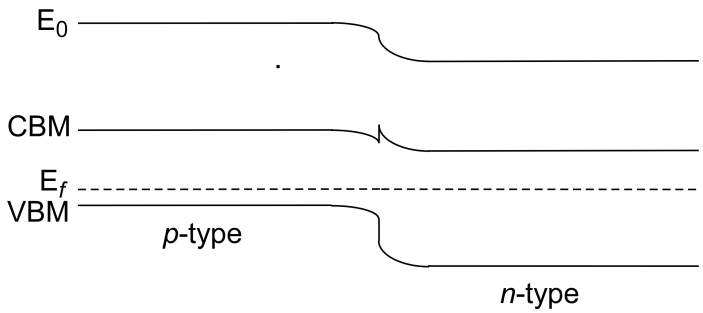

Figure C.3: Interface of a *pn* heterojunction. Shown is the interface of a smaller band gap *p*-type semiconductor and a larger band gap *n*-type semiconductor. In this case, there is a Schottky barrier at the conduction band interface; electrons must tunnel or otherwise overcome this barrier in order to pass from the *p*-type semiconductor to the *n*-type semiconductor.

the light absorption properties of the material. At single-material *pn* interfaces, the offset of E_{fn} and E_{fp}, the electric field at the interface, the width of the depletion layer, and the resistivity of the two sides of the interface are solely dependent on doping levels. At heterojunction interfaces, the offset of E_{fn} and E_{fp} depends on the offsets of the valence bands (VBs) and conduction bands (CBs) as well as the dopant concentrations in the two semiconductors; consequently, the electric field at the interface and the width of the depletion layer are largely independent of the resistivity of the two sides of the interface. By judicious selection of the two materials, it is possible to some degree to improve the electric field at the interface and to increase the width of the depletion layer without increasing the resistivity.

Light absorption can also be controlled to a limited extent by using two semiconductors instead of one. In a single-semiconductor device, the same spectrum of light is absorbed throughout all regions of the device. Since light absorption follows a decaying exponential with distance, if the depletion layer does not extend all the way to the front electrode (the electrode which faces the incoming light source), then much of the incoming light may be absorbed before it reaches the depletion layer. In a heterojunction device, however, if the wider band gap semiconductor is in con-

tact with the front electrode, then it absorbs photons with energies higher that its band gap, but is transparent to lower energy photons. Photons with energies that lie between the band gap energies of the two semiconductors are absorbed primarily in the depletion region. Thus it is possible to engineer a heterojunction device which absorbs more light in the depletion layer than a single-material photovoltaic with a depletion layer of the same width.

In addition to *pn* photovoltaics, there are multilayer photovoltaics such as *pin* (i = intrinsic) structures, *ppn* structures, etc., which are used to increase the width of the depletion layer and hence the width of the photoactive region of the device. Another increasingly attractive strategy is to increase the width of the depletion layer by increasing the surface area of a junction. This is accomplished by moving away from thin film structures and increasing the surface roughness at the heterojunction, either by selectively etching away an existing crystalline structure or by selectively depositing crystalline material in a specific pattern.[155,158,159] This strategy is the first step towards the use of nanomaterials in photovoltaic devices.

C.2 Photosynthesis

For highly efficient, truly nanostructured solar energy conversion, we must look to nature. Photosynthesis is the source of all free energy consumed by biological systems on earth. In photosynthesis, light energy from the sun is harvested by plants and photosynthetic bacteria and stored as chemical energy by converting carbon dioxide and water to carbohydrates and oxygen. Unlike *pn* junction photovoltaics, which rely on the same material for light harvesting and charge transport, photosynthesis is a multistep process in which light is harvested and charges separated in a series of different organic compounds, virtually eliminating charge recombination. Rather than using an electric field to separate charges, the photosynthetic process uses the charge transfer of electrons and holes from higher states in one material to lower

energy states in different materials to achieve charge separation.

Given the vast number of plant and bacterial species that use photosynthesis to produce energy, there are a variety of different photosystems. However, the basic architecture of each photosystem is similar. In each case, a light-harvesting antenna complex funnels excitons formed upon the absorption of light to a transmembrane photosynthetic reaction center. The reaction center separates the electron and hole through a series of chemical reactions to opposite sides of the membrane. Finally, a series of chemical reactions on each side of the membrane harvest the charges. While higher plants have more sophisticated light harvesting apparati to harvest a greater wavelength range of sunlight, the processes involved in harvesting that sunlight are completely analogous to those found in the simplest purple bacteria, with the essential elements of the reaction center also being identical. The photosystems of even these simple bacteria are strikingly efficient, with 99% of absorbed photons leading to charge separation across a membrane (99% photon-to-electron conversion efficiency).[154] We use purple photosynthetic bacteria to illustrate the basic components of light harvesting and charge transfer.

The light-harvesting complex of purple bacteria consists of two types of light-harvesting antenna (Figure C.4): light-harvesting antenna 1 (LH-I), which also contains the photosynthetic reaction center (RC), and light-harvesting antenna 2 (LH-II). LH-II contains two rings of bacteriochlorophyll. One ring consists of eight monomers of bacteriochlorophyll molecules that have a peak in their absorption spectra at 800 nm (B800), while the other ring consists of eight dimers of bacteriochlorophyll that absorb light around 850 nm (B850). Both B800 and B850 harvest the sun's light. Upon the absorption of a photon by either structure, an exciton, or bound electron-hole pair, is created in one of the chlorophyll molecules. Within the two rings of LH-II, the chlorophyll is in close proximity; the exciton can rapidly transfer from one molecule to the next by resonance energy transfer without loss of energy. Because

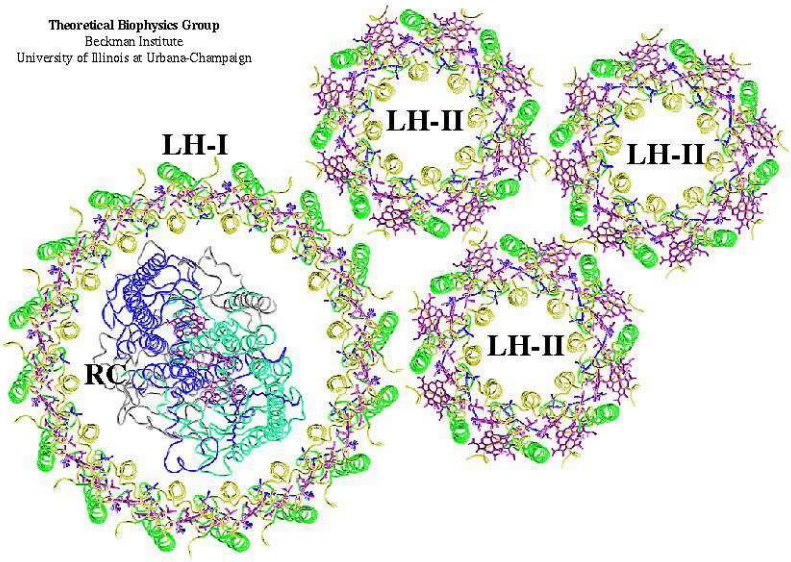

Figure C.4: Crystal structure of the light-harvesting antenna complex of purple bacteria. The ring structures of LH-I and LH-II form planar arrays, which serve to harvest light and funnel energy to the reaction center (RC). This image was made by the Theoretical Biophysics group, an NIH Resource for macromolecular modeling and bioinformatics, at the Beckman Institute, University of Illinois at Urbana-Champaign.

B850 has a lower-energy excited state than B800, eventually any excitons generated in the B800 ring shift to the B850 ring. LH-I has an exterior structure similar to that of LH-II. It consists of a ring of 16 chlorophyll dimers absorbing at 875 nm (B875), which surround the photosynthetic reaction center. B875 chlorophyll can either absorb photons and generate excitons or accept excitons from B850 or B800 on LH-II. From B875, excitons are funneled to two chlorophyll molecules known as the special pair, which are part of the reaction center at the center of LH-I.

Together, LH-I and LH-II harvest light and transfer the energy to the photosynthetic reaction center. These antenna structures pack together in large arrays, with a great excess of LH-II. Figure C.4 depicts a portion of this light-harvesting complex and illustrates the placement LH-II around LH-I, with the reaction center at the center of LH-I. The rings of both antenna structures are clearly visible. Once an exciton has been formed, it can transfer from chlorophyll to chlorophyll within a

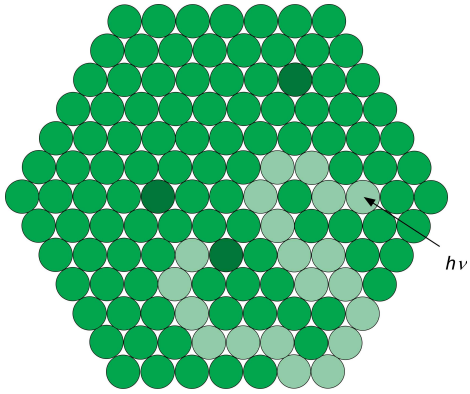

Figure C.5: Exciton transfer in a light-harvesting antenna complex. The light-harvesting complex consists primarily of LH-II units (green), with a few randomly placed LH-I units (dark green). When a photon is absorbed by LH-II, the resultant exciton hops from LH-II to LH-II in along a random path (light green) until it transfers to LH-I and the reaction center.

ring or to chlorophylls on adjacent rings. It can also transfer to chlorophylls whose excited-state energies are lower in energy (i.e., B850 to B875 or to the special pair in the reaction center). Because excitons cannot move spontaneously from a lower energy state to a higher energy state, this system funnels electronic excitation energy from LH-II to LH-I to the reaction center. The direction of each exciton transfer is random (Figure C.5); in order to efficiently harvest light, then, these transfers must occur very quickly, as excitons have a finite lifetime and spontaneously decay. Exciton transfer from B800 to B850 in LH-II occurs in 650 fs,[160] from B850 to B875 on LH-I in 3 ps,[161] and from the LH-I ring to the special pair in 37 ps.[162] These rapid transfer times eliminate losses from exciton decay for $> 99\%$ of photons absorbed.[154]

The reaction center acts to separate the electron and hole once they reach the special pair. Like exciton transfer among (and within) the light-harvesting units, the molecular components that comprise the essential elements of the reaction center are also energetically arranged such that initial charge separation is fast and efficient. These components are depicted in Figure C.6. As previously discussed, P, the special pair of chlorophyll, acts as the energy acceptor. The remaining components are the

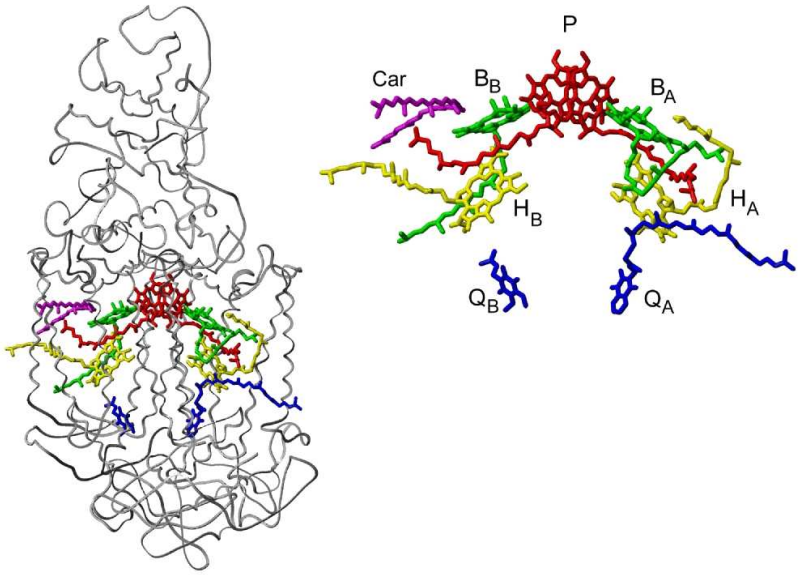

Figure C.6: Crystal structure (left) and cofactors (right) of the bacterial reaction center. Special pair (P), accessory bacteriochlorophylls (B), Bacteriopheophytin (H), and quinone (Q). A and B subscripts denote the active and non-active branches. Car represents the carotenoid. Figure adapted with permission from van Grondelle web site: www.nat.vu.nl/vakgroepen/bio/english/index.html.

accessory bacteriochlorophyll (B), pheophytin (H), and quinone (Q), arranged in two branches, one active (A) and one inactive (B). Not shown is an iron atom located between the two quinone molecules. The carotenoid depicted along the B side chain serves as a quencher of triplet chlorophyll that serves to protect against photooxidative damage.

Like the exciton transfer reactions leading to the reaction center, the chemical reactions leading to charge separation within the reaction center are very fast. In the first step, an electron is transferred from the special pair to the pheophytin in 2.7 ps.[163] The electron proceeds from the pheophytin to the quinone in 200 ps.[164] The electron and hole are now separated at opposite ends of the reaction center and on opposite sides of the membrane in which the light-harvesting array is incorporated. Heme groups located above the special pair (not shown) serve to funnel off the hole from the special pair, resulting in charge separation across the membrane and a return of the special pair to the ground state. Ultimately two electrons reduce Q_B, which can then accept two protons and exchange these to the membrane pool of quinones, forming a proton gradient, which is one of the bacteria's means of energy storage.

The light harvesting antenna structures and the reaction center serve as an illustration of a natural self-assembled system of molecular components organized in a nanostructure. This system is quite different from bulk semiconductor photovoltaics. First, light harvesting and charge transport occur in separate media, eliminating charge recombination. Second, because photosynthesis occurs in noncrystalline media, charges are transported through the system in a different manner. Charge carriers in bulk semiconductors are virtually always found as free electrons and holes and are transported through energy bands. Charge carriers in photosynthesis are found in the form of excitons or as parts of chemical species. The charge carriers do not travel through energy bands; they hop from molecule to molecule through a series of resonant energy transfers or chemical reactions. Third, the driving force for the

movement of charges through the photosynthetic system is not electric fields, as in bulk semiconductor devices; instead, the primary driving force for charge separation and transport is enthalpy. Charges move from one chemical species to the next because the reaction is exothermic, and the overall system moves to a lower energy state. Fourth, charge transfer reactions occur rapidly. As a result, charge carriers move through the charge generation and separation process so quickly that there is little time for competing mechanisms that result in charge recombination, and there is near unity photon-to-electron quantum yield.

Both bulk semiconductor devices and photosynthesis have features that are advantageous in novel photovoltaic designs. Photosynthesis is certainly the most efficient photovoltaic process known; however, we cannot hope to emulate the intricate engineering necessary to manufacture a photovoltaic device that is as efficient. Moreover, photosynthesis only involves the absorption of specific wavelengths of light; most of the solar spectrum is wasted. Bulk semiconductors are easier to produce, are very durable, and can absorb more of the solar spectrum, but they have very limited efficiency. Nanomaterial-based photovoltaics would ideally incorporate design parameters found both in natural photosynthesis and in bulk semiconductors in such a way as to produce a highly efficient device that is still reasonable to build in terms of cost, effort, and engineering.

C.3 Charge carrier conduction in nanomaterials

Nanomaterials, defined for the purposes of this thesis as any material whose dimensions are less than 100 nm in all directions (i.e., nanocrystals, polymers, buckminsterfullerene derivatives, dendrimers, and molecules with distinct chemical formulae), behave quite differently than bulk semiconductors. In order to understand the differences between the behavior of bulk semiconductor- and nanomaterial-based devices, we first review the optoelectronic behavior of various nanomaterials as it

pertains to charge conduction.

C.3.1 Band structures and charge carriers in nanomaterials

In bulk semiconductors, charge carriers exist primarily in the form of free electrons and holes which are delocalized over portions of the semiconductor. Electrons and holes travel through energy bands that extend throughout the semiconductor. A limited number of excitons can also form, but at device operating temperatures there are enough phonons present in the semiconductor that any excitons that form are quickly disrupted, resulting in free electrons and holes. In contrast, charge carriers in nanomaterials exist in many different forms, depending on the nature and macrostructure of the nanomaterial.

Individual molecules do not have energy bands; instead, they have series of discrete orbitals, with a highest occupied molecular orbital (HOMO) and a lowest unoccupied molecular orbital (LUMO). They do not have well-defined Fermi levels, since there are no 'free' charges unless the molecule is optically excited or accepts or donates an electron from an external source. Thus Fermi level alignment and band bending (Section C.1.1) do not apply to single molecules. Moreover, when a molecule accepts or donates an electron, the orbital structure of the molecule changes, which can affect the molecule's ability to conduct charge carriers. Many can only hold one type of charge carrier stably - either electrons or holes, but not both.

Semiconducting polymers and nanocrystals behave intermediately to bulk semiconductors and discrete molecules. Because each nanocrystal or strand of polymer has a number of orbitals with the same energy and shape, energy bands form, as in bulk semiconductors. However, a few discrete states also exist. These states originate primarily from orbitals at the ends of polymer strands or at the surface of nanocrystals. Such orbitals are not surrounded by identical orbitals; thus they do not form bands in a bulk fashion.

It is notable that any material forms semiconducting energy bands when individual molecules or unit cells are packed together in crystalline form. When nanomaterials form three-dimensional crystals, they display similar electronic behavior to bulk inorganic semiconductors. Theoretically both electrons and holes can travel through the crystalline matrix; however, when organic or molecular thin films are used, charge carrier transport may be limited by the same molecular constraints as noted above.

The forms that charge carriers can assume in nanomaterials are also different than in bulk semiconductors. Virtually all nanomaterials generate excitons because of the physical confinement imposed by the dimensions of a nanomaterial or because of the nature of bonding within the nanomaterial (e.g., carbon-carbon bonds, which do not easily ionize but which may more easily sustain a bound electron-hole pair). Because of bonding constraints, semiconducting polymers usually cannot transport single charges. Instead charges travel in the form of bipolarons - charge pairs (hole-hole pairs, electron-electron pairs, or excitons) in which the charges are a fixed distance apart on the polymer backbone. Likewise, C_{60} transports electrons almost exclusively in pairs and does not transport holes at all. For some molecular species, charge carriers are not electrons, holes, or combinations thereof, but instead are hidden in the form of chemical reactions with a second species. One example of this was shown in Section C.2 with the transport of electrons occurring in the form of the reduction of quinoline by protons. Another example is the transport of holes in the Grätzel cell (Section C.4.4), by the reaction of I_2 and I^- to form I_3^-. Because the nature of charge carriers in nonamaterials is often different than in bulk semiconductors, the physical and optoelectronic behavior also differs.

C.3.2 Conductivity in nanomaterials

A key consideration in NBPs is the resistance of nanomaterial films. Crystalline inorganic semiconductors typically have resistivities of $\rho = 10^{-2} - 10^{5}$ W-cm. Since resistivity is related to charge carrier mobility by[157]

$$\begin{array}{l} \rho = \frac{1}{q\mu_n n} \text{ } (n\text{-type semiconductor}) \\ \rho = \frac{1}{q\mu_p p} \text{ } (p\text{-type semiconductor}) \end{array} \tag{C.8}$$

where μ_n (μ_p) is the electron (hole) mobility, these materials typically have electron and hole mobilities of $10^{2} - 10^{5}$ cm^2/V-s and $10^{0} - 10^{3}$ cm^2/V-s, respectively.[157] In contrast, amorphous semiconductors have greater resistivities and lower charge carrier mobilities, because the much greater occurrence of defect sites (e.g., dangling bonds) leads to more scattering and trapping events during charge transport.[165] Studies on the electrical properties of amorphous silicon, for example, have shown resistivities of $100 - 735$ W-cm, as compared with crystalline silicon resistivities of about 50 W-cm.[166,167]

Nanomaterial films vary in degree of crystallinity but tend to be at least partially amorphous. As with bulk inorganic semiconductors, these amorphous regions create scattering centers and trap sites, and charge carrier mobility is reduced, often by orders of magnitude. An excellent example of this is the semiconducting polymer poly(3-hexylthiophene) (P3HT), whose structure is shown in Figure C.7. In the solid-state, it forms microcrystalline regions composed of stacked sheets of parallel polymer chains with interlocking hexyl groups (Figure C.7a). The sheets stack by $\pi - \pi$ interchain interactions to form nanocrystalline domains on the order of 10 nm within a larger amorphous matrix.[168] Hole transport through P3HT thin films is limited by the amorphous regions, and charge carrier mobility in films with depths of more than a few micrometers is on the order of $10^{-9} - 10^{-4}$ cm^2/V-s.[169,170] This mobility is very low compared to the mobilities of crystalline inorganic semiconductors; it is more comparable to the mobilities of amorphous insulators. Amorphous SiO_2, for example, has an electron mobility of 10^{1} cm^2/V-s and a hole mobility of

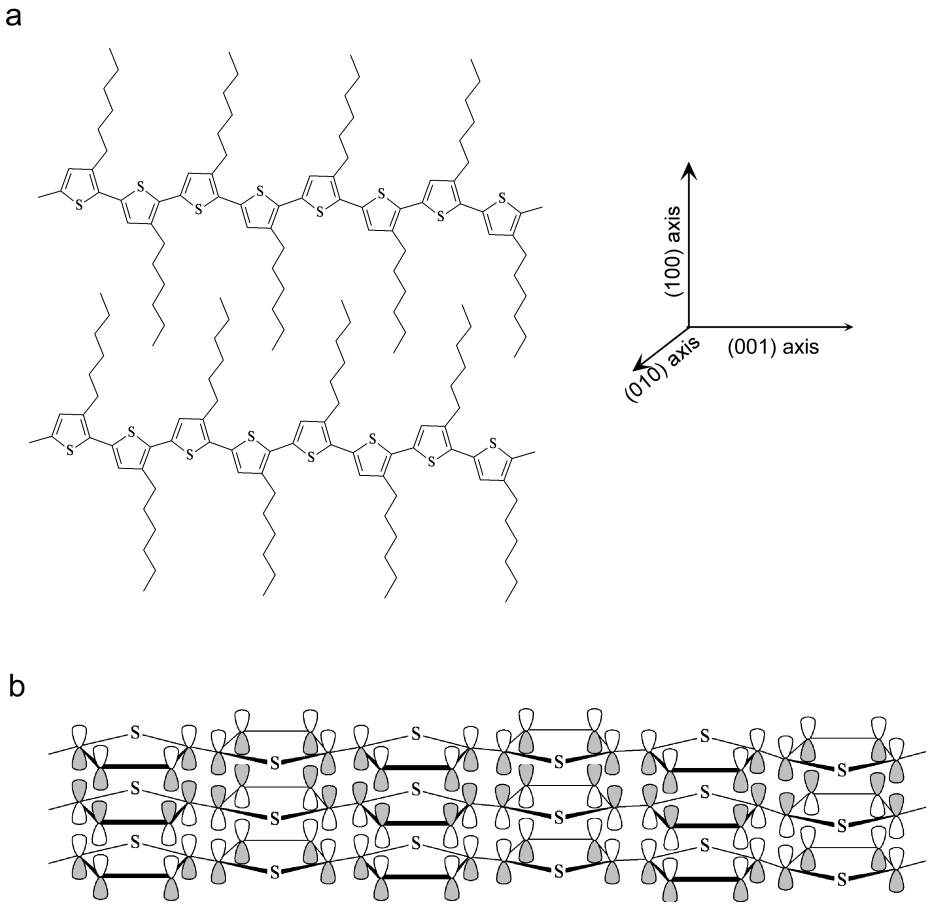

Figure C.7: Poly(3-hexylthiophene). (a) Structure of individual strands of P3HT. Orientational axes are provided for reference. In the solid-state, P3HT forms microcrystalline regions in which individual strands of polymer interlock to form lamellar sheets, which stack by interchain $\pi - \pi$ stacking. (b) $\pi - \pi$ stacking.

10^{-8} cm^2/V-s.[171]

While hole mobilities in thicker films of P3HT are low, mobilities in thinner films are much higher. When a thin film of P3HT is smaller than the crystalline domain size, there exist regions of crystallinity that extend the width of the film. As with inorganic semiconductors, charge carrier mobility in a crystalline region is much greater than in amorphous material. In the case of P3HT, there is a high degree of anisotropy in charge carrier mobility due to the lamellar structure of the crystalline regions, but in a novel experiment involving field-effect transistors with oriented crystalline P3HT as the channel material, Sirringhaus *et al.* determined hole mobility to be $10^{-5} - 10^{-2}$ cm^2/V-s along the (100) axis and $10^{-3} - 10^{-1}$ cm^2/V-s along the (010) axis, with the higher mobilities in each case corresponding to greater regioregularity.[168,172] Although the hole mobility along the (001) axis has yet to be determined, the π-conjugation of the polymer backbone provides a ready pathway for holes to travel. It is therefore presumed that hole mobility in this direction is much faster than along the other two axes. Thus hole mobility in P3HT is decreased by several orders of magnitude when holes must travel through amorphous regions.

The case of P3HT illustrates a general trend in nanomaterial-based solids. Except for some discrete molecules whose molecular formula is exact and whose structure is fairly rigid, it is not feasible to produce purely crystalline thin films; some amorphous regions are inevitable. These amorphous regions scatter charge carriers, reducing charge carrier mobility and increasing the resistivity of the material. It is therefore advantageous to minimize the width of any thin films with amorphous regions in NBPs.

There is an additional complication when considering films of 3-dimensional rigid structures such as nanocrystals or fullerenes - namely, the problem of empty space. When rigid 3-dimensional particles (spheres, ovoids, etc.) are packed together to form a solid, there is some degree of empty space in the solid. For example, in

a hexagonally close packed (*hcp*) arrangement (the densest arrangement possible) of spheres such as C_{60}, 74% of the total space is occupied by the spheres, leaving 26% of the space empty.[142] In a random packing there is even more empty space.[143] While theoretically it is possible to pack certain polyhedra (e.g., cubes) so that there is no free space in a solid, under practical laboratory conditions it is not possible to synthesize nanomaterials as exactly uniform polyhedra of a shape appropriate to perfect space-filling packing. Therefore films of nanocrystals, like films of C_{60}, necessarily enclose a significant portion of empty space. The empty spaces in these films cannot conduct charges; they act as scattering centers, and sometimes as trap sites and recombination centers when dangling bonds are present, reducing charge carrier mobility and increasing the resistivity of the film.

To illustrate the effect of empty space and grain boundaries on resistivity and charge carrier mobility, we consider the case of anatase TiO_2, which has found extensive use in photovoltaic devices, including as an electron conductor in the Grätzel cell (Section C.4.4). Anatase TiO_2 has been studied in three forms: single-crystal, polycrystalline, and sintered nanoparticles, formed by depositing nanocrystals of TiO_2 suspended in solution onto a substrate and sintering. Of these three types of film, the single-crystal form has the fewest defects or scattering centers. The polycrystalline form is predominantly crystalline, but has grain boundaries that act as a significant source of scattering. The film of sintered nanoparticles has both grain boundaries and empty space between adjacent particles. Thus the sintered nanoparticle film would be expected to have the lowest electron drift mobility. Experiment shows that this is indeed true. Electron drift mobility in anatase TiO_2 is 15 cm^2/V-s for the single-crystal form,[173] but decreases to < 4 cm^2/V-s in polycrystalline thin films[174] and to $10^{-7} - 10^{-4}$ cm^2/V-s for films of sintered nanoparticles.[175] Hole drift mobility likewise decreases from 10^{-3} cm^2/V-s for the single-crystal form[173] to 0 cm^2/V-s for the sintered nanoparticle film.[175] Though the electron drift mobility in the sintered

nanoparticle thin film is much lower than for the single-crystal form, it is noted that the free electron mobility (the mobility of free electrons in between traps) in the sintered nanoparticle film was determined to be 2.4 cm^2/V-s, which is on the order of that for the single-crystal form. The large difference between the free electron mobility and the electron drift mobility is attributed to trap states and scattering centers, a consequence of grain boundaries and unsatisfied bonds at nanoparticle surfaces.[175]

Most thin films made from nanomaterials are not composed of a single crystal; rather, they contain grain boundaries, amorphous regions, or empty space. Such areas cause charge carrier scattering, and can also act as traps or recombination centers. These effects work to lower charge carrier mobility and to increase the resistivity of the film, resulting in impaired device performance when compared to devices utilizing thin films of single-crystal inorganics. In general, nanomaterials are also limited to conducting excitons or only one type of charge carrier. Solid-state C_{60}, for example, can hold up to six excess electrons per molecule because of its conjugated π-bonds, so it is a good electron conductor,[176,177] but it is generally known not to conduct holes. Other materials, such as semiconducting polymers, have electron and hole mobilities that differ by several orders of magnitude, rendering one charge essentially immobile in comparison to the other. For NBPs to be economically viable, some other advantage must be gained, either by some physical property unique to nanomaterials, or by employing a device architecture that does not rely on thin films of a single material.

C.3.3 Nanomaterial-metal interfaces

The electronic behavior of nanomaterial-metal interfaces is still an emerging science. Because most nanomaterials are expected to have only weak interactions with metals at interfaces, researchers often estimate the interfacial electronic structure according to the Schottky-Mott limit, or the vacuum level alignment rule, in which the vacuum levels of the nanomaterial and metal are aligned; there is no dipole layer

or electric field at the interface.[2,178,179]

Research, however, suggests that there is often a measurable dipole layer at nanomaterial-metal interfaces.[180–212] In general, there are four causes of interfacial dipole layers: band bending to achieve Fermi level alignment, pinning of the Fermi level by midgap states, chemical interaction between the two species at the interface, and image effect polarization of the surface.[190,191] A measured dipole may be the result of one or a combination of these effects. Cowley and Sze[213] developed a general expression for inorganic semiconductor-metal interfaces detailing dipole layer formation from these sources; these equations may also be applied to interfaces involving nanomaterials, with certain limitations. The formulae presented below are the results of Cowley and Sze's study as applicable to nanomaterial-metal interfaces.

The first cause of interfacial dipole layer formation is Fermi level alignment. Fermi level alignment occurs at nanomaterial-metal interfaces when there is a source of free charge carriers in the nanomaterial; typically this occurs in doped films of nanomaterials. When there is a source of free charges, these films display the same electronic behavior as bulk semiconductors. Figure C.8 shows the key parameters involved in band bending at the interface. It is noted that because a metal has many more free charge carriers than a semiconductor, the space charge region at the interface is almost entirely contained in the nanomaterial; under the depletion approximation, all band bending, electric fields, the depletion layer, and all other interface phenomena are confined to the nanomaterial side of the interface.

Assuming the width of the depletion layer is less than the width of the nanomaterial film, then the potential drop across the depletion layer due to Fermi level alignment is[157]

$$\phi_i = \phi_m - \phi_s \tag{C.9}$$

An exact calculation of ϕ_i is more complex when the theoretical width of the depletion layer is greater than the width of the thin film, a common occurrence in nanomaterials,

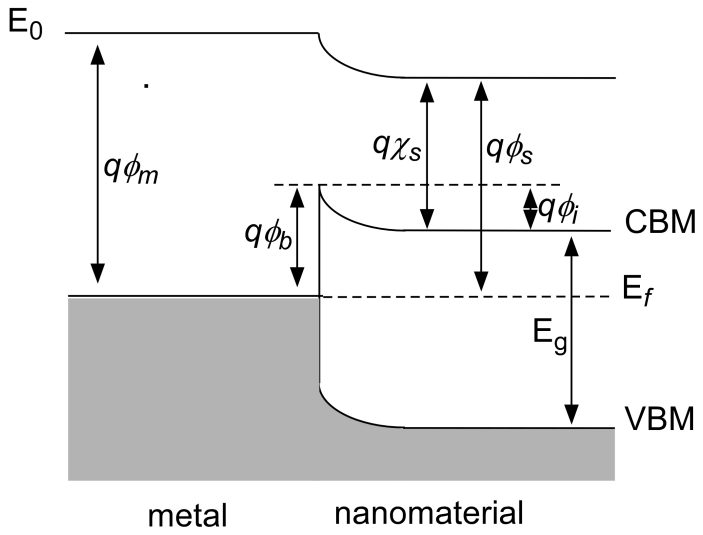

Figure C.8: Key parameters of nanomaterial-metal interfaces: metal work function (ϕ_m), nanomaterial work function (ϕ_s), electron injection barrier (ϕ_b), potential drop across the space charge region (ϕ_i), nanomaterial electron affinity (χ_s), and nanomaterial band gap (E_g).

which often have very few free charge carriers ($N_d \approx 0$). The result is a bending of the energy bands of the nanomaterial at the interface, making vacuum level alignment over the width of the nanomaterial film an invalid assumption.

A modified version of Fermi level alignment occurs at any nanomaterial-metal interface in which the work function of the metal is higher that the CBM (LUMO) of the nanomaterial. When $\phi_m > \chi_s$, the CB (LUMO) of the nanomaterial acts as a source of free holes; electrons transfer from the higher-energy occupied states of the metal to the lower-energy unoccupied states of the nanomaterial until thermodynamic equilibrium is achieved.[196] The result is a space charge region at the interface, creating an interfacial dipole layer and destroying vacuum level alignment. Interestingly, in addition to direct formation of a dipole layer, the transfer of charge may introduce midgap states because of the reorganization of orbitals in charged molecules,[188,214] which can lead to pinning of the Fermi level, another cause of dipole layer formation.

Fermi level pinning is a second source of interfacial dipole layers. Related to

Fermi level alignment, pinning occurs as a result of midgap states present either at the interface or throughout the semiconductor. These states may be intrinsic, as in midgap states at nanocrystal surfaces, or may stem from defect states,[157] impurities,[207,215] metal-induced gap states from diffusion of metal atoms into the nanomaterial,[214,216] or chemical reactions between the metal and the nanomaterial.[196,206,214] The midgap states act as charge reservoirs. As the Fermi level of the nanomaterial attempts to align with the metal work function, charge population of the midgap states either increases or decreases, depending on the direction of the attempted shift. This creates a space charge region at the interface, or a dipole layer.

Fermi level pinning is a material property of the nanomaterial and is independent of the metal electrode, excepting metal-induced gap states. The degree to which the Fermi level is pinned is measured by the index of interface behavior or slope parameter, S_ϕ, defined as[157]

$$S_\phi \equiv \left| \frac{d\phi_b}{d\phi_m} \right| \tag{C.10}$$

The potential drop, Δ, due to a dipole layer across the interface is related to S_ϕ by[216]

$$\Delta = (1 - S_\phi)\left(\phi_m - \chi_s + \phi_b^0 - \Delta_\phi\right) \tag{C.11}$$

where Δ_ϕ is the image force barrier lowering (discussed below), and ϕ_b^0 is the barrier height when no interfacial dipole exists and when ϕ_m is equal to the charge neutrality level of the interface states (typically estimated as exactly halfway between the VBM and CBM of a semiconductor).[157] (We distinguish potential drop due to Fermi level pinning and image force barrier lowering (Δ) from potential drop due to Fermi level alignment (ϕ_i) because Fermi level alignment is widely considered to be a normal and expected interface behavior in electrical engineering, while Fermi level pinning and image force barrier lowering are a perturbation of Fermi level alignment.) From Equation C.11 we see that an S_ϕ of unity corresponds to no Fermi level pinning, while $S_\phi = 0$ indicates complete Fermi level pinning; when $S_\phi = 0$, ϕ_i is completely independent of the metal work function.

Figure C.9 displays measured interface Fermi level positions, which vary linearly with ϕ_b, as a function of ϕ_m for six different organic molecules.[217] The theoretical barrier heights assuming ideal Schottky-Mott behavior are shown for each molecule as dashed lines for purposes of comparison. From Figure C.9 it is immediately evident that none of the six molecules display the idealized Schottky-Mott behavior. For F_{16}CuPc, PTCBI, and PTCDA, the measured injection barrier heights are completely independent of ϕ_m ($S_\phi = 0$). Thus, the Fermi levels are completely pinned for these molecules. Conversely, Alq_3 has a slope parameter of $S_\phi = 0.8$, so the Fermi level is almost completely unpinned. Interestingly, even though the Alq_3 film has a relatively unpinned Fermi level, the measured injection barrier heights nonetheless do not correspond to Schottky-Mott behavior; this indicates a source of interfacial dipole other than Fermi level pinning. Investigations of injection barrier height as a function of metal work function for molecules and polymers have demonstrated slope parameters ranging from 0 - 1.[188–192,217]

Although no studies have been performed on Fermi level pinning in nanocrystals, slope parameters in semiconductor nanocrystals are likely related to S_ϕ in bulk inorganic semiconductors, which range from 0.1 to 1, with lower values of S_ϕ being associated with covalent semiconductors (for example, Si has a slope parameter of 0.1) and higher values with ionic semiconductors (Figure C.10).[218] In bulk semiconductors, the primary source of Fermi level pinning is midgap states at the interface. Since films of nanocrystals have greater surface area, and because that surface is curved, we can expect a greater concentration of midgap states compared to their bulk counterparts. Thus it is reasonable to expect that the slope parameters of nanocrystals are less than their bulk counterparts.

A third cause of dipole layer formation at nanomaterial-metal interfaces is chemical reaction between metal and nanomaterial at the interface. While the effects of charge transfer across the interface are fairly predictable and follow traditional

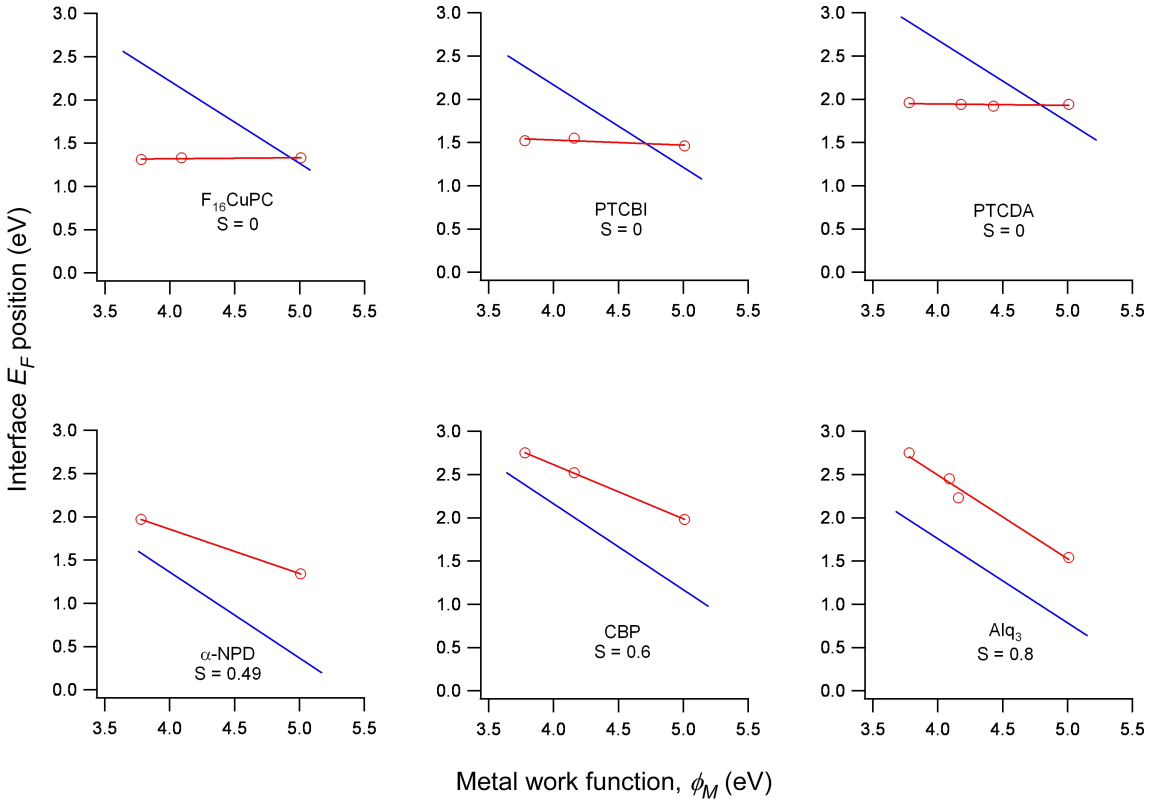

Figure C.9: Measurement of the slope parameter at six organic-metal interfaces. The theoretical Schottky-Mott behavior in each case is depicted as the dashed line. The degree to which the Fermi level is pinned is indicated by the slope, S, of the line connecting the measured interface Fermi levels. For F_{16}CuPc, PTCBI, and PTCDA $S_\phi = 0$; the Fermi level is completely pinned. Alq_3, α-NPD, and CBP all show lesser degrees of Fermi level pinning. Adapted from C. Shen, A. Kahn, and I. G. Hill, in *Conjugated Polymer and Molecular Interfaces*; A. Kahn, J.-J. Pireaux, W. R. Salaneck, and K. Seki, Eds.; Marcel-Dekker, New York, 351 - 400 (2001).[217]

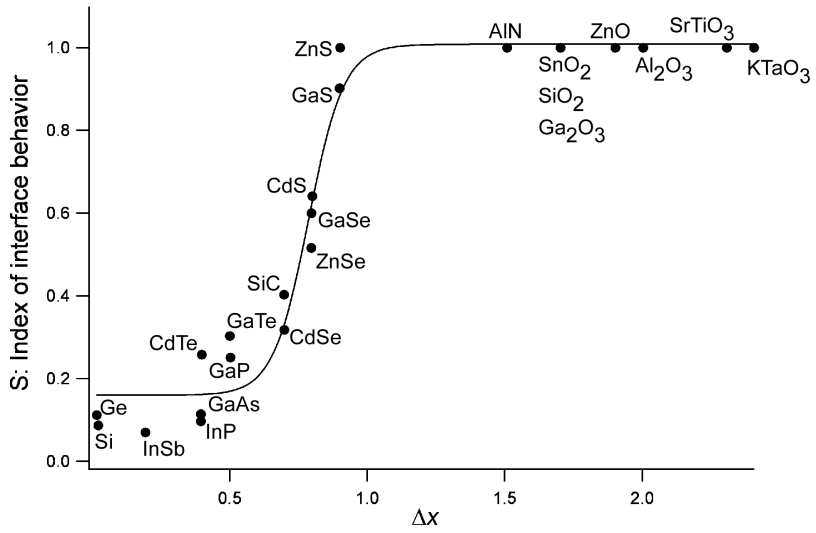

Figure C.10: Slope parameters for bulk semiconductors as a function of the difference in electronegativity of the component atoms. Adapted from Kurtin *et al.*[218]

semiconductor device physics, the effects of bond formation at the interface are difficult to predict, as metals and nanomaterials can react to form new molecules whose physical properties can be quite different from the original.

Some molecules adsorb to metal surfaces by reacting with surface metal atoms to create a chemical bond.[210,219–221] Examples of this behavior include thiols, which chemisorb on Au surfaces and are commonly used to form self-assembled monolayers (SAMs), and π-conjugated molecules such as CO and benzene. The nanomaterial may also react with metal atoms that have diffused into the semiconductor layer. These reactions are somewhat analogous to metal silicide formation in Si-based semiconductor devices. Redistribution of charge at the interface is the natural consequence of the formation of these metal-molecular bonds, and can change the work function at the interface.[190,195,203] Furthermore, the interfacial bond formation may also alter the molecular energy levels in such a way as to create midgap states,[214] possibly leading to pinning of the Fermi level.[196,203,210,219,222,223]

The fourth cause of dipole layer formation at nanomaterial-metal interfaces is

image force barrier lowering. The image effect in nanomaterials was first proposed by Ishii *et al.*[190] to explain organic-metal interfaces whose dipole layers could not be explained fully by Fermi level pinning or by chemical reactions at the interface. Nanomaterials that do not chemisorb to the metal surface instead physisorb through van der Waals interactions with the metal surface. The van der Waals interaction produces a slight electrical double layer - a small dipole layer at the interface. The magnitude of the image effect dipole layer depends on the polarizabilities of the metal and semiconductor and on the dielectric constant at the semiconductor surface, ϵ_{surf} (which may be different than the static dielectric constant).[157] The polarizabilities influence the strength of the van der Waals interaction and hence the electric field, ε, at the interface, and the image force barrier lowering is given by[157]

$$\Delta_\phi = \sqrt{\frac{q\varepsilon}{4\pi\epsilon_{surf}}} \tag{C.12}$$

As an example, Ishii *et al.* have theorized that the image effect is responsible for the difference in Δ between interfaces of N, N'-diphenyl-N, N'-(3-methylphenyl)-1, 1'-biphenyl-4, 4'diamine (TPD)/Au and TPD/ITO; Au is more polarizable than ITO, thus image force barrier lowering is greater in the TPD/Au system than the TPD/ITO system.[190] The image effect is not specific to nanomaterials but is seen to greater or lesser extent at all semiconductor-metal interfaces.[157]

Of nanomaterial-metal interfacial dipole layers, the following trends are noted. First, while chemical reactions or Fermi level pinning may or may not contribute to an interfacial dipole layer, some degree of image force barrier lowering is always present. Second, the likelihood of forming a strong dipole layer, and the nature of dipole layer formation, depend heavily on the type of nanomaterial at the interface. Organic molecules, polymers and fullerenes have no dangling surface bonds but are susceptible to chemical reactions with metal atoms at an interface, leading to charge redistribution or to the creation of organometallic complexes with midgap states, resulting in Fermi level pinning. The reactivity of these materials with metals is variable, however. Some

materials are very reactive, such as Alq_3,[195,203,206,214,219,224–230] while others, notably polymers and C_{60}, are relatively inert. C_{60}, however, readily accepts electrons, resulting in the creation of midgap states.[188] Nanocrystals have dangling surface bonds and an internal lattice structure that can support extra charges. These features make Fermi level pinning a strong possibility at metal-nanocrystal interfaces; otherwise they are expected to behave much like bulk semiconductors with respect to interface characteristics.

C.3.4 Nanomaterial-nanomaterial interfaces

The same effects that contribute to interfacial dipole layers at metal-nanomaterial interfaces also contribute to interfacial dipole layers at nanomaterial-nanomaterial (and nanomaterial-bulk semiconductor) interfaces. As discussed in Section C.3.3, dipole layers can be formed through chemical reactions involving charge transfer between the two materials, through Fermi level pinning by midgap states, and through van der Waals interactions at the interface. However, at these interfaces there is no metal to act as a ready source of mobile charge. We can reasonably expect, then, that most interfacial dipole layers will not be as strong as those seen in metal-nanomaterial interfaces, where there is frequently an interfacial voltage drop exceeding 1 eV.[184,190–192] Indeed, in the organic-organic interfaces studied thus far, interfacial dipole layers have been slight or nonexistent, not exceeding a potential drop of 0.5 eV across the interface.[184,190,192] Likewise, we might reasonably expect undoped polymer-polymer or polymer-organic interfaces to have only small interfacial dipole layers. Polymers, like small organic molecules, are closed-shell systems and are thus unlikely to participate in charge transfer across the interface, except in cases where the electron affinity of one material is lower in energy than the ionization potential of the other material.

Despite the lack of a large reservoir of mobile charge, we can expect some

degree of dipole layer formation due to Fermi level pinning at interfaces when midgap states are present, particularly when midgap states are present in both materials at the interface.[231] Therefore, nanomaterials such as nanocrystals, fullerenes, and doped organic and polymer films are also likely to show limited dipole layers at interfaces. We can also expect some dipole layer formation in cases where a chemical reaction occurs at the interface.

C.4 Nanomaterial-based photovoltaics

Nanomaterial-based photovoltaics (NBPs) are photovoltaics whose charge generating and transporting materials are discrete molecules, semiconducting polymers, or nanocrystals rather than bulk semiconductors. The physical properties of these nanomaterials are as varied as the materials themselves, allowing a tailoring of photovoltaic and physical properties impossible to achieve with bulk semiconductors. Moreover, because these materials are so small, NBPs can have architectures that are inaccessible to bulk semiconductor devices. There are three major classes of NBPs: Schottky photodiodes, thin film heterojunction solar cells, and bulk heterojunction solar cells. We discuss the photophysics of all three classes, with specific examples of synthesized devices. In particular, we concentrate on bulk heterojunction solar cells, as this device structure is unique to NBPs.

C.4.1 Schottky photodiodes

Schottky photodiodes are the simplest of all photovoltaic devices. The basic structure is a thin film of a photoactive insulator or semiconductor sandwiched between two conductors, typically with different work functions. There are numerous examples of Schottky photodiodes using nanomaterials as the photoactive layer, including photodiodes based on organic molecules,[178,232–250] polymers,[180,244,251–264] fullerenes,[265,266] and nanocrystals.[267,268] In most respects, the properties of these

photodiodes resemble that of similar devices produced using inorganic crystalline or amorphous thin films; however, the different structural and photophysical properties of molecular materials create some unique behaviors not found in traditional photodiodes.

The physics of nanomaterial-metal interfaces were discussed in Section C.3.3. In a Schottky photodiode there are two such interfaces. If the concentration of free charge carriers in the nanomaterial is sufficiently high for a film of given thickness, the depletion layers of the two interfaces are separate. However, usually nanomaterial films have very few free charge carriers. Under these circumstances, the depletion layer for each interface extends throughout the nanomaterial film. At thermodynamic equilibrium, the Fermi levels of the two metals align, creating a constant electric field and a potential drop of $\phi_i = \phi_{m1} - \phi_{m2}$ across the nanomaterial.[157,255,269] This promotes current flow in a single direction through the device.

As discussed in Section C.3.1, nanomaterials are different than bulk semiconductors in the way they conduct charges. Usually charges are conducted through nanomaterial films in the form of excitons until they reach an interface.[248,270] Because charges initially travel as excitons, the photoresponse of nanomaterial-based Schottky photodiodes is markedly different from bulk semiconductor devices. Of the models that have been developed to describe the behavior of organic Schottky photodiodes,[233,236,248,271,272] the exciton diffusion model of Ghosh and Feng[248] provides the most useful qualitative explanation of the photoresponse.

The basic assumption of the exciton diffusion model is that excitons must reach an interface to dissociate into free charges. Only free charges contribute to photocurrent, so excitons that do not reach an interface before they collapse contribute nothing. The model further assumes that only one type of charge carrier can travel through the organic layer. As a result, although excitons may dissociate at both electrodes, only dissociation at one electrode contributes to photocurrent.

Using these two assumptions, the photocurrent generated by an organic Schottky photodiode is simply the diffusion current of the neutrally charged exciton at the active electrode. Assuming that the thickness of the thin film, l, is significantly larger than the average diffusion length of an exciton, L (so that $e^{-l}/L \ll 1$), then if light is shone through the active electrode, this current is[248]

$$J_{sym} = \frac{\alpha \phi_{ex} N}{\beta + \alpha} \tag{C.13}$$

while if light is shone through the inactive electrode, the current is[248]

$$J_{anti} = \frac{\alpha \phi_{ex} N}{\beta - \alpha} e^{-\alpha l} \tag{C.14}$$

where α is the extinction coefficient of the incident light, $\beta \equiv 1/L$ is the inverse of the diffusion length, ϕ_{ex} is the quantum efficiency of exciton generation, and N is the number of incident photons.

The reason for the difference between Equations C.13 and C.14 is that if light is shone through the inactive electrode, the light must pass through the entire light-harvesting layer before reaching the photoactive region of the device. As the entire light-harvesting region absorbs light at the same wavelengths, Beer's law dictates that the intensity of (absorbable) light reaching the photoactive region is decreased to $e^{-\alpha l}$, as seen in Equation C.14. In contrast, if light is shone through the active electrode, it is at full intensity upon reaching the photoactive layer (Equation C.13). These concepts are depicted in Figure C.11.

One interesting consequence of Equations C.13 and C.14 is the anisotropy inherent in the spectral-photocurrent response of organic Schottky photodiodes with respect to the direction of incoming light.[248,257] If light is shone through the active electrode, the diode displays a *symbatic* response; the photocurrent is greatest where the organic layer has the highest absorption coefficients. Conversely, if light is shone through the inactive electrode, the device displays an *antibatic* response; the photocurrent is greatest where the organic layer has lower absorption coefficients.

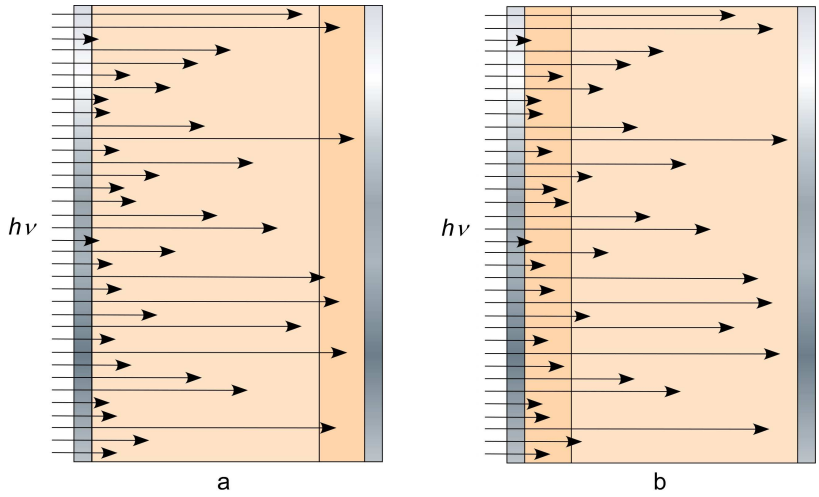

Figure C.11: Qualitative illustration of the exciton diffusion model by viewing an organic Schottky photodiode in cross-section. Gray regions represent electrodes, dark orange represents the portion of the light harvesting region that is photoactive, and light orange is the inactive portion of the light harvesting region. Excitons that do not reach an interface before they collapse do not contribute to the external power conversion efficiency, therefore there is a limited photoactive region near the active electrode, dictating a preferred orientation in the device. a) Light is shown through the inactive electrode, and most is absorbed before reaching the photoactive region. b) Light is shown through the active electrode. Because the light does not pass through the light harvesting layer first, most light reaches the photoactive region; thus more light is absorbed, resulting in more generated current.

A second consequence of Equations C.13 and C.14 is that in both cases there exists an optimum thickness for the organic layer. Only those excitons generated within a diffusion length of the active electrode contribute to the photocurrent; meanwhile, the resistance of the thin film increases with thicker films. Therefore, to maximize device efficiency, the thin film should be no thicker than the diffusion length of excitons in the film.

Nanomaterial-based Schottky photodiodes have low power conversion efficiencies (PCEs) under standard AM 1.5, 1 sun lighting conditions - typically $10^{-5} - 10^{-1}\%$.[178,180,233,234,236,237,239,240,243,245–247,250,251,258,264,272–278] These efficiencies are much less than those of commercially available photovoltaics. To increase the PCE, we must increase the width of the photoactive region of the device. According to the exciton diffusion model, in the case of NBPs, the width of this region is strictly dependent on the exciton diffusion length of the light harvesting material. Thus, the only way in which the active region of the device can be expanded is to introduce a second material.

C.4.2 Sandwich heterojunction photovoltaics

The natural extension of the Schottky photodiode is the sandwich heterojunction photovoltaic (SHP). In this structure there are two or more light-harvesting semiconductor layers sandwiched between two electrodes, analogous to the *pn* heterojunction bulk semiconductor photovoltaics of Section C.1.2. By using multiple light-harvesting layers, the photoactive region of the SHP is wider than that of Schottky photodiodes, resulting in a better photon-to-electron quantum yield and thus an improved PCE. In addition, the multilayer design offers advantages in terms of charge separation, spectral absorption and charge transport, which also contribute to an improved PCE.

The photophysics of nanomaterial-based SHPs under illumination are similar

to those of nanomaterial-based Schottky photodiodes. However, in the case of SHPs, the active region is always at the *pn* junction instead of at an electrode;[279–282] with an active region that spans the exciton dissociation lengths in both nanomaterials, the active region of this type of device is wider than for a Schottky photodiode, thereby increasing the PCE of the device. Additionally, with judicious choice of light harvesting materials, the absorption spectrum of the device can span more of the solar spectrum than a single layer device, also improving the PCE.

Because of the increased width of the photoactive region and increase in the range of wavelengths absorbed, nanomaterial-based SHPs have improved power conversion efficiencies when compared to Schottky devices.[277,283,284] However, the photoactive regions are still very narrow. Because the exciton depletion regions are still only a few nanometers wide and cannot be extended as in bulk semiconductor devices, bilayer SHPs still have the same fundamental problem as Schottky diodes: the widths of the photoactive regions cannot be extended to provide absorption of enough light to generate significant current. The PCEs for these devices are still less than $1-2\%$.[197,283,285–289]

C.4.3 Bulk heterojunction photovoltaics

The only way to increase the width of the photoactive region in a photovoltaic constructed of nanomaterials without changing the materials themselves is to increase the amount of light harvesting material that is within an exciton diffusion length of an interface. A bulk heterojunction photovoltaic (BHP) is a photovoltaic in which the photoactive region of the device is an interpenetrating network of two or more nanomaterials, such that an exciton generated at any point within the active region is near a heterojunction. This solves the problem of the limited width of depletion layers encountered by nanomaterial-based Schottky photodiodes and SHPs. BHPs are, by definition, a design unique to nanomaterials. The photoactive layer is usu-

ally produced by mixing at least two nanomaterials (one electron donating and one electron accepting) in solution, then spin-coating or drop-casting onto a conducting substrate. The result is a film whose contents are a random mixture of the materials.

Of all the photovoltaic designs, BHPs offer the most promise for the achievement of high efficiency photovoltaics. Since any part of the light-harvesting layer is at or very near a heterojunction, the entire light-harvesting region contributes to photocurrent. This is a critical improvement over the Schottky and sandwich heterojunction structures, whose photoactive regions are typically only a few nanometers wide. Because any exciton generated within the BHP's light harvesting layer can reach an interface and dissociate into an electron and a hole, we can expect a higher photon-to-electron internal quantum efficiency in BHPs than in other photovoltaic designs.

As with any photovoltaic design, there are a few key parameters that must be optimized in order to obtain maximum power conversion efficiency. Of these, the morphology of the photoactive layer and the rates of charge separation and recombination play particularly important roles in BHP device performance.

Film morphology dictates how easily excitons reach an interface to achieve charge separation and whether or not the separated electrons and holes can reach the electrodes. It is intuitively obvious that a completely random distribution of donor and acceptor materials maximizes the area of the heterojunction and best ensures that heterojunctions can be found throughout the photoactive layer, so this is the morphology most desirable in terms of charge separation. Once separated, charges can only pass through the photoactive layer to the electrodes if there exist unbroken pathways of both donor and acceptor materials from every part of the interface to the appropriate electrodes. Percolation theory dictates that in a completely randomized film, such pathways exist as long as the film is composed of at least 15% by volume of each material.[290] Thus, without considering other factors such as charge

recombination across the interface, the ideal morphology for a BHP is one in which the materials in the photoactive layer are uniformly distributed, with electron- and hole-conducting materials each comprising at least 15% of the volume of the film.

The key feature that makes BHPs such potentially efficient devices is the extremely large surface area of the donor/acceptor interface. For example, in the original report of the Grätzel cell, a *pin*-BHP, O'Regan and Grätzel observed that the surface area of the heterojunction of a device with a 10 μm thick photoactive layer was 780 times greater than for a sandwich heterojunction photovoltaic with the same dimensions.[291] However, the morphology poses a serious problem with respect to charge recombination at the interface, since any charge is essentially in contact with the interface throughout its path to the electrode. This problem is compounded by the fact that the charge mobility is many orders of magnitude smaller in a disordered medium of nanomaterials that for a crystalline semiconductor (Section C.3.2), meaning that separated charges must remain in the photoactive layer, and hence at the interface, much longer in BHPs than in other structures. It is therefore imperative to maximize the rate of charge separation while minimizing the reverse reaction.

As an example of how charge recombination can inhibit the device efficiency of BHPs, we consider Salafsky's study on the charge transport and recombination dynamics of PPV/TiO_2 nanocrystal composite BHPs.[292] In this system, PPV absorbs light, generating excitons which dissociate upon contact with TiO_2 nanocrystals dispersed through the polymer film. Holes then travel through the PPV network to the anode, while electrons are transported through the TiO_2 network to the cathode. Salafsky demonstrated that electron transport through the TiO_2 is dominated by a long average hopping time from nanocrystal to nanocrystal of $\tau_{hop} \approx 100$ μs, while charge recombination across the PPV/TiO_2 is also complete in $\tau_{re} \approx 100$ μs.[292,293] Since these competing processes occur on the same time scale, only electrons within

one or two monolayers of the cathode actually contribute to photocurrent; the rest are lost to recombination with holes in the active layer. Thus, while a photovoltaic of 67% by weight TiO_2 achieves $> 95\%$ exciton dissociation because of the composite geometry, the external power conversion efficiency (PCE) is quite low, on the order of 0.01%.

In contrast, the original Grätzel cell, which relies on a similar TiO_2 nanocrystalline network to transport electrons, shows markedly different behavior. In this case, the hole transport material is an I^-/I_3^- electrolyte solution rather than a hole conducting polymer. As in the PPV/TiO_2 photovoltaic, the average hopping time from nanocrystal to nanocrystal is $\tau_{hop} \approx 100$ μs; however, charge recombination in this system is much slower, on the order of $\tau_{re} = 0.1$ - 1 s.[293] Because $\tau_{hop} \ll \tau_{re}$, charge collection is extremely efficient, with an incident photon to electrical current efficiency of $> 80\%$,[291] comparable to the 99% efficiency of photosynthesis,[154] and an external PCE of 10.4%.[294] From these two TiO_2-based systems, it is clear that charge recombination across the heterojunction can play a major role in loss of efficiency in BHPs.

Interfacial charge recombination also occurs at photoactive layer-metal interfaces, and could potentially result in an even greater loss of device efficiency than recombination at heterojunction interfaces. Since the photoactive layer is a mixture of electron- and hole-conducting materials, both materials are in contact with each electrode. Metals, of course, accept both electrons and holes from other materials. Thus there is a degree of recombination both at the interface and within the metal as both electrons and holes are injected into each electrode. To some extent this effect is naturally mitigated by using electrodes with different work functions (or by applying a bias); when connected in circuit, the electric field resulting from the difference in work functions of the two electrodes promotes directional charge transport. In this way the number of charges flowing towards the wrong electrode, and therefore recom-

bination, is lessened. However, because of the low charge carrier mobilities of most nanomaterials, the drift velocity of charges may be small compared to the velocity due to thermal diffusion (for example, see Hamer[295]). If carrier transport is predominantly driven by thermal diffusion, then recombination at the metal interface is still very possible.

A further method of reducing charge recombination at the metal interface is to introduce an ultrathin layer at one or both interfaces that selectively conducts one type of charge.[3,296,297] By including this layer, only one type of charge is injected into each electrode, and charge recombination at the metal interface is virtually eliminated. One common technique is to use the *p*- and *n*-type materials themselves: a thin layer of *p*-type material separating the photoactive layer and the anode, and a thin layer of *n*-type material separating the photoactive layer and the cathode. Provided these spacing layers are sufficiently thin, they do not inhibit light penetration into the photoactive region.

Because the photoactive regions of BHPs can be made much wider than in SHPs and Schottky photodiodes, power conversion efficiencies for these devices tend to be much higher than for the other photovoltaic morphologies with corresponding materials despite greater losses due to recombination across interfaces.[298–300] To date greatest success has been achieved with polymer/fullerene BHPs,[283,296] which show efficiencies as high as 2.5%.[296] The particular success of these devices has been attributed both to C_{60}'s ability to carry up to six electrons at a time, and to low recombination rates between electrons on C_{60} and holes in certain polymers.

C.4.4 pin BHPs and the Grätzel cell

As with sandwich heterojunction photovoltaics, BHPs can function as *pin* heterojunction structures. In this device, a neutral (*i*) material, typically an organic dye, harvests light to form electrons and holes, which travel through *n*- and *p*-type

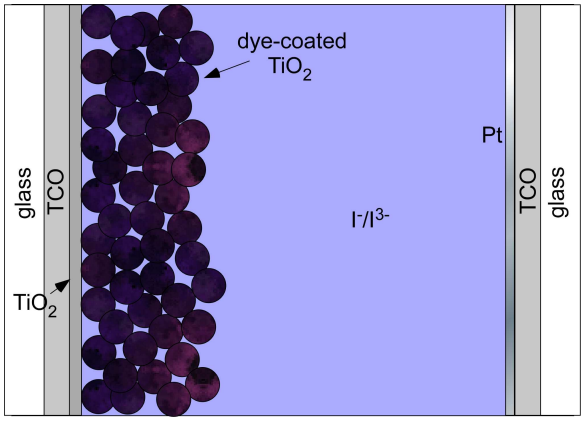

Figure C.12: Schematic of the Grätzel cell.

networks, respectively, to opposing electrodes. The photophysics of *pin* BHPs are similar to those of *pn* BHPs, save the separation of charge carrier generation from charge carrier transport, which may reduce charge recombination.

The bulk of research into *pin* BHPs has focused on the Grätzel cell. The structure of this photovoltaic involves a monolayer of an organic dye, typically Ru-based, adsorbed on the surface of a sintered anatase TiO_2 nanoparticle network (15 nm average nanoparticle diameter),[294] and mixed with a hole transporting material (Figure C.12). In this system the dye generates charges, which pass to the TiO_2 and hole conducting material for transport to the electrodes. The Grätzel cell is truly biomimetic in two important ways. First, the functions of light harvesting and charge transport are separated. Second, the initial charge separation step is ultrafast and essentially unidirectional, with the forward electron injection occurring on the femtosecond timescale.

Currently, the best efficiency of a Grätzel cell is 10.4%,[294] based on a design employing a liquid I^-/I^{3-} electrolyte solution as the hole conductor. This represents an extraordinary increase in efficiency over other nanomaterial-based photovoltaics, and puts the Grätzel cell in the range of commercial device efficiencies. Given that this photovoltaic is also cheap to manufacture (titania is an ingredient in many common

household products, including paints and toothpaste; dyes are similarly easy to find), the Grätzel cell shows great promise as an inexpensive alternative to silicon and other bulk semiconductor photovoltaics. Moreover, as the Grätzel cell does not require a crystalline structure, devices can be manufactured in a variety of shapes not available to traditional photovoltaics, such as curved surfaces, or flexible fibers.

The extraordinary success of the Grätzel cell is due to a combination of factors. First, as a consequence of its bulk heterojunction structure, the Grätzel cell absorbs more light than would be absorbed by a flat monolayer of dye. Moreover, all of the absorbed light contributes to power output, as opposed to the thick dye layers of Schottky diodes and SHPs, in which charge recombination is a major source of photocurrent loss because absorbing molecules are far from a heterojunction. Second, the cell is assembled by adsorbing the dye on the surface of the TiO_2. As a result, each dye molecule is in physical contact with both the TiO_2 and the I^-/I^{3-} electrolyte solution, so that charge carriers need not travel any distance before reaching the appropriate conducting material. Thus very few charges are lost to recombination within the dyes themselves.

Finally, although the electron and hole conductors are in contact throughout the cell, recombination of charges across the interface is very low. As mentioned in Section C.4.3, the rate of charge recombination between TiO_2 and I^{3-} in solution is extremely low, about 1 s^{-1}.[293] It is this slow recombination rate which allows most of the photogenerated charge carriers to reach the electrodes, despite the low mobility of electrons in nanocrystalline TiO_2.[175] This is unquestioningly one of the most critical advantages that the Grätzel cell has over other NBPs. Because of the low charge recombination rate, the internal photon-to-electron conversion efficiency of the most efficient Grätzel cell is >80%.[291] Thus this device is extremely efficient at converting light to energy in the wavelengths at which the photosensitizing dyes absorb.

Because the Grätzel cell has such a high power conversion efficiency in com-

parison with other molecular- and nanomaterial-based photovoltaics, a tremendous amount of research has gone into producing a solid-state version of the device. These are generally preferable from a commercial standpoint to devices incorporating a liquid phase, because they are usually more durable under extreme conditions. Undesirable properties of liquid electrolytes include solvent evaporation, thermal expansion, penetration by air and water, and freezing. However, building an efficient, solid-state Grätzel cell has proven surprisingly difficult. The crux of the problem is charge recombination within the photoactive layer.

As discussed in Section C.3.2, transport of electrons in nanocrystalline TiO_2, even when sintered, is a very slow process. As a result, in BHPs, electrons remain at or near the interface with the *p*-type material for an extended period of time, and recombination of charges across the interface is spatially allowed. In the liquid-based Grätzel cell, recombination is curtailed because it is thermodynamically unfavorable.[301] In this cell an I^-/I^{3-} electrolyte is the hole carrier. Holes are transferred from the photosensitizing dye to iodine via the reaction

$$3I^- + 2h^+_{VB}(\text{dye}) \rightarrow I^{3-} \tag{C.15}$$

The I^{3-} then diffuses through a solvent to an electrode. In solid-state devices, holes are transported electronically through a medium (i.e., along the *pi*-conjugated backbone of a hole conducting polymer), while the medium itself remains essentially motionless. In these devices it is not possible to use the I^-/I^{3-} system, because the iodine species would be physically incapable of significant diffusion. Unfortunately, recombination of electrons and holes in systems relying on electronic hole conduction is much more favorable than in systems using physical diffusion of hole carrying species. Therefore these devices show much lower power conversion efficiencies.

Recently W. Kubo *et al.*[302] devised a compromise, a quasi solid-state device that uses the same I^-/I^{3-} hole transport system as in the liquid-based Grätzel cells, except that in this case a low molecular weight gelator is substituted for the liquid

solvent. Like traditional liquids, the gel electrolyte allows easy diffusion of small molecules such as I^- and I^{3-}; however, gels have many of the desirable physical properties of solids. Using this gel electrolyte system, they have achieved a PCE of 5.91% under AM 1.5, 1 sun lighting conditions. This efficiency is far better than previous solid-state attempts, and in fact is only a factor of two smaller than the highest reported Grätzel cell efficiency. It is highly likely that further refinement of this system will result in a Grätzel cell with the efficiency of the liquid version, but with the greater durability of solid-state devices.

C.5 Ordered bulk heterojunction photovoltaics

As our knowledge of chemical self-assembly on the nanoscale and of nanomaterial properties increases, we can imagine more tailored photovoltaic designs, allowing precise control of cell properties. In some cases the unique properties of nanomaterials can be used to devise photovoltaics that simply cannot be duplicated by bulk semiconductors. Examples include photovoltaics employing liquid crystals or other moving parts, flexible solar cells, and even photovoltaic fibers for use in clothing. These unique designs will allow us to exploit sunlight in places and in ways not previously possible. In addition, several strategies can be employed to increase quantum efficiency of charge generation over a wide spectral range, minimize charge recombination, and increase intrinsic voltage across the device, all of which increase overall device efficiency.

One strategy that has been commonly theorized but rarely employed is the development of ordered bulk heterojunction photovoltaics (OBHPs). These BHPs are similar to those discussed in Section C.4; they meet the definition of 'bulk heterojunction' in that all of the light harvesting materials are located within the photoactive region, and in that the heterojunction has a large surface area relative to a flat surface. However, where typical BHPs use a randomly distributed mixture of p- and n-type

materials, OBHPs employ precisely placed nanomaterials, so that the exact structure of the device is known. In a sense, the Grätzel cell represents an intermediate stage between BHPs and OBHPs. In this photovoltaic, the sensitizing dye is attached via chemical self assembly to the supporting TiO_2 matrix. In this way the exact placement of the dye molecules adjacent to both the TiO_2 and the liquid electrolyte is ensured; this is a feature common to OBHPs. However, the overall morphology of the TiO_2 network is random, and because of the shape of the TiO_2 nanoparticles there are likely many patches of TiO_2 surface accessible by the electrolyte but not by the dye. These bare patches not only effectively reduce the surface area of the heterojunction but promote charge recombination of charges between TiO_2 and I^{3-}. This is a feature that we would hope to overcome by enforcing a higher degree of structure within the device.

Our knowledge of how to synthesize, control, and manipulate nanomaterials grows constantly. As our abilities increase, we find more and more ways to engineer molecular and nanomaterial based structures to a high degree of order. Techniques currently in use include chemical assembly through the formation of chemical bonds, control of solvent/solubility effects, phase segregation, even the use of large magnetic fields. Just the knowledge of how to use differing solubilities to induce phase segregation could be used to assemble a simple OBHP. Diblock copolymers have already been manipulated through solvent effects to form rods of one copolymer embedded in a matrix of the other copolymer; if these were light harvesting *p*- and *n*-type materials, the result would be a simple *pn* OBHP. However, *pn* devices do not incorporate the separation of charge generation and transport found in photosynthesis.

The Rosenthal group is currently working to assemble an OBHP utilizing PbS or PbSe nanocrystals as the light harvester and hexagonally close packed mesoporous TiO_2 (Figure C.13) as the nanocrystal substrate and electron transport material. However, originally, the design was based on CdSe nanocrystals, and the remainder

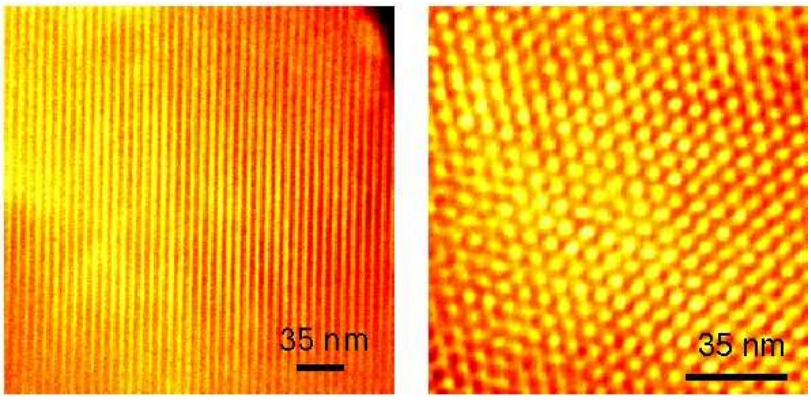

Figure C.13: Atomic number contrast scanning transmission electron micrographs (Z-STEM) of highly ordered mesoporous SiO_2. This sample of SiO_2 shows the hexagonally close packed organization desired for the hypothetical cell using TiO_2. Left is a view perpendicular to the axis of the pores. Right is a view looking down the axis of the pores.

of this appendix and the next are devoted to the CdSe-based design, which differs only in the type of nanocrystal used. This device, depicted in Figure C.14 is a *pin* structure that incorporates the best features of the Grätzel cell, but is solid-state, and has a highly structured geometry that allows the precise control of the photovoltaic properties. As in the Grätzel cell, the photoactive region of this device consists of TiO_2 covered by a single monolayer of the light harvesting material (i.e., nanocrystals), and the remaining space is filled by hole-conducting indium tin oxide (ITO). Thus each exciton generating unit is in contact with both the electron and hole conducting media. This promotes the efficient separation of charge carriers and minimizes charge recombination within the nanocrystals. Furthermore, as with the Grätzel cell the driving force behind charge separation in this device is primarily enthalpic in nature: electrons flow downhill in potential through the conduction bands of CdSe and TiO_2 to the aluminum electrode, while holes flow down in potential from CdSe to ITO (Figure C.5).

The first critical difference between this theoretical cell and the Grätzel cell is the nature of the TiO_2. Instead of the sintered nanoparticle film found in the Grätzel

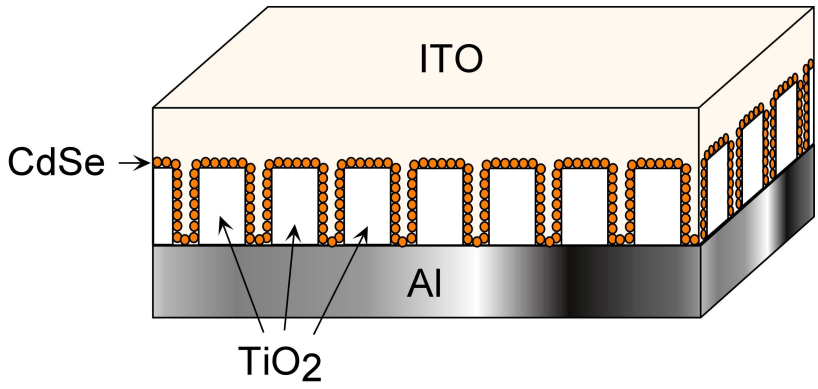

Figure C.14: The CdSe-based ordered bulk heterojunction photovoltaic. CdSe nanocrystals coat the pore walls of long-range ordered mesoporous TiO_2. The nanocrystals serve as the light harvester, and TiO_2 and ITO serve to transport electrons and harvest holes respectively. In such a device light harvesting and charge transport are separated, and electrons and holes are transported in spatially separated media. Device not drawn to scale.

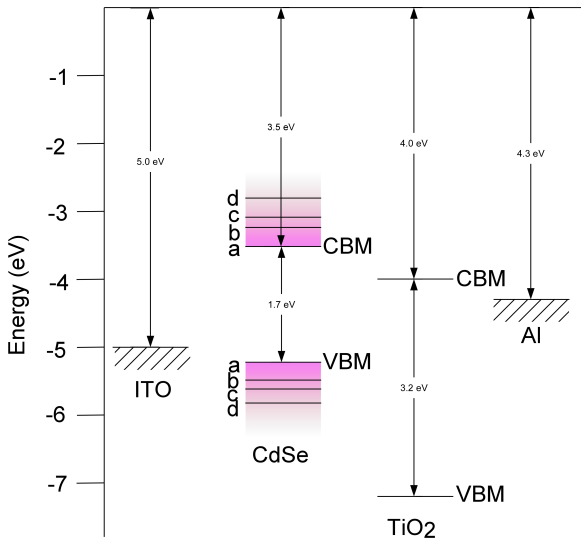

Figure C.15: Energy band diagram for the CdSe-OBHP. Energies are shown with respect to vacuum level because interface characteristics for the materials are not known. The valence band maximum (VBM) and conduction band minimum (CBM) for CdSe nanocrystals are size-dependent; shown here are calculated values for: a) bulk, b) 38.5 Å, c) 29.3 Å, and d) 20.6 Å CdSe.[39] TiO_2 VBM and CBM are from Finklea.[303]

cell, this device employs a highly ordered, hexagonally close packed mesoporous TiO_2. The necessity of using this type of TiO_2 is dictated by spatial constraints. CdSe nanocrystals are physically larger than the Ru-based dyes typically used in Grtzel cells, 2 - 15 nm in diameter, compared with < 1 nm for the Ru-based dyes.[294] Because they are so much larger, we must use a substrate large enough to accommodate the nanocrystals during self assembly of the device. Moreover, the hole conducting material must also be deposited within the pores, and the highly ordered mesoporous TiO_2 allows easier access to the pores than sintered nanoparticle films. Thus we can create a fully solid-state device without many of the problems encountered while incorporating a solid p-type material into the small, winding pores of the Grätzel cell.

Though the use of the highly ordered TiO_2 is necessitated by the materials being used as the light harvester and hole conductor, this film morphology offers some important advantages over sintered nanoparticles. The most important advantage is a probable increase in electron mobility. The TiO_2 is composed of anatase nanocrystals in an amorphous network and is intermediate to sintered nanoparticle films and polycrystalline films in geometry. As a result, electrons need not hop from nanoparticle to nanoparticle, but can travel through amorphous regions in between nanoparticles. Since the TiO_2 medium is more continuous than sintered nanoparticles, we predict a higher electron mobility. On the basis of geometry, the electron mobility of this form of TiO_2 should be greater than that of sintered nanoparticles but less than that of polycrystalline films: $10^{-7} - 10^2$ cm^2/V-s.[174,175]

The second major difference between this theoretical device and the Grätzel cell is the choice of light-harvesting material. CdSe nanocrystals are inorganic and are highly robust materials. Though they are somewhat bulkier than molecular dyes, they have very large absorption cross-sections, with size-dependent extinction coefficients on the order of $\epsilon = 10^6 - 10^7$ L/mol-cm at the band gap.[40] Because of their relatively large extinction coefficients, nanocrystals absorb more light per crystal than the dyes,

countering the smaller concentration of nanocrystals adsorbed on the TiO_2 surface.

Besides large extinction coefficients, CdSe nanocrystals have an important advantage in their size. Because of their bulk, with $10^3 - 10^5$ atoms per nanocrystal, they provide a nanometer-scale barrier between the TiO_2 and the ITO electrode when arranged in close packed formation on the TiO_2 surface. This barrier limits charge recombination. By reducing or eliminating charge recombination between the p- and n-type materials with a physical distancing barrier, we negate the largest impediment to the development of a solid-state Grätzel cell.

Finally, nanocrystals are ideal for use in photovoltaics because of the wide range of light they absorb. Unlike organic molecules, which typically absorb light at specific wavelengths, even a narrow size distribution of nanocrystals harvests light at any wavelength above the band gap. CdSe nanocrystals harvest light only in the visible (and higher energy) range; however, a smaller band gap material could be substituted for CdSe without significantly changing the other advantageous material properties shared by all nanocrystals. For example, PbSe has a band gap that permits absorption of infra red light. If we were to use PbSe in place of CdSe, the photovoltaic would be able to harvest virtually all of the solar spectrum, resulting in a much more efficient device. In terms of light absorption nanocrystals exhibit the best properties of both bulk semiconductors and small molecules; they have the absorption range and durability of bulk semiconductors and the magnified absorption cross sections and size of small molecules.

Currently the CdSe-OBHP is a purely theoretical device, though a synthesis is under development. However, in order to assemble an efficient structure, there are several parameters that must be optimized prior to assembly. Of critical importance are the precise structure and characteristics of the TiO_2. In particular, we need to determine the pore diameters, distances between pores, and TiO_2 film heights which will result in optimum device performance. Additionally, we would like to be able

to predict the behavior of the finished device. For these reasons, the next appendix models the behavior of the CdSe-OBHP under different device geometries.

APPENDIX D

MODELING OF THEORETICAL PHOTOVOLTAIC

In the previous appendix, we explored the photophysics of both conventional and nanomaterial-based photovoltaics, and learned why the Rosenthal group's nanocrystal-based ordered bulk heterojunction photovoltaic (here referred to as CdSe-OBHP) should be an excellent alternative to conventional photovoltaics. This appendix details a simple calculation of the theoretical efficiency of the photovoltaic based solely on the geometry of the device. The model makes the following assumptions:

1. CdSe nanocrystals are of uniform size and are spherical in shape.

2. The TiO_2 film has cylindrical pores of uniform diameter, which are oriented normal to the aluminum surface in a close-packed (*cp*) arrangement.

3. The nanocrystals completely coat the TiO_2 surface in a single *cp* layer of crystals; each nanocrystal is also in contact with the ITO electrode.

4. The only light-absorbing species is CdSe; ITO, TiO_2, and the linker molecule are optically transparent over the solar spectrum.

5. Incoming light neither scatters nor reflects. Photons pass straight through the device unless absorbed by CdSe.

6. Because the dimensions of the internal features of the device (i.e., nanocrystals, pores, distance between nearest-neighbor pores) are on the nanometer scale, an averaged areal density of nanocrystals is used when calculating light absorption; light absorption is treated as equally likely at any point in a plane parallel to the surface of the Al electrode, and varies only with depth.

7. Each photon absorbed results in an electron collected at the Al electrode and

a hole collected at the ITO electrode (the internal photon-to-electron quantum yield is 100%).

8. The potential across the device is equal to the difference in work functions between the two electrodes.

Clearly many of these assumptions are grossly inaccurate; however, the primary goal of this model was to determine an initial TiO_2 geometry with which to begin building devices; without more information on the electronic behavior of the materials involved in the device, this model represents a best guess.

D.1 Characterization of device geometry

In order to optimize the geometry of the CdSe-OBHP to maximize device efficiency, we need a means of calculating the density of nanocrystals within the device. Fortunately, the highly ordered structure of the TiO_2 allows an exact mathematic model of the placement of pores and nanocrystals on the TiO_2 surface. We first consider the structure of the TiO_2 itself. Figure D.1 depicts the structure of the TiO_2 looking down the axis of the pores. Because of the regular *cp* arrangement of the pores, a two-dimensional unit cell can be defined based on the distance (pitch) between nearest-neighbor pores, p. This cell contains one pore of diameter d_p and has an area of

$$a_{uc} = \frac{\sqrt{3}}{2} p^2 \tag{D.1}$$

so that the areal density of pores is

$$n_p = \frac{2}{\sqrt{3} p^2} \tag{D.2}$$

It is noted that all areal densities presented in this discussion are normalized to the surface area of the Al electrode.

At this point we can calculate one important measure of any BHP, the area enhancement factor (AEF). The AEF is a measure of the increase in the surface area

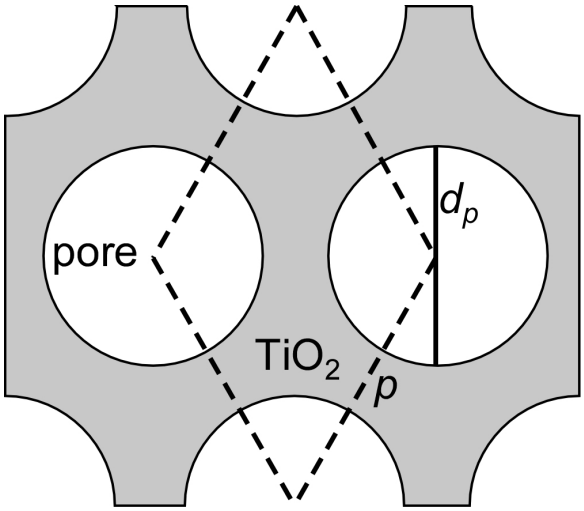

Figure D.1: Geometric characteristics of TiO_2 pores. The pores of the TiO_2 film are cylinders oriented normal to the Al electrode. This diagram, which shows a view of the TiO_2 film looking down the axis of the pores, illustrates how the highly ordered geometry of the film may be fully characterized by the pitch between pores, p, the diameter of the pores, d_p, and the height of the pores, h_p (not shown). A two-dimensional unit cell is also shown (dashed lines).

of the heterojunction over a planar structure, such as a SHP. It is also an indirect indication of the increase in efficiency of the BHP over a planar structure. By definition, a SHP has an AEF of 1. In the CdSe-OBHP, nanocrystals coat three surfaces in the device: the top surface of the TiO_2, the pore walls of the TiO_2, and the surface of the Al electrode at the base of the pores, the only part of the electrode not coated by TiO_2. All these surfaces are considered part of the heterojunction. Regardless of pore width and density, the sum of the surface areas of the top of the TiO_2 and the exposed Al is always 1 (normalized to the total surface area of the Al electrode). Given a height, h_p, of the TiO_2 film, the total normalized surface area of the pores is

$$a_p = \frac{2\pi d_p h_p}{\sqrt{3}p^2} \tag{D.3}$$

The AEF of the CdSe-OBHP is the sum of all three areas:

$$AEF = 1 + \frac{2\pi d_p h_p}{\sqrt{3}p^2} \tag{D.4}$$

For purposes of comparison, the original report of the Grätzel cell lists a calculated AEF of 2000 for a cell with a 10 μm TiO_2 film.[291] In a CdSe-OBHP with identical TiO_2 film height, a pore diameter to pitch ratio of greater than 7.4×10^{-3} results in an AEF greater than that of the Grätzel cell; this ratio is far smaller than the expected ratio for the synthesized TiO_2 film. Thus, the predicted AEF for the CdSe-OBHP is greater than that of a Grätzel cell of similar height.

With the geometry if the TiO_2 now defined, we can calculate the coverage of the TiO_2 surface by nanocrystals, which ultimately leads to the density of nanocrystals within the device. Under the assumption that the CdSe nanocrystals self-assemble in a *cp* architecture on the TiO_2 surface, a unit cell can be defined for nanocrystal packing that is similar to the unit cells of the TiO_2 pores. Assuming a flat surface, a unit cell containing one nanocrystal of diameter d_{nc} has an area of

$$a_{nc} = \frac{\sqrt{3}}{2} d_{nc}^2 \tag{D.5}$$

Equation D.5 describes the amount of surface occupied by one nanocrystal on the top of the TiO_2 film or on Al; however, it does not account for the curvature of the TiO_2 pores. Because of the concavity, a single nanocrystal occupies more surface in a pore than on a flat surface.

In order to determine the surface area occupied by a nanocrystal in a pore, we begin by defining, without loss of generality, a unit cell on a flat, vertical, xz-plane that is a rectangle $\frac{\sqrt{3}}{2} d_{nc}$ in the z-direction and d_{nc} in the x-direction (Figure D.2). For the purposes of this discussion, the shape of the unit cell is ultimately irrelevant; only the area is pertinent. The definition of a unit cell is a minimum connected area which can tessellate the plane surface with identical cells. Thus, the area of any shape of unit cell within the pore is identical. In this case each unit cell contains exactly one nanocrystal. In addition, we choose the unit cell such that one nanocrystal diameter is contained within the cell; this diameter is critical to later calculations. If we map this flat surface to the cylindrical surface of the pores, we can determine the surface

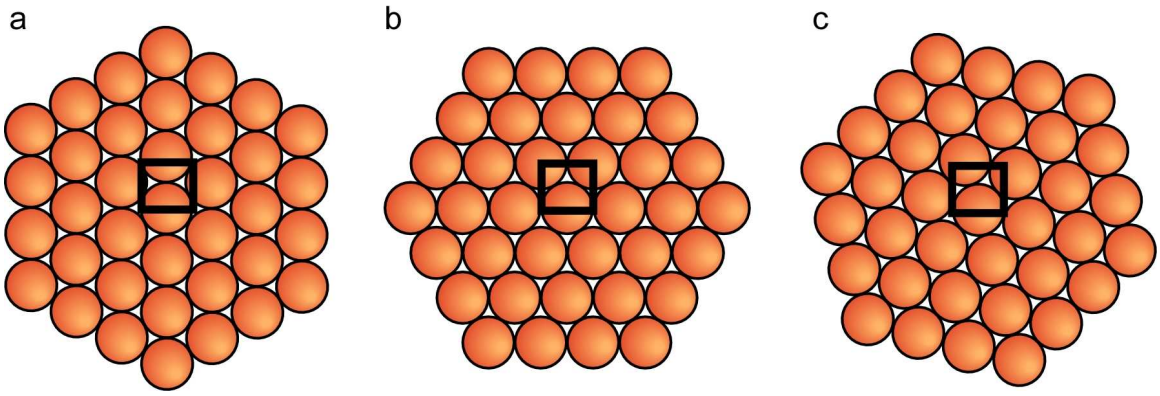

Figure D.2: Nanocrystal packing in pores. Depending on the ratio $d_{nc} : (d_p - 2l)$, the close-packed nanocrystals will align in columns (a), rows (b), or spirals (c) within the TiO_2 pores. Regardless of the orientation of the nanocrystals, a unit cell of width d_{nc} and height $\frac{\sqrt{3}}{2}d_{nc}$ can be defined on the corresponding flat surface such that one nanocrystal diameter is completely contained within the unit cell. In the examples shown here, the bottom edge of each unit cell is the diameter in the x-direction of a nanocrystal.

area of the unit cell in the pores.

The map used to transform the cylindrical coordinates of the pore to the Euclidean coordinates of a plane is similar to the transformation of the Poincaré model to the upper half-plane model of the hyperbolic plane.[304] For the CdSe-OBHP unit cell we construct the map

$$(x, y, z) = \left(\alpha\Theta, \frac{d_p}{2r}, z\right); \qquad (r, \Theta, z) \in \begin{cases} 0 \leq r \leq \frac{d_p}{2} \\ 0 \leq \Theta \leq 2\pi \\ 0 \leq z \leq h \end{cases} \tag{D.6}$$

where (Θ, r, z) are the standard cylindrical coordinates, (x, y, z) are the standard three-dimensional Euclidean coordinates, and α is a scalar contraction factor which accounts for the negative curvature of the pore wall (Figure D.3). Except for the points along the center axis of the pore, this map is one-to-one and onto, and it preserves the connectedness and angles of shapes from one space to the other. Since points along the center axis are not well defined in cylindrical coordinates with respect to Θ, the discontinuity at $r = 0$ is irrelevant to this discussion. Thus, the map defined in Equation D.6 is a good representation of the transformation of the space occupied

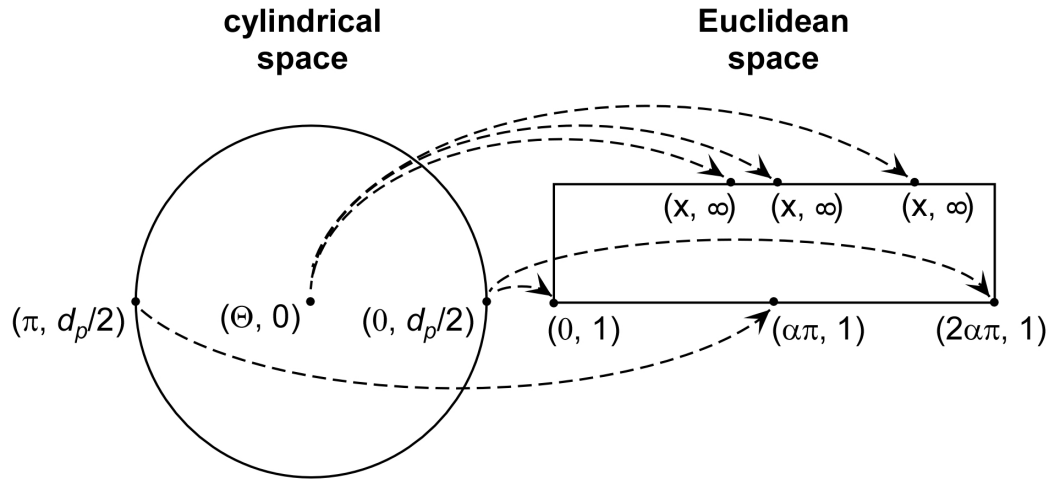

Figure D.3: Map from cylindrical space to Euclidean space. Above is a visual representation of the map given in Equation D.6. For both spaces, the z-direction is normal to the plane of the paper (not shown). This map provides both an intuitive and mathematically rigorous description of the behavior of the system in both spaces.

by a unit cell.

We can now use the map to determine the area of the nanocrystal unit cell on the pore wall. Since there is no curvature in the z-direction for either space, lengths in the z-direction are maintained by the map. Therefore, the height of the unit cell is $\frac{\sqrt{3}}{2}d_{nc}$ in both cylindrical and Euclidean space. The width of the unit cell in Euclidean space is d_{nc}. To find the corresponding width in cylindrical space, we use the construction detailed in Figure D.4.

We now consider a Θr-plane in cylindrical space and the corresponding xy-plane in Euclidean space. In cylindrical space, we add the circle $r = \frac{d_p}{2} - l$; in an actual TiO_2 pore, the area $\frac{d_p}{2} - l \leq r \leq \frac{d_p}{2}$ is occupied by the organic linker of length l that is used to attach the CdSe nanocrystals to the TiO_2 surface. We also draw a circle of radius $\frac{d_{nc}}{2}$ tangent to the circle representing the linker surface; this smaller circle represents the cross section of a nanocrystal attached to the linker layer. Finally, we draw two radii of the circle $r = \frac{d_p}{2}$ tangent to the 'nanocrystal' surface. Through simple geometric relations, it can be shown that the angle between the two

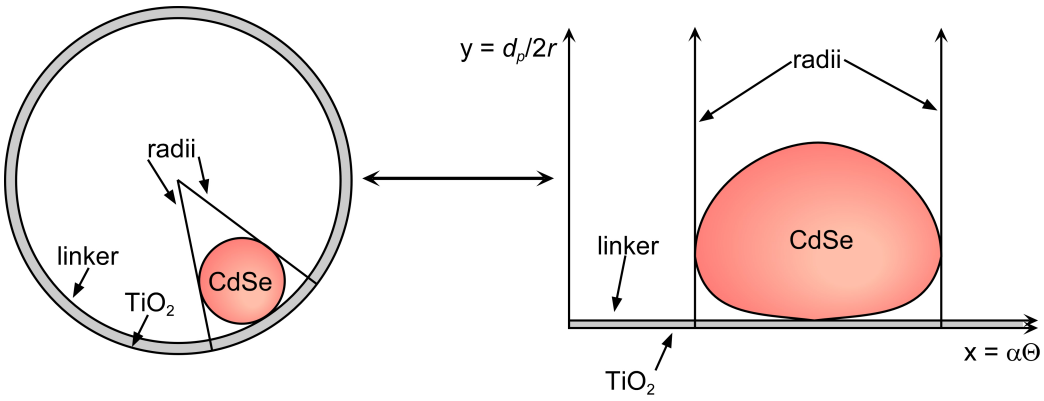

Figure D.4: Nanocrystal construction in pore and map to Euclidean space. This construction is used to define the value α in Equation D.6. Because of the way the mapping is defined, the projection of the nanocrystal diameter onto the wall of the TiO_2 pore from the center of the pore (left) is mathematically the same as the projection of the mapped nanocrystal onto a flat surface from a point infinitely far away. The distorted shape of the mapped nanocrystal is irrelevant to the efficacy of the map in relating Θ in cylindrical coordinates to x in Euclidean coordinates.

radii is

$$\theta = 2\left[\arcsin\left(\frac{d_{nc}}{d_p - d_{nc} - 2l}\right)\right] \tag{D.7}$$

and the arc along the TiO_2 pore surface has a length of $\frac{d_p\theta}{2}$. The circles representing linker and nanocrystal and the two radii are then mapped according to Equation D.6 to the Euclidean plane. Because of the connectedness of the map and the preservation of angles over the transformation, in both planes the 'nanocrystal' remains tangent to the 'linker' and both radii, and the radii are perpendicular to the TiO_2 and 'linker' surfaces. The mapped 'nanocrystal' and 'linker' are no longer circular; however, this map is used only as a means of defining α to compensate for the curvature of the pores in the area of the unit cell of the nanocrystals, a_{nc}. The shape of the mapped nanocrystal is irrelevant to this purpose.

The unit cell shown in Figure D.2 has a width of d_{nc}. This width is actually the projection of the nanocrystal diameter onto a flat surface from a point infinitely far away - the distance between the two lines tangent to the nanocrystal cross section

and perpendicular to the TiO_2 surface is d_{nc}. We now define α such that the distance between the two mapped radii in Figure D.4 is also d_{nc}. This distance is the projection of the mapped nanocrystal onto a flat surface from a point infinitely far away. From the map, it is also the projection of the nanocrystal in the pore from the center of the pore. This projection is the true width of the unit cell on the surface of the pore. Comparing the length of this arc with the corresponding length in Euclidean space,

$$\alpha = \frac{d_p \theta}{2 d_{nc}} \tag{D.8}$$

and the area of the nanocrystal unit cell in cylindrical space is

$$a'_{nc} = \frac{\sqrt{3}}{4} d_p d_{nc} \theta \tag{D.9}$$

We note that $\lim_{d_p \to \infty} \theta = 2$; thus, as pores lose their concavity and become flat surfaces, Equation D.9 approaches Equation D.5 in the limit, as expected. Combining Equations D.3 and D.9, the areal density of nanocrystals within the pores is

$$n_{nc}(pore) = \frac{8\pi h_p}{3 d_{nc} p^2 \theta} \tag{D.10}$$

Likewise, the areal density of nanocrystals on flat surfaces within the photovoltaic is

$$n_{nc}(flat) = \frac{2}{\sqrt{3} d_{nc}^2} \tag{D.11}$$

giving a total areal nanocrystal density of

$$n_{nc} = \frac{2}{\sqrt{3} d_{nc}^2} \left(1 + \frac{4\pi d_{nc} h_p}{\sqrt{3} p^2 \theta} \right) \tag{D.12}$$

Equation D.12 is the critical equation in the optimization of device geometry, as the nanocrystal density is directly related to the amount of light absorbed and hence to the overall efficiency of the device.

Because of the high degree of structure in the device, the device geometry has been fully characterized using five variable parameters: height of the TiO_2 film (h_p), pitch of the pores in the TiO_2 film (p), diameter of the TiO_2 pores (d_p), diameter of

the nanocrystals (d_{nc}), and length of the organic linker molecule (l). By adjusting the relative ratios of these parameters, it is now possible to optimize the device geometry to obtain maximum (theoretical) power conversion efficiency.

D.2 Optimization of device geometry

In order to maximize the power output of the CdSe-OBHP, it is necessary to optimize the device geometry. Ideally, the optimization should take into account the kinetics of charge generation and transport through the photovoltaic as well as basic geometric considerations. However, in the absence of data relating to quantum yields of charge injection across interfaces, recombination rates, etc., we present a simplified optimization related primarily to the density of CdSe nanocrystals in the device.

Under the assumptions made at the beginning of this appendix, every photon absorbed by a nanocrystal results in the production of an electron and a hole on the Al and ITO electrodes, respectively. This is equivalent to stating that maximum power results from maximum nanocrystal density. Maximum nanocrystal density is strictly dependent on the number and surface area of pores. From a purely mathematical standpoint, maximum TiO_2 surface area occurs when the pores have infinitely small diameters and are infinitely close together. However, physical and synthetic limitations impose minima on both these parameters. The CdSe-OBHP is a self-assembled structure; nanocrystals are introduced into the pores through wet chemical techniques after the TiO_2 has been synthesized. Because nanocrystals likely bind to the first exposed linker-coated TiO_2 surface they come in contact with, they would coat the pore walls closest to the top TiO_2 surface first, with new nanocrystals binding to successively lower portions of the pore walls until the walls are completely coated. This self-assembly process imposes a minimum possible pore diameter on the system. For the pore walls to be completely coated, the pore must be wide enough that, completely coated by linker and a layer of nanocrystals, free (unbound) nanocrystals can

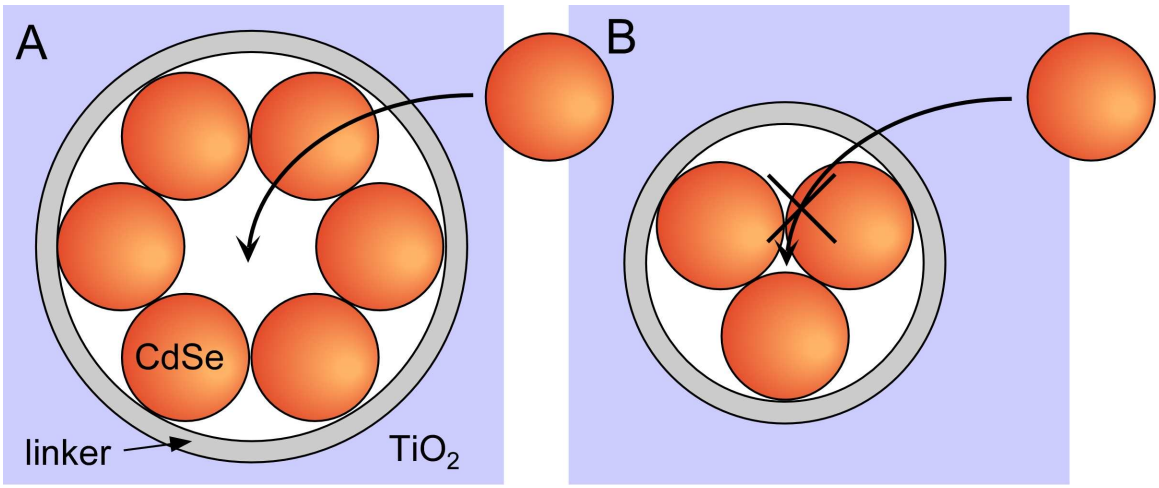

Figure D.5: Self-assembly of nanocrystals in pores. If $d_p \geq 3d_{nc} + 2l$ (A), then free nanocrystals are able to pass through the center of a pore to reach bare portions of the pore wall, even if nanocrystals have already coated parts of the pore closer to the exterior of the film. However, if $d_p < 3d_{nc} + 2l$ (B), the pore becomes blocked; free nanocrystals cannot reach the interior of the pore, and the pore does not contribute significantly to charge generation.

still pass through the center of the pore (Figure D.5):

$$d_p \geq 3d_{nc} + 2l \tag{D.13}$$

Given a constant width of the pore walls (defined as $w = p - d_p$), the maximum density of nanocrystals is obtained when $d_p(min) = 3d_{nc} + 2l$. Of course, in reality, the minimum pore diameter is somewhat greater than this, because this ratio assumes a uniform size of perfectly spherical nanocrystals, which is not possible to achieve synthetically. A greater pore diameter must be used to accommodate those nanocrystals with diameters greater than the average, as well as to accommodate the typically prolate shape of the nanocrystals.

A synthetic constraint is also placed on the minimum width, w, of the pore walls. In order for pores to be distinct entities, there must be at least a monolayer of TiO_2 between nearest-neighbor pores. In practice, the width is somewhat greater and depends on the synthesis used to create the TiO_2 thin film. Since the synthesis

to create a TiO_2 film with the physical characteristics necessary for the CdSe-OBHP film is still under development, w is still unknown. However, it is likely that the synthesis will be based partially on the synthesis of Yang *et al.*,[305] which lists a wall thickness of 50 Å. This is the thickness that is used in all further calculations. It is noted that, while in this calculation the thickness of the walls does not affect electron transport in the TiO_2, in reality the walls must be much thicker than the minimum of one monolayer to support large quantities of electrons.

The last parameter to be optimized is the height, h_p, of the TiO_2 thin film. Unlike the width of the pore walls, there is no practical synthetic limitation to the height of this film. As in other nanomaterial-based photovoltaics, increasing the height of the device beyond the penetration depth of light into the cell only results in a decrease in device efficiency. The increased volume does not contribute to charge generation, but it does add to series resistance, shorts, etc. The TiO_2 film composition is predicted to be composed of nanocrystalline regions within an amorphous framework. Added to the mesoporous architecture of the film and the CdSe nanocrystals within the pores, light scatter within the device is expected to prevent light penetration over long distances in the photovoltaic. In contrast, current syntheses of ordered mesoporous metal-oxides yield mesoporous materials with heights of as much as 1 inch (e.g., see Yao *et al.*[306]). In the next section, we show that this height is much greater than that needed to achieve near-total light absorption in the CdSe-OBHP; therefore h_p is limited not by synthetic constraints but by the amount of light which can penetrate the device. For purposes of comparison, in calculating the theoretical efficiency of the device, we used heights on the order of $10^{-6} - 10^{-4}$ m, about the height of the Grätzel cell.

Using the optimized ratio of $d_p : d_{nc}$ determined in Equation D.13, a pore wall thickness of 50 Å, and an organic linker molecule length of 1 nm, we can now simplify

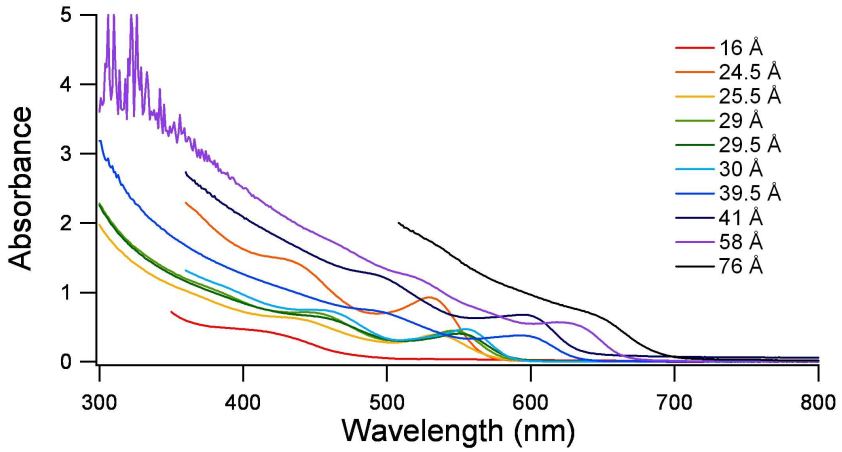

Figure D.6: Raw absorption spectra for nanocrystals used in geometry-based device efficiency calculations.

Equations D.7 and D.10. Given that

$$p = d_p + w \tag{D.14}$$

θ now has a fixed value of

$$\theta = 2\left[\arcsin\left(\frac{1}{2}\right)\right] = \frac{\pi}{3} \tag{D.15}$$

and the areal density of nanocrystals within the pores is

$$n_{nc}(pore) = \frac{8h_p}{d_{nc}\left(3d_{nc} + 70\ \text{Å}\right)^2} \tag{D.16}$$

D.3 Geometry-based device efficiency

The theoretical maximum efficiency of the CdSe-OBHP was calculated for ten sizes of nanocrystals, ranging in diameter from 16 Å to 76 Å. Absorption spectra for ten samples of nanocrystals, TOPO-coated and dissolved in toluene, were taken in the range 300 - 800 nm by a UV-visible spectrometer (Figure D.6), as detailed in Section 2.2. The spectra were then configured for the calculation as follows. First the spectra were normalized so that the minimum absorbance (A) over the range scanned

was 0. This involved either adding or subtracting a fixed value to all experimentally determined densities:

$$A_{norm}(\lambda) = A_{exp}(\lambda) + A_{corr} \tag{D.17}$$

Here $A_{norm}(\lambda)$ is the normalized absorbance, $A_{exp}(\lambda)$ is the experimental value, and A_{corr} is a small correction assumed to be independent of wavelength. The normalization was carried out because the UV-visible spectrometer has a wavelength-independent error which is not completely corrected by rezeroing the machine prior to spectrum acquisition.

Next, the spectra were adjusted to account for missing wavelengths and for absorbance measurements that were too large due to scatter by nanocrystal aggregates. The solar spectrum covers the range 295 - 2537 nm of the electromagnetic spectrum. None of the nanocrystal absorption spectra extend to 295 nm. In addition, in some cases the concentration of nanocrystals in the scanned sample was high enough that absorbance at small wavelengths was outside the spectrometer's operating range of $A = 0 - 2.5$. In Figure D.6, this problem is visible as a scatter in the data at higher absorbances (e.g., in the scan of 58 Å CdSe for $\lambda < 410$ nm). Absorbances for wavelengths in the range 295 - n nm (where n is the lowest wavelength giving reliable absorbance data) were extrapolated from the normalized absorption spectra by assuming a linear increase in light absorption over this range:

$$A_{\lambda<n} = A_n + [A_n - A_{n-1}]\,(n - \lambda) \tag{D.18}$$

Absorbances of 0 were assigned to all wavelengths greater than 800 nm, since these wavelengths are below the optical bandgap of CdSe nanocrystals. The final spectra used in the calculation of device efficiency are shown in Figure D.7.

To calculate the amount of light absorbed by the CdSe-OBHPs, the concentrations of nanocrystals were determined: a) in the solutions scanned by the UV/Vis spectrophotometer, b) on flat surfaces within the device, and c) in the TiO_2 pores.

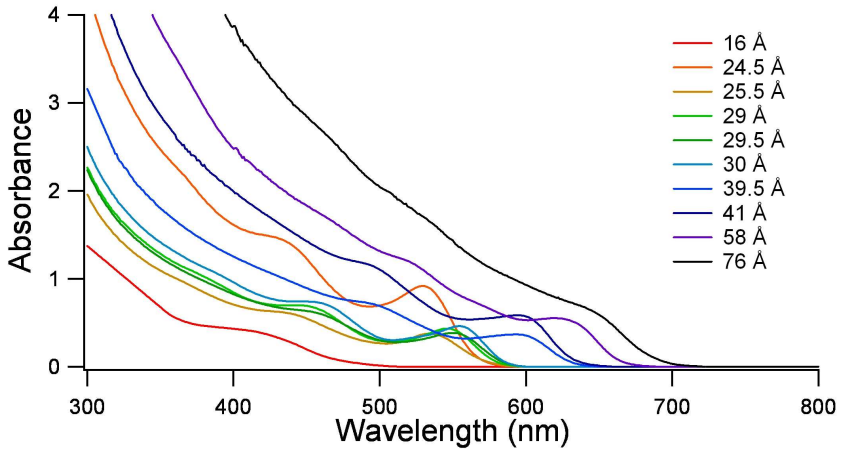

Figure D.7: Corrected absorption spectra for nanocrystals used in geometry-based device efficiency calculations.

According to the data presented in Appendix F, the extinction coefficient of the nanocrystals at the optical bandgap, E_g, is

$$\epsilon_{E_g} = \left(5.7 \times 10^4\right) e^{0.050 d_{nc}} \tag{D.19}$$

where ϵ_{E_g} has units of L/mol-cm and d_{nc} is the nanocrystal diameter in Ångstroms. Beer's law relates absorbance to the extinction coefficient of a sample by

$$A_\lambda = \epsilon_\lambda c L \tag{D.20}$$

where c is the concentration of nanocrystals and L is the path length of the light through the sample. For the spectra in Figure D.7, $L = 1$ cm; thus, the concentrations of nanocrystals in the scanned samples were determined by substituting ϵ_{E_g} from Equation D.19 and A_{E_g} from the scan into Equation D.20. The calculated concentrations of nanocrystals in the pores and on planar surfaces are simply the areal density divided by the height of the area in question (h_p for pores and d_{nc} for planes). From Equation D.16, the concentration of nanocrystals within the pores is

$$c_p = \frac{8}{d_{nc}\left(3d_{nc} + 70\ \text{Å}\right)^2} \tag{D.21}$$

and from Equation D.11, the concentration of nanocrystals on flat surfaces is

$$c_f = \frac{2}{\sqrt{3} d_{nc}^3} \tag{D.22}$$

Once the concentrations of nanocrystals in the three systems were determined, the total absorbance of the theoretical solar cells was determined. In a modification of Beer's Law, the absorbances of the systems in the cell are related to the absorbance of the scanned solution by

$$A_i(\lambda) = \frac{A_{scan}(\lambda)\, c_i L_i(\gamma)}{c_{scan} L_{scan}} \tag{D.23}$$

where i is the system (pore or plane) and the path length of light through the cell, $L_i(\gamma)$, is a function of the height, h_i, of the system, the angle, γ, relative to normal at which light passes through the cell, and a scattering factor, σ:

$$L_i(\gamma) = \frac{h_i \sigma}{\cos\gamma} \qquad 0 \leq \gamma < \frac{\pi}{2} \tag{D.24}$$

For these calculations $\sigma = 1$ and $\gamma = 0$, as this is the minimum path length of light through the cell and yields the minimum efficiency of the cell, all other factors being equal. Having calculated the absorbances of the two systems in the cell, the total absorbance of the cell is

$$A_{cell}(\lambda) = \sum_i A_i \tag{D.25}$$

It is noted that using Equations D.23 and D.25 it is easy to show that, given the assumption that light interacts with the cell only through absorption by CdSe nanocrystals, the fact that the nanocrystals on planar surfaces are on two different planes (on top of the TiO_2 and on top of the Al) makes no difference to the total absorbance of the system.

Once the absorbances of the theoretical photovoltaics were determined, the total efficiency of the device could be calculated. Absorbance is related to the intensity of light absorbed, I_{abs}, by

$$A(\lambda) = \log_{10}\left(\frac{I_{abs}(\lambda)}{I_0(\lambda)}\right) \tag{D.26}$$

The AM 1.5 solar spectrum was obtained from the *Terrestrial Photovoltaic Measurement Procedures*[307] and normalized to 1 sun intensity. Using this spectrum as $I_0(\lambda)$, $I_{abs}(\lambda)$ was calculated for each device (for example, Figure D.8 shows $I_{abs}(\lambda)$ for the ten sizes of nanocrystal in devices with TiO_2 film heights of 2 μm and 10 μm). Under the assumption that each photon of light absorbed results in an electron and a hole at opposite electrodes, the current produced by the photovoltaic, J_{cell}, can be calculated by

$$J_{cell} = \int_{\lambda} \frac{\lambda I_{abs}(\lambda)}{hc} d\lambda \tag{D.27}$$

and the power output of the photovoltaic is

$$P_{cell} = J_{cell} V_{cell} \tag{D.28}$$

At the beginning of this section the assumption was made that the potential across the device is the difference in work functions of the two electrodes:

$$V_{cell} = \phi_{ITO} - \phi_{Al} \tag{D.29}$$

Al has a work function of $\phi_{Al} = 4.3$ eV; however, the work function of ITO varies with composition and synthesis. Open-circuit voltage measurements of a similar photovoltaic with the same electrodes have yielded a device potential of 0.7 V.[297] Using this value for V_{cell}, the efficiency of each device was calculated by

$$\eta_{cell} = \frac{P_{cell}}{P_0} \tag{D.30}$$

The dependence of device efficiency on nanocrystal size and TiO_2 film thickness are shown in Figure D.9. This figure shows that η_{cell} increases rapidly for $h_p < 10$ μm, then remains nearly constant. This occurs because by this height the areal density of nanocrystals is so high that essentially all light is absorbed at those wavelengths at which the nanocrystals absorb. This can be seen in Figure D.8b, in which $h_p = 10$ μm. Here light absorption changes from none for $\lambda > \lambda_{E_g}$ to complete light absorption for

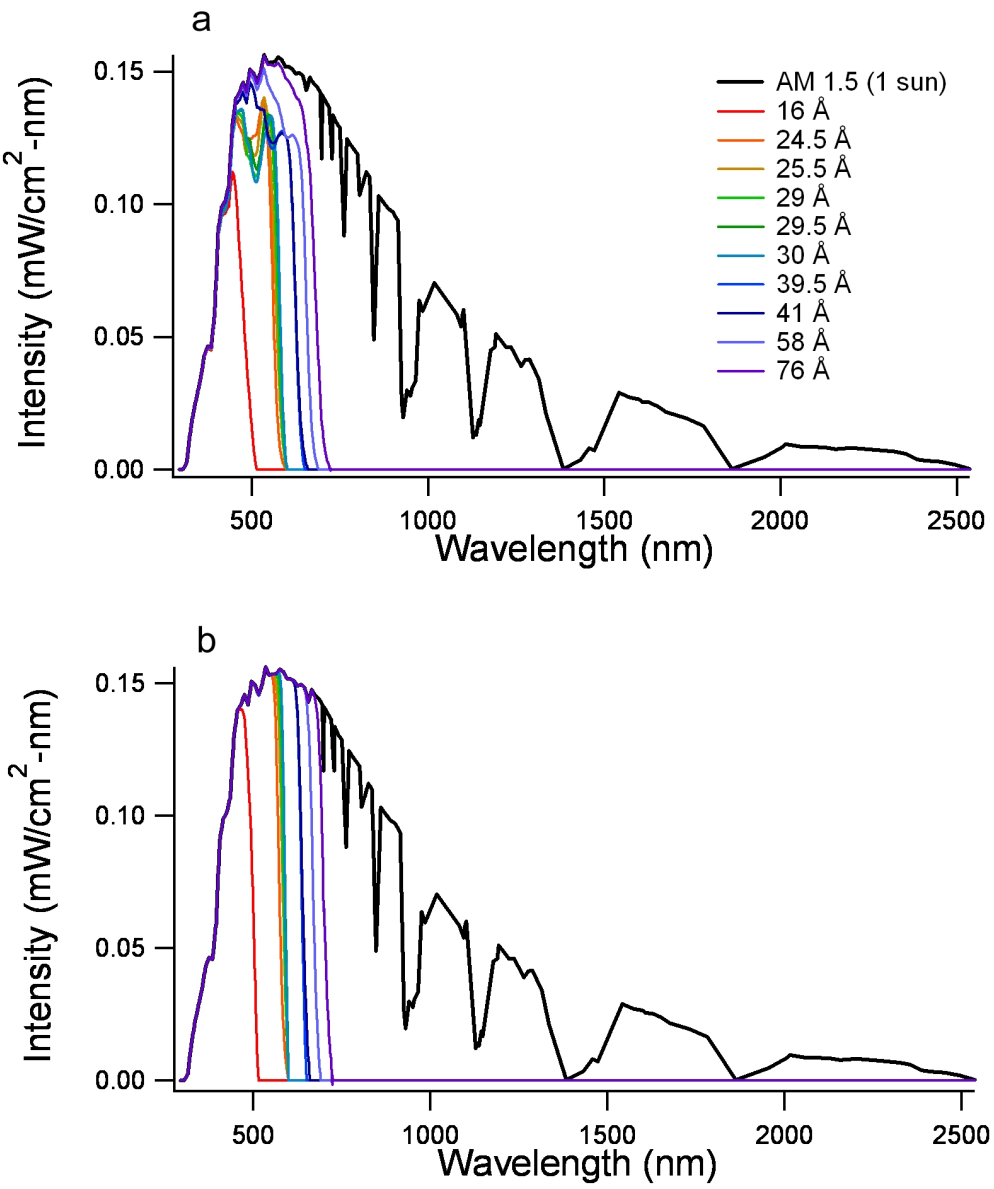

Figure D.8: Theoretical light absorption by CdSe-OBHPs. The wavelength-dependent intensity of the AM 1.5, 1 sun spectrum (black) absorbed by optimized, theoretical CdSe-OBHPs with nanocrystals ranging in size from 16 Å to 76 Å are shown for TiO_2 film heights of 2 μm (a) and 10 μm (b).

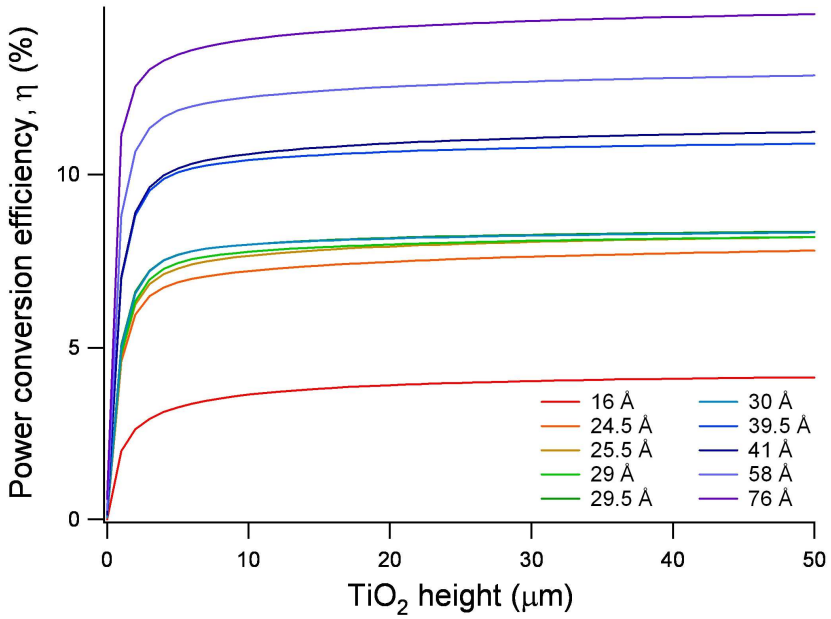

Figure D.9: Theoretical efficiencies of CdSe-OBHPs as a function of TiO_2 height for different sizes of CdSe nanocrystals.

$\lambda < \lambda_{E_g}$. In comparison, when $h_p = 2$ μm, as in Figure D.8a, light absorption for $\lambda < \lambda_{E_g}$ is incomplete, particularly at larger wavelengths.

Several important conclusions can be drawn from Figure D.9. First, this figure illustrates that the theoretical power conversion efficiencies of CdSe-OBHPs are ultimately limited by the band gap energies of the nanocrystals. Under the assumptions made at the beginning of this section, it is not possible to produce a device with an efficiency of greater than 20%. However, by changing the semiconductor material used to harvest light we can increase the range of light absorbed, thereby increasing device efficiency. For example, PbSe nanocrystals absorb infrared light. These nanocrystals have all the material and physical properties that are desirable in CdSe nanocrystals but absorb more of the solar spectrum. Figure D.10 shows the difference in light absorption between 80 Å CdSe nanocrystals and 58 Å PbSe nanocrystals, which have an optical band gap of about 2000 nm.[308] In using PbSe nanocrystals, the efficiencies of PbSe-OBHPs can be increased to more than 35%

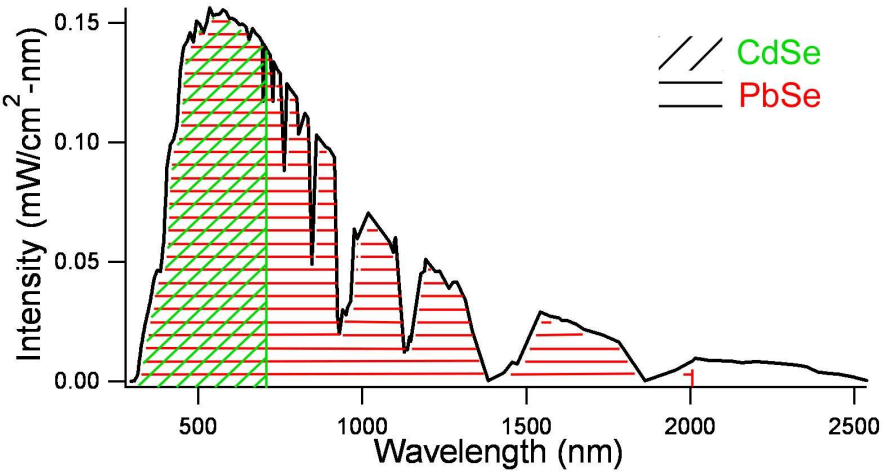

Figure D.10: Spectral absorption by 80 Å CdSe and 58 Å PbSe nanocrystals.

(e.g., 39.5% for 58 Å PbSe nanocrystals in a device with $V_{cell} = 0.62$ eV). A similar result may be achieved by changing the materials used as electrodes to increase V_{cell}. We note here that band alignment of all the materials in any device is critical to device performance. Even with perfect alignment of the CBM of TiO_2 with the CBM of the nanocrystals, and of the work functions of the electrodes with the CBM of TiO_2 and VBM of the nanocrystals, V_{cell} has an upper bound of the band gap of the nanocrystals. If $V_{cell} > E_g$, then many of the generated electrons and holes have insufficient energy to reach the electrodes, either because they are generated with insufficient energy or because they relax within the nanocrystals (or TiO_2) to energies less than the electrode band energies. If $V_{cell} = E_g$, then the maximum efficiency of the CdSe-OBHP ranges from 20 - 41%, higher efficiencies generally being associated with larger nanocrystals.

In spite of being capable of harvesting less of the solar spectrum than Si, the efficiencies of the CdSe-OBHP structures considered here are still commercially viable. In a real device, light scatter may improve light absorption by the nanocrystals and thus device efficiency; however, factors such as resistance, charge recombination, and inefficient nanocrystal packing decrease efficiency. It is likely that a single CdSe-

OBHP would not have the efficiency of commercial Si devices. However, we can boost the efficiency of the devices tremendously by taking advantage of the variable bandgaps of nanocrystals by stacking multiple OBHPs. For example, if CdSe-OBHPs are stacked with nanocrystals that are 16 Å, 24.5 Å, 30 Å, 41 Å, and 76 Å in diameter sequentially, with the smallest nanocrystals nearest the light source, and if $V_{cell} = E_g$ for each layer, the total efficiency of the stacked devices is greater than 52%. Alternately, by stacking a 76 Å CdSe-OBHP atop a 58 Å PbSe-OBHP, the stacked device achieves a total power conversion efficiency of 78.6%. This efficiency is quite simply unmatched by traditional bulk semiconductor photovoltaics.

One final point to note from Figure D.9 is that the TiO_2 films used in these devices need not be very thick to achieve near-optimum efficiencies. A 10 μm film yields a device efficiency that is typically greater than 90% of the efficiency of a device with an infinitely high TiO_2 film. Since these efficiencies are only determined by light absorption and do not take into account light scatter, resistance, etc., which increase with TiO_2 film height, efficiency in a real device is likely maximized by using a TiO_2 film height that is somewhat less than 10 μm.

APPENDIX E

PHOTOVOLTAIC TESTING

The following is a brief discussion on how photovoltaic device efficiencies are measured, including measurement conditions and calculation of power conversion efficiency.

E.1 Lighting conditions

To test the efficiencies of photovoltaic devices, researchers typically use one of two lighting conditions. The first method is to measure current-voltage characteristics under monochromatic light. The wavelength of the light typically corresponds to the wavelength of maximum light absorption by the photoactive material(s). The second method is to use white light to approximate the solar spectrum.

Since the intensity of light at each wavelength is influenced by light absorption by gas and vapor molecules in the atmosphere, air mass notation is used to define the relative intensities of wavelengths in the solar spectrum. Figure E.1 depicts how air mass is calculated. Air mass 0 (AM 0) corresponds to the solar spectrum as measured before passing through the atmosphere. All other air mass values are calculated by

$$AM = \sec \alpha \tag{E.1}$$

where α is the angular deviation from normal at which light hits sea level on the earth. Conceptually, air mass values denote the length of the path through the atmosphere that light travels compared to a path from space to sea level and normal to the earth's surface. Thus, AM 1 is the spectrum of direct sunlight (when the sun is directly overhead) and is the minimum air mass value for light on the surface of the earth. Industry standard is global AM 1.5 ($\alpha = 48.5°$), but AM 0, AM 1, and AM 2 are also used to evaluate photovoltaic device efficiency.

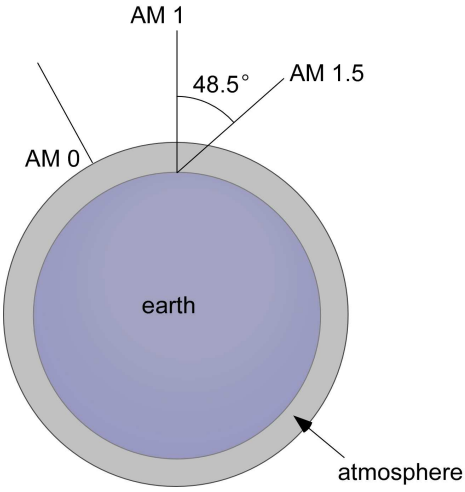

Figure E.1: Definition of air mass solar spectra. Air mass zero (AM 0) is the solar spectrum incident on the earth's atmosphere. Air mass one (AM 1) is the solar spectrum at the earth's surface with the sun directly overhead. The standard measurement used when evaluating photovoltaic performance is air mass 1.5, which is the spectral distribution of sunlight when the incidence angle of the sunlight is at 48.5°.

Although the air mass system sets the relative intensity of each wavelength, it does not define the absolute intensity of light. As seen in Figure E.2, the total intensity of light incident upon the earth's surface varies by region, as conditions such as water vapor and pollution affect the amount of light scatter in the atmosphere. Although exact definitions may vary, a standard light intensity of 1 sun is defined to be 100 mW/cm^2 (1000 W/m^2). Figure E.3 shows the AM 1.5 spectrum at 1 sun and 0.2 sun intensities. The relative wavelength intensities for both spectra are identical, but the total intensities of light differ by a factor of 5.

E.2 Calculating photovoltaic efficiencies

There are many parameters that detail the function of a photovoltaic device; a description of all of these is beyond the scope of this thesis. However, as the ultimate goal of any device is to maximize power output, one of the device parameters that is useful to know is the external power conversion efficiency (PCE), also called the device efficiency. The PCE of a device is found through the dependence of current

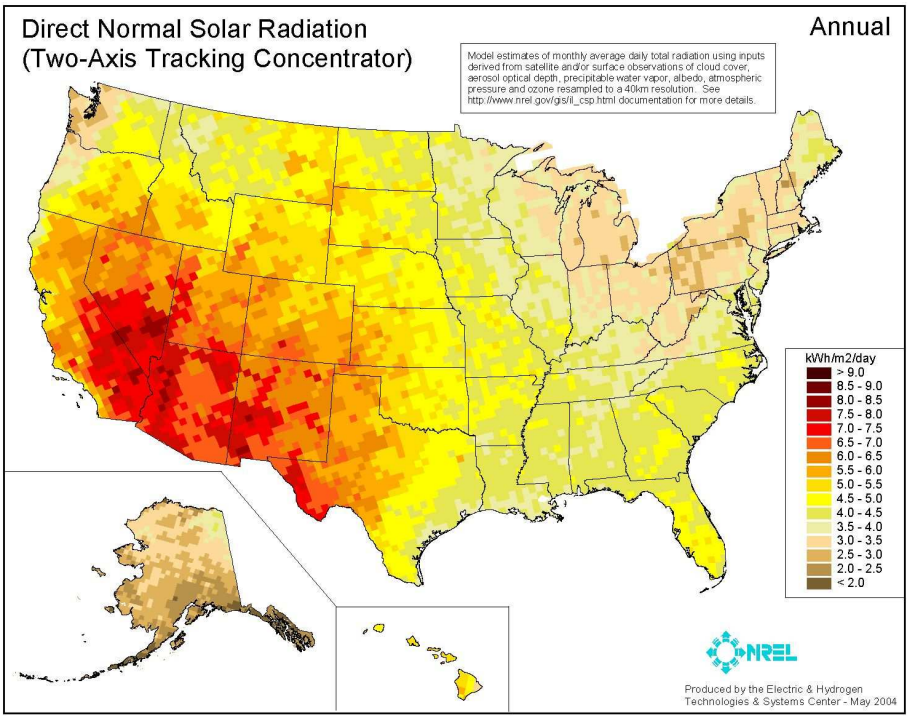

Figure E.2: Solar irradiance in the United States. This map shows the general trends in the amount of solar radiation received in the contiguous United States in units of kWh/m^2/day. It is a spatial interpolation of solar radiation values derived from the 1961-1990 National Solar Radiation Data Base (NSRDB). This image was obtained from the National Renewable Energy Laboratories Website, http://www.nrel.gov/gis/images/us_csp_annual_may2004.jpg,[309] and is based on the Climatological Solar Radiation (CSR) model, which is detailed by Maxwell *et al.*[310] and George *et al.*[311]

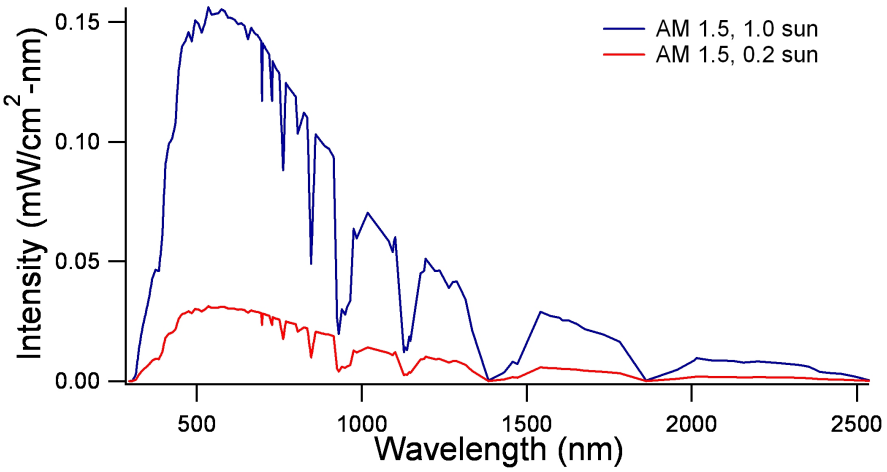

Figure E.3: Air mass 1.5 solar spectra at 1 sun (blue) and 0.2 sun (red) intensities.

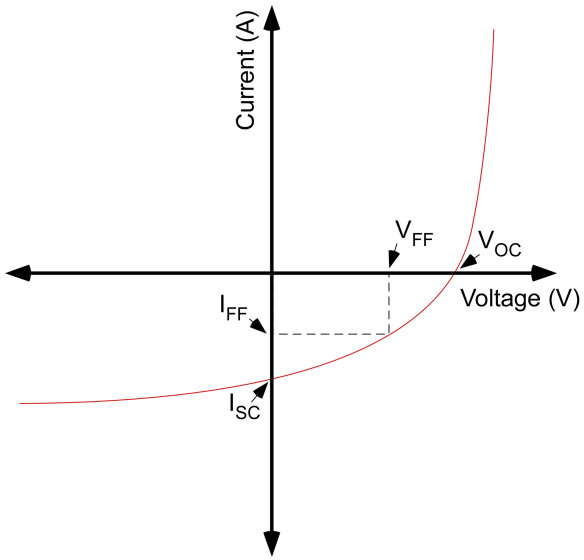

Figure E.4: Current-voltage characteristics of a photovoltaic device. The power conversion efficiency of a photovoltaic device is determined by measuring current as a function of applied bias (voltage). Maximum power is attained when a bias of V_{ff} is applied across the device (the resultant current is I_{ff}). These values are obtained by determining the maximum area of the rectangle inscribed along the I-V curve (the larger the area occupied by the rectangle, the greater the output power of the device).

output on voltage applied across the device (Figure E.4), and is given by

$$\eta = \frac{I_{sc} V_{oc} FF}{I_0} \tag{E.2}$$

Here I_{sc} is the short circuit current, V_{oc} is the open circuit voltage, I_0 is the intensity of incident light, and FF is the fill factor, given as

$$FF = \frac{\max\left(I \times V\right)}{I_{sc} V_{oc}} = \frac{I_{ff} V_{ff}}{I_{sc} V_{oc}} \tag{E.3}$$

The fill factor is an artificial construct, defined as the ratio of the maximum attainable power to the theoretical maximum power of the device ($I_{sc} V_{oc}$).

APPENDIX F

MOLAR ABSORPTIVITIES OF CdSe NANOCRYSTALS

This appendix details the determination of the molar absorptivities of CdSe nanocrystals using a combination of UV-visible absorption spectroscopy and Rutherford backscattering spectrometry. Since Yu *et al.*[40] published the molar absorptivities of CdS, CdSe, and CdTe before this work was completed, it was abandoned before the full range of nanocrystal sizes could be investigated. Nevertheless, it is included here because it was used in various calculations appearing in this dissertation.

We begin the study with the fact that nanocrystals absorb light according to Beer's Law:

$$\ln\left(\frac{I_0}{I_t}\right) = \epsilon c L \tag{F.1}$$

where I_0 is the light incident on the sample, I_t is the light transmitted through the sample, ϵ is the molar absorptivity, and L is the length of the light path through the sample. I_0, I_t, and ϵ all depend on the wavelength of light. The left-hand term of Equation F.1 is also called the absorbance, A, or the optical density (OD). The absorptivity is a particularly useful material property when considering photovoltaic applications, because it is used in the calculation of how much light is absorbed in a solar cell (Chapter D).

The absorptivity for the first optically allowed transition in a CdSe nanocrystal is proportional both to the oscillator strength of a CdSe diatom, f_1, and to the number of diatoms in the nanocrystal.[312] Since the number of diatoms is proportional to the volume, V, of a nanocrystal, we establish the relationship

$$\epsilon \propto f_1 V \tag{F.2}$$

In the strong confinement regime, when the diameter of the nanocrystal is less than twice the bulk Bohr radius, a_B ($d < 2a_B$), the oscillator strength varies as R^{-3}:[313]

$$f_1 \approx \frac{3}{4}\left(\frac{a_B}{R}\right)^3 f_{ex} \tag{F.3}$$

For CdSe, the bulk Bohr exciton radius is $a_B = 56$ Å,[43] and $f_{ex} = 4.24 \times 10^{-3}$ is the bulk exciton oscillator strength for the first optically allowed transition.[314] Since $V \propto R^3$, the absorptivity is theoretically independent of nanocrystal size.[49]

Prior to the work of Yu *et al.*,[40] investigations of the absorptivities of II-IV semiconductor nanocrystals drew contradictory conclusions. absorptivities of CdS and CdTe at the band edge were reported to be independent of nanocrystal size,[86,315] in agreement with theory. In contrast, all published work on CdSe shows size-dependence, ranging from linear to cubic in behavior.[40,316–318] Yu *et al.* showed size dependence for all three types of nanocrystal.[40] Within the Rosenthal group, absorptivities of CdSe nanocrystals were originally examined by Cody Folden,[319] who concluded that absorptivities were independent of size. However, through RBS and UV-visible absorption spectroscopy, we have found that, contrary to theory, the absorptivity does in fact depend on nanocrystal diameter.

The great difficulty in determining absorptivities lies in finding the concentration of nanocrystals in a given sample. Typically this is accomplished by first calculating how many Cd and Se atoms make up each nanocrystal (i.e., determination of the molecular weight of the nanocrystal), and then by determining what portion of a nanocrystal sample is nanocrystal as opposed to other material (ligand, etc.). To solve the first problem, most researchers have used the experimentally determined diameters (by TEM or XRD) and assumed a spherical nanocrystal morphology and a density identical to the bulk to calculate the molecular weight of the nanocrystals.[40,316,317] Atomic absorption spectroscopy (AAS) has then been employed to find the concentration of Cd in a sample of known weight, yielding the percentage of nanocrystals in a sample, except in the case of Leatherdale *et al.*,[316] who assumed

that their nanocrystal syntheses went to completion, so that no unreacted Cd or Se remained, which, combined with the molecular weight yielded the concentration of nanocrystals in solution. On the other hand, Striolo *et al.*[318] used molecular osmometry to determine molecular weight and assumed that no excess ligand or other material was present, thus bypassing the need to find the percent of CdSe in the samples.

All of these approaches have inherent flaws. AAS is an effective method of determining quantitatively the amount of Cd in a sample, but it has been shown that the ratio of Cd to Se in nanocrystals is not always 1:1,[95,320] which could significantly alter the amount of CdSe present, if 1:1 stoichiometry is assumed. The lattice contraction of CdSe nanocrystals when compared to the bulk is small enough ($< 0.5\%$[52]) that the density of the nanocrystals is essentially the same as the bulk, but nanocrystals are generally not spherical in shape; aspect ratios vary with synthetic technique and with nanocrystal size, with higher aspect ratios being associated with larger nanocrystals. Aspect ratios can easily be as high as 2:1, grossly altering the number of atoms per nanocrystal from the number in a spherical geometry. Molecular osmometry can give varying results, depending on the physical properties of the nanocrystal ligand and osmotic membrane (electrostatic attraction, flexibility of the ligand, etc.) and on the amount of ligand on the surface, which varies from sample to sample, and experience has shown that the assumption that all excess material has been washed away is not always accurate.[95] The assumption that a synthesis has gone to completion is likewise poor, particularly when the synthetic methodology is to stop the reaction when the desired nanocrystal size is achieved rather than when no more change is observed. Taylor *et al.*[95] showed that significant unreacted Cd and Se remain after synthesis, while Yu *et al.*[40] went as far as quantifying the amount of unreacted material as being $10 - 90\%$ of the original amounts. To bypass these problems, we used RBS in combination with Taylor's detailed analysis of nanocrystal volume based on the true

nanocrystal geometry[95] to calculate the molecular weight of CdSe nanocrystals as a function of (average) nanocrystal diameter, as well as to find the proportion of CdSe in each sample presented here.

The procedure for the experimental determination of the size-dependent absorptivities of the first absorption features of CdSe nanocrystals follows. TOPO-capped nanocrystals synthesized according to the TOPO/UI method (Section 2.1.1) were precipitated three times from methanol. The dried nanocrystals (0.5 - 15 mg) were then weighed and dissolved in 5 mL of toluene in a volumetric flask. Once the nanocrystals were completely dissolved, absorption spectra were taken of the resultant solutions. Several different weights and spectra were taken for each batch of nanocrystals. Finally, RBS was also performed on each sample.

HR-TEM data was not available for all nanocrystal samples, so absorption spectroscopy in combination with the "experiment" curve in Figure 2.7 (Equation 2.1) was used to determine the average diameter of the nanocrystals. Likewise, a rough estimate of the size distribution of each sample was obtained by fitting the lower-energy half of the band edge absorption feature in a plot of absorbance versus photon energy (rather than wavelength) to a Gaussian:

$$f(E) = \frac{x}{\sigma\sqrt{2\pi}} e^{-\frac{1}{2}\left(\frac{E-E_g}{\sigma}\right)^2} \tag{F.4}$$

(Here E is energy, E_g is the band gap energy, fixed by hand in the fit, x is an amplitude parameter, and σ^2 is the variance.) Assuming that the spread of the first absorption peak was due solely to variations in nanocrystal size, then σ is an overestimation of the standard deviation in nanocrystal size.

In order to calculate molar absorptivities, it was necessary to determine the concentration of nanocrystals in each sample. The first step towards determining this value was discovering what portion of the weighed sample was CdSe and what portion was TOPO. The atomic percent of CdSe to TOPO for each nanocrystal batch was calculated from the RBS spectra, as detailed in Section 2.4. Since it had previously

been determined that only TOPO was bound to the surface of the nanocrystals in the UI:TOPO synthesis,[114] the relative number of P atoms was directly proportional to the amount of non-nanocrystalline atoms in each sample. The relative weight of CdSe in a sample was calculated as

$$W^*_{CdSe} = \frac{N_{Cd}}{N_{Se}} (112.41 \text{ g}) + 78.96 \text{ g} \tag{F.5}$$

where N_x is the areal density of atom x. Given a molecular weight for TOPO of 386.63 g·mol^{-1}, then the relative weight of TOPO in the sample was

$$W^*_{TOPO} = \frac{N_P}{N_{Se}} (386.63 \text{ g}) \tag{F.6}$$

Since the total weight, W, of each sample was the sum of the weights of CdSe and TOPO, the true weight of CdSe, W_{CdSe}, was

$$W_{CdSe} = \frac{W^*_{CdSe}}{W^*_{CdSe} + W^*_{TOPO}} W \tag{F.7}$$

The next step in determining the concentration of nanocrystals in a sample was determining the molecular weight of the nanocrystals. To accomplish this, original data from previous RBS experiments by Taylor *et al.*[83] was reanalyzed to yield a calibration curve of the molecular weight of bare nanocrystals (with no ligands attached) as a function of nanocrystal diameter. In this data, the ratio of cadmium to selenium per nanocrystal had already been determined for nanocrystals whose diameters had been determined by XRD and HR-TEM. This work also gave a detailed formula for the volume of a nanocrystal as a function of several shape parameters, shown graphically in Figure F.1:[95]

$$V = \frac{\sqrt{3}}{4} \left[\left(\mu a^3 - \left(a^3 - \alpha a^3 \right) \tan \theta \right) + \alpha^2 \mu a^3 \right] \tag{F.8}$$

From Kadavanich,[89] $\theta = 37°$ and

$$\mu = 0.98 + 0.0063d \tag{F.9}$$

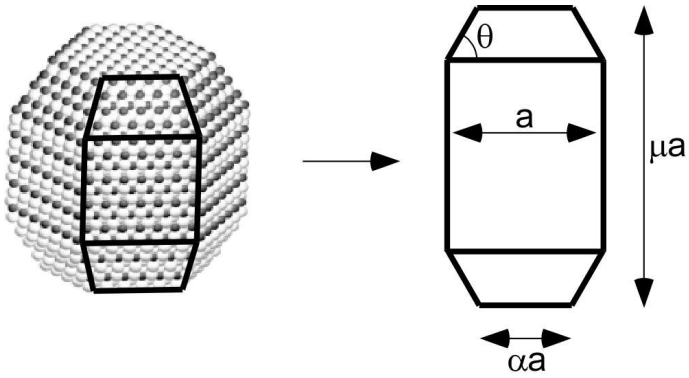

Figure F.1: Parameters for the calculation of nanocrystal volume. From Taylor *et al.*[95]

where d is the average nanocrystal diameter (in Å). Since the average nanocrystal diameter is the average of the long and short axes,

$$a = \frac{2d}{1+\mu} \tag{F.10}$$

Finally, α was measured for each batch of nanocrystals and ranged from 0.5 to 0.72. These parameters were substituted into Equation F.8 to obtain the volume of each nanocrystal. This volume was divided by the average volume occupied by an atom in bulk CdSe (11.2 Å^3) to obtain the total number of atoms per nanocrystal, n_{Cd+Se}. With this value and the ratio of cadmium to selenium, the number of cadmium atoms was calculated by

$$n_{Cd} = \frac{N_{Cd}}{N_{Se}} \frac{n_{Cd+Se}}{1+\frac{N_{Cd}}{N_{Se}}} \tag{F.11}$$

and the number of selenium atoms was calculated analogously. The molecular weight was then

$$w_{CdSe} = n_{Cd}\,(112.41\ \text{g·mol}^{-1}) + n_{Se}\,(78.96\ \text{g·mol}^{-1}) \tag{F.12}$$

The dependence of molecular weight on diameter was fit to a power dependence, and was determined to be

$$w_{CdSe}(d) = 3.8d^{2.9} \tag{F.13}$$

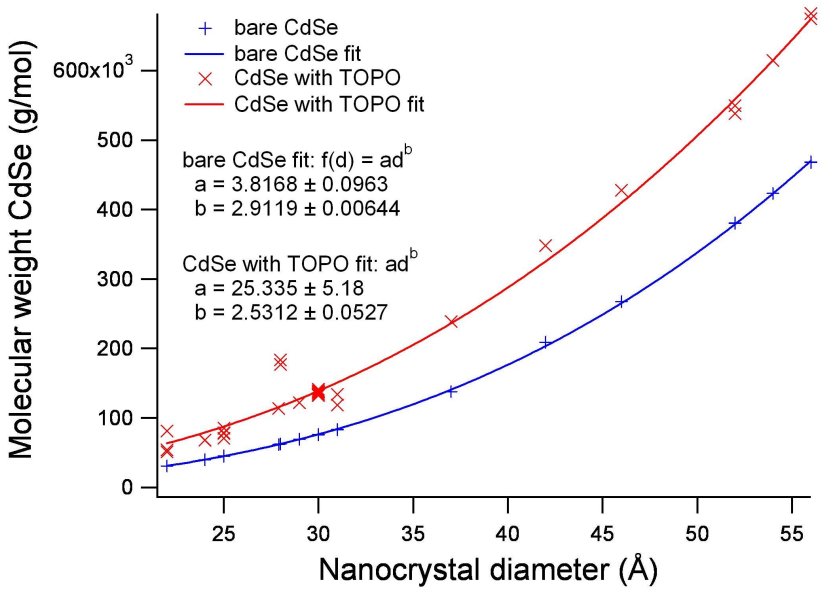

Figure F.2: Molecular weight of CdSe nanocrystals with (red) and without (blue) TOPO ligands.

In addition, because RBS data was not available for Folden's samples, Taylor's RBS data was used to estimate the weight of CdSe in Folden's samples. The ratio of the areal densities of phosphorus and cadmium was multiplied by the number of cadmium atoms per nanocrystal to find the number of TOPO ligands per nanocrystal. This number was multiplied by the molecular weight of TOPO, then added to the molecular weight of the nanocrystals to find the molecular weight of CdSe with a surface layer of TOPO. This molecular weight was fit to a power dependence to obtain the relationship

$$w_{CdSe+TOPO}(d) = 25d^{2.5} \tag{F.14}$$

The molecular weights with and without TOPO are shown graphically in Figure F.2. The molecular weights of the CdSe with TOPO show much more scatter than those without TOPO. It is extremely difficult to obtain the same proportion of CdSe to TOPO from batch to batch; excess TOPO is the typical cause, but sometimes too much TOPO is removed by the cleaning process, as well. This graph emphasizes the need to use RBS to analyze ligand surface coverage in every case in which surface

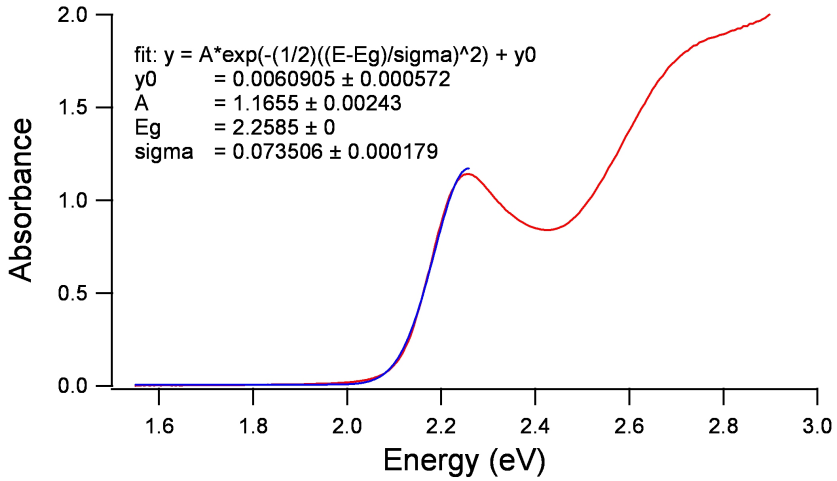

Figure F.3: Gaussian fit (blue) to absorption spectrum (red) of 33 Å CdSe nanocrystals. Because the high-energy side of the band edge absorption feature is obscured by additional electronic transitions, only the low-energy side was fit, with the band gap, E_g, fixed manually. The fit was then integrated over all energies ($E : -\infty \rightarrow \infty$) to obtain the integrated absorbance - in this case, 1.14.

coverage is important. Regardless, since no RBS data was available for Folden's samples, Equations F.13 and F.14 were used to calculate the molecular weights of CdSe with and without TOPO, so that the true weight of CdSe in Folden's samples was estimated

$$W_{CdSe} = \frac{w_{CdSe}}{w_{CdSe+TOPO}} W \tag{F.15}$$

Once the weight and molecular weight of CdSe in each sample had been determined, then the concentration of nanocrystals in the absorption experiment was simply

$$c = W_{CdSe} \times \frac{1}{w_{CdSe}} \times \frac{1}{5 \text{ mL}} \tag{F.16}$$

Next, the optical density of the band gap transition was determined from the absorption spectrum for each sample. Primarily because of the size dispersity of each sample, the transition appears over a range of wavelengths in the absorption spectrum. Therefore, the spectra were fit to Equation F.4 as in Figure F.3, and the fit was integrated over all energies to find the integrated absorbance. Since the path length of light in the experiment was 1 cm, a plot of the integrated absorbance versus

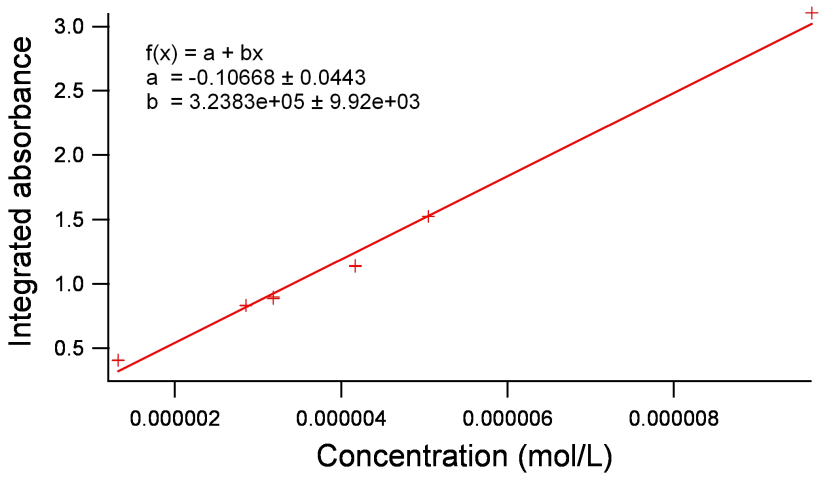

Figure F.4: Integrated absorbance versus nanocrystal concentration for 33 Å CdSe nanocrystals. The slope of this graph is the molar absorptivity for this sample of nanocrystals.

nanocrystal concentration for a given batch of nanocrystals yielded a slope equal to the integrated molar absorptivity (e.g., Figure F.4).

Figure F.5 shows the dependence of molar absorptivity on size for fourteen samples of CdSe nanocrystals ranging in diameter from 27 Å to 72 Å. The molar absorptivities, ranging in value from 2×10^5 L/mol-cm to 1.5×10^6 L/mol-cm, increase with increasing diameter. Although more data at greater diameters would yield a more definitive dependence, the data in Figure F.5 were empirically fit to obtain the relationship

$$\epsilon = 253d^{2.00} \tag{F.17}$$

For comparison, Yu *et al.* determined an empirical dependence of[40]

$$\epsilon = 1.6E_g d^3 \tag{F.18}$$

where E_g is the optical band gap. Clearly there is some discrepancy between Yu's results and these, although the absorptivities determined by both methods are on the same order. Partly, this may be accounted for by the fact that both experiments relied on sizing curves to obtain the diameters of the nanocrystals; these curves were

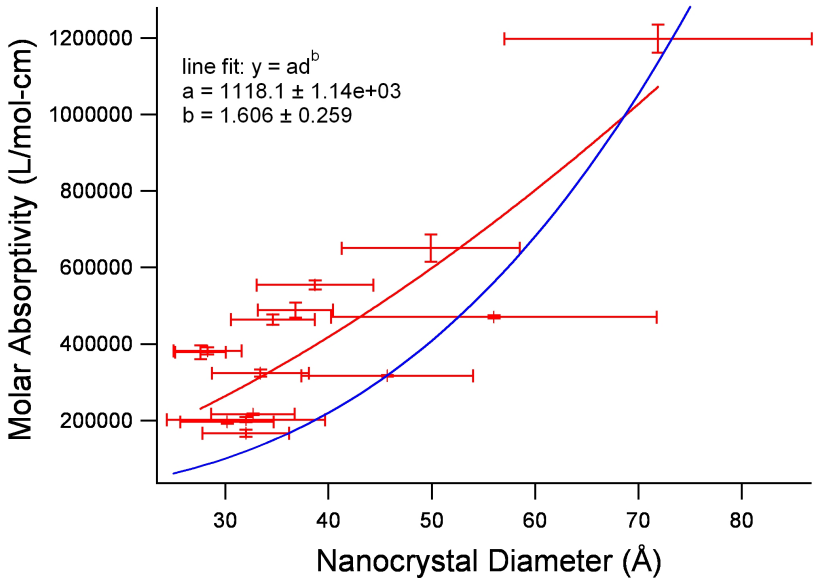

Figure F.5: Molar absorptivity of CdSe nanocrystals at the band edge (red). For comparison, the fit obtained by Yu *et al.*[40] (Equation F.18) is also provided (blue). E_g in this fit was calculated according to Equation 2.1.

not identical, introducing a systematic error into the reported diameters. In addition, Yu's concentrations were determined by performing atomic absorption spectroscopy to determine the amount of cadmium in solution. As previously mentioned, this method does not account for the fact that many nanocrystal samples have nonstoichiometric Cd:Se ratios, which could introduce error into the concentration of nanocrystals.

That the molar absorptivity of CdSe nanocrystals is size-dependent in contradiction to theory requires some explanation. We believe that there are two likely causes. First, we note that the $1/R^3$ dependence of the oscillator strength only applies to the strong confinement regime. While all of the nanocrystals studied here are in this regime, the larger a nanocrystal is, the less it behaves as though it is in the strong confinement regime. In Figure F.5, nanocrystals less than 40 Å in diameter show relatively constant molar absorptivities; as the diameter increases, the absorptivity increases more and more rapidly. This is likely a major cause of the deviation from theory. Secondly, and less obviously, the Bohr exciton radius is a function of

the dielectric constant:[321]

$$a_B = \frac{\varepsilon_{sc}\hbar}{\mu^* e^2} \tag{F.19}$$

Where $\varepsilon_s c$ is the semiconductor dielectric constant and μ^* is the reduced mass of the exciton. The dielectric constant, in turn, is size-dependent, increasing with increasing diameter.[39] The result is that as the nanocrystal diameter decreases, so does the Bohr exciton radius. The reduced mass also likely varies with size, further altering a_B. From Equation F.3, the oscillator strength varies as the cube of the Bohr exciton radius, thus introducing a size-dependence into the molar absorptivity. Undoubtedly, there are additional explanations for the size-dependence (e.g., a slight contraction of the lattice with decreasing diameter,[37] leading to a change in the electronic structure); however, we believe that the explanations offered here can explain the majority of the observed size-dependence.

APPENDIX G

SECOND-HARMONIC GENERATION AT Si(111)/CdSe NANOCRYSTAL INTERFACES

One of the questions which arose while attempting to model the behavior of the proposed photovoltaic (Appendix D) was how the energy bands of the CdSe nanocrystals aligned with those of the adjacent materials, TiO_2 and ITO. To first approximation, one could assume vacuum level alignment, i.e., that the energy difference between the conduction band minima equals the energy difference between the electron affinities (Sections C.3.3 and C.3.4). Yet while electron affinities and ionization potentials have been calculated for few sizes of CdSe nanocrystals,[39] these values have never been determined experimentally.

Second-harmonic generation (SHG) and, more specifically, time-dependent electric field-induced second-harmonic (TD-EFISH) generation are contactless, non-destructive techniques for studying surface and interface dynamics of semiconductor nanostructures. Recently, TD-EFISH was used to find the energy band offsets of SiO_2 with respect to Si,[322] in agreement with previous experiment. In addition, TD-EFISH yields information about trap densities and lifetimes, charge injection and transport, and other interface effects. This makes the technique one of the most sensitive and versatile techniques available for characterization of the charge dynamics at interfaces and surfaces. Initially it was thought that by determining the band offsets of CdSe nanocrystals with respect to crystalline Si, whose band energies are well known, we could determine the size-dependent CBM and VBM of these nanocrystals. Later, it was realized that interfacial dipole layers would likely make this determination impossible from the band offsets, yet the band offset measurements remained interesting as a first look at the way nanocrystals behave at interfaces. This appendix presents the theory, experimental protocol, and results obtained from the SHG experiments.

G.1 Theory

G.1.1 Phenomenological description of second-harmonic generation

SHG is a nonlinear optical phenomenon in which a material interacts with light at frequency ω to produce light at frequency 2ω. To understand what causes SHG, we first review Pankove's semi-classical description of the phenomenon based on the polarization of a semiconductor by an electric field.[323] An electric field acts to align the electron-nuclear dipole at each atom in the semiconductor - the atoms are polarized. The degree to which the electric field polarizes an atom is dictated by the material's electric field susceptibility, χ. At lower electric fields, the response is linear, so that the polarization is proportional to the driving electrical field. However, as the applied electric field approaches that created by Coulomb attraction between electron and nucleus (about 10^7 V·cm^{-1}), the polarization begins to saturate (becomes nonlinear); the electrical susceptibility of a semiconductor and therefore its index of refraction are no longer constant. Because of the nonlinear index of refraction in these conditions, when an intense sinusoidal electromagnetic wave, as from a laser, interacts with the material, the shape of the wave is distorted. The maximum amplitude of the electric field in the wave is damped, while lower amplitudes remain unchanged. Such a distorted wave contains harmonics of the fundamental frequency, and is described mathematically as the sum of harmonic sine waves:

$$f(t) = a_1 \sin(\omega t) + a_2 \sin(2\omega t) + a_3 \sin(3\omega t) + \ldots \tag{G.1}$$

where a_i is the amplitude of the i^{th} term. Since the second term of this equation has a frequency of 2ω, and so represents second-harmonic light; similarly, 3ω gives third-harmonic light, and so on.

The wave distortion can be symmetric or asymmetric, depending on whether or not the material is polarized without the presence of the electromagnetic field. In a centrosymmetric material, the individual electric fields from each atom cancel each other out. If no external electric field is applied to the system, then the only electric

field polarizing the atoms is the oscillating optical field. Therefore, the positive and negative amplitudinal maxima of the field are equally damped. Mathematically, equal damping of both the positive and negative fields occurs when only odd harmonics are present ($a_2 = a_4 = \ldots = 0$ in Equation G.1). Thus, second-harmonic generation does not occur. On the other hand, in a noncentrosymmetric material, the individual electric fields from each atom do not cancel each other out, resulting in an intrinsic electric field that polarizes the atoms. In this case, the polarization from the sinusoidal optical waves saturates at a lower field when the electric vector is lined up with the natural polarization than when it opposes the natural polarization. When this occurs, both even and odd harmonics are present. It is noted that in centrosymmetric materials, symmetry is broken at a surface or at an interface, or if an electric field (other than the optical field) is present, so second-harmonic generation occurs under these circumstances as well.

This semi-classical description of second-harmonic generation is entirely analogous to acoustic harmonic generation. In the case of optical harmonic generation, the potential energy function for the average displacement, x, of an electron with respect to the nucleus of an atom is that of a harmonic oscillator:[324]

$$U(x) = \frac{1}{2} m_e \omega_0 x^2 \tag{G.2}$$

where m_e is the electron effective mass and ω_0 is the characteristic frequency of the electron in its potential well. In any real system, however, nearby atoms perturb the parabolic shape of the potential well, and the electron acts as an anharmonic oscillator. In a centrosymmetric system, the perturbation is symmetric about $x = 0$, while for a noncentrosymmetric system the perturbation is asymmetric. The perturbation leads to modified potential energies:

$$U(x) = \sum_{n=1}^{\infty} \frac{1}{2n} m_e c_n x^{2n} \approx \frac{1}{2} m_e \omega_0 x^2 + \frac{1}{4} m_e c_2 x^4 \tag{G.3}$$

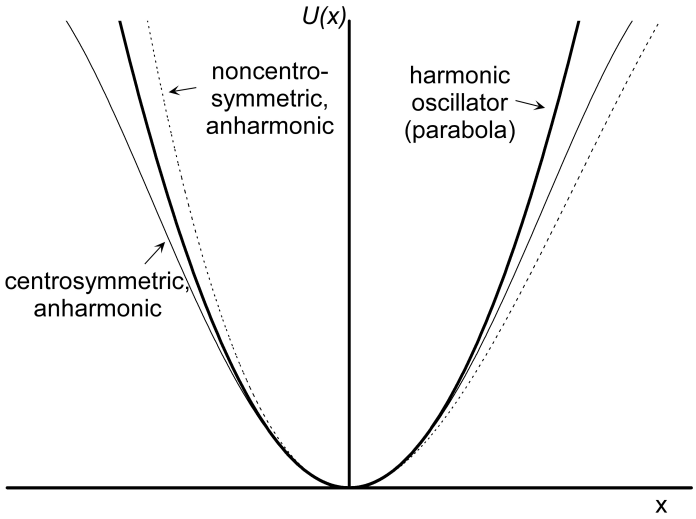

Figure G.1: Potential energy wells for the average displacement of an electron as an harmonic oscillator and as an anharmonic oscillator in centrosymmetric and noncentrosymmetric media.

for centrosymmetric media and

$$U(x) = \sum_{n=1}^{\infty} \frac{1}{n+1} m_e c_n x^{n+1} \approx \frac{1}{2} m_e \omega_0 x^2 + \frac{1}{3} m_e c_2 x^3 \tag{G.4}$$

for noncentrosymmetric media, where c_n is constant ($c_1 = \omega_0$). The potential energy wells for the two types of media are shown graphically in Figure G.1.

Likewise, in acoustical harmonic generation, an ideal string whose ends are both held immobile has a vibrational energy equal to that of a harmonic oscillator (in this case x is the perpendicular displacement of the string). In reality, anharmonicities perturb the ideal behavior of any string, in the same manner as Equations G.3 and G.4. If a string on a violin or a guitar is plucked lightly, a mellow tone sounds. If the same string is plucked harder, that is, if more tension is put on the string initially, the tone is louder and harsher. The tone is harsher because, as more force is applied to the string, the anharmonicities in the string become more prominent; more harmonics are produced, and those harmonics are louder compared to the fundamental tone. It is also possible to hear these harmonics by pressing one key on a piano so that it

does not play and, while holding that key down, playing the key one octave higher. Even after the octave note has been released, one can hear its tone faintly sounding. Because the octave note has twice the frequency of the first, the anharmonicity in the strings of the lower key allows those strings to resonate at the higher frequency.

G.1.2 General theory of SHG

The intensity of SHG is strongly dependent on the polarization of the medium by electric or magnetic fields. In general, electric field-induced polarization is expressed:

$$P = \sum_i \left[\chi^{(1)} : E_i\right] + \sum_{i,j} \left[\chi^{(2)} : E_i E_j\right] + \sum_{i,j,k} \left[\chi^{(3)} : E_i E_j E_k\right] + \cdots \tag{G.5}$$

where $\chi^{(n)}$ is the n^{th} order susceptibility, E_i is the i^{th} electric field present, and $i \neq j \neq k$. In the case of SHG, exactly two electric fields must be from incident photons:

$$P(2\omega) = \chi^{(2)}(2\omega;\omega,\omega) : E(\omega)E(\omega) + \sum_i \left[\chi^{(3)}(2\omega;\omega,\omega,0) : E(\omega)E(\omega)E_i\right] + \cdots \tag{G.6}$$

Because higher-order susceptibilities are much smaller than lower-order susceptibilities, Equation G.6 is typically truncated to include only the first two terms. The intensity of SHG is simply the square of the polarization, leading to the basic equation for SHG:

$$I^{(2\omega)} = \left|\chi^{(2)} + \chi^{(3)} E_{DC}(t)\right|^2 \left[I^{(\omega)}\right]^2 \tag{G.7}$$

Here we assume that the only electric field present other than photons is a simple direct-current field, E_{DC}.

Equation G.7 applies to one material. In the system under study, there are three crystalline materials which contribute to SHG: the bulk Si, the Si at the interface, and the CdSe nanocrystals. These materials contribute differently to SHG because of differences in symmetry and nonlinear susceptibilities. Since bulk Si is centrosymmetric, its $\chi^{(2)}$ is negligible (see Boyd[324] for a mathematical derivation of

this), leading to the more correct form of the equation:

$$I^{(2\omega)} = \left[|\chi^{(3),bulk}E_{DC}(t)|^2 + |\chi^{(2),surf} + \chi^{(3),surf}E_{DC}(t)|^2 + \right.$$
$$\left. + |\chi^{(2),CdSe} + \chi^{(3),CdSe}E_{DC}(t)|^2\right]\left[I^{(\omega)}\right]^2 \quad \text{(G.8)}$$

Equation G.8 demonstrates one reason why SHG is so useful as an interface probe. Because the response from the bulk is confined to the interaction between $\chi^{(3),bulk}$ and E_{DC}, and because E_{DC} is located primarily near the interface, the bulk response does not overwhelm the interface response, as normally occurs in optical or electrical measurements. It is noted that, although this equation is more precise than Equation G.7, distinguishing between the different $\chi^{(2)}$ and $\chi^{(3)}$ components is beyond the scope of this work; therefore, the general equation used in studying the system is Equation G.7.

G.1.3 General theory of time-dependent electric field-induced second-harmonic generation

Time-dependent electric field-induced second-harmonic (TD-EFISH) generation comes about as a direct result of the electric field component, $E_{DC}(t)$, of Equation G.7. Provided the electric field influencing the material generating the SH light is time-dependent, so is the intensity of the SH light. In general, there are three possible sources for electric fields in the crystal. An electric field may be intrinsic to the system under study. This is particularly true at the interface between two different materials, such as at a semiconductor heterojunction, in which the different band energies of the two materials create a depletion region at the interface, which has an intrinsic electric field (see Section C.1.1 for a more detailed discussion of this).[171] An electric field is also intrinsic to materials with nonzero dipole moments, such as CdSe nanocrystals, which have one face composed of only positively charged Cd atoms and an opposing face composed of only negatively charged Se atoms.[115,325] Intrinsic electric fields are by definition time-independent. Alternately, an electric field may be induced in the

material by placing the material in an externally generated electric field, or by putting a bias across the material using external leads. This type of electric field is externally controlled by the investigator, and is particularly useful in probing the behavior of semiconductor device structures (e.g., see Jun *et al.*[326,327]). Finally, an electric field can be induced by generating free charges in the material and somehow causing those charges to move directionally, electrons in one direction and holes in another. This type of electric field is particularly useful in investigating the native charge dynamics at a single interface or surface, since there is no external influence on the system other than that stimulating the charge generation.

The system under study in this work is the interface between Si(111) and CdSe nanocrystals. This is a semiconductor heterojunction; therefore, there is an intrinsic electric field at the interface of the two materials. However, the electric field under investigation is induced by using laser light to generate free electrons and holes within the Si. If any of the photogenerated charge carriers have sufficient energy, there is a finite probability that they will cross over the interface and into the nanocrystal layer. Usually, one type of charge carrier preferentially crosses the interface, due to the alignment of the energy bands of the two materials, and other effects. This creates a time-dependent electric field, as more and more charges of one type cross the interface, while charges of the other type remain in the Si. However, opposite charges attract, so Coulombic attraction is a force promoting the recombination of the two charge carriers by pulling the charges on CdSe back over the interface into the Si. The electric field can only grow if there is some reason that the charges are held apart from each other. Such reasons include band bending at the interface and trap states, both of which can lower the energy of the charge carriers to the extent that recombination is either not possible or very unlikely (Figure G.2). Without loss of generality, we shall refer to all forces preventing charge recombination as 'trap states' for the remainder of this dissertation, unless specifically stated otherwise; mathematically, all the forces

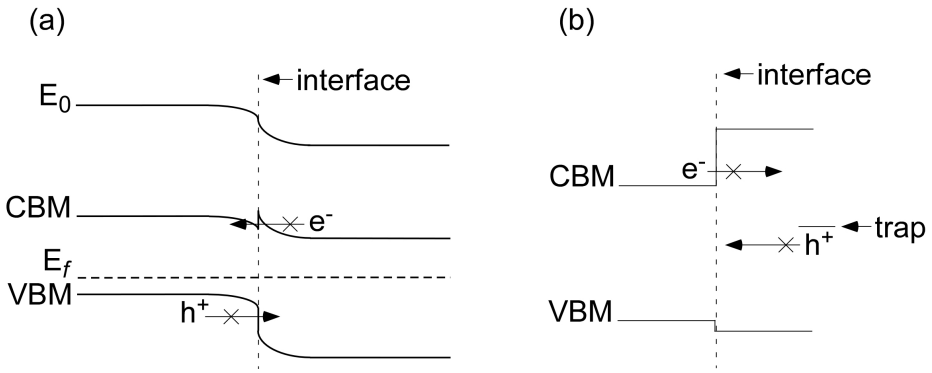

Figure G.2: Phenomena promoting prolonged charge separation across an interface. Band bending at the interface (a) and trap states (b) can make it energetically unfavorable for electrons and holes to recombine. CBM = conduction band minimum, VBM = valence band maximum, E_0 = vacuum level energy, E_f = Fermi level energy.

are equivalent. It is noted that trap states generally trap electrons or holes, but not both.

With this information, we can now develop an expression for the change in the electric field at the interface as a function of time. In any system, there are a limited number of trap states. Assume for the moment that there is only one type of trap state (e.g., the midgap states present on the surfaces of CdSe nanocrystals). We define $n(t)$ as the number of empty trap states (available to trap charges) and $n_0 - n(t)$ as the number of filled trap states (trapped charges) at time t, where n_0 is the initial number of available trap states. Given a constant source of illumination, and hence a constant number of charge carriers available for trapping, each of the empty traps have a probability, p_t, of trapping a charge carrier. Meanwhile, filled traps have a probability, p_d of detrapping, letting the charge carrier pass back across the interface and recombine with its opposite. Therefore the change in the number of empty traps is

$$\frac{dn(t)}{dt} = -p_t n(t) + p_d \left[n_0 - n(t)\right] \tag{G.9}$$

Integrating, the number of empty traps at time t is

$$n(t) = \frac{n_0}{p_t + p_d}\left[p_d + p_t e^{-(p_t+p_d)t}\right] \tag{G.10}$$

From a kinetics standpoint, $p_t + p_d$ is the net rate at which trap states fill. We define the lifetime, τ, of the trap states to be the inverse of the net rate, so that the number of empty traps at time t is now

$$n(t) = n_0\tau\left[p_d + p_t e^{-\frac{t}{\tau}}\right], \qquad \left(\tau \equiv \frac{1}{p_t + p_d}\right) \tag{G.11}$$

There is a simple relationship between the number of empty trap states and the electric field at the interface. Although the charge carriers may be found at different depths on both sides of the interface, the system behaves like a capacitor - the electric field is proportional to the net charge on each side of the interface. The net charge on each side at time t is simply the total number of available trap states at $t = 0$ less the number of empty trap states at time t, leading to a trap-induced time-dependent electric field of

$$E_{DC,trap}(t) = cn_0\left[1 - p_d\tau - p_t\tau e^{-\frac{t}{\tau}}\right] \tag{G.12}$$

where c is a constant. In addition to the time-dependent electric field, there is also the intrinsic electric field, $E_{DC}(0)$, and the total electric field is simply the sum of these. Substituting the two components of the interfacial electric field back into Equation G.7, we find that TD-EFISH generation displays the following time dependence:

$$I^{(2\omega)} = |\chi^{(2)} + \chi^{(3)}\left[E_{DC}(0) + cn_0\left[1 - p_d\tau - p_t\tau e^{-\frac{t}{\tau}}\right]\right]|^2\left[I^{(\omega)}\right]^2 \tag{G.13}$$

However, in the scope of this work we do not distinguish between the $\chi^{(2)}$ contribution to SHG and the time-independent $\chi^{(3)}$ contributions to SHG. Therefore, the basic working equation for the time dependence of second harmonic generation in a system with one type of trap is

$$I^{(2\omega)} = |a_0 + a_1 e^{-\frac{t}{\tau}}|^2\left[I^{(\omega)}\right]^2 \tag{G.14}$$

where a_0 and a_1 are constants corresponding to the appropriate values in Equation G.13.

It is possible, however, that there is more than one trap state present in a system. As an example of this, if the two systems in Figure G.2 were combined, band bending would create electron 'traps' in the right-hand semiconductor, while the midgap trap states would create hole traps. The question becomes, what happens to the time dependence when more than one trap state is present?

In the case where all traps are for one type of charge carrier, the answer is trivial. Since $E_{DC,trap}(t)$ is proportional to the net charge on one side of the interface, it would be proportional to the sum of all filled trap states of any type. Each type of trap would fill with the decaying exponential of Equation G.12, with its own characteristic trapping lifetime and amplitude, so the electric field due to trapping would be a sum of the individual exponentials. In the case where some traps are electron traps, and other traps are hole traps, the situation is a little more complicated because of the possibility of charge recombination.

If an electron and a hole are on the same side of the interface, then they contribute nothing to the interfacial electric field. This is implied by the proportionality of the electric field and the net charge on each side of the interface. Likewise, if the electron and hole recombine, they still contribute nothing to the interfacial electric field. Yet charge recombination represents a (potential) source of detrapping - a filled trap state is emptied when the trapped charge recombines with its opposite. Therefore, the presence of traps for both electrons and holes may change the probability of detrapping for each type of trap from what it would be if only one type of trap were available. However, the electric field is still the sum of exponential decays. Thus, the general equation for TD-EFISH generation is

$$I^{(2\omega)} = |a_0 + \sum_i a_i e^{-\frac{t}{\tau_i}}|^2 \left[I^{(\omega)}\right]^2 \tag{G.15}$$

where i is the i^{th} type of trap. It is noted that the amplitude a_i has opposite signs

for electrons and holes. Equation G.15 is the equation used to fit all TD-EFISH data in this dissertation.

G.1.4 Band offset measurements using TD-EFISH

Because TD-EFISH yields information on charge transfer across an interface, it can be used to elucidate the energy band offset between two semiconductors. The theory of using TD-EFISH to measure band offsets was pioneered by Marka *et al.* in the Tolk research group at Vanderbilt University, and was presented in their original paper on using the technique to measure the band offsets of the Si/SiO_2 interface.[322] A slightly different form of the theory is presented here.

The key to band offset measurements by TD-EFISH generation lies in the probability of a charge crossing the interface and being trapped by the opposite semiconductor (p_t of Equation G.10). To illustrate the effect, we use the hypothetical system of two semiconductors, A and B, shown in Figure G.3. In this system TD-EFISH is generated by exciting electrons from the valence band of semiconductor A to the conduction band of semiconductor B, where some trapping mechanism prevents these charges from moving back across the interface and recombining with holes. Although the following discussion is directed towards electrons, the same principles apply to holes as well.

In order for electrons to be trapped in the conduction band of semiconductor B, they must first attain sufficient energy to cross the interface. This is achieved through a combination of single- and multi-photon processes; regardless of the path of charge excitation, however, the probability of an electron absorbing k photons is proportional to k^{th} power of the intensity of the exciting beam, I:[328,329]

$$W(abs = k) \propto I^k \tag{G.16}$$

It is intuitively apparent that Equation G.16 holds true for the simultaneous absorption of k photons; it is less obvious, but nonetheless true, when the excitation pathway

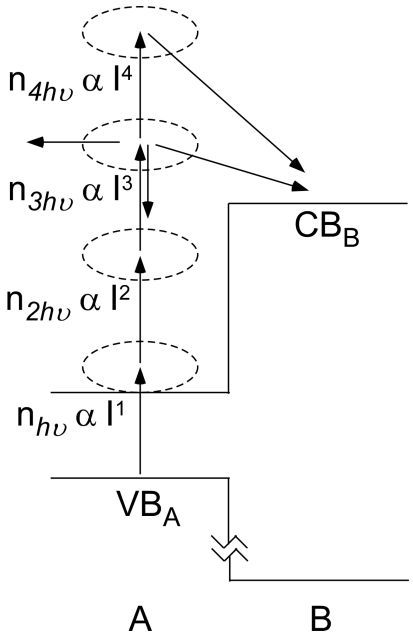

Figure G.3: Charge transfer across a semiconductor-semiconductor interface. In this case electrons are excited through a multi-photon process from the valence band of semiconductor A to the conduction band of semiconductor B.

involves multiple absorption events separated by some time interval. Likewise, the probability that a charge absorbs at least an energy of E_{min} through absorption of photons with frequency ω is:

$$W_\omega \left(E > E_{min}\right) = \sum_{k\hbar\omega > E_{min}} K_k I^k \tag{G.17}$$

where K_k is a proportionality constant dictating the probability of absorbing k photons. Of course, the dominant contribution in Equation (G.17) is made by the smallest value of k to satisfy the condition $k\hbar\omega > E_{min}$, as the absorption of k photons is much more likely than the absorption of $k+1$ photons.

When trying to determine band offsets, we are specifically interested in the energy required to transfer an electron from the valence band maximum (VBM) of the smaller bandgap material to the conduction band minimum (CBM) of the larger bandgap material (or a hole from the CBM of the smaller bandgap material to the VBM of the larger bandgap material). For the system described in Figure

G.3, we want to find the energy $E_{bo} = E_{VBM_A} - E_{CBM_B}$. When a laser beam with frequency ω and intensity I is shone on the system, a series of populations at energies $E_{VBM_A} + k\hbar\omega$ is created in the conduction band of semiconductor A. In order to promote an electron from VBM_A to CBM_B, the condition $k\hbar\omega > E_{bo}$ must be satisfied; here $k \geq 3$. Assuming that electrons initially in the conduction band of A (e.g., intrinsic free electrons) do not contribute significantly to charge transfer across the interface, then, the probability of any electron having sufficient energy to cross the A-B interface is:

$$W_{excite}\left(\omega; I;\, E > E_{bo}\right) = \sum_{k\hbar\omega > E_{bo}} K_k I^k \approx K_{\lceil \frac{E_{bo}}{\hbar\omega} \rceil} I^{\lceil \frac{E_{bo}}{\hbar\omega} \rceil} \tag{G.18}$$

As illustrated in Figure G.3, the electrons so excited do not maintain either their spatial position or energy. Once in the conduction band, they may travel throughout semiconductor A. In addition, as with any excited system, the electrons immediately begin to relax back to lower energy states, through thermalization processes, photoemission, and other relaxation pathways. Only a portion of those electrons excited higher than CBM_B actually cross the A-B interface. The probability of charge transfer across the interface is related to an electron's initial distance from the interface z, initial energy E, and the z-component of any electric field $\mathcal{E}(z)$ present:

$$W_{interface} : f\left(z;\, E;\, \mathcal{E}(z)\right) = \begin{cases} 0 & E < E_{bo} \\ 0 \leq W_{interface} \leq 1 & E \geq E_{bo} \end{cases} \tag{G.19}$$

In order for charge transfer to be detected by SHG, the charges must remain across the interface on a time scale compatible with the time scale of the experiment, seconds in the case of the work presented here. Since remaining in the higher energy states of the conduction band of material B as well as remaining separated from the photogenerated holes in material A is thermodynamically unfavorable for electrons that have crossed the A-B interface, electrons must be trapped in material B on the time scale of the experiment. The probability of an electron in the conduction band

of material B being trapped in a particular trap state is proportional to the number of trap states which are empty:

$$W_{trap} \propto n(t) \tag{G.20}$$

Combining Equations G.17 - G.20, the overall probability of an electron being injected from material A into material B is dependent on the probability of charge excitation to sufficient energy, the probability of transfer across the A-B interface, and the probability of trapping in material B:

$$p_t = W_{excite} W_{interface} W_{trap} \tag{G.21}$$

Notably, of the three processes involved in charge injection and trapping, only charge excitation is dependent on the intensity and wavelength of incoming light. Therefore the total probability of injection has the same dependence as the probability of charge excitation:

$$p_t \propto I^{\lceil \frac{E_{bo}}{\hbar\omega} \rceil} \tag{G.22}$$

This relationship is the key to band offset measurements using TD-EFISH.

We must now relate Equation G.22 to the parameters that we can actually measure in this experiment. Since the hypothetical A-B interface has only one type of trap, the measured TD-EFISH generation would obey Equation G.14. Ignoring any changes in the amplitudes a_0 and a_1, the probability of charge injection, p_t is related to the lifetime of the trap by $\tau = \frac{1}{p_t + p_d}$ (Equation G.11), where p_d is the probability of detrapping. However, since τ is not a simple function of p_t, we must find a simple way to relate τ and p_t, such that p_d becomes unimportant. To do this, we make the observation that, if TD-EFISH is to be used successfully to determine band offsets, there must actually be significant time dependence - the number of empty traps must decrease reasonably quickly. By Equation G.9, this implies that $p_t \gg p_d$, leading to the approximation

$$\tau \approx \frac{1}{p_t} \tag{G.23}$$

so that

$$I^{(2\omega)} \approx \left|a_0 + a_1 e^{-p_t t}\right|^2 \left[I^{(\omega)}\right]^2 \tag{G.24}$$

Since p_t depends geometrically on the intensity of the laser, and since p_d is independent of the intensity of the laser, this approximation is particularly correct at high beam intensities.

To determine band offsets, TD-EFISH must be measured over a wide range of wavelengths, and at each wavelength, TD-EFISH must be measured for a variety of powers of the beam exciting charges in the system (the 'pump' beam). In a one-color experiment, this beam is the same as the beam used to generate SH light (the 'probe' beam); in a two-color experiment, the two phenomena are separated (Section G.1.5). Using Equation G.24, p_t is determined for all wavelengths and powers. Then the dependence of p_t on pump power is determined at each wavelength. By Equation G.22, a plot of the log of p_t as a function of the log of pump power yields a straight line with a slope of $\lceil \frac{E_{bo}}{\hbar\omega} \rceil = k(\omega)$, where $k(\omega)$ is the (integer) number of photons necessary for charge injection with a pump frequency of ω:

$$\ln(p_t) = k(\omega)\ln(I_{pump}) + c \tag{G.25}$$

Finally, the number of photons required for charge injection is plotted as a function of pump photon energy. Plotted over a sufficient range of energies, $k(\omega)$ manifests abrupt changes in value at energies corresponding to $\frac{E_{bo}}{n}$ ($n \in \mathbb{N}$). For example, Figure G.4 is a plot of $k(\omega)$ as a function of pump photon energy for a Si/SiO_2 interface.[322] Here $k(\omega)$ changes from three photons to two photons at a pump photon energy of 2.25 eV, and from two photons to one photon at 4.5 eV. The energy at which $k(\omega)$ changes from two photons to one is therefore the band offset energy of the Si/SiO_2 interface - the difference in energy between the VBM of Si and the CBM of SiO_2. This energy, 4.5 eV, is in agreement with previous experiment.[330–335] It is noted that it is not necessary to specifically find the $k : 2 \rightarrow 1$ transition - Marka notes that the

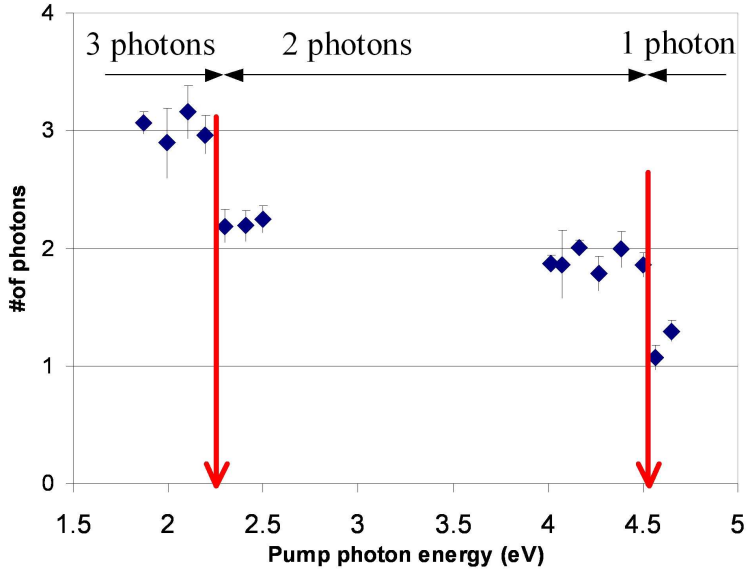

Figure G.4: Number of photons required for charge injection at a Si/SiO_2 interface. The number of photons required for injection from the valence band of Si into the conduction band of SiO_2 changes abruptly from three photons to two photons at a pump photon energy of 2.25 eV, and from two photons to one photon at 4.5 eV. Figure adapted from Marka *et al.*, *Physical Review B* **67** (4), 045302 (2003).[322]

$k : 3 \rightarrow 2$ transition also gives the correct band offset with no greater error than the $k : 2 \rightarrow 1$ transition.[322]

G.1.5 Power dependence of TD-EFISH

In order to determine band offsets using TD-EFISH, it is necessary to take measurements at a variety of beam powers and wavelengths. Yet, as we shall see in Section G.1.6, $\chi^{(2)}$ and $\chi^{(3)}$ both depend on wavelength, not only with respect to magnitude, but also with respect to phase, so that these two components can interfere differently depending on wavelength, producing different patterns and magnitudes of SHG. In an experiment in which wavelength is a variable, these changes potentially could have a significant effect on results. Thus, it is desirable to separate the phenomenon under study (charge injection) and the method of study (SHG). For this experiment, the key lies in using the power dependence of SHG to split charge injection and SHG into phenomena created by separate beams: a 'pump' beam that stimulates charge injection, and a 'probe' beam that produces SH light.

Looking at Equation G.15, it appears that the magnitude of TD-EFISH generation simply depends on the square of the power of the fundamental beam because of the term $\left[I^{(\omega)}\right]^2$. However, it was shown in Sections G.1.3 and G.1.4 that the electric field also depends on the fundamental. In fact, both the lifetimes, τ_i, and the amplitudes, a_i, depend on the power of the fundamental. These parameters vary with power because they all depend on p_t, the probability of charge injection, and p_t depends geometrically on beam intensity.

Because p_t depends geometrically on beam intensity, the rate of charge injection can be greatly increased or decreased by changing the power of the fundamental. For example, for the Si/SiO_2 interface at a wavelength of 800 nm, $p_t \propto I^3$, so halving the power decreases the rate of charge injection by a factor of eight. Meanwhile, the rate of detrapping, p_d, remains constant. Thus, if the power is sufficiently low, the

rates of charge injection and detrapping become equal, so that the interfacial electric field remains constant, and SHG is no longer time dependent. In the case of Si/SiO_2, a beam power of 100 mW at 800 nm and a beam spot of 30 μm is low enough that time dependence is suppressed.[322]

The elimination of time dependence on the basis of power allows us to separate the generation of charge injection into two separate beams. The probe beam is set at a wavelength and intensity that generates SH light, and therefore can be used to measure the interfacial electric field, but does not generate enough free charges to actually affect the field. The pump beam, meanwhile, can be set to any desired wavelength and power. While it is true that the pump beam also generates SH light, it turns out that the direction in which SH light travels is dependent on the angle at which the fundamental beam hits the surface of the sample (Section G.1.6). If the pump and probe beams impinge on the sample surface at different angles, then the SH light from each source reflects off at a different angle, allowing the easy selection of SHG only from the probe beam. Thus the pump beam is specifically dedicated to generating charges and changing the interfacial electric field, while the probe beam is specifically dedicated to monitoring the change in electric field.

It is noted that, although the two beams are referred to as 'pump' and 'probe', they are not pump and probe beams in the traditional sense. They can be used in the traditional sense, in that the time delay between the two beams hitting the sample can be changed by means of a delay stage in order to obtain information on the ultrafast charge dynamics within a system (e.g., see Glinka *et al.*[336,337]). However, in the experiments presented here, the timing of the two beams is not varied, because the events of interest occur on a much longer timescale (seconds to minutes) than the repetition rates of the two beams.

By separating the sources of charge injection across the interface and SHG into pump and probe beams, and by keeping the probe beam at a constant wavelength

and power, we can eliminate any potential skewing of results due to wavelength- or power-dependent peculiarities in SHG. In addition, using a two-beam experimental setup allows us to specifically examine the recovery behavior of the system when the pump beam is blocked.[322,338] When the pump beam is blocked, further charge injection is eliminated. Under these conditions, any time dependence to the SH signal must be due to charges detrapping and recombining with their opposites. This is a unique method of determining the rate of detrapping, p_d, and could be critical to the analysis of TD-EFISH. Since the measured lifetime, τ, of a trap state is a convolution of the rates of trapping and detrapping (Equation G.11), specific knowledge of the rate of detrapping allows us to calculate more accurately the true rate of trapping, rather than making the approximation of Equation G.23 that the trap lifetime is simply the inverse of the rate of trapping. This is particularly important when the rates of trapping and detrapping are on the same order.

While two-beam SHG eliminates the problem of wavelength- and power-dependent SHG, it is a more complicated experiment than single-beam SHG, which uses the same beam for both charge generation and SH measurement. In particular, there are two issues in the two-beam experiment which must be addressed before the experiment can be conducted successfully: beam overlap and probe beam intensity.

The generation of charges by a laser beam and the subsequent manipulation of the electric field is an extremely local effect. Testing has shown that the pump and probe beams must be perfectly overlapped; any change in the beam overlap has an enormous effect on the magnitude of SHG. To limit this effect, in the work presented here, the diameter of the probe beam is much smaller than that of the pump beam - approximately 30 μm and 100 μm, respectively. This gives a little leeway in the placement of the two beams, but even so, moving the probe beam by 5 - 10 μm within the area of the pump beam has still been observed to change the magnitude of SHG by 10% or more. For the sake of consistency in testing, the beams are first overlapped

visually with the aid of a magnifying camera, then overlapped by manipulating the placement of the probe beam to maximize SH signal and time dependence.

As mentioned earlier, the probe beam must have low enough power that it does not provoke significant charge injection into the system. However, aside from the dependence of SHG on the electric field, SHG still varies as square of the intensity of the probe beam. As the probe beam decreases in power, the magnitude of SHG also decreases, and so does the signal-to-noise ratio. Therefore, the probe beam ideally should have the maximum power that still reasonably suppresses probe-induced time dependence. If this power is too low to obtain good results, a second option is to use a probe power that induces a small amount of charge injection, then wait with just the probe beam on the sample until the SH signal levels off before introducing the pump beam. Otherwise, a single-beam experiment is indicated, with the risk that effects from SHG can skew the results.

G.1.6 Angular dependence of SHG

Thus far we have seen that the intensity of SHG depends on the second- and third-order nonlinear susceptibilities of the material producing the SH light, $\chi^{(2)}$ and $\chi^{(3)}$, the intensity of the electric field experienced by the material, $E_{DC}(t)$, and the intensity of the fundamental beam on the material, $I^{(\omega)}$. As it happens, the magnitude of SHG from any crystal also depends on the polarization, angle of incidence, and azimuthal (rotational) angle of the fundamental light on the crystal surface. Sipe *et al.* developed expressions for SHG in cubic centrosymmetric crystals that depend on these three parameters.[339] Because the experiments presented here were performed using a nonstandard angle of incidence (30° from normal to the CdSe/Si interface instead of the more typical 45°), and because the (111) surface of Si shows a strong dependence on the azimuthal angle of the fundamental light, we present here Sipe's theory for the behavior of (111) surfaces of cubic media.

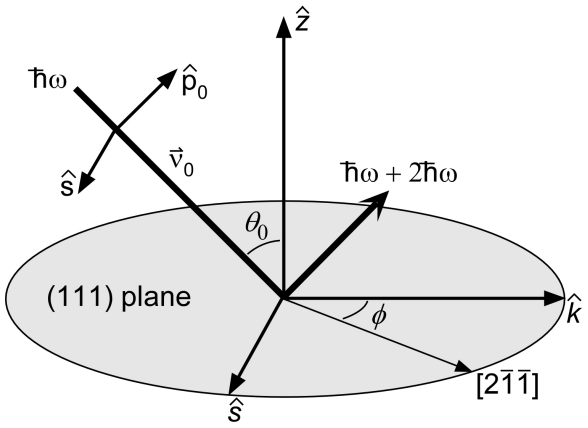

Figure G.5: Schematic of orientational parameters describing anisotropy of SHG.

Figure G.5 depicts a beam of light with frequency ω incident on a Si(111) surface. This fundamental light travels along a vector $\vec{\nu}_0$ and is incident on the surface at an angle θ_0 from the surface normal. A coordinate system is defined to allow a geometric analysis of the interactions between light and crystal. The coordinate system has three perpendicular axes: the z-axis, which is normal to the (111) surface; the s-axis, which is perpendicular to the direction of the incoming fundamental light and parallel to the (111) surface; and the k-axis, which is perpendicular to the z- and s-axes. The angle of incidence of the fundamental light with respect to the z-axis is θ_0, while the azimuthal angle, ϕ, is by convention the angle between the $[2\bar{1}\bar{1}]$ direction in the (111) plane and the k-axis.[340] Using this coordinate system, we define s-polarized light as light polarized in the direction of the s-axis and p-polarized light as light polarized perpendicular to $\vec{\nu}_0$ and $\widehat{s}$; mathematically, the direction of p-polarized light is given by

$$\widehat{p}_o = \cos(\theta_0)\widehat{k} + \sin(\theta_0)\widehat{z} \tag{G.26}$$

Figure G.6 shows the geometry of the system in the kz plane. In order to understand the behavior of SH light in this system, we must first characterize the behavior of the fundamental light. The energy field of the incident fundamental light

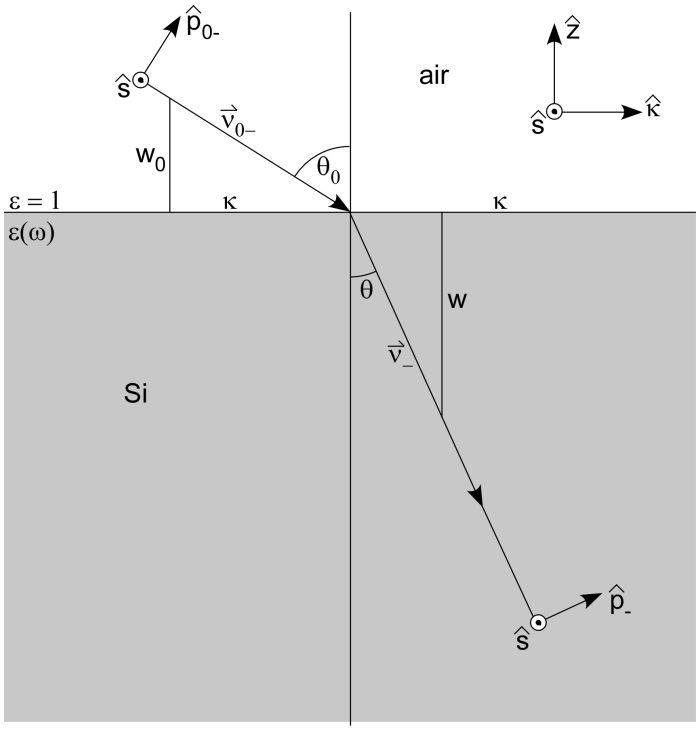

Figure G.6: Side view of SHG geometry.

can be expressed

$$E_0(r,t) = E_0 e^{i\nu_0 \cdot r - i\omega t} \tag{G.27}$$

where ν_0 is the periodicity of the light ($\nu_0 = \frac{1}{\lambda_0}$, where λ_0 is the wavelength of the fundamental). The light is a combination of s-polarized (E_{0s}) and p-polarized (E_{0p}) light:

$$E_0 = E_{0s}\hat{s} + E_{0p}\hat{p} \tag{G.28}$$

and is composed of a wave-vector component perpendicular to $\hat{z}$

$$\kappa = \hat{k}|\nu_0| \sin\theta_0 \tag{G.29}$$

and a component parallel to $\hat{z}$

$$w_0 = \hat{z}|\nu_0| \cos\theta_0 \tag{G.30}$$

A similar set of equations may be used to describe the fundamental light transmitted into the Si. Assuming a dielectric constant of 1 for the outer medium

and $\epsilon(\omega)$ for the Si, the wave vector of the fundamental in the Si is given by

$$\vec{\nu} = \kappa - w\widehat{z} \tag{G.31}$$

where

$$w = \sqrt{\widetilde{\omega}^2\epsilon(\omega) - \kappa^2} \tag{G.32}$$

and

$$\widetilde{\omega} = \frac{\omega}{c} \tag{G.33}$$

As indicated by Equations G.31 and G.32, the direction of s-polarization remains unchanged, but the direction of p-polarization is now

$$\widehat{p} = \frac{\kappa\widehat{z} + w\widehat{k}}{n\widetilde{\omega}} \tag{G.34}$$

where

$$n = \sqrt{\epsilon(\omega)} \tag{G.35}$$

is the complex refractive index of Si for frequency ω. As before, the electric field from the fundamental in Si is

$$E(r,t) = Ee^{i\nu\cdot r - i\omega t} \tag{G.36}$$

where E is again a combination of s- and p-polarized light:

$$E = E_s\widehat{s} + E_p\widehat{p} \tag{G.37}$$

The magnitude of E_s and E_p at the interface can be calculated from E_{0s} and E_{0p} using the Fresnel coefficients for transmission of s- and p-polarized light:

$$E_s = \frac{2w_0}{w_0 + w}E_{0s} \tag{G.38}$$

$$E_p = \frac{2nw_0}{w_0\epsilon(\omega) + w}E_{0p} \tag{G.39}$$

Assuming that the majority of SHG occurs at or very near the Si surface, light absorption by Si is negligible, and the electric field of Equation G.36 is quantitatively the field contributing to SHG.

We can develop an analogous set of expressions for SH light within and without Si. The most important of these are listed below, using capital letters to denote properties of the SH light:

$$\widetilde{\Omega} = 2\widetilde{\omega} \tag{G.40}$$

$$K = 2\kappa \tag{G.41}$$

$$N = \sqrt{\epsilon(2\omega)} \tag{G.42}$$

$$W_0 = \sqrt{\widetilde{\Omega}^2 - K^2} \tag{G.43}$$

$$W = \sqrt{\widetilde{\Omega}^2\epsilon(2\omega) - K^2} \tag{G.44}$$

$$\widehat{P}_0 = \frac{K\widehat{z} - W_0\widehat{k}}{\widetilde{\Omega}} \tag{G.45}$$

$$\widehat{P} = \frac{K\widehat{z} - W\widehat{k}}{N\widetilde{\Omega}} \tag{G.46}$$

Having established the base geometry of the system, we can now summarize the results of Sipe *et al.* for the (111) surface. The anisotropy is described according to the polarization of fundamental and second harmonic light. SH light can be either *s*- or *p*-polarized regardless of the polarization of the incoming fundamental light; thus there are four polarization combinations for SHG: *pp*, *sp*, *ps*, and *ss* (e.g., *sp* is *p*-polarized SH light generated from an *s*-polarized fundamental beam). The intensity of SHG as a function of the polarization of the fundamental light can be described as[339]

$$\frac{E_{pp}^{(2\omega)}}{\left[E_p^{(\omega)}\right]^2} = A_p\left[a_{pp} + c_{pp}\cos(3\phi)\right] \tag{G.47}$$

$$\frac{E_{sp}^{(2\omega)}}{\left[E_s^{(\omega)}\right]^2} = A_p\left[a_{sp} + c_{sp}\cos(3\phi)\right] \tag{G.48}$$

$$\frac{E_{ps}^{(2\omega)}}{\left[E_p^{(\omega)}\right]^2} = A_s b_{ps}\sin(3\phi) \tag{G.49}$$

$$\frac{E_{ss}^{(2\omega)}}{\left[E_s^{(\omega)}\right]^2} = A_s b_{ss}\sin(3\phi) \tag{G.50}$$

The coefficients a, b, and c are discussed in more detail below; the coefficients A_s and A_p are given by

$$A_s = \frac{4\pi\widetilde{\Omega}}{W_0 + W} \tag{G.51}$$

and

$$A_p = \frac{4\pi\widetilde{\Omega}N}{W_0\epsilon(2\omega) + W} \tag{G.52}$$

and are related to the transmission of light across the Si surface. Because the fundamental light used in the experiments presented here was p-polarized, we neglect Equations G.48 and G.50 for the remainder of the discussion, though we note that these equations are functionally identical to Equations G.47 and G.49.

As a consequence of Equations G.47 and G.49, SHG by Si(111) surfaces and interfaces with other materials is highly anisotropic with respect to the azimuthal angle, ϕ, of the fundamental with the Si surface (e.g., see Tom *et al.*[341]). Because the intensity of SHG is insensitive to whether the generated second harmonic field is positive or negative ($I^{(2\omega)} \propto |E^{(2\omega)}|^2$), Equation G.49 dictates a six-fold symmetry over the range $0 \leq \phi \leq 2\pi$. The peaks at $\phi = 0$, $\frac{2\pi}{3}$, and $\frac{4\pi}{3}$ stem from

$$E_{ps} = A_s b_{ps} \left[E_p^{(2\omega)}\right]^2 \tag{G.53}$$

while the peaks at $\phi = \frac{\pi}{6}$, $\frac{\pi}{2}$, and $\frac{5\pi}{6}$ stem from

$$E_{ps} = -A_s b_{ps} \left[E_p^{(2\omega)}\right]^2 \tag{G.54}$$

In contrast to *ps*-polarized SHG, *pp*-polarized SHG displays only three-fold symmetry, with alternating tall and short peaks; this is due to interference between the a_{pp} and c_{pp} terms. Combining Equations G.47 and G.49, the total SHG by any Si(111) interface should display three-fold symmetry (Figure G.7). We note that the contributions of *pp*- and *ps*-polarized SHG to the total SHG are purely additive; because s- and p-polarizations are by definition orthogonal, the fields generated by s- and p-polarized light are likewise orthogonal and cannot interfere. Additionally, we note

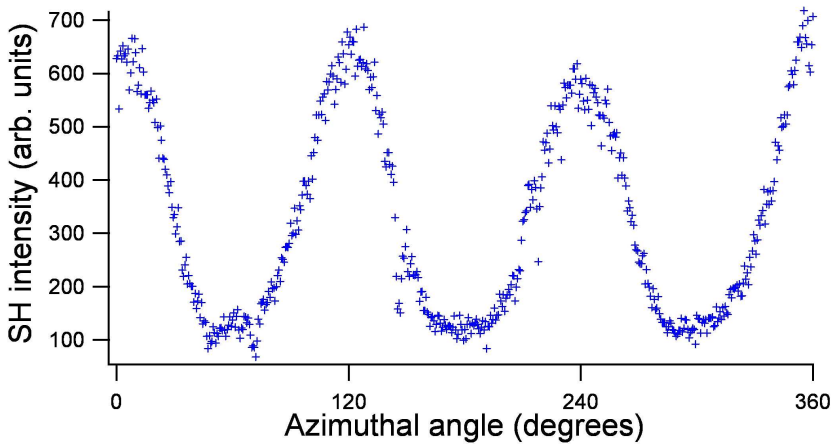

Figure G.7: SHG as a function of ϕ for a typical CdSe nanocrystal/Si(111) interface. The dependence of SH intensity on ϕ shows the three-fold symmetry indicative of Si(111) surfaces. As is typical with Si(111) interfaces, *pp*-SHG dominates, as evidenced by alternating very strong and very weak peaks. SH signal was generated using a 800 nm, *p*-polarized fundamental beam incident on the Si(111) at an angle of 30° to the surface normal.

that although the relative magnitudes of a_{pp}, b_{ps}, and c_{pp} depend on the angle of incidence, θ_0, as well as on the wavelength of the fundamental, the symmetry of the system is independent of θ_0, as indicated by Equations G.47 and G.49.

Having considered qualitatively the azimuthal dependence of SHG, we now look in greater detail at the three coefficients a_{pp}, b_{ps}, and c_{pp}. In terms of the physical properties and geometry of the system in Figures G.5 and G.6, the coefficients have the values[339]

$$\begin{aligned} a_{pp} &= i\widetilde{\Omega}\left[\zeta\Gamma\left(\frac{4}{3}F_s f_c - \frac{2}{3}f_s F_c f_c^2 - \frac{8}{3}F_s f_s^2 f_c + \frac{4}{3}f_s^3 F_c\right)_{(a)} + F_s\gamma_{(i)} + \right. \\ &\quad \left. + \left(F_s f_c^2\epsilon(2\omega)\partial_{31} + F_s f_s^2\epsilon(2\omega)\partial_{33} - 2f_s f_c F_c\partial_{15}\right)_{(s)}\right] \end{aligned} \tag{G.55}$$

$$b_{ps} = i\widetilde{\Omega}\left[\zeta\frac{\sqrt{8}}{3}\Gamma\left(f_c^2 - 2f_s^2 f_c\right)_{(a)} + \left(f_c^2\partial_{11}\right)_{(s)}\right] \tag{G.56}$$

$$c_{pp} = -i\widetilde{\Omega}\left[\zeta\frac{\sqrt{8}}{3}\Gamma\left(F_c f_c^3 - 2f_s^2 F_c f_c + F_s f_s f_c^2\right)_{(a)} + \left(F_c f_c^2\partial_{11}\right)_{(s)}\right] \tag{G.57}$$

where the subscripts i, a, and s denote bulk isotropic (i), bulk anisotropic (a), and surface (s) contributions; Γ, f_s, f_c, F_s, and F_c are the relationships

$$\Gamma = \frac{n\widetilde{\Omega}}{8(2w+W)} \tag{G.58}$$

$$f_s = \frac{\kappa}{n\widetilde{\omega}} \tag{G.59}$$

$$f_c = \frac{w}{n\widetilde{\omega}} \tag{G.60}$$

$$F_s = \frac{K}{N\widetilde{\Omega}} \tag{G.61}$$

$$F_c = \frac{W}{N\widetilde{\Omega}} \tag{G.62}$$

γ is a bulk, isotropic phenomenological constant; and $\partial_{15} = \chi_{\parallel\perp\parallel}$, $\partial_{31} = \chi_{\perp\parallel\parallel}$, $\partial_{33} = \chi_{\perp\perp\perp}$, and $\partial_{11} = \chi_{\xi\xi\xi}$ are elements of the surface nonlinear susceptibility tensor:[339]

$$\begin{bmatrix} P_x^s \\ P_y^s \\ P_z^s \end{bmatrix} = \begin{bmatrix} \partial_{11} & -\partial_{11} & 0 & 0 & \partial_{15} & 0 \\ 0 & 0 & 0 & \partial_{15} & 0 & -\partial_{11} \\ \partial_{31} & \partial_{31} & \partial_{33} & 0 & 0 & 0 \end{bmatrix} \begin{bmatrix} E_x(\omega)^2 \\ E_y(\omega)^2 \\ E_z(\omega)^2 \\ 2E_y(\omega)E_z(\omega) \\ 2E_x(\omega)E_z(\omega) \\ 2E_x(\omega)E_y(\omega) \end{bmatrix} \tag{G.63}$$

where P_i^s is the surface polarization in the i-direction (here the y-axis is defined perpendicularly to the plane of symmetry normal to the surface), and with $\parallel$ and $\perp$ referring to the directions parallel and perpendicular to the (111) surface, respectively, and ξ referring to the axis defined by the projection of the [100] crystal axis on the (111) surface.[341]

Equations G.55 - G.57 are obviously fairly complex, but some generalizations can be made about their form and function. Most importantly, three elements contribute to SHG in Si: a bulk, isotropic contribution; a bulk, anisotropic contribution; and a surface contribution. Notably, both bulk, anisotropic and surface elements are present in a_{pp}, b_{ps}, and c_{pp} (the bulk, isotropic effect contributes only to a_{pp}); thus, the separation of SHG into bulk and surface contributions is not as simple for Si(111)

as for Si(100), in which the surface contribution to SHG is contained wholly within the a_{pp} coefficient.[339]

The relationship between the intensity of SHG and the angle of incidence, θ, of the fundamental light on the sample (Figures G.5 and G.6), adds an additional layer of complexity. As implied by Equations G.55 - G.62, changing the angle of incidence can also change the dependence of SHG on the azimuthal angle. Because of this, the relationship between SHG and θ is best discussed with the aid of 3-dimensional graphs showing the relationship between SHG, θ, and ϕ. As examples, three such systems are presented in Section G.3.1: a sample of 72 Å CdSe nanocrystals on Si(111) from the research presented in this document, and H-passivated Si(111) and a Si(111)/SiO_2 interface from the work of Mitchell *et al.*[342] The discussion of this topic is therefore left to that section.

G.1.7 Angular dependence of EFISH and phase effects

Like SHG, EFISH shows a strong angular dependence in Si(111). The equations for the dependence of $\chi^{(3)}$ and thus EFISH intensity on azimuthal angle follow the same general forms given in Equations G.47 - G.50 for SHG; however, the coefficients have different values, reflecting the different symmetry elements of the second- and third-order nonlinear susceptibilities. Interestingly, past experiments on Si(111) have shown that SHG is insensitive to electric fields at 60° away from the maximum SH signal in azimuthal scans, and that SHG is at its most sensitive to electric fields at the maximum SH signal in azimuthal scans - $\chi^{(2)}$ and $\chi^{(3)}$ are in phase.[343,344] Thus, we could predict that, at azimuthal angles where SH is maximized in azimuthal scans, SHG would be most dependent on time, while at azimuthal angles where SH is minimized in azimuthal scans, SHG would be completely independent of time. If $\chi^{(2)}$ and $\chi^{(3)}$ are not in phase, however, TD-EFISH scans taken at different azimuthal angles would show a gradual change in the shape of the time dependence.

G.2 Experimental protocol

G.2.1 Sample preparation

The nanocrystals used in the SHG experiments were CdSe nanocrystals prepared according to the TOPO/UI method (Section 2.1.1) and capped with pyridine. Nanocrystals were capped with pyridine using a ligand-exchange technique developed by Katari *et al.*[114] Nanocrystals were dissolved in the minimum amount of pyridine required for complete nanocrystal dissolution (usually about 1 mL) and heated at 60 °C overnight. The pyridine-capped nanocrystals were then isolated by precipitation once with hexanes. To effect complete ligand exchange (in this case defined as approximately 30% TOPO coverage of the surface),[114] the pyridine exchange process was performed three times on each batch of nanocrystals, washing once with hexanes after each exchange.

Because pyridine is such a labile ligand, pyridine-capped nanocrystals are not very stable. When dried, the pyridine readily leaves the surface of the nanocrystals, which agglomerate into insoluble clumps. Even when left in solution, pyridine-capped nanocrystals slowly aggregate, though this process is much slower in pyridine than in other solvents. To prevent nanocrystal aggregation, the pyridine-capped nanocrystals were never dried before use. When long-term storage was required, the nanocrystals were left in solution in the pyridine of the third ligand exchange and were not precipitated until just prior to use. Provided they were not heated, the nanocrystals remained relatively aggregate-free for weeks.

Usually a pyridine exchange was performed when ligand-free nanocrystals were desired, as in the SHG experiments. Occasionally, however, pyridine exchange was performed as an intermediate step to coating the nanocrystals with a third ligand.[18,345] Pyridine was used as an intermediate because it both readily displaces TOPO and is readily displaced by other ligands. In such a case, the pyridine-coated nanocrystals were resuspended either in the ligand of choice or in a noncoordinating

solvent (e.g., chloroform) which supported both nanocrystals and the desired ligand. The solution was then stirred overnight at 60 °C and isolated using an appropriate solvent to crash the nanocrystals out of solution. Ligand exchange was confirmed by RBS or by the behavior of the nanocrystals (e.g., biological activity or solubility in specific solvents).

For SHG experiments, pyridine-capped nanocrystals were spin-cast onto Si(111) substrates. Si(111) wafers were obtained from University Wafer. Wafers were *p*-type, doped with boron to a resistivity of 10 - 20 Ω-cm (corresponding to a boron concentration of $10^{14} - 10^{15}$ cm^{-3}),[171] had a thickness of $605 - 645$ μm, and were polished on one side. The thickness of native oxide on the polished surface was too small to be detected by RBS.

To prepare the Si wafers for spin-casting, the as-received wafers were first cut into chips small enough to fit inside the sample holder for the SHG experiments, a circle 0.75 inches in diameter. The chips were then cleaned according to Kern.[346] To remove surface organics, the chips were swirled in a steaming mixture of 5:1:1 by volume deionized (DI) water (18 Ω-cm resistivity) : concentrated H_2SO_4 : concentrated H_2O_2 for 5 minutes. Next, to remove metals, the chips were swirled in a steaming mixture of 5:1:1 DI water : concentrated H_2SO_4 : concentrated HNO_3 for 5 minutes. Finally, to remove the native oxide layer, the chips were dipped in a steaming mixture of 20:1 DI water : concentrated HF. Immediately following cleaning, the Si wafer chips were moved into the dri-box in order to prevent reoxidation. As RBS scans of chips left exposed to the atmosphere of the dri-box over extended periods (i.e., weeks) revealed the deposition of phosphorus- and titanium-containing compounds (as in Figure 2.11), the chips were cleaned and moved to the dri-box on the same day as spin-casting.

Spin-casting was performed in the nitrogen atmosphere dri-box using a Chemat Technology KW-4A spin-coater. Pyridine-coated nanocrystals were suspended in

chloroform at a concentration yielding an absorbance of 0.5 - 2.0 at the band edge. A Pasteur pipet was used to completely cover the polished side of a cleaned Si wafer chip with the nanocrystal solution. The chip was immediately spun at 1300 rpm until all chloroform spun off or evaporated. This was observable as a slight change in the coloration or reflectivity of the sample, and usually occurred in less than 5 seconds. This process was repeated multiple times to build up the thickness of the nanocrystal layer on the Si surface; typically 4 - 20 castings were made per Si chip. After spin-casting, the CdSe/Si samples were placed in the dri-box antechamber and kept under vacuum at 10^{-3} Torr for at least 8 hours to remove all pyridine from the nanocrystal surface, as well as any remaining chloroform. The finished samples were then stored in sealed, plastic wafer containers inside the dri-box until use.

The fact that both bare CdSe nanocrystals and Si-H surfaces are known to form oxide layers in the presence of ambient atmosphere posed an experimental dilemma. Prior to the CdSe experiments, SHG experiments were performed in air, yet oxidation of the CdSe and Si surfaces would cause changes in the optoelectronic properties of the samples. To prevent oxidation, the CdSe/Si samples were encased in an air-tight sample chamber (Figure G.8). The chamber was composed of a Edmond Industrial Optics Tech Spec^{TM} UV fused silica 25 mm diameter $\times$ 2 mm thick window; a 0.8 inch diameter o-ring; and a 1 inch diameter, 3 mm thick circular aluminum heat sink machined on site. These were sealed together by a Thorlabs nested 1" lens holder with inner ring. Samples were affixed to the Al heat sink using electrically conductive double-sided carbon scanning tunneling microscopy (STM) tape. The sample chambers with the CdSe/Si samples were assembled in the nitrogen atmosphere of the dri-box; all experiments were carried out using this atmosphere within the sample chamber.

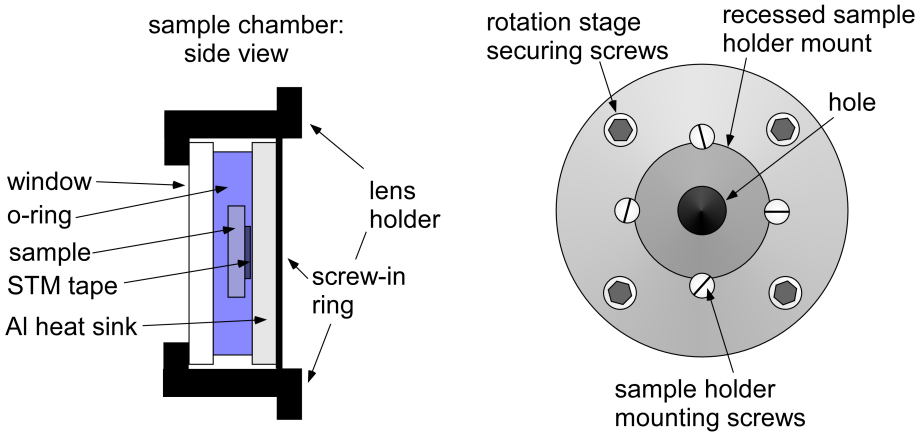

Figure G.8: Oxygen- and water-free sample holder (left) and mount (right) for SHG experiments. The sample holder was designed by Tadd Kippeny of the Rosenthal research group. The mount was affixed to the rotation stage used in SHG experiments via four hex screws. The nitrogen-atmosphere SHG sample holder fit exactly within a recessed inner disk. The sample holder was secured in place by four screws overlapping the lip of the sample holder.

G.2.2 Experimental setup

Two laser systems were used in the SHG experiments. The two setups, one at the W. M. Keck Free-Electron Laser (FEL) Center and one owned by the Center for Molecular and Atomic Studies at Surfaces (CMASS), were virtually identical in function, so only the CMASS setup, which was used for the majority of experiments, is detailed here.

The laser system (Figure G.9) was a series of seven commercial units. A Coherent Verdi diode-pumped Nd:YVO_4 laser (**1**), producing a continuous-wave (CW) beam of 532 nm light with an average power of 5 W, acted as a seed for a Coherent Mira 900D Ti:Sapphire laser (**2**). The Mira 900D is a modelocking laser tunable over the range 700 - 980 nm, with dual femtosecond and picosecond modes. For this experiment the laser was set to 800 nm in the femtosecond mode. The emitted light was polarized horizontally to the laser table (*p*-polarization) and had a pulse length of 100 fs, a repetition rate of 76 MHz, and an optimized power of 750 mW. The beam then

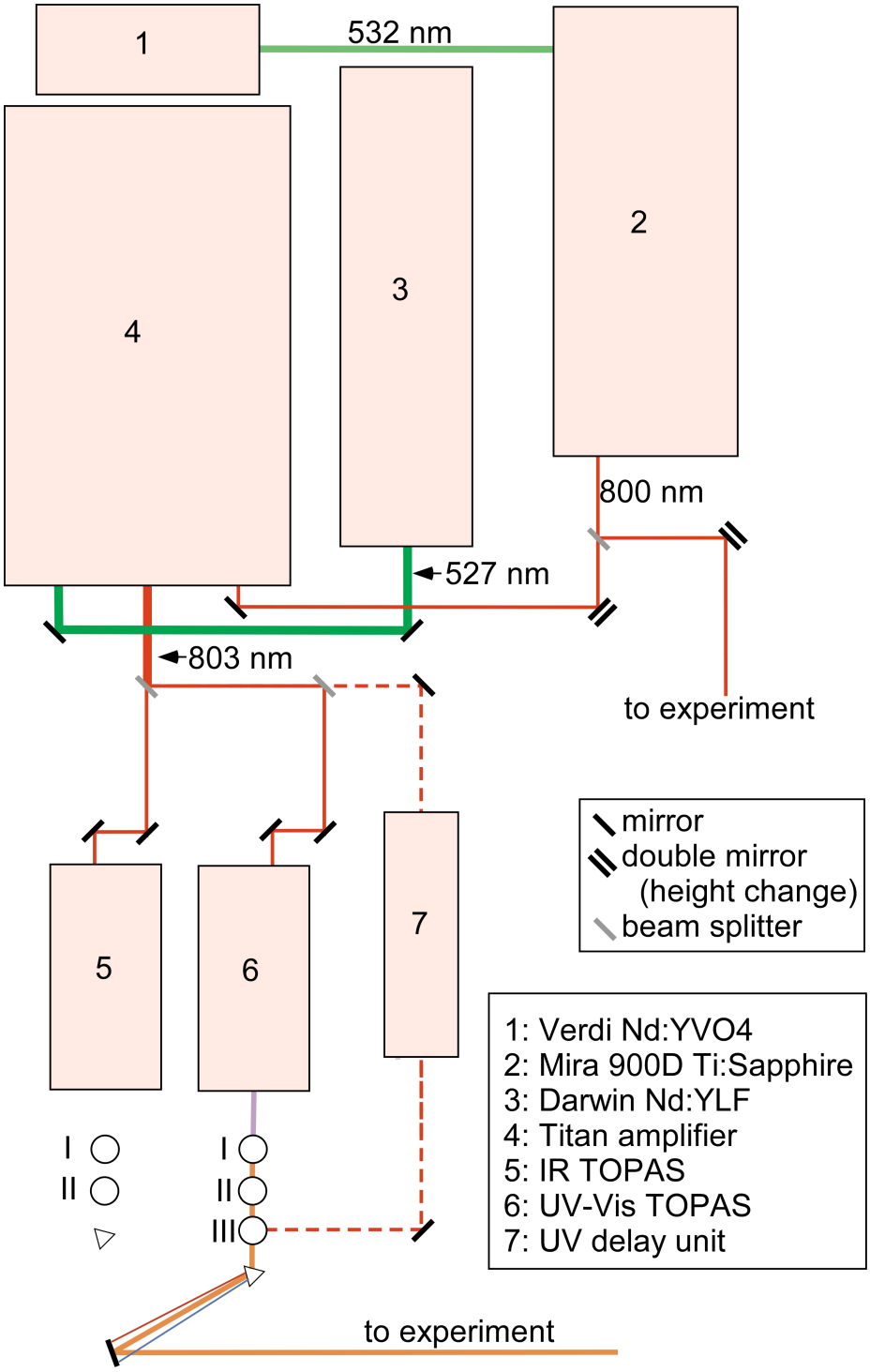

Figure G.9: Laser system used in SHG experiments.

passed through a beam splitter; half the beam was diverted to the CdSe/Si sample to act as the probe beam, and half the beam was used as seed light for the Quantronix Titan Ti:Sapphire amplifier (**4**). The Titan is a combination regenerative amplifier / multipass amplifier system. Its power source was a Quantronix Falcon diode-pumped Nd:YLF laser (**3**), which produced a beam of 527 nm light with a 1 kHz repetition rate and operated at an average power of ∼19 W. The Titan dumped power from the 527 nm beam from the Falcon into the 800 nm beam from the Mira. The result was a beam of 803 nm light with a pulse length of 150 fs, a repetition rate of 1 MHz, and an average power of ∼3.2 W. This light was split with a 50:50 beam splitter, then passed through two Quantronix TOPASes (**5** and **6**), or Traveling-wave Optical Parametric Amplifiers of Superfluorescence, a wavelength-tunable system. The TOPAS produced a beam composed of two wavelengths, the signal and the idler, with wavelength ranges of 1200 - 1600 nm and 1600 - 2300 nm, respectively. The signal and idler then passed through two mixing crystals, mixer I (**MI**) and mixer II (**MII**). One of the TOPASes contained optics suitable for the generation of IR light, while the other generated visible light. Optionally, the light running to the visible-light TOPAS could be split, with some of the light passing through a delay unit (**7**), then recombining with light from the visible-light TOPAS to generate UV light in mixer III (**MIII**). The TOPASes, the delay unit, and all mixing crystals were computer-controlled via the WinTOPAS interface program. Together, the TOPASes and the delay unit generated light of wavelengths ranging from 200 nm - 20 μm (0.06 - 6.0 eV), with a 1 kHz repetition rate and a pulse width of 150 fs. Once the desired wavelength was achieved, the beam passed through a prism, which separated light of the desired wavelength from residual 803 nm light, residual signal and idler, and any other unnecessary wavelengths generated by the TOPASes and mixers (e.g., second-harmonic of the signal, if second-harmonic of the idler was desired). Finally, the correct wavelength was reflected off a mirror towards the experiment.

Procedures for the operation and tuning of the laser system can be found in Appendix H.

The SHG experimental setup is shown in Figure G.10. The probe beam from the Mira passed through a red filter to eliminate bleed-through of 532 nm light from the Verdi (this light affected the detected SHG through unknown means; often it appeared as a long timescale sine wave in the time dependence). It was reflected onto the sample at a 30° angle to the sample normal, focused to a ∼50 μm diameter spot size on the sample using a 15 cm focal lens mounted on a z-translation micrometer stage. The second harmonic light generated by the sample traveled along the same path as the reflection of the fundamental light from the sample through a 30 cm focusing lens (mounted on a x-, y-, and z-translation micrometer stage) into a prism, which separated the fundamental and the SH. It is noted that reflections from the glass window in front of the sample were often present, visible as a series of blue (400 nm) spots when viewed on a business card after the prism. The correct spot, which contained no glass reflections, was visually brighter than the other spots. The prism was angled so that the true SH beam passed through the center of an iris, which was closed enough to block fundamental light and SH light that had been reflected by the glass window. After the iris, the SH beam reflected off a mirror and passed through a blue filter to eliminate any possible remaining fundamental light before hitting a photon counter.

The correct wavelength of light for the pump beam was selected by the prism following the TOPAS (Figure G.9). This light was partially focused on the sample using a 30 cm focal lens mounted on a z-translation micrometer stage, at an angle of 10° to the surface normal. The spot size was much larger for the pump than the probe (∼150 μm dimeter), so that the observed SHG did not suffer from pump edge effects. In addition, the power from the pump beam was so great that samples were often damaged (i.e., by the pump beam drilling a hole in the sample), even with strong

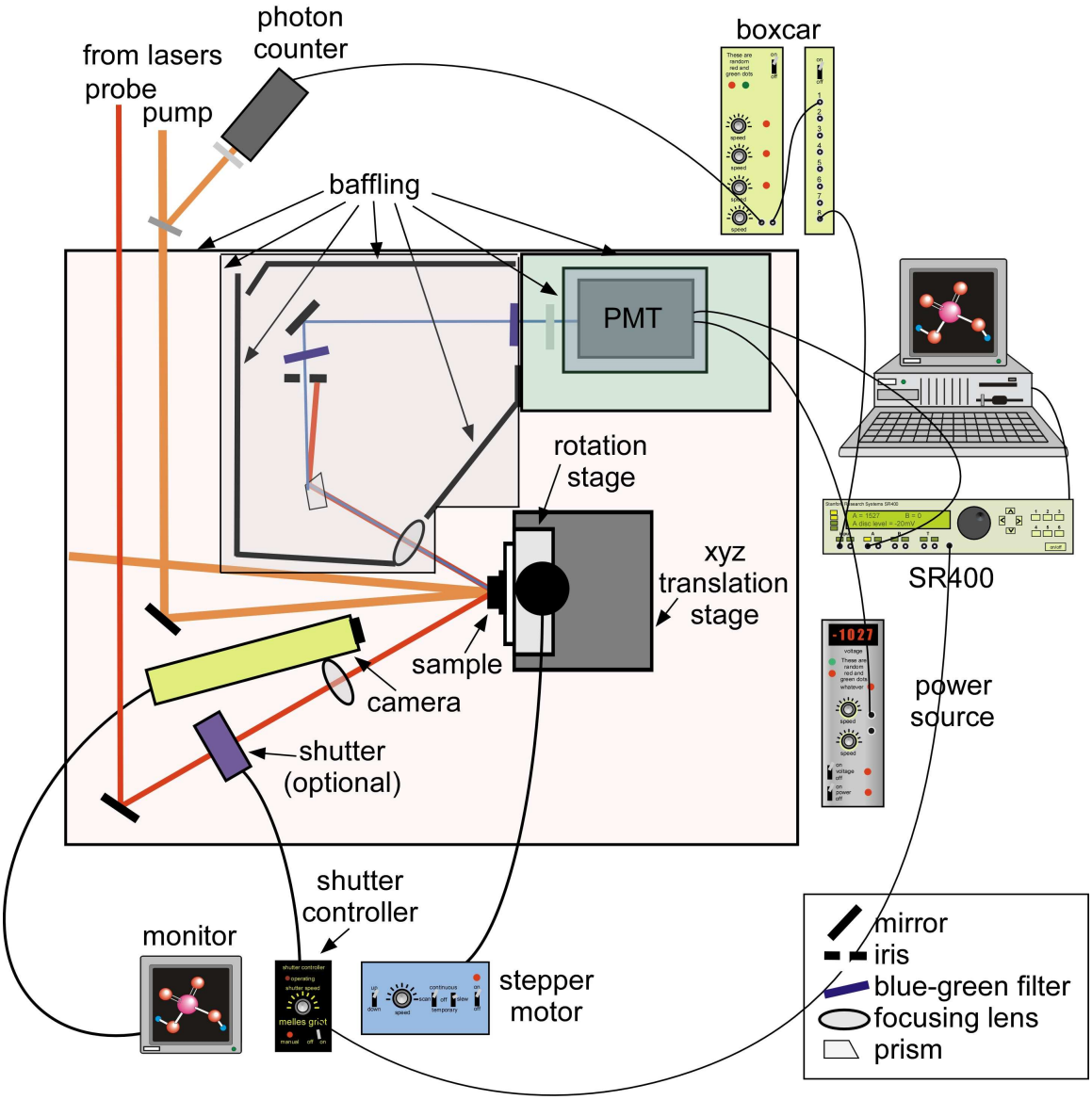

Figure G.10: Second-harmonic generation experimental setup. Not drawn to scale.

neutral density filters in place. By not focusing the beam fully, damage of this sort was lessened. A neutral density filter wheel was permanently fixed in place along the pump beam path, and the reflection off this was diverted to a second photon counter, so that the power of the pump beam could be monitored during the experiment.

The photon counters monitoring pump intensity and the PMT monitoring SHG were attached to a Stanford Research Systems SR400 two channel gated photon counter interfaced via a GPIB card to a MacIntosh computer running Lab Director, a LabView™ program written by Mike Albert of the Tolk group at Vanderbilt University. Lab Director was a versatile data collection program that could be configured to monitor a variety of different sources, with up to three different data sources active simultaneously (i.e., the program accepted input from up to three separate pieces of equipment simultaneously).

G.2.3 Alignment of the experiment

Because the experimental setup was different for the nanocrystal samples than for other samples (because of the air-free sample holder), and because the laser system had multiple users and experiments other than SHG, the experiment needed to be completely realigned at the beginning of each data collection period. The experiment was aligned in two parts: alignment of the probe beam, and overlap of the pump and probe beams.

To align the probe beam, four mirrors and two irises were placed between the beam splitter splitting the output from the Mira and the lens focusing the beam on the sample. The first two mirrors raised the beam height to that of the TOPAS units' output. The third directed the beam towards the experiment, and the fourth directed the beam through the lens to the sample. The irises were placed between the third and fourth mirrors. First, the second and third mirrors were used to walk the beam through the center of both irises. The irises were placed such that a beam passing

through the center of both irises hit roughly the center of the fourth mirror. Once the beam was centered in the irises, the fourth mirror was used to pass the beam roughly through the center of the focusing lens. An alignment sample consisting of Si/SiO_2 was placed in the air-free sample holder and affixed to the mount. Then, the x-, y-, and z-translation micrometer stages on the sample mount were adjusted to move the sample so that beam from the lens hit roughly the center of the sample. Because the sample holder moved the sample forward more than 1 cm from its placement without the holder, it was also necessary to remove the entire holder, mount, and base from the table and move it back when another user had been working with the experiment. When the sample mount was removed, the focus of the lens was found by moving a business card along the beam path; at the focus, the card began to smoke. This point was marked visually, and the sample mount was reinstalled so that the front surface of the sample was approximately at the focal point.

Next, a neutral density filter wheel was placed in the probe beam path before the beam splitter leading to the PMT, and a second-harmonic generating BBO crystal was placed in the probe beam path close to the sample. This crystal transmitted SH light along the beam path of the fundamental, which then reflected off the sample along the path that SH light generated by the sample would follow. SHG by the BBO crystal was orders of magnitude more powerful than SHG by the sample, allowing the user to perform a visual alignment of the experiment. Using the SH light, the prism after the sample was adjusted to send the SH light through the center of the iris leading to the PMT's steering mirror. The steering mirror was then used to direct the beam through the center of the next iris to the PMT. The PMT was approximately aligned so that a beam passing through the center of the iris entered the center of the photon counter aperture; however, the alignment was not precise due to difficulties in fixing the PMT in place. Therefore, the iris before the PMT was then opened, and a business card was used to verify that the SH light actually passed into the PMT.

Once a visual alignment had been made, the laboratory lights were turned off, and the PMT was turned on. Using the 'Adjust' mode in Lab Director, the prism and steering mirror were further adjusted to maximize signal from the PMT, using the neutral density filters as necessary to avoid saturating the PMT. Once signal had been maximized, the BBO crystal and filter wheel were removed.

The next step in the alignment procedure was to repeat the alignment using the previously mounted Si/SiO_2 alignment sample. The alignment sample was simply any available piece of $Si(100)/SiO_2$ wafer. $Si(100)/SiO_2$ was used for three reasons. First, as mentioned in Section G.1.6, SHG from Si(111) shows a strong dependence upon the azimuthal angle of the sample, with SHG at certain angles being nearly nonexistent. In contrast, SHG from Si(100) is less dependent on angle, and is always substantial.[339] Second, commercially available Si/SiO_2 samples have very uniform characteristics, including film thickness. During alignment of the SHG experiment, the beam sometimes moved on the surface of the sample. If the surface film was uneven or had other non-uniform properties, a decrease or increase in measured SHG might be due to changes in the film properties rather than due to changes in the alignment. The CdSe films used in this experiment were sometimes visibly nonuniform; therefore, they were unsuitable for alignment purposes. Finally, numerous previous experiments on $Si(100)/SiO_2$ had established that SHG from this type of sample monotonically increased with time.[322] It was therefore quite easy to determine if a change in measured SHG was due to alignment or due to time-dependence. The same could not be said for the CdSe samples, which did not show monotonic time dependence.

With the $Si(100)/SiO_2$ alignment sample in place and Lab Director in adjust mode, the alignment of the prism and steering mirror were further refined by maximizing signal. In addition, the z-translations of the sample and the lens before the sample were adjusted to maximize signal. For the z-translation adjustments, the z-

translation of the lens was adjusted first to maximize signal without having to change the alignment of the prism and steering mirror for the SH light. If the lens reached the end of its translation stage without maximizing signal, then the lens was moved back to the middle of its translation stage, and the sample was translated instead, with corresponding adjustments to the following optics and to the x-translation of the sample, to keep the beam on the sample. Once a rough alignment had been achieved again, then the lens translation was reoptimized, and the alignment of the prism and steering mirror were further refined. Finally, the rotation stage was set in motion, and the x- and y-translations of the sample were adjusted so that the fundamental beam hit the sample near the rotation axis (this was necessary for the later rotation scans of the CdSe samples). After this point, the z-translation of the sample and the positions of the mirrors leading up to the experiment were not changed again.

Because light from the TOPAS units was separated by a prism, alignment of the pump beam occurred every time the wavelength changed. The TOPAS prism was rotated to direct the correct wavelength to the first of two steering mirrors that directed the beam down the table towards a mirror leading to the experiment. The two steering mirrors were used to walk the beam through the center of two alignment irises placed between the second steering mirror and the final mirror leading to the experiment. The filter wheel in the pump beam path was set to a reasonably high optical density (an OD of $\sim$3 was usually sufficient) to prevent damage to the sample. Next, the last pump mirror leading to the experiment was adjusted to visually overlap the pump and probe beams on the sample. At the same time, the 30-cm pump focusing lens was adjusted in the x- and y-directions using its translation mount to center the beam in the lens. Several iterations of the mirror/lens adjustments were generally necessary the first time the beams were overlapped after z-translation of the sample.

Next, a closed-circuit, telescoping camera was installed and hooked up to a

television monitor. The camera was focussed on the probe spot on the sample, with the pump beam blocked. The image of the beam on the sample surface usually appeared as a series of three faint spots on the monitor, as a result of reflections from the sample window. Once the probe beam had been identified, the pump beam was unblocked and identified by the camera as a series of three larger, slightly brighter spots. Still using the camera, the pump steering mirror was manipulated to overlap the two beams on the camera screen. Usually when overlap was obtained, a bright pulsing effect was observed on the monitor.

The camera-based overlap was somewhat better than the visual overlap because of the magnification provided by the camera. However, it was not necessarily exact because of the faintness of the spots, as well as because the two laser beams hit the sample at two different angles, while the camera viewed the sample from a third. These effects, combined with the distortion and reflections from the sample window, made overlap incomplete, even if it appeared correct on the monitor. Therefore, after the camera overlap had been performed, correct overlap was achieved by using the adjust mode of Lab Director. When correctly overlapped, SHG (and the rate of increase in TD-EFISH generation) was maximized. Finally, the z-translation of the pump beam focusing lens was adjusted to maximize SH signal. The Si/SiO_2 alignment sample was removed from the sample mount, and the Si/CdSe sample to be investigated was mounted in its place.

G.2.4 SHG measurements

Upon loading a Si/CdSe sample, the rotation stage was turned on, and a scan was performed without the pump beam present while the sample rotated. These scans were used in determining the azimuthal dependence of SHG (Section G.3.1), but they were also used to find the angle yielding maximum SHG, which was the angle used in the power- and wavelength-dependent measurements. For the studies

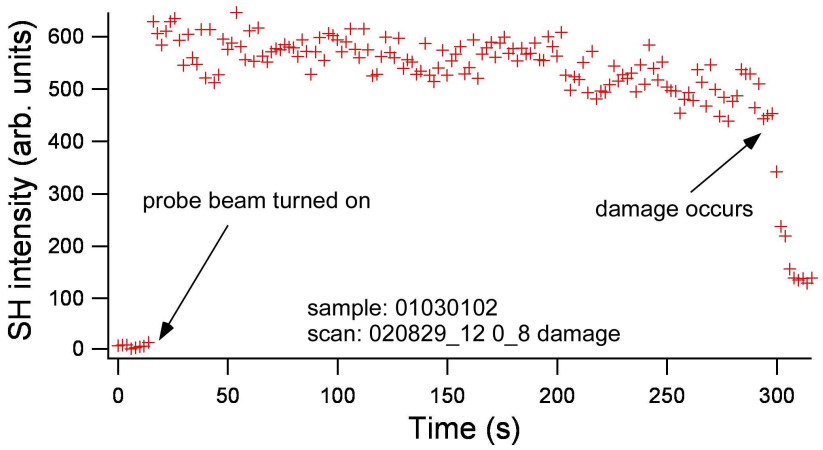

Figure G.11: The effect of damage on measured SHG.

of the azimuthal dependence of SHG, the angle giving maximum signal was noted using a rotation scale included on the rotation stage. Three time-dependent scans were taken using only the probe beam. Then, using the scale, the sample was rotated by 15°, and three scans were performed at the new azimuthal angle. This procedure was repeated until scans had been taken over a 60° range.

When the pump beam was to be used, the next step in preparing to take measurements was to establish the safe working range of the pump beam, as well as to calibrate its power. These steps needed to be taken every time the wavelength of the pump beam was changed, any time adjustments were made to the TOPAS in use, and at the beginning of every day. This beam was powerful enough that at full power, it quickly damaged the sample, literally by blasting holes in it. Damage was evident on the monitor as a bright, strobing light; as a pit formed in the sample, more light scattered in the direction of the camera. When taking data in Lab Director, damage was evident by a rapid decrease in SHG (Figure G.11).

Initially, the pump beam was blocked before the filter wheel and between the beam splitter and the photon counter. With Lab Director in adjust mode and the probe beam incident on the sample, the filter wheel was set to minimize pump beam

power, and the path of the pump beam to the sample was unblocked (leaving the photon counter blocked). While watching both the camera monitor and Lab Director for signs of damage, the power of the pump beam was increased until damage occurred; this power exceeded the maximum usable power of the experiment, so the power was backed off by one or two filter degrees. Having established the maximum safe pump power, the photon counter was unblocked, and neutral density filters were added in front of the photon counter, increasing the degree of filtering until the red overload indicator on the boxcar to which the photon counter was attached turned off and remained off for a few minutes. The power of the pump beam was extremely unstable with time, particularly at the FEL Center (Figure G.12); however, because of the periodic power oscillation, a few minutes was usually enough time to verify that the filtering in front of the photon counter was sufficient. Next, with Lab Director in adjust mode again, the pump beam was repeatedly blocked and unblocked while adjusting the boxcar's voltage offset and magnitude, until the voltage registering in Lab Director with the beam blocked was $\sim$0 V and the voltage registering with the beam unblocked was $\sim$0.9 V on average and never more than 1.0 V. It is noted that the boxcar converts incoming signal to voltage, and it was the voltage from the boxcar that Lab Director measured. As before, the instability of the light from the TOPAS made it necessary to spend several minutes verifying that the voltage from the boxcar did not exceed 1.0 V. The 1.0 V limit was set because the photodiode's response was nonlinear with respect to the beam intensity for voltages greater than this (Figure G.13).

To calibrate the voltages registering in Lab Director with the intensity of the pump beam on the surface of the sample, both pump and probe beams were blocked (the pump beam before the beam splitter), and a power meter with time-averaging capabilities was placed directly in front of the sample mount. Lab Director was allowed to collect data for at least 30 seconds to establish the 'zero' level for the

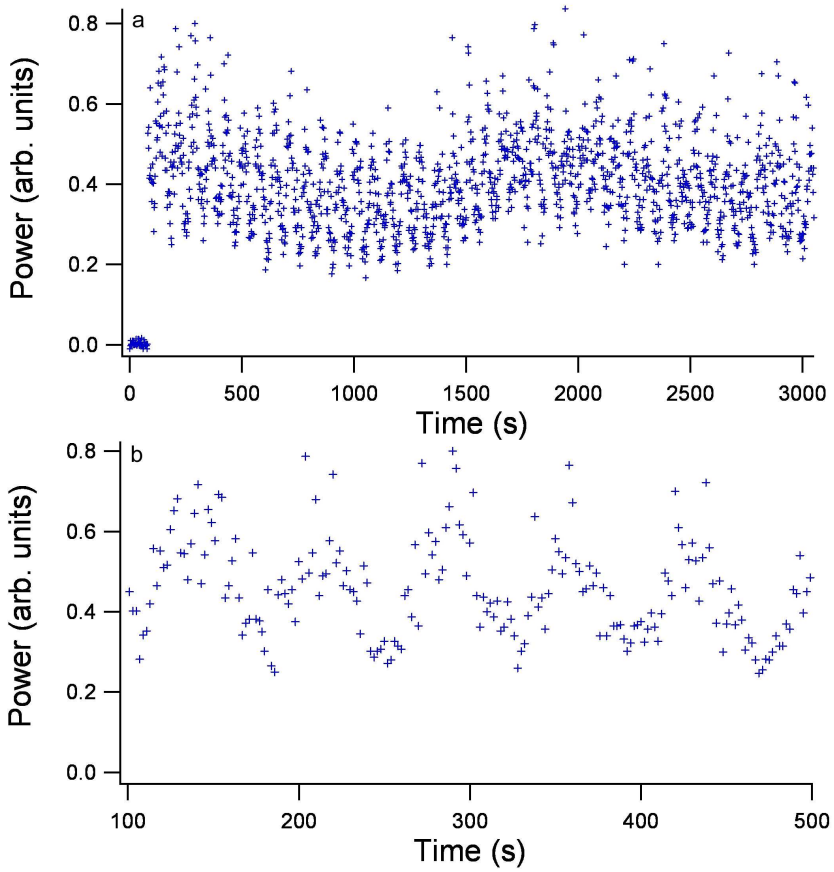

Figure G.12: Power instability of the FEL Center's Titan/TOPAS lasers. Light output from the TOPAS was diverted into a photon counter, and the power of the output was monitored for 50 minutes. (a) shows the total scan; both short- and long-term instability is evident. (b) expands a small portion of the data in (a), showing more clearly the short-term instability. This instability has a period of ∼1 minute, and is attributed to the switching on and off of the solenoid controlling the chilled water flow to the YLF and the Titan. This particular problem was unique to the FEL Center's system, as the other system had a different chiller. It is noted that each data point shown here represents the sum power of pulses over a 0.1 s period of time; the actual pulse-to-pulse instability was even greater than that shown here.

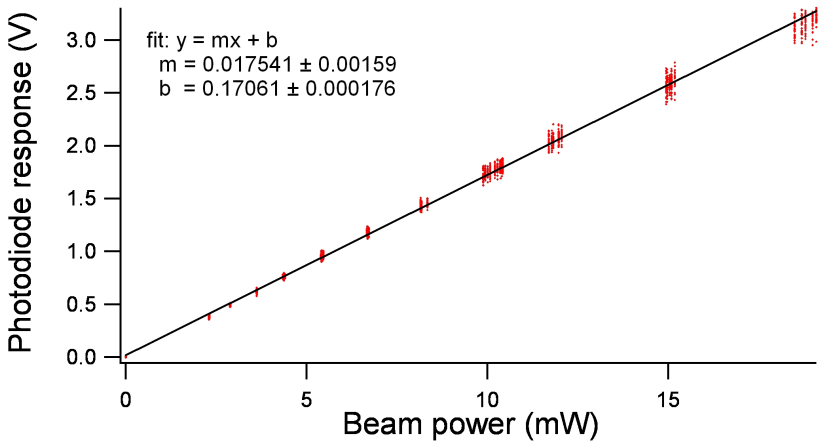

Figure G.13: Linearity of photodiode response. Here the intensity of light was varied by placing neutral density filters of increasing density in front of the photodiode and measuring the output voltage. In this case, the boxcar was set to amplify the signal by a factor of three, so that a 'reference signal' of 3 V corresponded to a photodiode output voltage of 1 V. This figure demonstrates that the Si photodiode used in the SHG and IPE experiments showed a linear response to light intensity in the range 0 - 1.0 V of photodiode output voltage. At voltages of greater than 1 V, the response became nonlinear.

calibration. Then the power meter was set to average data over a 30 s time period and turned on simultaneously with the removal of the block from the pump beam. The 30-second averaged power was recorded by hand for 3 minutes (a total of 6 readings), while Lab Director registered the intensity of light reaching the photon counter (Figure G.14).

In the case of one-color experiments, the power of the single beam was simply measured by placing the power meter in front of the sample and averaging the power over the course of 30 s. Since the single beam was generated by the more stable Mira, it was assumed that the power remained constant throughout any scan; no equipment was used to monitor the power of this beam during the course of a scan.

In preparation for taking a new TD-EFISH measurement, both beams were first blocked (the pump beam before the beam splitter). Then, to ensure that the portion of the sample under investigation began in the ground state at $t = 0$, the sam-

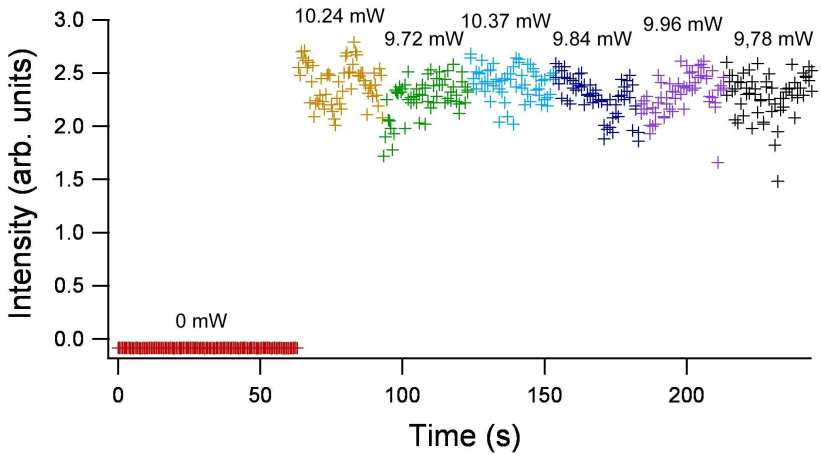

Figure G.14: Sample calibration data for TOPAS output at 680 nm. The data points were recorded by Lab Director, while the written power levels were recorded by a power meter averaging 30 s of data. The 30 s of data to which each power meter measurement corresponds is delineated by a change in color.

ple was translated systematically in the x- and y-directions before each scan. The effects of optical pumping on the sample were very localized - translating the sample by 0.5 mm was more than enough to avoid charge excitation from the previous scan. Lab Director was started and allowed to collect data for ∼12 s to establish the 'zero' level for the data run. Ideally, the probe beam would then be unblocked, and the experiment would be allowed to run with just the probe beam until no time dependence was observed in Lab Director's observation screen before unblocking the pump beam. However, in the case of the Si/CdSe samples this was logistically impossible (time dependence was observed to continue for more than an hour), so both pump and probe beam were unblocked simultaneously. Once both beams were unblocked, the experiment was usually allowed to proceed without further manipulation. Alternately, if information on system recovery was desired, the pump beam could be blocked and unblocked as necessary.

The length of each scan depended on the time dependence observed during the course of the scan. Ideally, measurements continued until well after time dependence

had ceased; however, again as a result of the long time dependence evident in the Si/CdSe system, this was not possible for the Si/CdSe samples. Generally, scans were taken at a rate of one measurement per second, and Lab Director allowed a maximum of 3000 data points; therefore, measurements on the Si/CdSe were conducted for the maximum allowed time, 50 minutes.

To determine band offsets using SHG, TD-EFISH measurements were taken for a range of powers at each wavelength for a range of wavelengths. In order to determine the offsets, the wavelengths needed to span at least one offset or integer multiples thereof (see Section G.1.4). The probe beam power was kept constant at ∼50 mW. At each wavelength and power, at least three different scans were performed. This was particularly important for scans of the Si/CdSe system, because the roughness of the CdSe layer meant that sometimes the beams were focused on a spot that was not representative of the sample as a whole (e.g., a particularly bare spot, or a particularly thick one). If all three scans appeared visually equivalent, then the experiment could be set up for a new power or wavelength. Otherwise, more scans were taken until three visually equivalent scans were obtained; the others were considered outliers and were not included in analysis. Generally, there was no more than one outlying scan for a given set of conditions.

G.3 Results and discussion

G.3.1 Angular dependence of SHG

In Section G.1.6 we saw that the magnitude of SHG from Si(111) depends greatly on both the angle of incidence, θ_0, and the azimuthal angle, ϕ, of the fundamental light on the surface of the silicon. This section examines how the CdSe nanocrystal/Si(111) interface behaves with respect to the angle and orientation of incoming light, and compares the results to hydrogen-passivated Si(111) (Si(111)-H) and Si/SiO_2 interfaces.

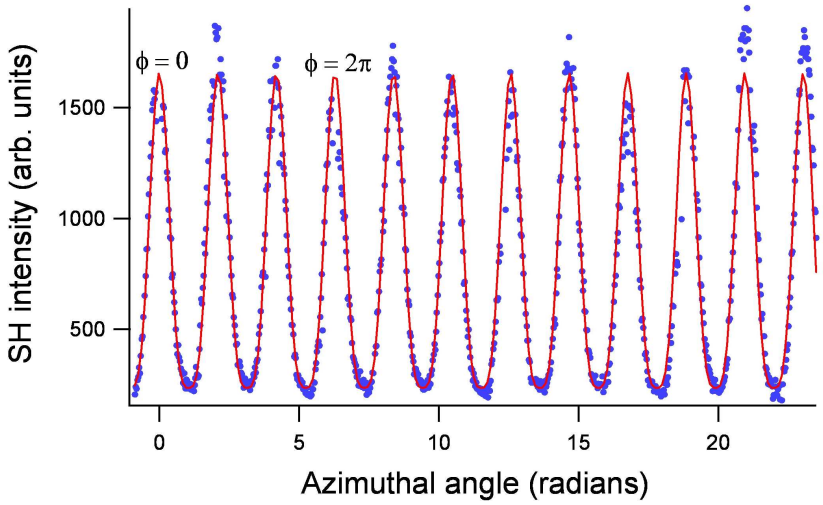

Figure G.15: SHG as a function of ϕ for a 72 Å CdSe nanocrystal/Si(111) interface. This data was fit to Equations (G.68) - (G.74) in order to determine the parameters ζ, ∂_{11}, $\left(\frac{\gamma}{\epsilon(2\omega)} + \partial_{31}\right)$, $(\partial_{33} - \partial_{31})$, and ∂_{15}, assuming the values $n = 3.68 + 0.013i$, $N = 5.68 + 0.21i$, $\epsilon(\omega) = 13.5 + 0.096i$, and $\epsilon(2\omega) = 32.2 + 2.4i$.[347,348] SH signal was generated using a 800 nm, p-polarized fundamental beam incident on the Si(111) at an angle of $\theta = 30°$.

The angular behavior of the interface can be characterized by the frequency-dependent material parameters: n, N, $\epsilon(\omega)$, $\epsilon(2\omega)$, ζ, ∂_{11}, $\left(\frac{\gamma}{\epsilon(2\omega)} + \partial_{31}\right)$, $(\partial_{33} - \partial_{31})$, and ∂_{15}.[339,342] Ideally, these parameters would be determined by multiple scans, varying both the angle of incidence and the azimuthal angle, over a range of nanocrystal sizes. However, since the goal of the angular dependence experiments was simply to get a rough idea of how EFISH generation varied with azimuthal angle, and to see what effect having a nonstandard angle of incidence (30° instead of 45°) had on EFISH generation, and since the experimental setup did not allow variation of the angle of incidence, the results presented here are based on azimuthal (time-independent) scans of 72 Å nanocrystals on Si(111), with an angle of incidence of 30° (Figure G.15).

The complex refractive indices and dielectric constants for Si at $\lambda = 400$ nm and 800 nm for the CdSe/Si experiments, and at $\lambda = 415$ nm and 830 nm for the Si(111)-H and Si/SiO_2 comparisons, were calculated using the real parts of the

refractive indices, η, and extinction coefficients, k, obtained from Hulthen[347] and Philipp[348]. The complex refractive index n is

$$n = \eta + ik \tag{G.64}$$

where k is related to the absorption coefficient α by

$$k = \frac{\alpha\lambda}{4\pi} \tag{G.65}$$

The complex dielectric constant is simply the square of the complex refractive index:

$$\epsilon = n^2 \tag{G.66}$$

Since no effort was made to separate the p- and s-polarized SH light, the relationship between the intensity of SHG and the generated SH electric field was

$$I^{(2\omega)} = |E_{pp}|^2 + |E_{ps}|^2 \tag{G.67}$$

(E_{pp} and E_{ps} are defined in Equations G.47 and G.49). However, because all the parameters in which we are interested are complex, it was necessary to split E_{pp} and E_{ps} into their real and imaginary components, denoted hereafter by the subscripts r and i, respectively, in order to fit the data in Figure G.15. Thus, the data in Figure G.15 were first fit to the equation

$$\begin{aligned} I^{(2\omega)} &= \left(A_{pr}^2 + A_{pi}^2\right)\left[\left(a_{ppr} + c_{ppr}\cos\left(3\phi\right)\right)^2 + \left(a_{ppi} + c_{ppi}\cos\left(3\phi\right)\right)^2\right] + \\ &\quad + \left(A_{sr}^2 + A_{si}^2\right)\left(b_{psr}^2 + b_{psi}^2\right)\sin^2\left(3\phi\right) \end{aligned} \tag{G.68}$$

where A_{pr}, A_{pi}, A_{sr}, and A_{si} are given in Table G.1. It is noted that the azimuthal angle corresponding to the $[2\bar{1}\bar{1}]$ projection of the fundamental beam on the Si(111) surface was not known. However, because of the form of Equation G.68, and because it is generally known that the contribution from b_{ps} is small for Si(111), peaks in SHG over an azimuthal scan must correspond to $\phi = \frac{2\pi}{3}n$, or to $\phi = \frac{2\pi}{3}n + \frac{\pi}{3}$.[339,342,343]

Table G.1: Equations for modeling the dependence of SHG on the angle of incidence, θ. These equations were used to separate the parameters in the equations of Sipe *et al.*[339] for the angular dependence of SHG into their real and imaginary components for incorporation into a spreadsheet program which calculated relative magnitudes of SHG as a function of θ and ϕ. Parameters not shown have equations corresponding to those presented above (e.g., $F_{sr} = \frac{KN_r}{\widetilde{\Omega}\left(N_r^2+N_i^2\right)}$, similar to $f_{sr} = \frac{\kappa n_r}{\widetilde{\omega}\left(n_r^2+n_i^2\right)}$).

$\nu_0 = \frac{1}{\lambda_0}$
$\omega = \frac{c}{\lambda_0}$
$\epsilon(\omega)_r = n_r^2 - n_i^2$
$\epsilon(\omega)_i = 2n_r n_i$
$\kappa = \nu_0 \sin(\theta_0)$
$w_r = \sqrt{\frac{1}{2}\left(\widetilde{\omega}^2\epsilon(\omega)_r - \kappa^2 + \sqrt{\left(\widetilde{\omega}^2\epsilon(\omega)_r - \kappa^2\right)^2 + \widetilde{\omega}^4\epsilon(\omega)_i^2}\right)}$
$w_i = \frac{\widetilde{\omega}^2\epsilon(\omega)_i}{2w_r}$
$t_p = \frac{2nw_0}{w_0\epsilon(\omega)+w}$
$t_{pr} = \frac{2\left[n_r w_o^2\epsilon(\omega)_r + n_r w_0 w_r + n_i w_0^2\epsilon(\omega)_i + n_i w_0 w_i\right]}{w_0^2\epsilon(\omega)_r^2 + w_r^2 + 2w_o w_r\epsilon(\omega)_r + w_0^2\epsilon(\omega)_i^2 + w_i^2 + 2w_0 w_i\epsilon(\omega)_i}$
$t_{pi} = \frac{2\left[-n_r w_o^2\epsilon(\omega)_i - n_r w_0 w_i + n_i w_0^2\epsilon(\omega)_r + n_i w_0 w_r\right]}{w_0^2\epsilon(\omega)_r^2 + w_r^2 + 2w_o w_r\epsilon(\omega)_r + w_0^2\epsilon(\omega)_i^2 + w_i^2 + 2w_0 w_i\epsilon(\omega)_i}$
$A_{sr} = \frac{4\pi\widetilde{\Omega}(W_0+W_r)}{W_0^2+2W_0W_r+W_r^2+W_i^2}$
$A_{si} = \frac{-4\pi\widetilde{\Omega}W_i}{W_0^2+2W_0W_r+W_r^2+W_i^2}$
$A_{pr} = \frac{4\pi\widetilde{\Omega}[N_r W_0\epsilon(2\omega)_r + N_r W_r + N_i W_0\epsilon(2\omega)_i + N_i W_i]}{W_0^2\epsilon(2\omega)_r^2 + 2W_0W_r\epsilon(2\omega)_r + W_r^2 + W_0^2\epsilon(2\omega)_i^2 + 2W_0W_i\epsilon(2\omega)_i + W_i^2}$
$A_{pi} = \frac{4\pi\widetilde{\Omega}[N_i W_0\epsilon(2\omega)_r + N_i W_r - N_r W_0\epsilon(2\omega)_i - N_r W_i]}{W_0^2\epsilon(2\omega)_r^2 + 2W_0W_r\epsilon(2\omega)_r + W_r^2 + W_0^2\epsilon(2\omega)_i^2 + 2W_0W_i\epsilon(2\omega)_i + W_i^2}$
$\Gamma_r = \frac{\widetilde{\Omega}[2n_r w_r + n_r W_r + 2n_i w_i + n_i W_i]}{8\left[4w_r^2 + 4w_r W_r + W_r^2 + 4w_i^2 + 4w_i W_i + W_i^2\right]}$
$\Gamma_i = \frac{\widetilde{\Omega}[2n_i w_r + n_i W_r - 2n_r w_i - n_r W_i]}{8\left[4w_r^2 + 4w_r W_r + W_r^2 + 4w_i^2 + 4w_i W_i + W_i^2\right]}$
$f_{sr} = \frac{\kappa n_r}{\widetilde{\omega}\left(n_r^2+n_i^2\right)}$
$f_{si} = \frac{-\kappa n_i}{\widetilde{\omega}\left(n_r^2+n_i^2\right)}$
$f_{cr} = \frac{w_r n_r + w_i n_i}{\widetilde{\omega}\left(n_r^2+n_i^2\right)}$
$f_{ci} = \frac{w_i n_r - w_r n_i}{\widetilde{\omega}\left(n_r^2+n_i^2\right)}$

Without loss of generality, the peaks in this case were assumed to correspond to $\phi = \frac{2\pi}{3}n$.

All parameters in b_{psr}, b_{psi}, c_{ppr}, and c_{ppi} were calculated from the equations in Table G.1 except for ζ_r, ζ_i, ∂_{11r}, and ∂_{11i}. These values were then determined by solving the real and imaginary components of Equations G.56 and G.57:

$$\begin{aligned} b_{psr} &= -\widetilde{\Omega}\left[\frac{\sqrt{8}}{3}\left(\zeta_i\Gamma_r + \zeta_r\Gamma_i\right)\left[f_{cr}^2 - f_{ci}^2 + \left(-2f_{sr}^2 + 2f_{si}^2\right)f_{cr} + 4f_{sr}f_{si}f_{ci}\right] + \right. \\ &\quad + \frac{\sqrt{8}}{3}\left(\zeta_r\Gamma_r - \zeta_i\Gamma_i\right)\left[2f_{cr}f_{ci} - 4f_{sr}f_{si}f_{cr} + \left(-2f_{sr}^2 + 2f_{si}2\right)f_{ci}\right] + \\ &\quad \left. + 2f_{cr}f_{ci}\partial_{11r} + \left(f_{cr}^2 - f_{ci}^2\right)\partial_{11i}\right] \end{aligned} \tag{G.69}$$

$$\begin{aligned} b_{psi} &= \widetilde{\Omega}\left[\frac{\sqrt{8}}{3}\left(\zeta_r\Gamma_r - \zeta_i\Gamma_i\right)\left[f_{cr}^2 - f_{ci}^2 + \left(-2f_{sr}^2 + 2f_{si}^2\right)f_{cr} + 4f_{sr}f_{si}f_{ci}\right] - \right. \\ &\quad - \frac{\sqrt{8}}{3}\left(\zeta_i\Gamma_r + \zeta_r\Gamma_i\right)\left[2f_{cr}f_{ci} - 4f_{sr}f_{si}f_{cr} + \left(-2f_{sr}^2 + 2f_{si}2\right)f_{ci}\right] + \\ &\quad \left. + \left(f_{cr}^2 - f_{ci}^2\right)\partial_{11r} - 2f_{cr}f_{ci}\partial_{11i}\right] \end{aligned} \tag{G.70}$$

$$\begin{aligned} c_{ppr} &= \widetilde{\Omega}\left[\frac{\sqrt{8}}{3}\left(\zeta_i\Gamma_r + \zeta_r\Gamma_i\right)\left[F_{cr}\left(f_{cr}^3 - 3f_{cr}f_{ci}^2\right) - F_{ci}\left(3f_{cr}^2f_{ci} - f_{ci}^3\right) + \right.\right. \\ &\quad + \left(\left(-2f_{sr}^2 + 2f_{si}^2\right)F_{cr} + 4f_{sr}f_{si}F_{ci}\right)f_{cr} - \left(-4f_{sr}f_{si}F_{cr} + \left(-2f_{sr}^2 + \right.\right. \\ &\quad \left.\left. + 2f_{si}^2\right)F_{ci}\right)f_{ci} + \left(F_{sr}f_{sr} - F_{si}f_{si}\right)\left(f_{cr}^2 - f_{ci}^2\right) - 2\left(F_{si}f_{sr} + \right. \\ &\quad \left. + F_{sr}f_{si}\right)f_{cr}f_{ci}\right] + \frac{\sqrt{8}}{3}\left(\zeta_r\Gamma_r - \zeta_i\Gamma_i\right)\left[F_{ci}\left(f_{cr}^3 - 3f_{cr}f_{ci}^2\right) + \right. \\ &\quad + F_{cr}\left(3f_{cr}^2f_{ci} - f_{ci}^3\right) + \left(-4f_{sr}f_{si}F_{cr} + \left(-2f_{sr}^2 + 2f_{si}^2\right)F_{ci}\right)f_{cr} + \\ &\quad + \left(\left(-2f_{sr}^2 + 2f_{si}^2\right)F_{cr} + 4f_{sr}f_{si}F_{ci}\right)f_{ci} + \left(F_{si}f_{sr} + F_{si}f_{sr}\right)\left(f_{cr}^2 - \right. \\ &\quad \left. - f_{ci}^2\right) + 2\left(F_{sr}f_{sr} - F_{si}f_{si}\right)f_{cr}f_{ci}\right] + \left(F_{ci}\left(f_{cr}^2 - f_{ci}^2\right) + \right. \\ &\quad \left.\left. + 2F_{cr}f_{cr}f_{ci}\right)\partial_{11r} + \left(F_{cr}\left(f_{cr}^2 - f_{ci}^2\right) - 2F_{ci}f_{cr}f_{ci}\right)\partial_{11i}\right] \end{aligned} \tag{G.71}$$

$$\begin{aligned} c_{ppi} &= -\widetilde{\Omega}\left[\frac{\sqrt{8}}{3}\left(\zeta_r\Gamma_r - \zeta_i\Gamma_i\right)\left[F_{cr}\left(f_{cr}^3 - 3f_{cr}f_{ci}^2\right) - F_{ci}\left(3f_{cr}^2f_{ci} - f_{ci}^3\right) + \right.\right. \\ &\quad \left. + \left(\left(-2f_{sr}^2 + 2f_{si}^2\right)F_{cr} + 4f_{sr}f_{si}F_{ci}\right)f_{cr} - \left(-4f_{sr}f_{si}F_{cr} + \left(-2f_{sr}^2 + \right.\right.\right. \end{aligned}$$

$$
\begin{aligned}
&+2f_{si}^2\big)\,F_{ci}\big)\,f_{ci}+\left(F_{sr}f_{sr}-F_{si}f_{si}\right)\left(f_{cr}^2-f_{ci}^2\right)-2\left(F_{si}f_{sr}+\right.\\
&\left.+F_{sr}f_{si}\right)f_{cr}f_{ci}\big]-\frac{\sqrt{8}}{3}\left(\zeta_i\Gamma_r+\zeta_r\Gamma_i\right)\big[F_{ci}\left(f_{cr}^3-3f_{cr}f_{ci}^2\right)+\\
&+F_{cr}\left(3f_{cr}^2f_{ci}-f_{ci}^3\right)+\left(-4f_{sr}f_{si}F_{cr}+\left(-2f_{sr}^2+2f_{si}^2\right)F_{ci}\right)f_{cr}+\\
&+\left(\left(-2f_{sr}^2+2f_{si}^2\right)F_{cr}+4f_{sr}f_{si}F_{ci}\right)f_{ci}+\left(F_{si}f_{sr}+F_{si}f_{sr}\right)\left(f_{cr}^2-\right.\\
&\left.-f_{ci}^2\right)+2\left(F_{sr}f_{sr}-F_{si}f_{si}\right)f_{cr}f_{ci}\big]+\left(F_{cr}\left(f_{cr}^2-f_{ci}^2\right)-\right.\\
&\left.-2F_{ci}f_{cr}f_{ci}\right)\partial_{11r}-\left(F_{ci}\left(f_{cr}^2-f_{ci}^2\right)+2F_{cr}f_{cr}f_{ci}\right)\partial_{11i}\big] \qquad \text{(G.72)}
\end{aligned}
$$

Next, the data in Figure G.15 were refit using Equation G.68, substituting in the previously fit values for b_{psr}, b_{psi}, c_{ppr}, and c_{ppi}, the calculated values for ζ_r and ζ_i, and the equations for a_{ppr} and a_{ppi}:

$$
\begin{aligned}
a_{ppr} \;=\; & -\widetilde{\Omega}\left[\frac{1}{3}\left(\zeta_i\Gamma_r+\zeta_r\Gamma_i\right)\big[4F_{sr}f_{cr}-4F_{si}f_{ci}+\left(-2f_{sr}F_{cr}+2f_{si}F_{ci}\right)\left(f_{cr}^2-\right.\right.\\
&\left.-f_{ci}^2\right)+\left(4f_{si}F_{cr}+4f_{sr}F_{ci}\right)f_{cr}f_{ci}+\left(-8F_{sr}\left(f_{sr}^2-f_{si}^2\right)+16F_{si}f_{sr}f_{si}\right)f_{cr}+\\
&+\left(8F_{si}\left(f_{sr}^2-f_{si}^2\right)+16F_{sr}f_{sr}f_{si}\right)f_{ci}+\left(4f_{sr}^3-12f_{sr}f_{si}^2\right)F_{cr}-\left(12f_{sr}^2f_{si}-\right.\\
&\left.\left.-4f_{si}^3\right)F_{ci}\big]+\frac{1}{3}\left(\zeta_r\Gamma_r-\zeta_i\Gamma_i\right)\big[4F_{sr}f_{ci}+4F_{si}f_{cr}-\left(2f_{si}F_{cr}+2f_{sr}F_{ci}\right)\left(f_{cr}^2-\right.\right.\\
&\left.-f_{ci}^2\right)+\left(-4f_{sr}F_{cr}+4f_{si}F_{ci}\right)f_{cr}f_{ci}-\left(8F_{si}\left(f_{sr}^2-f_{si}^2\right)+16F_{sr}f_{sr}f_{si}\right)f_{cr}+\\
&+\left(-8F_{sr}\left(f_{sr}^2-f_{si}^2\right)+16F_{si}f_{sr}f_{si}\right)f_{ci}+\left(12f_{sr}^2f_{si}-4f_{si}^3\right)F_{cr}+\left(4f_{sr}^3-\right.\\
&\left.\left.-12f_{sr}f_{si}^2\right)F_{ci}\big]+F_{sr}\epsilon(2\omega)_r\left(\frac{\gamma}{\epsilon(2\omega)}+\partial_{31}\right)_i+F_{sr}\epsilon(2\omega)_i\left(\frac{\gamma}{\epsilon(2\omega)}+\partial_{31}\right)_r+\right.\\
&+F_{si}\epsilon(2\omega)_r\left(\frac{\gamma}{\epsilon(2\omega)}+\partial_{31}\right)_r-F_{si}\epsilon(2\omega)_i\left(\frac{\gamma}{\epsilon(2\omega)}+\partial_{31}\right)_i+\left(\left(F_{si}\left(f_{sr}^2-\right.\right.\right.\\
&\left.\left.\left.-f_{si}^2\right)+2F_{sr}f_{sr}f_{si}\right)\epsilon(2\omega)_r+\left(F_{sr}\left(f_{sr}^2-f_{si}^2\right)-2F_{si}f_{sr}f_{si}\right)\epsilon(2\omega)_i\right)\left(\partial_{33}-\right.\\
&\left.-\partial_{31}\right)_r+\left(\left(F_{sr}\left(f_{sr}^2-f_{si}^2\right)-2F_{si}f_{sr}f_{si}\right)\epsilon(2\omega)_r-\left(F_{si}\left(f_{sr}^2-f_{si}^2\right)+\right.\right.\\
&\left.\left.+2F_{sr}f_{sr}f_{si}\right)\epsilon(2\omega)_i\right)\left(\partial_{33}-\partial_{31}\right)_i-2f_{sr}f_{cr}F_{cr}\partial_{15i}-2f_{sr}f_{cr}F_{ci}\partial_{15r}-\\
&-2f_{sr}f_{ci}F_{cr}\partial_{15r}+2f_{sr}f_{ci}F_{ci}\partial_{15i}-2f_{si}f_{cr}F_{cr}\partial_{15r}+2f_{si}f_{cr}F_{ci}\partial_{15i}+\\
&\left.+2f_{si}f_{ci}F_{cr}\partial_{15i}+2f_{si}f_{ci}F_{ci}\partial_{15r}\right] \qquad \text{(G.73)}
\end{aligned}
$$

$$
\begin{aligned}
a_{ppi} \;=\; & \widetilde{\Omega}\left[\frac{1}{3}\left(\zeta_r\Gamma_r-\zeta_i\Gamma_i\right)\big[4F_{sr}f_{cr}-4F_{si}f_{ci}+\left(-2f_{sr}F_{cr}+2f_{si}F_{ci}\right)\left(f_{cr}^2-\right.\right.
\end{aligned}
$$

$$
\begin{aligned}
&-f_{ci}^2\big) + \left(4f_{si}F_{cr} + 4f_{sr}F_{ci}\right) f_{cr}f_{ci} + \big(-8F_{sr}\left(f_{sr}^2 - f_{si}^2\right) + 16F_{si}f_{sr}f_{si}\big) f_{cr} + \\
&+ \big(8F_{si}\left(f_{sr}^2 - f_{si}^2\right) + 16F_{sr}f_{sr}f_{si}\big) f_{ci} + \left(4f_{sr}^3 - 12f_{sr}f_{si}^2\right) F_{cr} - \big(12f_{sr}^2f_{si} - \\
&-4f_{si}^3\big) F_{ci}\big] - \frac{1}{3}\left(\zeta_i\Gamma_r + \zeta_r\Gamma_i\right)\big[4F_{sr}f_{ci} + 4F_{si}f_{cr} - \left(2f_{si}F_{cr} + 2f_{sr}F_{ci}\right)\big(f_{cr}^2 - \\
&-f_{ci}^2\big) + \left(-4f_{sr}F_{cr} + 4f_{si}F_{ci}\right) f_{cr}f_{ci} - \big(8F_{si}\left(f_{sr}^2 - f_{si}^2\right) + 16F_{sr}f_{sr}f_{si}\big) f_{cr} + \\
&+ \big(-8F_{sr}\left(f_{sr}^2 - f_{si}^2\right) + 16F_{si}f_{sr}f_{si}\big) f_{ci} + \left(12f_{sr}^2f_{si} - 4f_{si}^3\right) F_{cr} + \left(4f_{sr}^3 - \\
&-12f_{sr}f_{si}^2\right) F_{ci}\big] + F_{sr}\epsilon(2\omega)_r\left(\frac{\gamma}{\epsilon(2\omega)} + \partial_{31}\right)_r - F_{sr}\epsilon(2\omega)_i\left(\frac{\gamma}{\epsilon(2\omega)} + \partial_{31}\right)_i - \\
&-F_{si}\epsilon(2\omega)_r\left(\frac{\gamma}{\epsilon(2\omega)} + \partial_{31}\right)_i - F_{si}\epsilon(2\omega)_i\left(\frac{\gamma}{\epsilon(2\omega)} + \partial_{31}\right)_r + \big(\big(F_{sr}\left(f_{sr}^2 - \\
&-f_{si}^2\right) - 2F_{si}f_{sr}f_{si}\big)\epsilon(2\omega)_r - \left(F_{si}\left(f_{sr}^2 - f_{si}^2\right) + 2F_{sr}f_{sr}f_{si}\right)\epsilon(2\omega)_i\big)\left(\partial_{33} - \\
&-\partial_{31}\right)_r - \big(\big(F_{si}\left(f_{sr}^2 - f_{si}^2\right) + 2F_{sr}f_{sr}f_{si}\big)\epsilon(2\omega)_r + \left(F_{sr}\left(f_{sr}^2 - f_{si}^2\right) - \\
&-2F_{si}f_{sr}f_{si}\right)\epsilon(2\omega)_i\big)\left(\partial_{33} - \partial_{31}\right)_i - 2f_{sr}f_{cr}F_{cr}\partial_{15r} + 2f_{sr}f_{cr}F_{ci}\partial_{15i} + \\
&+2f_{sr}f_{ci}F_{cr}\partial_{15i} + 2f_{sr}f_{ci}F_{ci}\partial_{15r} + 2f_{si}f_{cr}F_{cr}\partial_{15i} + 2f_{si}f_{cr}F_{ci}\partial_{15r} + \\
&+2f_{si}f_{ci}F_{cr}\partial_{15r} - 2f_{si}f_{ci}F_{ci}\partial_{15i}]
\end{aligned}
\tag{G.74}
$$

This fit yielded values for $\left(\frac{\gamma}{\epsilon(2\omega)} + \partial_{31}\right)_r$, $\left(\frac{\gamma}{\epsilon(2\omega)} + \partial_{31}\right)_i$, $\left(\partial_{33} - \partial_{31}\right)_r$, $\left(\partial_{33} - \partial_{31}\right)_i$, ∂_{15r}, and ∂_{15i}. This two-part fit was necessary because the fitting program, Igor Pro™, is incapable of handling an equation as long as the full equation. The final fit values had large errors (two to three orders of magnitude greater than the values) due to the complexity of the fitting equation and the relatively small quantity of data; again, a thorough study of angular dependence would have involved changing the angle of incidence as well as the azimuthal angle. As an example, the second fit yielded slightly different values for a_{ppr} and a_{ppi} than the first fit, though $\|a_{pp}\|$ remained the same. Finally, it is noted that the terms E_p and t_p, which is used to calculate E_p, were excluded from the fit and essentially incorporated into the calculated fit parameters. t_p changes only when θ varies, and thus E_p and t_p were constant for all the data in the azimuthal scan. E_p and t_p are relevant only in quantitatively determining the surface nonlinear susceptibilities, and we were concerned only with the relative relationship

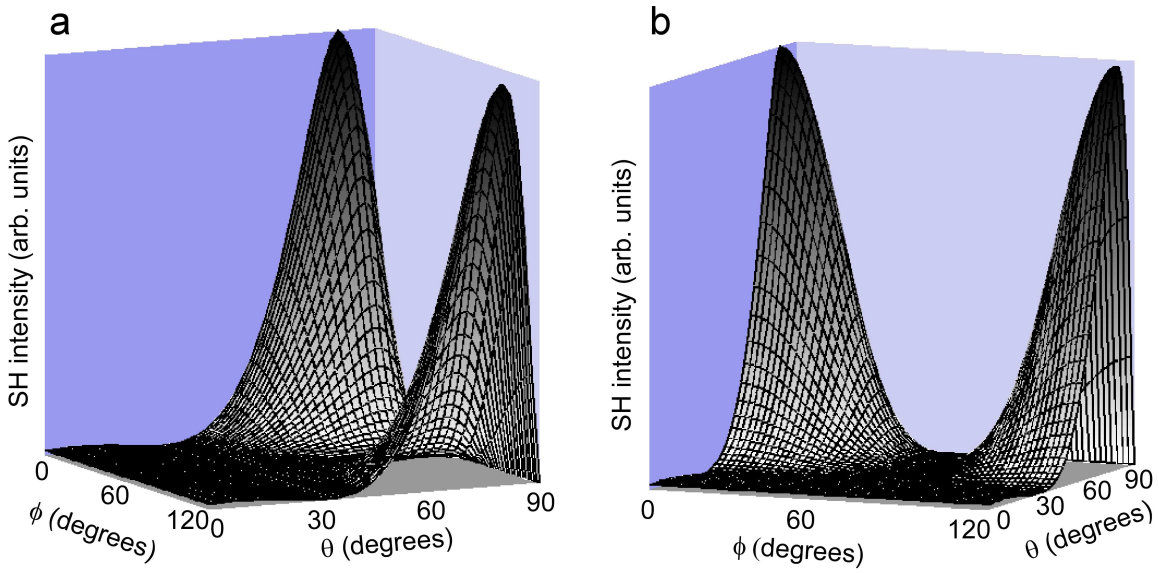

Figure G.16: Calculated angular dependence of SHG for a 72 Å CdSe nanocrystal/Si(111) interface. The dependence was calculated using parameters listed in Table G.2 and Equation G.68. To account for the change in light penetrating the Si surface, Equation G.68 was multiplied by the square of the real part of the Fresnel coefficient for the transmission of p-polarized light, t_{pr}, given in Table G.1. Graphs (a) and (b) show different views of the same data.

between different susceptibilities.

The material parameters used to study the angular dependence of SHG are listed in Table G.2. The magnitudes of the surface nonlinear susceptibilities are arbitrary from sample to sample, as $E_p^{(2\omega)}$ is not known, so values for these parameters normalized to $\zeta = 1$ are given in parentheses below the experimentally determined values. Using the normalized susceptibilities, the relative intensities of SHG as a function of θ and ϕ were then calculated. These intensities are shown for the CdSe/Si(111), Si(111)-H, and Si(111)/SiO_2 systems in Figures G.16 - G.18, Figures G.19 and G.20, and Figures G.21 and G.22, respectively.

A few points are immediately notable. First, it is evident that, for all three systems, SHG is maximized at a high angle of incidence - 80° for CdSe/Si, and 79° for Si-H and Si/SiO_2. This stems predominantly from a larger ratio $I^{(2\omega)} : \|E_p\|$ at large

Table G.2: Material parameters used in angular dependence of SHG.
[a] *From Philipp.*[348]
[b] *From Hulthen.*[347]
[c] $\epsilon = n^2$.
[d] *From fit to experimental data.*
[e] *From Mitchell et al.*[342]

system	λ_0	n	N	$\epsilon(\omega)$
72 Å CdSe/Si(111)	800 nm	[a] $3.68 +$ [b] $0.013i$	[a] $5.68 +$ [b] $0.40i$	[c] $13.54 + 0.096i$
Si(111)-H	830 nm	[a] $3.65 +$ [b] $0.010i$	[a] $5.05 +$ [b] $0.40i$	[c] $13.32 + 0.072i$
Si(111)/SiO_2	830 nm	[a] $3.65 +$ [b] $0.010i$	[a] $5.05 +$ [b] $0.40i$	[c] $13.32 + 0.072i$

system	$\epsilon(2\omega)$	ζ
72 Å CdSe/Si(111)	[c] $32.10 + 4.56i$	[d] $-0.0180 + 0.0341i$ (1)
Si(111)-H	[c] $25.34 + 4.01i$	[e] 44 (1)
Si(111)/SiO_2	[c] $25.34 + 4.01i$	[e] 44 (1)

system	∂_{11}	$\left(\frac{\gamma}{\epsilon(2\omega)} + \partial_{31}\right)$
72 Å CdSe/Si(111)	[d] $7.46 \times 10^{-4} - 15.63 \times 10^{-4}i$ $(-0.0448 + 0.00180i)$	[d] $1.31 \times 10^{-5} - 3.93 \times 10^{-5}i$ $(-0.00106 + 0.000176i)$
Si(111)-H	[e] -5.8 (-0.132)	[e] $-0.213 - 0.166i$ $(-0.00484 - 0.00378i)$
Si(111)/SiO_2	[e] -8.1 (-0.184)	[e] $-0.513 - 0.462i$ $(-0.0117 - 0.0105i)$

system	$(\partial_{33} - \partial_{31})$	∂_{15}
72 Å CdSe/Si(111)	[d] $-2.73 \times 10^{-4} + 4.35 \times 10^{-4}i$ $(0.0133 + 0.000995i)$	[d] $7.24 \times 10^{-5} - 11.91 \times 10^{-5}i$ $(-0.00361 - 0.000220i)$
Si(111)-H	[e] $-18.4 + 13.8i$ $(-0.417 + 0.315i)$	[e] $-6.25 + 2.92i$ $(-0.142 + 0.0663i)$
Si(111)/SiO_2	[e] $-0.489 + 28i$ $(-0.0111 + 0.636i)$	[e] $-9.97 + 4.65i$ $(-0.227 + 0.106i)$

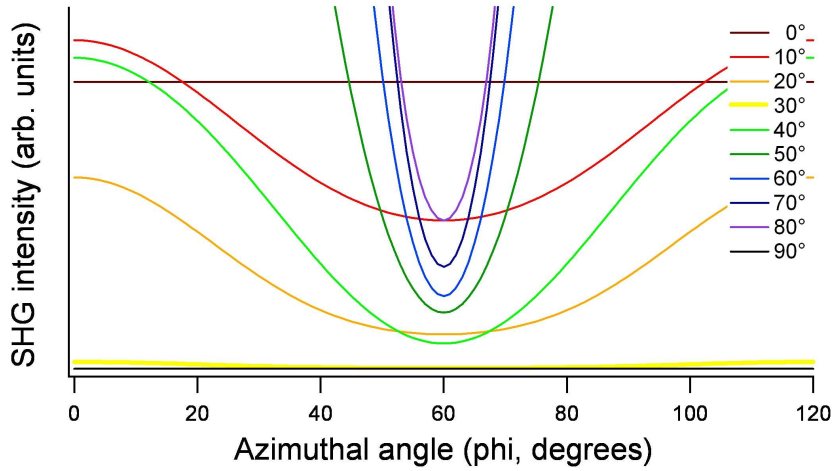

Figure G.17: Calculated dependence of SHG on azimuthal angle of the incident beam for a 72 Å CdSe nanocrystal/Si(111) interface. Each line shows the azimuthal dependence at a different angle of incidence of the fundamental beam. A 3-dimensional view is given in Figure G.16. Notably, SHG at $\theta = 45°$ is much greater than at $\theta = 30°$.

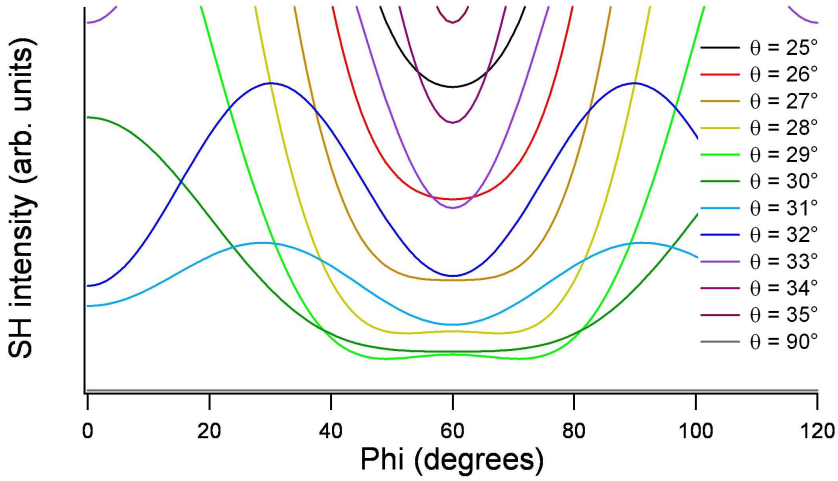

Figure G.18: Close up view of the dependence of SHG on azimuthal angle of the incident beam for a 72 Å CdSe nanocrystal/Si(111) interface near $\theta = 30°$. Each line shows the azimuthal dependence at a different angle of incidence of the fundamental beam. A 3-dimensional view is given in Figure G.16. According to calculations, minimum SHG occurs near $\theta = 30°$.

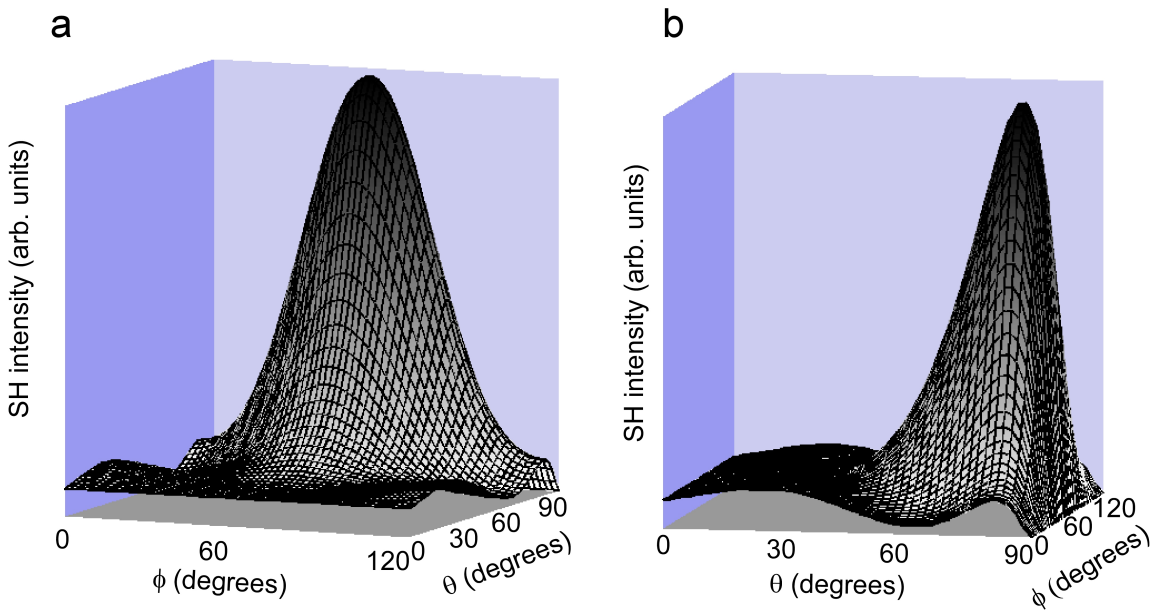

Figure G.19: Calculated angular dependence of SHG for a Si(111)-H interface. The dependence was calculated using parameters listed in Table G.2 and Equation G.68. To account for the change in light penetrating the Si surface, Equation G.68 was multiplied by the square of the real part of the Fresnel coefficient for the transmission of p-polarized light, t_{pr}, given in Table G.1. Graphs (a) and (b) show different views of the same data.

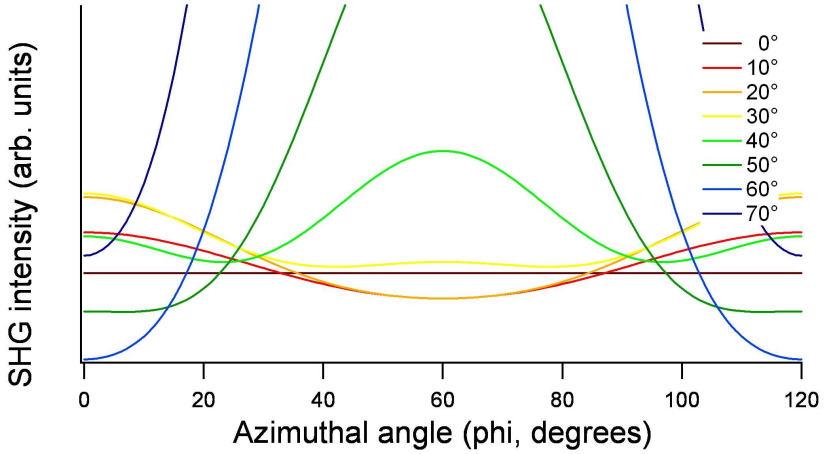

Figure G.20: Calculated dependence of SHG on azimuthal angle of the incident beam for a Si(111)-H interface. Each line shows the azimuthal dependence at a different angle of incidence of the fundamental beam. A 3-dimensional view is given in Figure G.19. SHG at $\theta = 45°$ is slightly greater than at $\theta = 30°$, and maximum SHG at $\theta = 45°$ occurs at $\phi = 60°$, while maximum SHG at $\theta = 30°$ occurs at $\phi = 0°$.

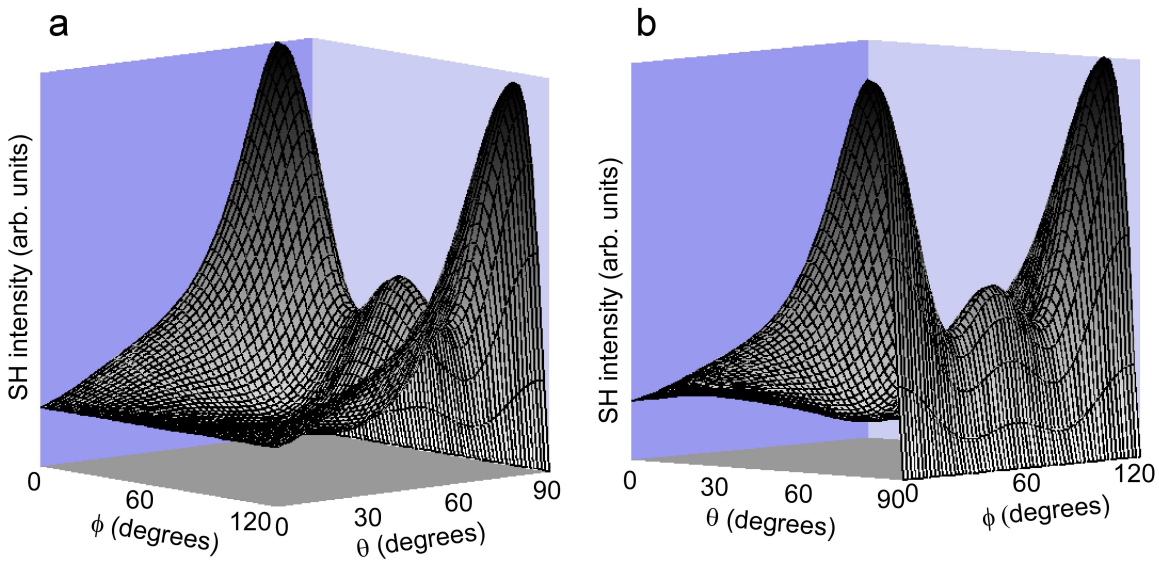

Figure G.21: Calculated angular dependence of SHG for a Si(111)/SiO_2 interface. The dependence was calculated using parameters listed in Table G.2 and Equation G.68. To account for the change in light penetrating the Si surface, Equation G.68 was multiplied by the square of the real part of the Fresnel coefficient for the transmission of p-polarized light, t_{pr}, given in Table G.1. Graphs (a) and (b) show different views of the same data.

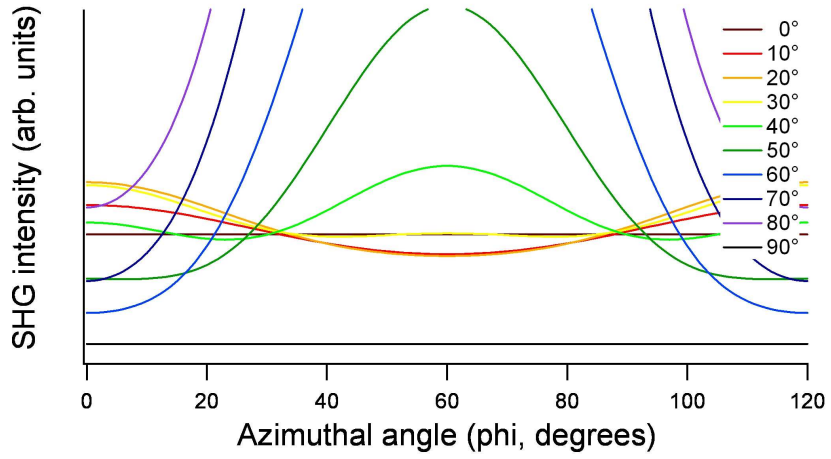

Figure G.22: Calculated dependence of SHG on azimuthal angle of the incident beam for a Si(111)/SiO_2 interface. Each line shows the azimuthal dependence at a different angle of incidence of the fundamental beam. A 3-dimensional view is given in Figure G.21. In this case SHG is always maximized at $\phi = \frac{2\pi}{3}n$, and SHG at $\theta = 45°$ is somewhat larger than at $\theta = 30°$.

θ than at small θ. The Fresnel coefficient of transmission of the fundamental light into Si shows the opposite relationship, with the result that $\|E_p\| : \|E_{0p}\|$ is larger at small θ than at large θ. Consequently in each case there exists an optimum angle of incidence. In all cases, the magnitude of SHG at $\theta = 30°$, the angle used in the research presented here, and $\theta = 45°$, the angle commonly used in SHG studies, is much less than at the optimum θ. In fact, as evident in Figure G.18, SHG is actually minimized at $\theta = 31°$ for the CdSe/Si system (for the Si-H and Si/SiO_2 systems SHG is minimized at $\theta = 0°$). For the CdSe/Si system SHG at 45° is greater than SHG at $\theta = 30°$ by a factor of 140. For the other systems this difference is much less - a factor of 1.5 for Si-H and 1.3 for Si/SiO_2 - but still present.

Second, the azimuthal angle at which maximum SHG occurs for a given angle of incidence is different at different θ, and further depends on the system under study. For the CdSe/Si(111) system (Figures G.17 and G.18) at small θ, $I_{pp}^{(2\omega)}$ dominates and SHG is maximized at $\phi = \pm\frac{2\pi}{3}n$. As θ increases, however, the contribution from $I_{ps}^{(2\omega)}$ briefly dominates ($\theta = 31° - 35°$), resulting in maximum SHG in the range $\phi = \pm\left(\frac{2\pi}{3}n, \frac{2\pi}{3}n + \frac{\pi}{6}\right)$. Finally, as θ continues to increase, the original pattern of maximum SHG at $\phi = \pm\frac{2\pi}{3}n$ is restored. Because of the large errors in the parameter fits, it is possible that the shift in the angle of maximum SHG is an artifact of the fit and not truly present. The $Si(111)/SiO_2$ system shows such a pattern; in this case SHG at $\phi = \pm\frac{2\pi}{3}n$ always dominates. The Si(111)-H system follows a different pattern for maximum SHG than the CdSe/Si(111) system; maximum SHG changes from $\phi = \pm\frac{2\pi}{3}n$ at small θ ($\theta \leq 35°$) to $\phi = \pm\left(\frac{2\pi}{3}n + \frac{\pi}{3}\right)$ at large θ ($\theta > 35°$).

While the brief dominance of $I_{ps}^{(2\omega)}$ in the CdSe/Si(111) system may be an artifact of the fit used to derive the parameters listed in Table G.2 (the errors for these parameters are large; this dominance has been neither predicted nor observed for other systems), the differences in behavior between the three systems also highlights the sensitivity of SHG as an interface probe. Since in all cases the bulk contributions

are the same, the differences in the angular dependence of SHG stem from differences in the relative magnitudes and phases of the surface nonlinear susceptibilities, which are dependent of the nature of the interface.

G.3.2 Angular dependence of EFISH

Having determined that the CdSe nanocrystal/Si(111) interface behaves in the expected manner with respect to time-independent SHG, we now examine how TD-EFISH generation varies with azimuthal angle. In previous experiments on Si(111) interfaces, it has been found that time-dependence is eliminated at azimuthal angles 60° from the angles giving maximum (time-independent) SHG.[343,344] However, these scans were performed at an angle of incidence of 45°. Since the experiments presented here were performed at an angle of incidence of 30°, two questions emerged. First, would changing the angle of incidence change the fundamental behavior of the time-dependence? Second, does the CdSe nanocrystal/Si(111) interface behave similarly to previously studied Si(111) interfaces?

To answer the first question, time-dependent scans were performed at several azimuthal angles on a sample of Si(111)-H. The results are displayed in Figure G.23. The scans shown are not offset, but show the correct relative magnitudes of SH intensity. The intensities at $t = 0$ are those seen in azimuthal scans of the sample. With respect to time dependence, the data show that maximum time dependence occurs in the scan at $\phi = 0°$, where the time-independent SH intensity is also maximized. The time dependence decreases as the azimuthal angle increases, until it has completely disappeared at $\phi = 60°$. This behavior is consistent with previous investigations of Si(111) interfaces, in which the angle of incidence was 45°. So in this respect, changing the angle of incidence did not affect the ability of the experimental setup to detect changing electric fields in the samples.

To answer the second question, whether the nanocrystal/Si(111) interface be-

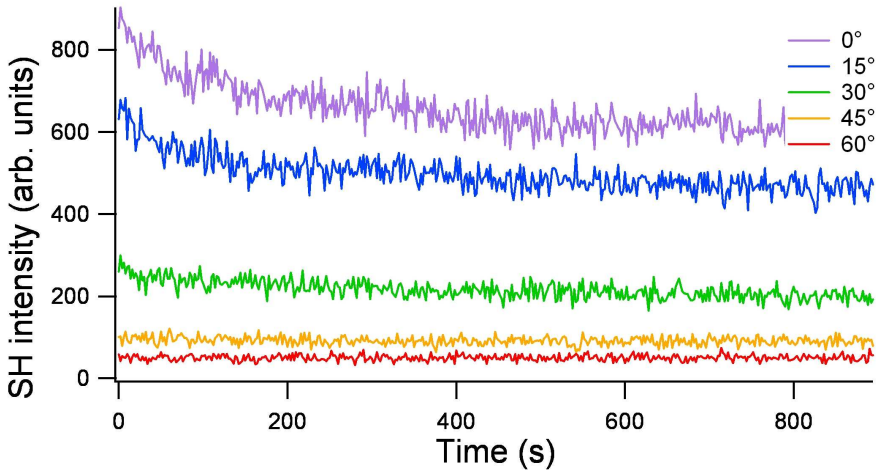

Figure G.23: TD-EFISH of Si(111)-H as a function of azimuthal angle. 0° corresponds to the angle yielding maximum time-independent SHG in an azimuthal scan of the sample. Scans were performed using a single-beam SHG setup at 800 nm.

haves like other Si(111) interfaces, time-dependent scans were performed at several azimuthal angles on a sample made from 72 Å nanocrystals, with surprising result. Figure G.24 shows that, like other Si(111) interfaces, maximum time dependence occurs at $\phi = 0°$ and decreases until minimum time dependence occurs at $\phi = 60°$. However, the time dependence never completely disappears. Even more interestingly, the nature of the time dependence changes. At angles other than $\phi \approx 60°$, the time dependence fits to three exponentials, but at $\phi \approx 60°$, the time dependence fits to only one exponential.

The change from three exponentials to one indicates a fundamental change in the behavior of the system. Two processes occur during TD-EFISH scans. The first is the absorption of light by Si, which generates free charges and hence an electric field across the interface. The second is the generation of the second-harmonic light, the intensity of which is dependent both on the electric field generated in the first process and on the angle at which the fundamental hits the sample. Since every Si(111) interface studied to date shows no time dependence at $\phi = 60°$ (except CdSe/Si(111)),

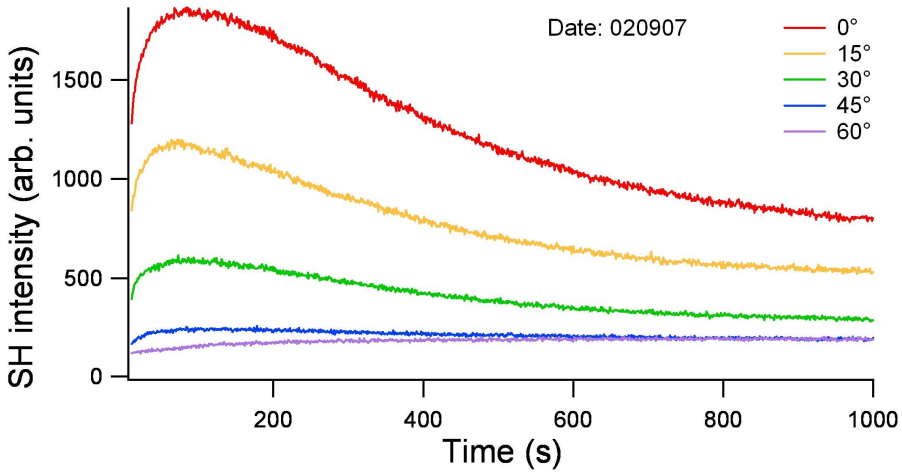

Figure G.24: TD-EFISH of 72 Å CdSe nanocrystal/Si(111) as a function of azimuthal angle. 0° corresponds to the angle yielding maximum time-independent SHG in an azimuthal scan of the sample. Scans were performed using a single-beam SHG setup at 800 nm.

it is likely that $\chi^{(3)} = 0$ at this angle regardless of the nature of the other half of the interface. This does not explain the continued time dependence of CdSe/Si(111) at $\phi = 60°$. Neither is this result explained by any change in extinction coefficient with changing azimuthal angle. A changing extinction coefficient would change the number of free charges available for transport across the interface, but not the nature of the 'trap' states in the nanocrystal layer. Therefore, a change in the generation of free charges would result in a change in the magnitude of SHG, not a change in the shape of the time dependence.

If the shape of the data at $\phi = 60°$ can be explained neither by SHG by Si nor by a change in the generation of free charges, and since the azimuthal scans of Si(111) (Figure G.23) show no signs of additional effects, such as sample heating, that might create time dependence in the data, then the only possibility remaining is that the time dependence stems from SHG by the CdSe nanocrystals.

Thus far we have not discussed SHG by the nanocrystals themselves. Initially it was not known whether or not the nanocrystals would generate SH light.

Wurtzite CdSe nanocrystals have C_{3v} symmetry, so they do not have inversion symmetry. In addition, the opposing Cd and Se faces generate a large dipole moment, and therefore an internal electric field of $\frac{0.25}{d}$ V, where d is the nanocrystal diameter (in Å), throughout the nanocrystal.[325] Both of these indicate that SHG by the nanocrystals should occur, and in fact SHG by CdSe nanocrystals in solution has been documented.[105,349,350] However, the nanocrystals in the CdSe/Si(111) samples were in contact with each other, in the form of a thin film, and were randomly oriented within that thin film. It was possible that the electric fields of the individual nanocrystals would interfere in such a way as to cancel out the electric field over the entire film; moreover, while each nanocrystal had no inversion symmetry, the overall structure of the film, being disordered, did have inversion symmetry, albeit on a scale larger than the crystalline lattice.

Finally, and perhaps most importantly, the nanocrystal film was extremely thin - typically between 0.5 and 3 monolayers (of nanocrystals), as measured by RBS. Even if the nanocrystals did generate SH light, there were so few of them present that it was thought that they could not contribute significantly to SHG by the sample as a whole. Then, too, what light was actually produced by the nanocrystals would be dispersed by the different angles of the nanocrystal facets. As seen in Section G.1.6, the angle of incidence of the fundamental beam on the sample surface determines the angle at which the SH light is emitted. Given the disordered nature of the nanocrystal layer and the numerous facets of each individual nanocrystal (20 in an ideal nanocrystal; somewhat more than that in reality), much of the light that hit the nanocrystals would hit facets that were not parallel to the Si(111) surface; any SH light produced by these non-parallel facets would not be emitted at the same angle as SH light generated by the Si(111). While the experimental setup included a focusing lens for the SH light, the lens was several centimeters from the sample, and the photon detector was a few decimeters from the sample, so that most of the SHG

from the nanocrystals would disperse and not be detectable by the counter.

So, it was first thought that detectable SHG by the CdSe nanocrystals was unlikely, until the results of Figure G.24 were obtained. The next question to answer was, could SHG by the nanocrystals explain the single-exponential shape of the curve at $\phi = 60°$? Well, possibly. The time dependence from Si(111) results from charges crossing the CdSe/Si interface and trapping in the CdSe; the nanocrystals therefore experience the same electric field, and this should cause the same triple exponential shape to the time dependence of SHG from CdSe. However, the nanocrystals have a second electric field affecting SHG: the previously mentioned internal electric field caused by the opposing Cd and Se faces. This field is very large, and may overwhelm the response from the interfacial electric field. In this case, any charge entering a nanocrystal would spend the majority of its time near (or on) the face with opposing charge - electrons near the positive Cd face, and holes near the negative Se face. The effect of this would be that any charge crossing the interface would act to oppose the internal electric field of the nanocrystal it inhabited, regardless of the sign of the charge. This would cause a unidirectional change in the magnitude of the electric field, provided there was only one type of charge per nanocrystal. Of course, if two charges of opposite sign entered the same nanocrystal, they could recombine, regenerating the original internal field. Between the two competing electric fields that each nanocrystal experiences, internal and interfacial, it is difficult to tell how SHG from the nanocrystals would change in time.

As an additional complicating factor, CdSe nanocrystals can also move about on the surface of a substrate. This has been directly observed during HR-TEM. It is possible that the nanocrystals could actually align themselves so that their internal fields opposed the interfacial field being generated by charge transfer. If this occurs, then there would be no effect on the electric field experienced by the Si, but the net electric field experienced by each nanocrystal would be reduced. The align-

ment of the nanocrystals would occur over a long period of time because of dangling bonds holding the nanocrystals in place, and because alignment would require most nanocrystals to move from resting on one facet to another. Alignment would occur with a greater probability of alignment as the interfacial field grows. What force is required to shift a significant portion of the population is unknown, so how much of a factor nanocrystal alignment is in the observed time dependence is also unknown. Regardless, between the nanocrystals' internal electric fields and ability to physically move on the substrate, it is possible, even likely, that the time dependence observed at $\phi = 60°$ is attributable to SHG by the nanocrystals rather than by Si.

G.3.3 Band offset measurements

Unfortunately, preliminary results revealed that band offset measurements of the Si/CdSe system would not be feasible. There are a number of reasons for this conclusion. First, obtaining good overlap of the pump and probe beams proved exceedingly difficult due to reflections from the sample holder window. While overlap could be obtained using Si/SiO_2 samples, whose time-dependent behavior was established without the use of a sample window, the overlap obtained using these samples did not quite translate to the Si/CdSe samples. In switching between the samples, there were small but significant changes in the location of the sample surface in the z-direction. Since the time-dependent behavior of the Si/CdSe samples was not known, it was thus difficult to make adjustments to the pump beam placement to improve overlap by relying on the resultant SH intensity. Ultimately, this problem could have been resolved by using a cryostat in place of the home-built sample chamber; however, at the time no cryostats were available for use.

In addition to the difficulty in overlapping the two beams, the time required for measurements was much longer than expected. As discussed in Section G.2.4, the maximum scan time allowed by Lab Director was 50 minutes, which was insufficient

time to allow the system to equilibrate (for time-dependence to cease). As a result, fitting the data yielded fits with large uncertainties. In comparison, the Si/SiO_2 system equilibrated in less than 10 minutes,[322] making band offset measurements using this technique more feasible.

A third difficulty in using this technique on the Si/CdSe system lay in the fact that the system showed time-dependence at all probe intensities. The two-beam experiment was originally designed so that the probe beam was at such low intensity that the probe beam applied by itself to the sample provoked no charge transfer across the interface, and therefore no time-dependence. Since this was not possible in the Si/CdSe system, the measured time-dependence in pump-probe scans was caused by charge transfer due to the probe beam as well as the pump beam, complicating analysis. The solution to this problem was to move to a single-beam experiment, in which the probe beam served both to promote charge transfer and to interrogate the interfacial electric field; however, in view of other difficulties with the experiment, this was never attempted. It is noted, however, that the fact that the probe beam always elicited charge transfer indicates that the barriers to charge injection in this system are small.

The small barriers to charge injection resulted in yet another problem, namely that we observed at least three different trap states, as discussed in Section G.3.2. By changing wavelengths, it should be possible to observe these states turning on and off, yet the fact that two of the trap states were for one charge carrier, while the third was for the other charge carrier, complicated analysis. It was unknown which trap state(s) corresponded to which charge carrier, and SHG is insensitive to the sign of the electric field. There was no method of distinguishing charges.

Ultimately, however, the primary reason that the SHG experiments were abandoned was the instability in the Quantronix Titan amplifier. As demonstrated in Figure G.12, the Titan at the Free Electron Laser Center showed massive instability

as a result of a design flaw in the chiller used to cool the Titan and its YLF pump laser. The CMASS Titan had a more stable chiller, yet was still remarkably unstable. According to John Kozub at the Free Electron Laser Center, the shot-to-shot variation in pulses output by the Titan is supposed to be ±50%. Added to this instability is the fact that neither laboratory in which experiments were conducted had sufficient temperature control to keep the long-scale power of the Titan from drifting. In fact, the alignment of the Titan had to optimized approximately once an hour to maintain power. Given that scans lasted for 50 minutes, the Titan had to be optimized once per scan. Often, power decreased or increased abruptly mid-scan due to temperature changes in the room. As detailed in Section G.2.4, a photon counter was used to monitor the power of the pump beam during scans, so it was possible to normalize SH intensity to the power of the beam. However, band offset measurements involved measuring the power-dependence of the lifetime of trap charging, measured over an entire scan. Because of the instability in the Titan, the long-term power of the pump beam wandered so much over the course of a scan that it was impossible to take power-dependent measurements. Thus, band offset measurements of the Si/CdSe system were abandoned shortly after the completion of the preliminary experiments.

APPENDIX H

LASER OPERATION AND ALIGNMENT

As mentioned in Appendix G, two essentially identical laser systems were used to conduct SHG experiments. The systems were composed of a Verdi laser, a Mira laser, a Nd:YLF laser, a Titan amplifier, and two TOPAS optical parametric generators. As these systems have not previously been used by members of the Rosenthal group, this appendix details the procedures used during the daily operation of the lasers. In addition, as the systems were extremely unstable and required frequent realignment, alignment protocols for aligning the Mira and Titan are also included, as the published manuals, particularly the Titan, proved inadequate for actually aligning the lasers. The procedures outlined here are based on the procedures given in the laser manuals, discussions with Dr. John Kozub of the W. M. Keck Free-Electron Laser Center at Vanderbilt University, and discussion with various technicians at Coherent and Quantronix, as well as on personal experience.

H.1 Daily laser operation

This section details the procedures used to turn on, operate, and turn off the lasers on a daily basis, when the lasers are in good alignment.

H.1.1 Turning on the lasers

This subsection provides a step-by-step procedure for turning on the laser system for daily operation.

1. Before turning on the lasers, make sure that:

   (a) There is adequate deionized water in both the Mira chiller and in the YLF/Titan chiller;

(b) The valve on the chilled water line leading to the YLF/Titan chiller is open;

(c) The temperature in the lab is approximately 72 °F; and

(d) The Mira's output aperture is blocked, and the Mira's controller is on and set to "CW" (continuous-wave mode).

2. Turn on the "LASER IN USE" sign.

3. Turn the key on the Verdi's controller from "standby" to "on". Push the "shutter open" button beside the display on the controller. Quickly turn on the Mira's chiller using the switch at the bottom rear of the right side of the chiller.

4. Verify that the chiller's set point is 19 - 20 °C. When operating properly, the chiller cycles between 17 °C and 22 °C over the course of a minute. If the set point is incorrect, set it properly using the front panel display.

5. After several seconds, the Verdi output should begin to appear. Verify that the power setting on the Verdi's controller is set to its last operating power (in the range $.00 - 5.5$ W.

6. Turn on the line voltage on the Medox, which controls the Titan.

7. Wait at least 45 minutes for the Mira to warm up.

8. Set a fast photodiode attached to a high-frequency (at least 400 MHz) oscilloscope to monitor the Mira's output. The full power of the Mira overloads a photodiode, so the beam should be attenuated through the use of filters or other methods. Alternately, detach the BNC cable from the "RF input" hookup on the Medox and attach it to a high-frequency oscilloscope - this cable is attached to the Mira's internal photodiode.

9. Set up a spectrometer to monitor the Mira's output. As with the photodiode, it is necessary to attenuate the beam.

10. On the Mira's controller, switch the Mira from "CW" to "modelock". Place a power meter directly in front of the Mira's output.

11. Using the dial on the Mira that controls slit width (the only unmarked dial accessible through the Mira's cover), dial the slit width until the power on the power meter reads 750 mW. Optionally, the power of the Mira can be optimized according to the procedure given in Section H.2.5. On the Mira's controller, toggle the "peak reset" switch to center the lower power display on the controller. Remove the power meter and direct the output to the photodiode and spectrometer.

12. Using the "CW" display on the Mira's controller, the spectrometer, and the photodiode, verify that the Mira modelocks properly. When the laser is modelocked, no CW registers on the controller, the oscilloscope trace shows stable, isolated peaks with a period of 13.1 nm, and the spectrometer shows a Gaussian peak, with no strong spikes. If any of the three monitors appears other than described, CW is present. In addition, the peak on the spectrometer should be centered at 803 nm, with a full-width at half-maximum (FWHM) of at least 12 nm. If CW is present, or if the beam profile on the spectrometer is incorrect, refer to Section H.2.4.

13. Once modelock and proper beam profile have been achieved, completely unblock the beam. Make sure the beam travels unimpeded to the Titan. If the Mira's internal photodiode was hooked up to an oscilloscope, unplug the BNC cable at the oscilloscope and return it to the "RF input" on the Medox.

14. Turn on the high voltage on the Medox. Turn on the oscilloscope above the Titan. Verify that a BNC cable leads from the Titan's internal photodiode to channel 1, and that a BNC cable leads from the output on the Medox to the external trigger on the oscilloscope. Use the beam blocks on the TOPAS units to block input into the TOPAS units.

15. Turn the key on the YLF controller to "ON".

16. After a few seconds, turn on the YLF's and Titan's chiller using the toggle just to the left of the key on the YLF controller. Five lights should turn on: a green light indicating that the chiller is on, and four indicator lights monitoring water level, flow, temperature, and ion content. The indicators can be green, indicating optimal conditions, yellow, indicating marginal conditions, or red, indicating unacceptable conditions. Water level and flow should be green. If water level appears yellow or red, turn off the chiller and the controller key and add 18 Ω deionized water to the chiller; water from water purifiers stationed throughout Stevenson Center is sufficient. If the flow light appears yellow or red, refer to the YLF's operating manual or contact Quantronix. The temperature indicator may initially be red, but should quickly turn yellow. If the temperature remains red, refer to the YLF's operating manual. The ion indicator initially appears red, but should eventually turn green. The length of time required for the ion indicator to turn green depends on the amount of time that has passed since the chiller was last turned on; generally it takes less than 30 seconds when the YLF is in daily use, but it has been known to take more than 10 minutes when the YLF has been left off for more than a month. If the light fails to turn green, the water in the chiller should be drained and replaced with fresh deionized water.

17. Once the indicators for water level, flow, and ion content are green and the temperature indicator is yellow, the current toggle, located just to the right of the chiller indicators, should be switched on. After a few seconds, the digital readout just to the right of the current toggle should change from about 0 A to about 6.6 A. Use the dial next to the readout to increase the current to its normal operating value. This value slowly increases over time as the YLF's lamp ages; the correct amperage can be found by consulting the operating log book for the latest value. The amperage should never exceed 35 A, as this much current rapidly degrades the YLF's lamp.

18. Verify that the Titan's chiller controller, a small box protruding slightly from the side of the Titan, is turned on.

19. The display to the right of the current display shows the frequency at which the YLF is lasing. Verify that this reads approximately 1.00 kHz (1.01 kHz or 1.02 kHz is also acceptable). If the frequency is wrong, use the dial next to the display to obtain the proper frequency.

20. Open the YLF shutter using the right-most switch on the YLF controller. Immediately verify that the YLF's output appears as a bright, stable beam that travels unimpeded to the Titan. If strobing is evident, or if an object is in the beam, immediately close the shutter, and, if necessary, turn off the YLF until the problem can be identified and rectified.

21. Observe the pulse train on the Titan's oscilloscope. It should appear s a series of sharp spikes, first increasing, then (possibly) decreasing in intensity, similar to that shown in Figure H.16. If a pulse train appears but is deformed, close the YLF's shutter until the source of the deformity is determined and rectified. The source of the problem is usually traceable to the output from the Mira or the YLF, or to an object impeding the Mira or YLF beams, though misalignment of

the Titan is also a possible source. If no pulse train appears, and the oscilloscope settings are correct, then disconnect Delay 2 on the Medox. If a pulse train still fails to appear, then likely the optics leading up to the Titan or within the Titan are misaligned. Close the YLF shutter until the misalignment has been identified and rectified.

22. If a normal pulse train appears, then verify that Delay 2 is connected and wait 3 hours for the YLF and Titan to warm up. During this period, the pulse train should be closely monitored for signs that the pulse train is failing. A failing pulse train registers on the oscilloscope as fewer and fewer spikes. If the number of spikes decreases to three or fewer, the last seed and pump input mirrors (the mirrors next to the Titan that direct the Mira and YLF beams into the Titan) should be adjusted slightly to regain power. Otherwise the Titan should be left alone. Periodically, the power display on the Mira's controller and the current display on the YLF's controller should be checked to ensure that the Mira and YLF beams have the correct power. Frequently, small adjustments to the Mira's slits and the YLF lamp current are necessary during the warm up period to maintain correct power.

    It is noted that once the Titan is running, it cannot be left unattended. If something happens to destabilize the system, the optics within the Titan can be damaged in a matter of seconds.

23. Place a power meter directly in front of the Titan's output without blocking the YLF beam. Observe the pulse train on the oscilloscope. The pulse train should be 'chopped' one or two peaks after the peak with maximum intensity. If it is not, change Delay 2 until power is maximized on the power meter. The last peak before chopping should be at full height.

24. Ideally, the power should read at least 3.2 W, although the system has been operated on as low as 2.9 W. If the power is low, try tweaking the last two mirrors on both the Mira and YLF beams before input into the Titan. Note that the second-to-last mirrors are more sensitive that the last mirrors, so these should be tuned with care. If these are adjusted, then Delay 2 should also be adjusted according to the previous step.

25. Remove the power meter. Record the date, the YLF's lamp current, and the Titan's output power in the log book.

26. Use a business card to observe the Titan's output beam just in front of the beam block of each TOPAS that is to be used. The beam should be a structureless, round spot, with no visible clipping. If structure or clipping is observed, the Titan likely needs to be realigned.

27. If no structure or clipping is evident, and if the beam passes through the approximate center of the aperture before the beam block, then unblock the beam.

28. Place a business card between the TOPAS(es) and the mixing crystal. A large, purple spot should appear on the card. If no spot is evident, or if the spot shows structure or clipping, then either the mirrors leading from the Titan to the TOPAS or the TOPAS itself are misaligned. If the spot appears normal, remove the business card.

29. Wait 15 minutes for the TOPAS(es) to warm up.

30. On the computer by the TOPAS units, open the WinTOPAS program. Select the appropriate TOPAS - the UV/Vis TOPAS has a blue background in the program, while the IR TOPAS has a black background. Enter the desired wavelength into the program and hit "Enter". The program uses a calibration file to automatically change the position of the crystal within the TOPAS so

that the correct output is obtained. Adjust the crystal and mirror settings within the TOPAS to maximize power. Verify the output wavelength using a spectrometer.

H.1.2 Laser operation

Once the lasers have warmed up and are operating properly, very little maintenance is required to keep them running well. About once an hour, the power display on the Mira's controller and the current display on the YLF's controller should be checked to ensure that these beams have the correct power, with adjustments to the Mira's slits and the YLF's lamp current as necessary. At the same time, the Titan's seed and pump input mirrors should be adjusted to maximize power from the Titan, and Delay 2 should be checked to verify that the power train is still chopped correctly. Changes in room temperature and humidity, as well as other effects, make significant changes in beam alignment over the course of the day. Every time the wavelength of a TOPAS is changed, the TOPAS input mirrors should also be tweaked for maximum power. If only one wavelength is to be used, the TOPAS input mirrors should be tweaked after the Titan's input mirrors are tweaked.

Although the system is more or less stable, it cannot be left unattended because of the potential for damage should the system destabilize. To that end, if it is necessary to leave the system for less than an hour, the YLF shutter should be closed. Upon returning, the shutter should be opened and the system given enough time to stabilize - a few minutes for shorter absences, and longer (20 - 30 min.) for longer absences. If it is necessary to leave the system for more than an hour, then the shutdown procedures detailed in the following section should be followed until the YLF has been shut down and the Mira beam has been blocked. Upon returning, the startup procedures should be followed in total.

H.1.3 Laser shutdown

1. Close the WinTOPAS program. Use the TOPAS' beam blocks to block the input from the Titan.

2. Close the YLF shutter. Dial down the YLF's lamp current to its minimum value and turn it off. Wait 5 minutes for the YLF and Titan to cool down, then turn off the YLF's chiller and then its power key.

3. Use a beam block to block the Mira's output. Switch the Mira from modelock to CW mode. At this point, the laser can be left unattended for long periods of time.

4. Turn the key on the Verdi's controller from "ON" to "STANDBY". Quickly turn off the Mira's chiller. Press the "OPEN SHUTTER" button on the Verdi's controller to close the Verdi's shutter.

5. Turn off all remaining equipment, not including the controllers or the computer controlling the TOPAS units: oscilloscopes, power meters, etc.

6. Turn off the "LASER IN USE" sign.

H.2 Mira 900 alignment

H.2.1 Preliminary remarks

The Mira 900 operating manual[351] provides a good procedure for aligning the Mira 900 laser. The procedure given here is based on that given in the manual. It differs in the few places where the manual is confusing or insufficient, and it is geared specifically towards alignment of the Miras used to seed the Titan amplifiers in the SHG setups.

Figure H.1 shows the optics of the Mira 900. The primary components of the system are 13 mirrors (P1 - P4 and M1 - M9), two Brewster's prisms (BP1 and BP2),

a birefringent filter (BRF), a butterfly starter, and a slit assembly. The function of each of these optics is given in Table H.1. Pump beam mirrors (P1 - P4) are labeled in the order used (e.g., P1 is the first mirror that the pump beam encounters, while P4 is the last). Laser cavity mirrors are labeled in the order used, starting with the output coupler (M1) and ending with the end mirror (M7, or M9 when the auxiliary cavity is used).

The path of light through the Mira can be broken into four major components. The first section (containing P1 - P4 and a focusing lens) is the path of the pump beam from the input window to the Ti:sapphire crystal. Alignment of this section is trivial; provided the beam does not clip the edges of any of the optics, particularly the Ti:sapphire itself, the pump beam path will not prevent lasing. The second section is the auxiliary cavity (M5, M8, and M9). The sole purpose of the auxiliary cavity is to allow alignment of M1 - M4, which, together with the starter, the slit assembly, and the birefringent filter, comprise one-half of the main lasing cavity. Aside from functioning as half the lasing cavity, this third section selects the wavelength at which the laser lases, modelocks the system, and provides control of the power of light emitted by the laser. The fourth section (M5 - M7, BP1, and BP2) is the other half of the main cavity and controls the bandwidth and duration of the laser pulses.

The following three sections discuss the full alignment of the Mira 900. Section H.2.2 details alignment of the auxiliary cavity and mirrors M1 - M4 of the main cavity. Section H.2.3 details alignment of mirrors M6 and M7 of the main cavity. Section H.2.4 details alignment of the birefringent filter, BP1, BP2, and the slit assembly.

H.2.2 Auxiliary cavity alignment

Auxiliary cavity alignment should be performed only in the event that the laser is not lasing, as moving BP1 changes both the stability of the laser and the temporal/spectral shape of the output pulses. Auxiliary cavity alignment aligns M1

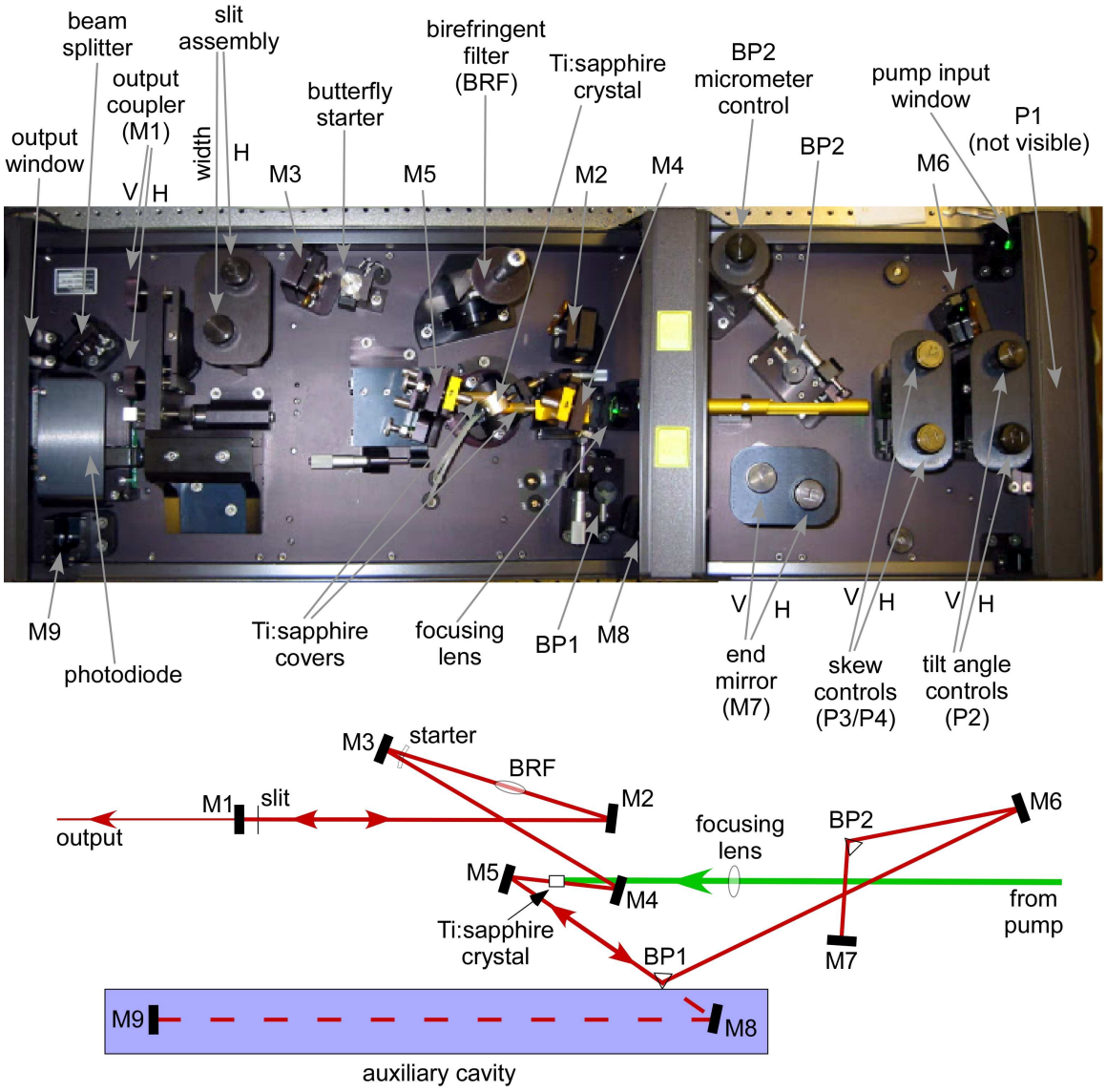

Figure H.1: The Mira 900 laser.

Table H.1: Primary optics in the Mira 900 and their functions.

optic	function
P1	Directs the pump beam into the cavity.
P2	Changes the tilt angle of the pump beam, or the angle at which the pump beam is incident on the Ti:sapphire crystal.
P3/P4	Change the skew of the beam. One set of controls both mirrors jointly, changing the horizontal and vertical placement of the pump beam on the Ti:sapphire, but not the angle at which the beam hits the crystal.
M1	The output coupler. This 95% reflective mirror is one of the two end mirrors for the laser cavity. The 5% transmitted light is the output from the laser.
M2	Directs light from M3 and the butterfly starter to M1 and back again. Used during alignment to find the retroreflection from M1.
M3	Part of the starter assembly. Light passes through one 'wing' of the butterfly starter, hits M3, and reflects through the other wing of the starter.
M4	Directs light from the Ti:sapphire crystal to the starter assembly.
M5	Directs light from the Ti:sapphire crystal to either M8 (during auxiliary cavity lasing) or BP1 (during normal operation).
M6	Directs light from BP1 into BP2. Used in alignment to find the retroreflection from M7.
M7	The 100% reflective main cavity end mirror.
M8	Directs light from M5 to M9 during auxiliary cavity lasing. Used during alignment to locate the retroreflection from M9.
M9	The 100% reflective auxiliary cavity end mirror.
BRF	The birefringent filter. Selects the wavelength at which lasing occurs.
BP1	Together with BP2, controls the path length of the beam inside the cavity, thus influencing bandwidth and pulse duration.
BP2	Together with BP1, controls the path length of the beam inside the cavity, thus influencing bandwidth and pulse duration. Also has a minor effect on the wavelength at which lasing occurs.
butterfly starter	Modelocks the laser by momentarily disrupting the beam path whenever continuous-wave (CW) light is detected.
slit assembly	Controls the power output by the laser by limiting the width of the beam hitting M1. Also influences the stability of the lasing by limiting the width of the beam.

- M4, one-half of the main laser cavity, and provides lasing light which can be used in alignment of the other half of the main laser cavity (Section H.2.3).

Laser goggles that filter out the 532 nm light from the Verdi pump laser should be used both to protect the eyes and to better see the red light from the Ti:sapphire crystal. The Mira also has an alignment tool which should be used to vertically align the system. Finally, an IR viewer is useful, as much of the output from the Ti:sapphire is IR. Before changing anything about the setup inside the Mira, record the micrometer settings on the birefringent filter and both Brewster's prisms.

1. Remove the slit assembly. If the birefringent filter has been moved and the original placement or correct micrometer settings are unknown, remove the birefringent filter. Be sure to mark its exact placement in the laser cavity, as its mounting screws allow it to rotate.

2. Dial the power from the Verdi down from 5 W to 100 mW to prevent eye damage. Verify that the Mira is in CW mode.

3. Verify that the exterior knobs controlling tilt and skew (P2 - P4) are near the center setting. Each knob can make 36 complete turns; to ensure that future adjustments are possible, the knobs should be set between 12 and 24 turns.

4. Verify that the pump beam does not clip the edges of any of the pump mirrors (P1 - P4). If the beam clips any edge, then either the Verdi pump laser is misaligned with the Mira, or P1 is out of alignment; refer to the section entitled "Mira Installation" of the Mira 900 Operating Manual.[351]

5. Slide back the covers for the Ti:sapphire crystal. Verify that the pump beam passes cleanly through the Ti:sapphire crystal, somewhere near the center of the crystal. If the beam hits the edge of the crystal, it can burn the crystal. If the beam is near the edge, or if there is visible damage to the area through which

the beam passes, use the pump skew and tilt controls to move the beam into good alignment on the crystal. If skew and tilt cannot fix the problem, refer to the section entitled "Mira Installation" of the Mira 900 Operating Manual.[351] Slide the covers back into place.

6. Dial the power from the Verdi back to 5 W.

7. Turn the micrometer on BP1 until BP1 is completely out of the path of the beam. Use the M5 horizontal control to horizontally center the beam on M8.

8. Turn the micrometer on BP1 until no light is present on M8. Turn roughly an additional four turns. The green pump light should appear as a bright spot on the M6 mount, while red fluorescence from the Ti:sapphire crystal should appear as a broad band that is mostly on M6; it may clip the edge of the mirror in the direction of the green spot. Use the M5 vertical control and the Mira's vertical alignment tool to vertically align the beam on M6. Then back BP1 out of the path of the beam.

9. Use the M8 adjusts to center the pump beam on M9. Note that the M8 controls are reversed from the normal positioning - the horizontal adjust is at the top, and vertical is at the bottom.

10. Use M9 controls to position the retroreflected pump beam one beam diameter to the right of the original beam spot (so that the two spots touch).

11. Place a white business card directly in front of M3. Use M4 vertical control to vertically center the red beam in the shadow of the butterfly prism. Note that the beam is larger than the height of the prism, so it should clip both on the top and on the bottom. Remove the card.

12. Rotate the M3 alignment aperture exactly over M3. Use M4 horizontal control

to horizontally center the red beam on M3. DO NOT vertically center the beam in the aperture. Remove the aperture.

13. Place a business card directly in front of the output coupler (M1) to block the retroreflection on M2. Rotate the M2 alignment aperture exactly over M2. Using the vertical alignment tool and the M3 vertical control, vertically align the beam on M2. Using the M2 alignment aperture and the M3 horizontal control, horizontally align the beam on M2. A portion of the beam that does not pass properly through the prism appears just above the true beam; ignore this. Note that the M3 controls are reversed from normal.

14. Remove the business card from M1. Use M2 controls and the vertical alignment tool to center the beam on M1.

15. Use M1 controls to center the retroreflection from M1 in the alignment aperture on M2. The knob nearest the Titan is the vertical adjust. Remove the aperture.

16. At this point the cavity may lase. If it does not, make small adjustments to the two end mirrors, M9 and M1. Typically M9 is the mirror that needs adjustment to make the auxiliary cavity lase, as the placement of its retroreflection is less exact than M1's. Once the system begins lasing, make slight adjustments to M9 and M1 to maximize power output. Then adjust the tilt angle controls (P2) to maximize power. A well-aligned auxiliary cavity (without the birefringent filter) should output at least 1.2 W with a pump power of 5 W.

17. If the birefringent filter has been removed, replace it at this point and repeat the alignment of M2 and M1 and power maximization (steps 13 - 16).

18. If the birefringent filter has been removed, tune it to peak power. Note that power output will increase and decrease several times while scanning through

all angles, and lasing can disappear at certain wavelengths. Once the beam is at 800 nm, power output should be approximately 1.2 W.

H.2.3 Main cavity alignment

1. Verify that the exterior knobs controlling M7 are near the center setting. Each knob can make 36 complete turns; to ensure that future adjustments are possible, the knobs should be set between 12 and 24 turns.

2. Turn the micrometer on BP1 until the auxiliary cavity is lasing at 30 - 50% of full power. A green spot, a red band, and a red spot will appear on M6. The red spot should be somewhere near the center of M6. Center the M6 aperture on the spot.

3. Use M6 controls to steer the reflection of the red spot through BP2 to near the center of M7. At 805 nm, the beam should be exactly centered; at 800 nm, the beam should be slightly towards the output coupler.

4. Use M7 controls to steer the retroreflection back through BP2 to the center of the aperture on M6. Remove the aperture on M6.

5. Make small adjustments to M7 until the main cavity begins to lase (the power on the photodiode will increase above the level of the auxiliary cavity lasing). Continue to adjust M7 until power is maximized.

6. Turn the micrometer on BP1 until all light passes through the prism and no light goes to the auxiliary cavity. Turn the micrometer an additional 4 turns. Adjust M1, M7, and P2 to maximize power.

7. Reinstall the slit assembly. Open the slit fully, and use the horizontal slit adjust to maximize power.

8. Close the slit until the laser is lasing at half power. Use the horizontal slit adjust to maximize power. Repeat until no further improvements can be made. Open the slit fully again.

9. Turn off the Verdi. Clean all the optics with spectroscopic-grade methanol or acetone then methanol, including the Verdi output window, which can be accessed by unscrewing the silver ring surrounding the window.

H.2.4 Modelocking and obtaining the proper pulse shape

Modelocking the Mira and obtaining the proper spectral/temporal pulse shape for input into the Titan are primarily accomplished by adjusting the birefringent filter (BRF), BP1, and BP2, all of which have interrelated functions. The BRF tunes the average wavelength of the pulse. BP1 and BP2 jointly control the bandwidth and the pulse duration, which follow an inverse relationship: the broader the spectrum of a pulse, the shorter the duration of the pulse. BP2 in particular also changes the average pulse wavelength, though its influence on wavelength is much less than that of the BRF. Thus it is necessary to adjust all three components simultaneously.

1. Remove the Mira trigger cable from the RF input port of the Titan's Medox controller and plug it into an oscilloscope via a 50-Ω termination cap. Set the time scale on the oscilloscope to 5 nm or 10 nm. This provides a graphic measure of the degree of modelock.

2. Close the slit width until a power meter placed just outside the Mira registers 750 mW. On the Mira controller, toggle PEAK RESET to center the lower power bar on 750 mW. Then remove the power meter head. The lower power bar can now be used as a measure of the power output of the Mira when the power meter head is not in the beam path. (It is noted that when the alignment inside the Mira is changed, the photodiode reading on the controller

also changes; it is not an absolute measure of power. However, changes to the BRF, BP1, BP2, or any of the exterior adjustment knobs do not change the alignment, so the photodiode can be used to monitor power.)

3. Place a spectrometer in the beam path. Turn the micrometer on the BRF until the average wavelength is 803 nm. If power drops very slightly, open the slit until power is again 750 mW. The slit should not be opened fully. If the power drops significantly (e.g., more than 10%), adjust BP1 and BP2 until power is again 750 mW.

4. On the Mira controller, switch from CW mode to MODELOCK. There are three measures for modelock: 1) the Mira controller does not show any CW on the CW display; 2) the oscilloscope attached to the Mira photodiode displays a series of nearly Gaussian peaks that are completely stable (in particular, there should be no fluttering of the signal at the base of the peaks) and that have a period of 13.2 ns (Figure H.2); and 3) the emission spectrum is Gaussian, with no spiking present at the central wavelength. It is possible for one or two of the three indicators of CW to show CW present, while the other indicator(s) shows only modelock; therefore, all three indicators should be used when checking for modelock. For purposes of comparison, Figure H.3 shows an oscilloscope trace of CW with no modelock whatsoever. In cases where only a little CW is present, the oscilloscope trace appears very similar to that in Figure H.2, but a slight instability is present at the base of the pulses. Figure H.4 shows the oscilloscope trace of the Mira cavity aligned so that a 'double pulse' is present. Notably, the Mira controller cannot detect when double pulsing is present, and its display usually indicates that the Mira has modelocked without any problems. Double pulsing is only detectable by oscilloscope. When good modelock is obtained, the system should maintain modelock when the operator taps anywhere on the

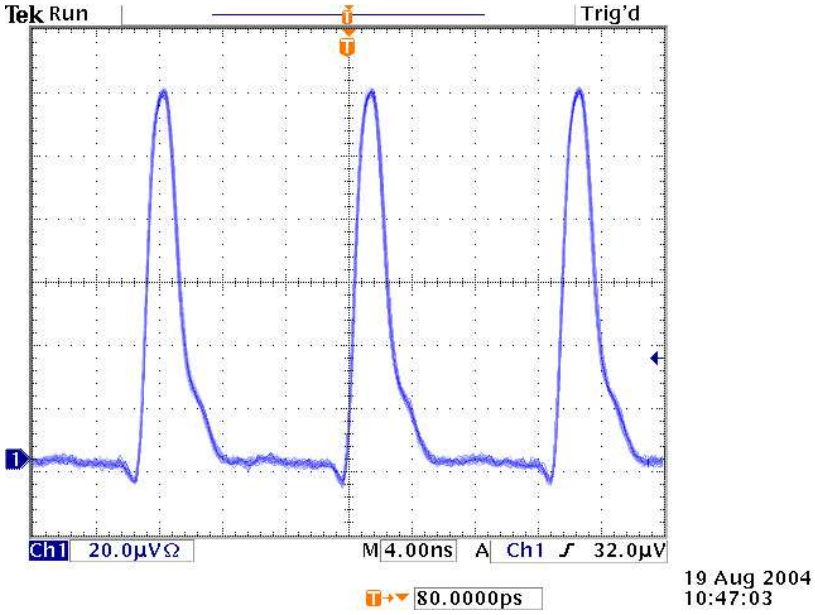

Figure H.2: Modelocked Mira 900 pulses.

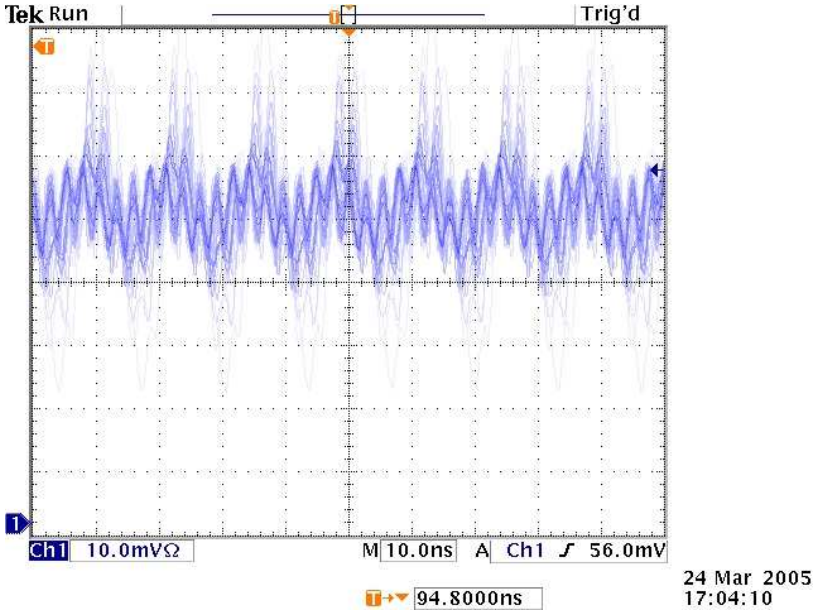

Figure H.3: Oscilloscope trace of CW from the Mira.

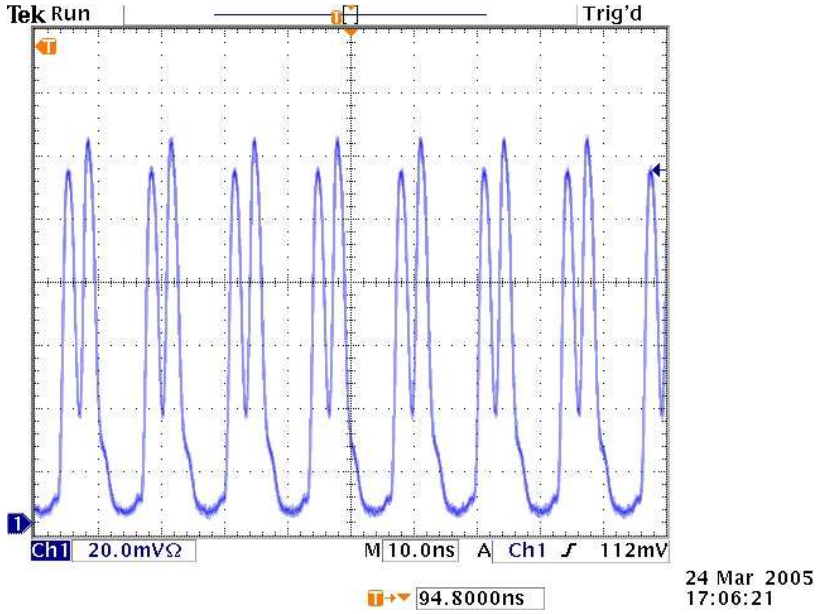

Figure H.4: Oscilloscope trace of double pulsing within the Mira.

Mira's case. If the system automatically modelocks, skip to step 9.

5. Using the micrometers, vary the positioning of BP1 and BP2 until modelock is achieved. This can be accomplished in a variety of ways. One suggestion is to move BP1 through all positions at which the Mira lases, find the most stable position by looking at the photodiode oscilloscope, then scan BP2 through all positions to find the point at which the Mira is most stable. Repeat as many times as needed, making successively smaller adjustments to BP1, then BP2, until the most stable position is achieved. As moving BP1 and BP2 also changes the path of the beam, it is recommended that M7 also be adjusted periodically to regain stability.

6. If the laser is still not modelocked, try adjusting the horizontal slit control, the end mirrors, the tilt angle controls, and the skew controls. Usually the horizontal slit positioning has a dramatic effect on the stability of the laser.

7. Using the BRF, readjust the central wavelength to 803 nm. Using the slit width control, readjust the power to 750 mW.

8. Verify that modelock is maintained. If not, repeat steps 5 - 7 until stable modelock is achieved at 750 mW and 803 nm.

9. Using the spectrometer, find the full width at half maximum (FWHM) of the output spectrum. For proper seeding of the Titan, the bandwidth should be 10 - 12 nm (having sufficient bandwidth also ensures that the pulse duration is sufficiently short).

10. If the bandwidth is too small, increase the path length of the beam through BP1 by changing BP1's position. Stop when the laser begins to lose modelock. Compensate by adjusting the end mirrors, then the horizontal slit control, the tilt angle controls, and the skew controls.

11. As before, use the BRF to move the central wavelength back to 803 nm and the slit width to obtain a power of 750 mW. Repeat steps 10 and 11 until at least 10 nm bandwidth is obtained while the system is stably modelocked.

12. Place the power meter head back into the beam and verify that the laser is stable over a wide power range. At least 670 - 830 mW is recommended. If the laser loses modelock within this range, increase or decrease the power until the laser is barely modelocked and make fine adjustments to the BRF, BP1, BP2, M1, and all external controls until modelocking has stabilized. Make sure to maintain the proper wavelength, bandwidth, etc. Repeat, working up or down in power until the desired power range is achieved.

13. Replace the Mira's cover panels and allow the laser to thermally equilibrate (about 45 min.).

14. Pressure from the cover panels slightly changes the alignment of the laser. Verify that modelock is maintained over the power range 670 - 830 mW with the correct pulse wavelength and shape. If necessary, make small adjustments to the exterior controls, particularly M7, to regain stable modelock. If stable modelock cannot be achieved, go back to step 12 and repeat with the Mira's covers on.

15. Check the alignment of the Mira output. The beam should clip neither the beam splitter nor the first mirror leading to the Titan. While it is extremely unlikely that clipping occurs with a good alignment, if it does, try moving the beam with the skew controls. If this does not correct the problem, repeat the modelocking procedure, or the alignment of the main cavity.

H.2.5 Daily power optimization

This section details an optimization of the Mira's power that is performed when the Mira has been operating stably. It can be performed without removing the laser's covers and does not significantly change the profile of beam, nor its direction; therefore, this optimization is suitable for use on a daily basis to keep the Mira in good operating condition. In general, it should be performed before turning on the Titan. Refer to Figure H.1 for locations of various optics and their adjustment dials.

1. Put the Mira in CW mode. Fully open the Mira's slits. Note the power reading on the Mira's controller.

2. Close the slits until the power on the Mira's controller is half its initial (fully open) value.

3. Maximize power on the controller using the slits' horizontal adjust.

4. Repeat steps 2 and 3 until no further improvement can be obtained.

5. Open the slits fully again.

6. Use the vertical adjust on P2 to maximize power.

7. Use the vertical adjust on M7 to maximize power.

8. Repeat steps 6 and 7 until no further optimization can be obtained.

9. Use the horizontal adjust on P2 to maximize power.

10. Use the horizontal adjust on M7 to maximize power.

11. Repeat steps 9 and 10 until no further optimization can be obtained.

12. Repeat steps 6 - 11 until no further optimization can be obtained.

13. Repeat steps 1 - 5.

14. Switch the Mira from CW mode to modelock. Place a power meter directly in front of the Mira's output.

15. Close the slits until modelock is achieved. Note the power registering on the power meter; it should be well above the desired power. If the modelocked power is less than or only slightly above (< 15 mW) than the desired power, refer to Section H.2.4.

16. Continue to close the slits until the desired power is achieved.

H.3 Titan alignment

H.3.1 Preliminary remarks

With only five alignment apertures to align dozens of optics, most of which are used by multiple beam passes, alignment of the Quantronix Titan amplifier is a daunting task. The Titan user's manual[352] provides specifications, diagrams, and alignment procedures; however, because there are many possible Titan configurations,

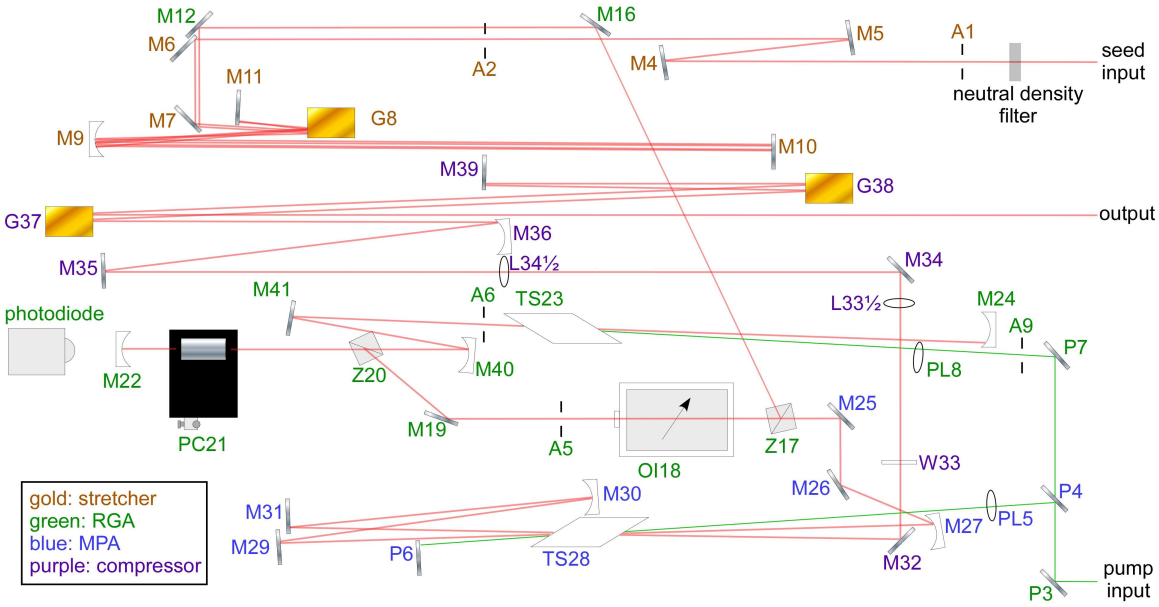

Figure H.5: The Titan amplifier.

the information provided by the manual is often vague, or even incorrect, for our setup. It does provide a good description of how the Titan should operate, though, and the diagrams are mostly correct. The procedures contained herein for the alignment of the Titan are based on the manual, but are augmented (or outright changed) based upon conversations with Mike Crumb of Quantronix and John Kozub of Vanderbilt's W. M. Keck Free-Electron Laser Center, as well as upon personal experience in realigning the Titan.

A schematic of the Titan amplifier is given in Figure H.5. There are four major components of the Titan's layout: the stretcher, the regenerative amplifier (RGA), the multipass amplifier (MPA), and the compressor.

In general, it is recommended that the optics inside the Titan not be touched unless power drops and cannot be recovered by adjusting the exterior optics, or unless power output drops from a TOPAS unit when the TOPAS is properly aligned. It is also recommended that the cause of power loss is determined *prior* to moving any of the optics. A list of potential problems and solutions is given in Table H.2. This

is by no means a comprehensive list, so use best judgment when encountering a new problem.

A notable difference between alignment of the Mira and alignment of the Titan is that, due to spatial constraints within the Titan, beams in the Titan rarely hit the center of any optic; frequently they are on the very edge of the optic in question, and on occasion clip the edge slightly.

When realigning the system, always check the Ti:sapphire crystals for damage, visible as small brown spots, before letting light into the Titan's case. If damage is visible, the beam can be moved to an undamaged spot. Also, as with the Mira alignment, record all micrometer positions before making any changes.

WARNING: When aligning the Titan, it is imperative not to interrupt the path of the beam through the compressor when the pump beam is active, as damage to the compressor can result.

H.3.2 Input seed beam path

Aligning the input seed beam path is one of the most crucial alignment procedures. Theoretically, if the Titan is aligned but the beam alignment in the Mira has been changed (by moving the skew controls, the birefringent filter, BP1, BP2, or the output coupler), aligning the input seed beam path through A1 and A2 is sufficient to realign the Titan.

The input seed beam path should be checked prior to turning on the YLF laser.

1. Verify that the output beam from the Mira has the proper pulse shape (beam centered at 800 nm with a FWHM bandwidth of 10 - 12 nm, Section H.2.4) and power (750 mW as measured just outside the Mira case).

2. Remove the back cover of the Titan. Optionally, remove the neutral density filter to make viewing the beam easier.

Table H.2: Problems and potential solutions for the Titan.

problem	solution
no Titan output	Check for stretcher output at M16 (Section H.3.3); OR Check for RGA output between TS28 and M29 with pump beam path from P4 to PL5 blocked (Section H.3.5); OR Check for MPA output between M34 and M35 (with M36 blocked prior to opening YLF shutter; Section H.3.6); OR Check compressor alignment (Section H.3.7)
no pulse train on oscilloscope	Verify oscilloscope settings, including reducing trigger level; OR Verify placement of photodiode (Section H.3.5); OR Unplug/adjust Delay 2
Titan power drop	Check MPA Ti:sapphire crystal (TS28) for burns; OR Check Delay 2; OR Adjust last mirror before input for both seed and pump; OR Peak power and BURT (Section H.3.8); OR Verify proper Mira power/pulse shape (Section H.2.4); OR Clean the optics.
TOPAS power drop	If no drop in power from Titan and TOPAS properly aligned, verify correct contrast ratio between Titan main pulse, prepeak, and postpeak (Section H.3.5); OR Verify Titan output polarization (see Titan manual.[352])
structured output	Check for clipping in Titan; OR Check for spatial dispersion in stretcher (Section H.3.4); OR Check for spatial dispersion in compressor (see Titan manual.[352])

3. Three mirrors outside the Titan steer the seed beam from the Mira into the Titan (M1 - M3). If there is no misalignment of the Mira, then the beam should appear on at least the first mirror (M1). If the beam does not appear properly on M1, some realignment of the Mira is necessary (see step 15 in Section H.2.4).

4. The stretcher output appears on the left side of M12 without clipping on M6. It should also not appear clipped on the right side. Using the IR viewer and a business card, block and unblock the beam between M6 and M7. The output beam on M12 should appear and disappear without changing the brightness of the spot on M6. If any clipping is evident, or if the spot on M12 is noticeably dimmer than the spot on M6, then proceed with the seed input alignment; otherwise the stretcher is well aligned.

5. (*If necessary.*) Using M1, steer the beam to roughly the center of M2. Using M2, steer the beam to roughly the center of M3. Using M3, steer the beam to the exact center of iris A1. The power just after the neutral density filter at the seed entrance to the Titan should be $\sim 45 - 50$ mW.

6. Open A1. Look for the beam on A2. If the beam does not pass through the exact center of A2, walk the beam into alignment in the following manner: Using M3, steer the beam to the exact center of A2 (or as close as possible without clipping). Then use M2 to steer the beam back to the exact center of A1. Repeat until the beam passes through the exact center of both irises. An IR viewer may be helpful for this.

7. Open both irises. With a business card in front of M6, check the shape of the beam. It should appear round or slightly oblate. If the beam appears clipped or diffracted, check to make sure that it is passing through the collimating telescope (M4 and M5) without clipping. If clipping is evident, use the horizontal adjusts of M2 and M3 to walk the beam into place in the telescope. A properly aligned

beam should not clip on M4 or M5, and should appear at the extreme right edge of M6.

8. Block the beam in front of M10 and use the IR viewer to spot the beam on M6. It should hit the extreme right edge of the mirror, and may appear to clip very slightly. It should not appear at all on M12, which is just to the right of and slightly behind M6. If the beam is not on the very edge of M6, or if it clips enough that a business card held between M6 and M7 shows visible clipping, it is likely that the beam does not pass properly through the stretcher.

9. Unblock the beam between M9 and M10 while using the IR viewer to spot both the beam on M6 and the beam on M12 (assuming that the stretcher is properly aligned). The beam on M6 is the input into the stretcher, while the beam on M12 is the stretcher output. The stretcher output on M12 should not clip on M6 and should also not appear clipped on the right side. Using the IR viewer and a business card, block and unblock the beam between M6 and M7. The output beam on M12 should appear and disappear without changing the brightness of the spot on M6. If any clipping is evident, or if the spot on M12 is noticeably dimmer than the spot on M6, then proceed to stretcher alignment.

10. If spots are present on both M6 and M12 without clipping or significant dimming, check the size of both beams; they should be the same. If the spots show a large difference in size, the collimating telescope (M4 and M5) needs to be adjusted. Place a mirror between M5 and M6 and project the beam roughly two meters onto a piece of paper. Use the micrometer on M4 to translate M4 until the beam appears collimated. This can be seen by moving a business card along the beam path and looking for a change in beam size.

11. If the neutral density filter was previously removed, replace it at this time.

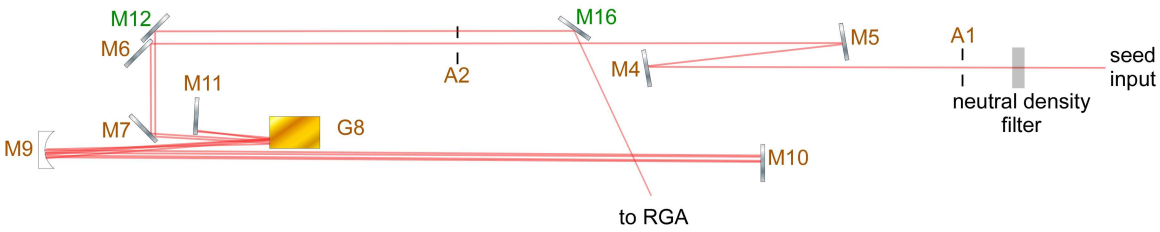

Figure H.6: The Titan stretcher.

H.3.3 Stretcher alignment

Alignment of the stretcher (Figure H.3.3) is not a trivial procedure. No optics should be moved if the stretcher output beam is fully on M12 and if the beam does not clip on any of the optics during its path through the stretcher. The correct path for the beam through the stretcher is: M6 → M7 → G8 → M9 → M10 → M9 → G8 → M11 → G8 → M9 → M10 → M9 → G8 → M7 → M12. On G8, the first and fourth spots should appear round and the second and third spots as very long oval spectra. The second and third spots may overlap to the extent that they are indistinguishable. The visibly stretched oval spectrum also appears on some of the other optics within the stretcher. All spots should be centered at a vertical height of 4 inches.

If the beam is not in place on M12 without clipping within the stretcher, then the stretcher should be aligned. Any of the optics in the stretcher may be moved during the alignment EXCEPT the grating (G8), unless specifically stated. It is noted that at each stage, the vertical height should be adjusted to 4". It should also be kept in mind that the routing mirrors (M2 and M3) may need to be adjusted slightly during this procedure. Finally, it is noted that during stretcher alignment, several iterations of the alignment may be necessary. If the beam cannot be placed in its proper position during a given step, back up several steps and start again in order to more closely align the beam. The stretcher alignment is not complete until there is absolutely no clipping.

1. Verify that the YLF laser is either off, or that the pump beam is blocked between P1 and P2.

2. (*Optional.*) Remove the neutral density filter placed just inside the entrance to the Titan. This filter prevents feedback from the Titan into the Mira, but feedback from the stretcher alone is unlikely and would not cause much damage. Removing the filter makes viewing the beam easier.

3. Realign the input seed beam path through the exact centers of apertures A1 and A2 according to the procedure in Section H.3.2.

4. Block the beam in front of M10 and adjust M6 so that the input beam spot on M7 is about two beam diameters (the manual says 1/4") from the left edge of the mirror. Note that the upper tuning knob on M6 controls horizontal aim. The placement of the spot is not exact, and it can be moved during the course of the alignment.

5. Adjust M7 so that the spot on G8 is about two beam diameters right of center (the manual says 1/3" from the right edge) of the grating.

6. Contrary to what the manual states, DO NOT adjust G8's mount OR its rotation stage. Moreover, the beam should not hit the center of M9. Instead, adjust M7 so that the beam reflecting from G8 to M9 passes exactly 1/2" to the left of the leftmost edge of M7 (this edge actually belongs to the back side of the mirror). By adjusting M7 again, the spot on G8 naturally moves. This is okay, provided the spot stays at least two beam diameters from the right edge of G8. If this cannot be accomplished, try adjusting M6 so that the spot on M7 is slightly closer to the left edge of the mirror (but leave room for the output beam, which must pass between the input beam and the edge of the mirror). Then repeat this step so that there is 1/2" between M7 and the beam path to

M9.

7. At this point, the spot should appear as an elongated oval somewhere on the left half of M9 (not in the center, as stated by the manual). If it instead appears as a round or slightly flattened spot (fat rather than tall), then the grating is not working properly. Verify that the spots on M6, M7, and G8 are all exactly 4" off the base of the Titan's breadboard, vertically adjusting M2 to fix the height on M6, M3 to fix the height on M7, and M6 to fix the height on G8, and walking the beam as necessary. If this does not fix the problem, and if the spot on M9 is not centered at a height of 4", then the grating does not have the proper tilt angle. Using the vertical adjust on G8, make slight adjustments to G8's tilt until the beam is an elongated spot centered 4" high on M9.

8. Unblock the beam in front of M10 and block the beam in front of M11 in such a way that only one very elongated spot is present on M10. Adjust M9 so that the spot on M10 very close to the left edge of the mirror without appearing to clip the edge when viewed with an IR viewer (the manual states 1/3" from the left edge). Verify that the beam does not clip on M7 as it passes from M9 to M10, though a corona may be present on M7 when viewed through an IR viewer. Placement of this spot need not be exact.

9. Adjust M10 so that the retroreflection on M9 occurs roughly 1/4" right of the original spot on M9. Do not adjust the micrometer-driven translation stage on M10.

10. Find the stretched spectrum on G8. It should appear roughly 1/3" to the left of the original spot. If it does not, or if the beam clips on M7, adjust M10. The second spot on M9 will move - this is okay.

11. Unblock M11 and locate the spectrum on M11 using a business card. It should

appear near the inner left edge of the mirror. Adjust M10 so that the spectrum is as far from the edge of M11 as possible without clipping any part of the spectrum. The spectrum may appear tilted - this is okay. Remove the card and use the IR viewer to verify that the beam does not clip on the edge of M11 or on the back of M7, though a corona may be present in both places. It may be necessary to repeat the entire stretcher alignment multiple times to achieve this.

12. Adjust M11 so that the third spectrum on G8 (the retroreflection from M11) is slightly to the right of the second. The two spots should overlap somewhat.

13. Further adjust M11 so that the fourth beam incident on G8, a spot, is one beam diameter right of the first beam, also a spot (the manual states that the fourth should be roughly 1/4" to the right of the first beam). The fourth beam should not clip on the edge of G8, but again, a corona may be present. The second and third beams (stretched spectra) may or may not overlap. Again, multiple iterations of the stretcher alignment may be necessary to achieve this.

14. Verify that the output beam on M7 is near the left edge of the mirror, approximately one beam diameter left of the input beam (the manual states 1/4"). Adjust M11 if clipping occurs. Verify that the fourth spot on G8 is still fully on G8.

15. The output beam should narrowly miss the right edge of M6 and hit M12 instead. Using an IR viewer and a business card, block and unblock the beam between M6 and M7. The output beam on M12 should appear and disappear without changing the brightness of the spot on M6. Adjust M11 as necessary, making sure that the beam does not clip anywhere along its path from M11 to M12. Again, multiple iterations of the stretcher alignment may be necessary to

achieve this. The output beam should appear as a round spot if the stretcher is properly aligned.

16. If M2 or M3 has been moved during the stretcher alignment, check the shape of the input beam by holding a business card in front of M6. It should appear round or slightly oblate. If the beam appears clipped or diffracted, verify that it passes through the collimating telescope (M4 and M5) without clipping. If clipping is evident, use the horizontal adjusts of M2 and M3 to walk the beam into place in the telescope, and repeat the stretcher alignment.

17. Using a business card, deflect the light from M12 into a spectrometer. Verify that the spectrum remains centered at 800 nm. If it is not, then the horizontal angle of the grating is incorrect. Make slight adjustments to the horizontal tilt knob on G8 (and corresponding adjustments on any mirrors required to keep the beam traveling properly through the stretcher) until the wavelength of the output beam is centered at 800 nm.

18. Check the sizes of both the input beam on M6 and the output beam on M12; they should be the same. If the spots show a large difference in size, the collimating telescope (concave mirrors M4 and M5) needs to be adjusted. Place a mirror between M5 and M6 and project the beam roughly two meters onto a piece of paper. Use the micrometer on M4 to translate M4 until the beam appears collimated. This can be seen by moving a business card along the beam path and looking for a change in beam size.

19. The path of the beam from the stretcher is M12 → M16 → Z17 → OI18 → A5 → M19. Using only M12 and M16, steer the beam so that it passes without clipping all the way to M19.

20. Place a mirror between A5 and M19 to divert the beam out of the Titan. Some

distance from the Titan ($\sim$ 3 m), use a business card to image the beam. It should be round and structureless. If structure is evident, then the beam is clipping (this causes problems later). Find the source of the problem, and realign the stretcher as necessary.

21. Remove the diverting mirror, and replace the neutral density filter.

    Note that stretcher output should be vertically polarized.

H.3.4 Stretcher spatial dispersion correction

If the stretcher is aligned properly, then every part of the stretched beam has the same optical spectrum - the stretched beam is not spatially structured. If there is spatial dispersion, then the amplified beam exiting the Titan is also structured. Spatial dispersion in the stretcher can be detected and corrected in the following manner:

1. Verify either that the YLF laser is off, or that the pump beam is blocked between P1 and P2.

2. Place two mirrors somewhere between M12 and M16 to route the stretcher output to a spectrometer at a distance of 2 - 3 meters from the stretcher. Optimize the position of the spectrometer for maximum signal input.

3. Set up a narrow vertical slit in front of the spectrometer. Optimize the position of the slit for maximum signal input.

4. Set up a narrow horizontal slit in front of the vertical slit. Adjust the horizontal slit's height to maximize signal input. Then open the vertical slit until the previous signal intensity is obtained.

5. Tune the vertical adjust of the mirror nearest the spectrometer to scan vertically through the entire beam. If the stretcher is properly aligned, then the amplitude

of the spectrum changes uniformly and proportionately throughout the beam. If it does not, adjust the micrometer on M10 to translate M10 in the z-direction. Make small adjustments until the spatial dispersion has been corrected.

H.3.5 Regenerative amplifier (RGA) alignment

The procedures contained in this section are used to align the RGA in the case that neither the Pockels cell nor the Ti:sapphire crystal in the RGA are grossly out of alignment. Alignment proceeds in four stages: alignment of seed input into the RGA, pump beam cavity lasing, overlap of the pump and seed, and coarse optimization of the Pockels cell. Alignment of the seed input ensures that the seed beam travels properly from the stretcher output (M12) into the RGA and back to Z17 on its path towards the MPA, and provides a coarse alignment of the RGA cavity. In pump beam cavity lasing, the pump input and end mirror M24 are adjusted to achieve RGA cavity lasing. Overlap of the pump and seed is self-explanatory; it is only when the two beams are overlapped that the RGA acts as an amplifier. Finally, the Pockels cell is put in roughly the correct attitude to minimize leakage current and to obtain a good beam profile for input into the MPA. RGA alignment is necessary only if the alignment of these optics is off to the extent that the RGA cannot operate properly (e.g., it is not possible to obtain a good pulse train, there is clipping within the RGA, or the output power from the Titan is very low).

As we shall see in this section, the RGA and the optics leading up to it (and immediately after it) operate through a series of polarization changes of the light. Because the path that the light travels very much depends on its polarization, and because light improperly polarized from the Titan causes the TOPAS units to operate poorly, *it is highly recommended that none of the polarizing optics be adjusted in any way.* The Pockels cell is the sole exception to this.

Path of the seed beam through the RGA

This section does not contain any alignment instructions; instead, we discuss the operation of the optics involved in directing the beam from the stretcher to the RGA, through the RGA, and on towards the MPA. This system of optics, from M16 to the Pockels cell (PC21), involves some unusual optics to maintain the directionality of the beam, and the Titan manual does not explain their functions in adequate detail. The alignment of these optics follows in the next section.

In order to prevent feedback from the RGA into the stretcher and the Mira, and in order to route all light from the stretcher first into the RGA and then into the multipass amplifier (MPA), the seed beam undergoes a series of polarization changes during its path into, and then out of, the RGA. Starting from M12, the beam reflects off M16 to reach Z17, a polarizer that reflects vertically polarized light and transmits horizontally polarized light. As the beam from the stretcher is vertically polarized, it reflects off of Z17 and enters the optical isolator (OI18).

According to Coherent's RegA manual,[353] an optical isolator, also known as a Faraday isolator, has three main components: a set of permanent magnets, a rod of Faraday material, also known as a Faraday rotator, and an optical rotator (such as a quarter-wave plate or a quartz crystal; the Titan manual does not specify). According to the magneto-optic effect, when light enters a Faraday rotator in the presence of a magnetic field, its plane of polarization is rotated proportionally to the intensity of the component of the magnetic field in the direction of the beam of light, in case of the optical isolator by 45°. This means that in the optical isolator, if the Faraday rotator rotates the seed input beam by 45° clockwise (looking in the direction of propagation of the light), then any light traveling in the opposite direction is rotated by 45° counterclockwise. In contrast, the optical rotator rotates all light in the same direction regardless of direction, in this case by 45°. Thus the Faraday and optical rotator rotations are not symmetric; in one beam direction they add, while in the

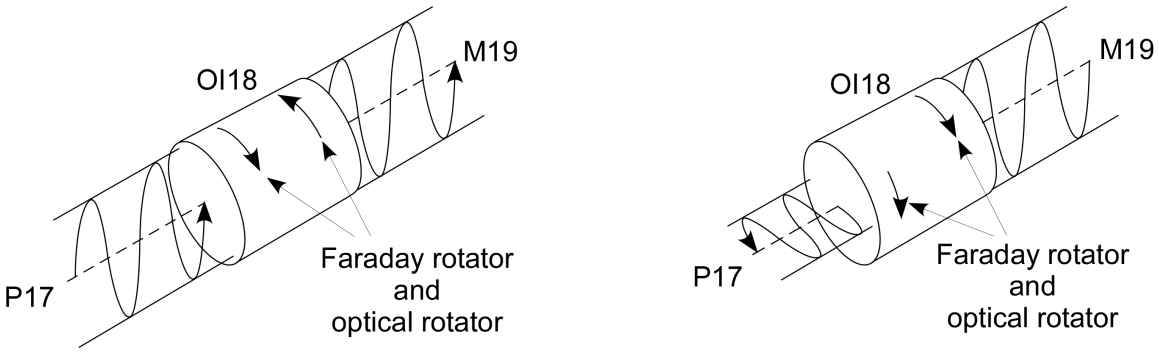

Figure H.7: The optical isolator. When light travels from the stretcher to the RGA (left), the rotations of the Faraday rotator and optical rotator cancel each other out, and the beam remains vertically polarized. When light travels from the RGA to the MPA (right), the rotations of the Faraday rotator and optical rotator add together, and the beam changes from vertically polarized to horizontally polarized.

opposite direction they cancel each other out. In the Titan, light from the stretcher passing through the optical isolator to the RGA remains vertically polarized, while light traveling in the opposite direction is rotated from vertically to horizontally polarized. This is shown graphically in Figure H.7.

From OI18, the incoming beam reflects off M19 and hits Z20, another polarizer that reflects vertically polarized light but transmits horizontally polarized light. The seed beam thus reflects off of Z20 and enters the Pockels cell (PC21). The Pockels cell serves several functions in the Titan. We discuss here its function in directing light to and from the RGA.

The Pockels cell has three states. In its static operating state, it acts as a quarter-wave plate, rotating the polarization of the light by 45°. The vertically polarized incoming light is rotated by 45°, reflects off of M22, and passes back through PC21, where it rotates by an additional 45° to become horizontally polarized. It then passes through Z20 and into the rest of the RGA. When the light returns to the Pockels cell, it is converted in the same manner to vertically polarized light. This reflects off of M22, passes back through PC21, and travels back along its path of entry

until it reaches OI18. There, as previously mentioned, it is converted to horizontal polarization. When it returns to Z17, it is transmitted through the polarizer because of its orientation. From there it passes through the MPA and out of the Titan as leakage energy.

When it is time to generate an amplified pulse in the RGA, the 'first step' voltage is applied to the Pockels cell, which then functions as a half-wave plate. As a result, the Pockels cell no longer changes the polarization of light entering it. Light within the RGA, which is horizontally polarized, remains horizontally polarized. Thus, it continues to be transmitted through Z20, and simply bounces back and forth between M22 and M24, picking up power from the pump-excited Ti:sapphire crystal with each pass through the crystal. Meanwhile, light from the stretcher, which is vertically polarized, remains vertically polarized. When it is reflected by M22, it reflects off Z20 and passes into the MPA along the same path as light from the Pockels cell when it is in its static state.

When it is time to send the amplified pulse from the RGA into the MPA, the 'second step' voltage is applied to the Pockels cell, which then functions as a three-quarters-wave plate. Functionally, this state is identical to the static state - the horizontally polarized amplified pulse becomes vertically polarized and passes into the MPA along the same path as the leakage energy. Any light coming from the stretcher behaves as though the Pockels cell is in its static operating state.

These pathways are shown graphically in Figure H.8.

RGA seed input alignment

1. Verify either that the YLF laser is off, or that the pump beam is blocked between P1 and P2. The high voltage on the Medox should be on, as it controls the Pockels cell and allows seed light into the RGA. Disconnect Delay 2 on the Medox.

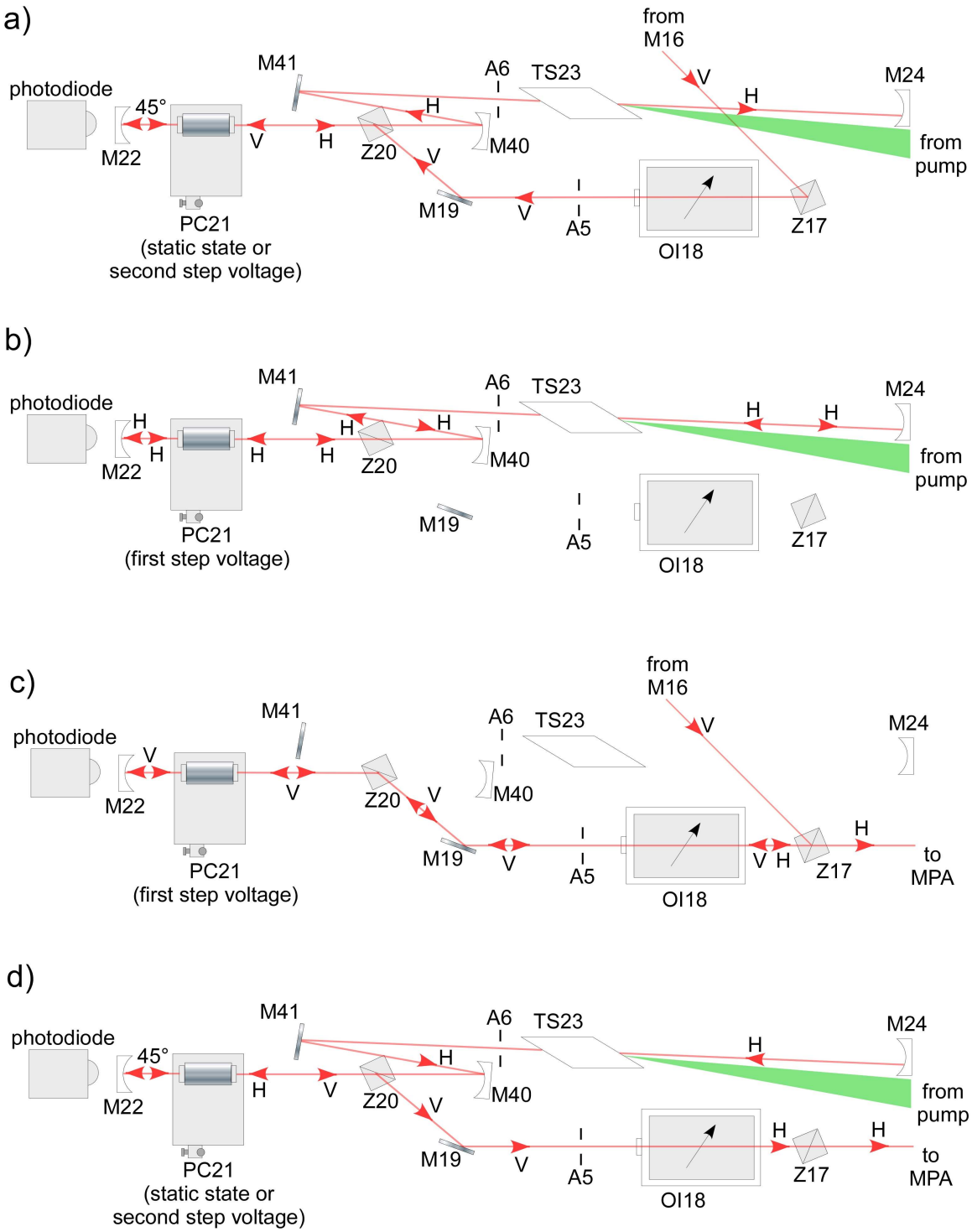

Figure H.8: Polarization changes to the seed beam near the regenerative amplifier. a) The path of the beam leading into the RGA. b) The path of the beam during amplification in the RGA. c) The path of leakage light during pulse amplification. d) The path of the beam leading out of the RGA. H indicates horizontal polarization (parallel to the plane of the table), while V indicates vertical polarization (perpendicular to the plane of the table).

2. Use M12 to adjust the height of the spot on M16 to 3". It should also be roughly centered horizontally.

3. Use M16 to center the spot on A5. Verify that the beam remains at a height of 3" from M16 to PC21. If not, vertically adjust M16 and M19 as necessary.

4. The beam should pass through the approximate center of PC21's entrance and exit windows without clipping at any stage along the seed input beam path. If the beam does not pass through the approximate center of PC21, walk the beam into position using M12 and M16. If it clips on any optic before PC21 (Z17, OI18, M19, or Z20), it may also be necessary to make horizontal adjustments to M19. Make sure the beam remains centered at A5.

5. Find the zero-wave position (*This procedure is only necessary if the Pockels cell is so far out of alignment that RGA cavity lasing cannot be achieved with the correct beam profile (e.g., Figure H.9), and if the following step (quarter-wave alignment) does not fix the problem. Once the Pockels cell has been put in zero-wave position, then it is necessary to realign the RGA cavity again from this step forward, including finding the quarter-wave position in the following step.*):

   (a) Mark M22's position on the Titan's breadboard with pencil or with a pen whose ink can be easily removed with acetone or other solvent, then remove M22. Block the beam between Z20 and M40.

   (b) Tape a piece of paper on the photodiode behind PC21 to act as an observation plane. Tape a piece of lens cleaning tissue over PC21's input aperture to diffuse the laser beam.

   (c) Place a polarizer that transmits horizontally polarized light and blocks vertically polarized light directly behind PC21 in place of M22. Place a business card below the polarizer so that it reflects any light reflected by

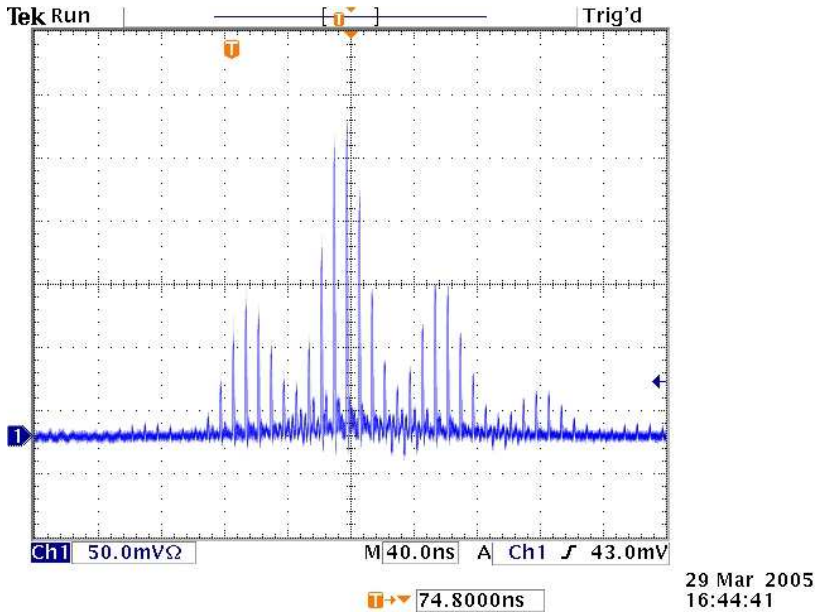

Figure H.9: Modulated pulse train. This pulse train is indicative of an improperly aligned Pockels cell.

the polarizer onto the Titan's breadboard (preventing stray beams from damaging eyes).

(d) Use an IR viewer to find the center of the transmitted light on the observation plane. It should appear as a bright spot. If no spot is visible, try adjusting the placement of the polarizer. Alternately, remove the lens cleaning tissue. Mark the center of the spot, and replace the lens tissue.

(e) Somewhere on the paper, a dark cross should be visible due to crystal birefringence-induced interference (Figure H.10). Use PC21's vertical and horizontal adjust to center the cross on the spot of transmitted light. This position of the Pockels cell is called the zero-wave position, because in this position, the Pockels cell acts as a zero-wave plate.

(f) Remove the polarizer and replace M22. Remove the lens cleaning tissue and the paper acting as the observation plane.

(g) Using M22, center the reflected seed beam on A5.

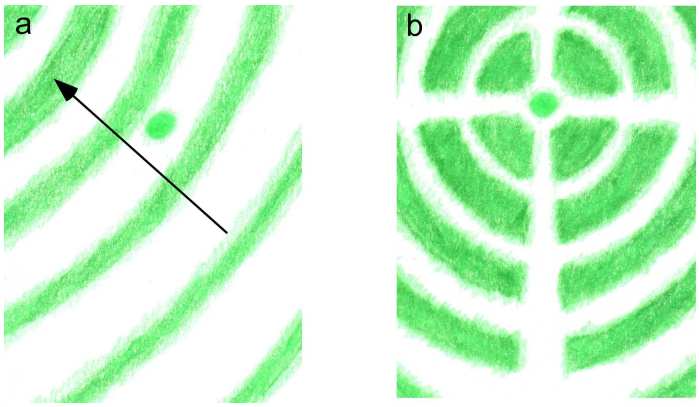

Figure H.10: Pockels cell diffraction patterns. In (a), the Pockels cell is very misaligned. In order to align the Pockels cell in the zero-wave position, the spot should be moved towards the center of the diffraction rings (arrow). In (b), the Pockels cell is in the zero-wave position).

6. Find the quarter-wave position (*As with the previous step, this procedure is only necessary if the Pockels cell is so far out of alignment that RGA cavity lasing cannot be achieved with the correct beam profile. It may be attempted without the previous step (zero-wave alignment), or it may be used as a necessary follow-up to the previous step.*):

   (a) Place a sensitive power meter behind Z20 such that it measures light that is transmitted through Z20 after reflecting off M22. This is the light that would ordinarily travel to the Ti:sapphire crystal in the RGA.

   (b) The Pockels cell has four static quarter-wave positions. If a zero-wave alignment was not previously performed, and particularly if the RGA was already in good alignment, only one of these results in the best alignment of the RGA. Look at the tilt of the top of the Pockels cell; one corner should be lower than the other three. When finding the quarter-wave position, try to keep this corner down.

   (c) Use PC21's vertical and horizontal adjust to maximize the power transmitted through Z20. The maximized power should be approximately 25

mW. This position of the Pockels cell is called the quarter-wave position. If a zero-wave alignment was previously performed, the quarter-wave alignment is approximately three turns of one knob and six turns of the other. It is noted that the Pockels cell often sticks in place rather than moving with the adjusts; tapping hard on the top of the Pockels cell as the adjusts are turned prevents it from sticking.

(d) Remove the power meter. Block the beam between Z20 and M40. Retune M22 to center the retroreflection on A5. Unblock the beam.

(e) As moving M22 changes the path of the return beam through PC21, and moving PC21 changes the path of the beam to M22, repeat steps 6a - 6d until no further improvement can be achieved.

(f) Using a Sharpie or some other removable mark, indicate on the Pockels cell which corner is lowest.

NOTE: After this step, M22 should not be moved again for the remainder of the Titan alignment, unless otherwise specified. Moving M22 can change the alignment of the beam through the Pockels cell to the extent that the Pockels cell is no longer in zero-wave (or later quarter-wave) position. Figure H.9 shows the pulse train that resulted when M22 was slightly adjusted; zero-wave alignment of the Pockels cell showed that following the adjustment to M22, optimization of the Pockels cell resulted in a false alignment (so that it was no longer in quarter-wave position). It may be helpful to think of M22 as the mirror that defines the cavity axis, while M24 is used to achieve resonance.

Kozub employs a different method of finding the quarter-wave alignment. We have not tried this technique, but we include it because future users may find it useful.

(a) Turn off the high voltage on the Medox. Place a business card in front of

M24.

(b) Tune PC21 to visually maximize the intensity of the beam on the business card. This is the static quarter-wave alignment. As with the other quarter-wave alignment procedure, if one corner of the Pockels cell is lower than the others, try to keep it lower while finding the quarter-wave alignment.

(c) Turn on the high voltage on the Medox and remove the card.

7. Block the beam between TS23 and M24. Use M40 or M41 to center the beam on A6. Verify that the beam narrowly misses M40's mount on its path from M41 to A6. It may appear to clip using an IR viewer, but a business card should show no clipping. Unblock the beam.

8. The incoming seed beam should pass through the approximate center of the Ti:sapphire crystal. If it does not, walk it into position using M40 and M41, making sure to keep the beam passing through the center of A6. The horizontal placement of the beam is more important than the vertical placement, as changing the horizontal placement changes the cavity axis and therefore the reflectivity of the beam on the crystal surface.

9. Ti:sapphire crystal alignment (*This procedure was included in the Titan manual,*[352] *but really should not be used unless absolutely necessary, such as when the cavity axis has changed.*):

(a) Rotate TS23's mount assembly (as opposed to the mount itself) about the vertical axis to minimize reflection from the crystal surface.

(b) Remove TS23's mount from the assembly. Do not remove the crystal from the mount. Note that the seed beam path displaces by about 2 - 4 mm in the horizontal plane.

(c) Set a polarizer in the path of the seed beam after the crystal assembly. Using an IR viewer and observation plane or a photodiode placed after the polarizer to monitor the intensity of transmitted light, rotate the polarizer in its mount to minimize the transmitted light.

(d) Replace the crystal mount on the assembly. Do not tighten.

(e) Rotate the crystal mount to minimize the intensity of light transmitted through the polarizer. Tighten the crystal mount in the assembly. Remove the polarizer.

10. The seed beam should hit the right side of M24 so that it closely lines up with the path of the pump beam. Using M40 and M41, walk the beam so that it is as close to PL8 as possible without actually clipping, while still passing through the center of A6.

11. Place a business card with a hole punched in it or the specially machined alignment tool near the back face of TS23 (the face facing M24) such that the light initially transmitted through TS23 passes through the center of the hole. Tune M24 to send the retroreflection back through the center of the hole. Remove the business card/alignment tool.

12. Close A6 until the beam is just able to pass from M41 to TS23. Tune M24 to send the retroreflection back through the center of A6. Open A6.

13. Using an IR viewer, look at the surface of M41. Two spots should be visible: one 2 - 2.5 mm in diameter (the initial beam) and one $\sim$1 mm in diameter. Tune M24 to overlap the two beams.

14. Using an IR viewer, look at the surface of M24. Up to three spots may be visible. Tune M24 to overlap all three spots.

15. Verify that the beam from the RGA follows the path OI18 → Z17 → M25 → M26 → M27 → TS28 → M29 without clipping. Adjust M25, M26, and M27 as necessary.

16. Place a business card between M27 and TS28 or in front of M29. Several spots may be visible. One of these is seed leakage, distinguishable as the only remaining spot when the RGA is blocked between TS23 and M24. One or more of the spots are from the RGA. Using M24, try to overlap all the spots. If the RGA spot(s) cannot be made to overlap the leakage spot without clipping somewhere before M25, it may be necessary to make slight adjustments to M22. Adjusting M22 translates both the leakage and the output spots equally in space. Once they have been translated so that clipping ceases, M24 should once again be adjusted to overlap the leakage and RGA spots.

    NOTE: It is possible that some of the spots from the RGA are not truly part of the beam to be amplified. For example, we have found that some of the vertically polarized light that should reflect off the surface of Z20 instead is transmitted through Z20 and reflects off the back surface of the polarizer, resulting in a double beam - the true beam reflecting off the front surface, and a beam that is not amplified reflecting off the back surface. Both of these spots can be seen sometimes in the MPA. When these 'false' spots are visible, no amount of adjustment will overlap them to the 'true' spots. These spots should be identified and ignored.

17. Check to make sure that only one spot remains visible on M41, M24, and on the business card in the MPA. If a single spot has been achieved in all three locations, the RGA cavity should be resonating (or very close to resonating). If more than one spot is visible in any location, adjustments should be made as necessary to collapse all spots into one. It may be necessary to repeat much of

the RGA alignment.

18. Remove the business card from the MPA and place a power meter directly in front of M29 facing TS28. Block the RGA lasing cavity between TS23 and M24. Note the power registering on the power meter. This power is leakage from the seed and should be very small (< 6 mW).

19. Unblock the RGA. The power of the resonating seed beam should be $\sim 16 - 19$ mW. If not, adjust M12, M16, and M24 to optimize power. If the power remains low, look for clipping along the beam path by diverting the beam out of the Titan using mirrors. A business card placed about three meters from the Titan should be able to pick up structure (e.g., diffraction patterns) indicative of clipping. Clipping may occur in the stretcher, RGA, or MPA. If no clipping is detected, and if there is no problem with the power from the Mira, it may be necessary to repeat the RGA alignment (e.g., translating M40, M41, or M21 (slightly), then regaining resonance). Once suitable power has been obtained, proceed to "Pump beam cavity lasing" (below).

Pump beam cavity lasing

The procedure outlined here is highly modified from that given in the Titan manual, and is based upon a procedure outlined by Kozub. This procedure varies from that given by the Titan manual in that the pump beam is overlapped to the seed beam while the seed beam is running through the cavity. This method is advantageous in that it provides a systematic method of obtaining pump beam lasing, unlike the guessing that the Quantronix procedure entails, and because the seed beam begins to pick up power from the pump when the pump beam approaches alignment, giving the user a means of knowing when the pump is close to alignment.

1. Block the path of the pump beam between P4 and P5. Place a power meter between TS28 and M29 so that it faces TS28. This meter is used to detect and

optimize pump beam lasing, as the alignment procedures can change the beam position enough that using the photodiode and oscilloscope may not give an accurate optimization.

2. Find the beam output from the RGA on M25. Make sure that the beam passes without clipping from M25 to M26 to M27 and through TS28 so that it hits the power meter properly.

3. Turn on the YLF laser according to the daily operating procedure (Section H.1.1), but do not increase the lamp current beyond its initial value of ~ 6 A. Turn on the Titan's chiller controller. Disconnect Delay 2. The path of the pump beam to the RGA should be unobstructed, but the path of the pump beam to the MPA should be blocked.

4. The path of the pump beam to the RGA is: P1 $\rightarrow$ P2 $\rightarrow$ P3 $\rightarrow$ P4 $\rightarrow$ P7 $\rightarrow$ A9 $\rightarrow$ PL8 $\rightarrow$ TS23. Verify that the beam does not clip on any of these optics. If necessary, adjust any of the mirrors (P1, P2, P3, or P7) to eliminate clipping. Note that moving P1, P2, or P3 causes the MPA alignment to change, so moving these optics horizontally should generally be avoided, except when the beam is clipping. The beam should be centered at 3 inches throughout its path to TS23.

5. Adjust P3 to center the pump beam on A9.

6. Close A9 to the point that only a small spot of light is visible on TS23. Using the IR viewer, adjust P7 to overlap visually the pump and seed beams on TS23 while simultaneously remaining centered on A9. It may be necessary to block and unblock the seed and/or pump beams to find the overlap.

7. A business card can be used to view both the seed and pump beams simultaneously when placed between A6 and TS23 or between TS23 and M24. The spots should be viewed by looking towards the incoming pump beam (i.e., so that

TS23 is closer to the eye than M24). This way the user can see the scatter of the weaker seed beam and the transmission of the stronger pump beam. Using the business card in the two locations as two points of reference, use P3 and P7 to vertically walk the pump into the same horizontal plane as the seed beam. The same technique can be used to overlap the beams horizontally in TS23 if overlapping the beams using the IR viewer proves too difficult. Place the business card at a specific distance from the center of TS23 first on one side of the crystal and then on the other; if the beams are properly overlapped, then the distance between them should be the same on either side of the crystal.

8. Block the seed beam between M16 and Z17 so that the beam path within the RGA and from the RGA to the power meter remains unobscured. Increase the current on the YLF controller to normal operating current. Open A9. The power measured on a power meter placed between PL8 and TS23 should be ~ 2.8 W (the Titan manual gives a range of 2.5 - 3.0 W). If it is not, adjust the YLF current accordingly.

9. Unblock the seed beam. Make small adjustments to P7 until the pump beam begins lasing in the RGA. This can be done systematically by translating the beam horizontally across the crystal surface, then up or down by one beam diameter, and repeating the process until the pump beam begins to lase. When the pump beam begins to lase, the power meter between TS28 and M29 shows an abrupt increase in power (by more than 5 mW), provided the optics leading from Z17 to TS28 are in at least rough alignment. A pulse train may or may not be visible on the oscilloscope measuring the photodiode response of the RGA. If the pump beam does not begin to lase, try making small adjustments to M24 (less than 1/4 turn) with the pump and seed visually overlapped. If this fails, realign the RGA cavity, starting with "RGA seed input alignment" (page 299).

10. Using the power meter to monitor power, make slight adjustments to M24 and P7 to increase the power to >100 mW.

11. Block the seed beam between M16 and Z1. The pump beam should continue to lase. Continue to adjust M24 and P7 until the power is optimized. The vertical adjust of P3 can also be used, and, as a last resort, the horizontal adjust of P3. It should be possible to attain a lasing power of > 200 mW; if not, try repeating the RGA seed input alignment (page 299) and then the pump beam cavity lasing alignment (page 308). If this does not work, proceed to "RGA cavity free-running" (page 313).

12. Observe the shape of the lasing beam. It should be roughly round and featureless. If it is not, look for clipping by using a mirror to throw the beam out of the Titan and using a business card at a distance of three meters to check for structure. If no clipping is evident, try adjusting the Pockels cell according to steps 5 and 6 of "RGA seed input alignment" (page 303). If this does not fix the problem, proceed to "RGA cavity free-running" (page 313).

13. Slowly close A6 while observing the pump's lasing power. If the power begins to decrease, make small adjustments to P7 and M24 to optimize the power. Continue this process until A6 is open no more than 3 - 4 mm. The power with A6 nearly closed should be nearly the same as the power when A6 is fully open. If this cannot be achieved, try going back to "RGA seed input alignment" (page 299) and starting over. *It is absolutely critical that the lasing beam path pass through the center of A6.*

14. Locate the bleedthrough from M22 on the surface the photodiode. Verify that the spot is in fact on the active area of the photodiode, a small, protruding dark spot that can be seen through the lens tissue covering it. If necessary, reposition the photodiode so that the spot appears on the active area.

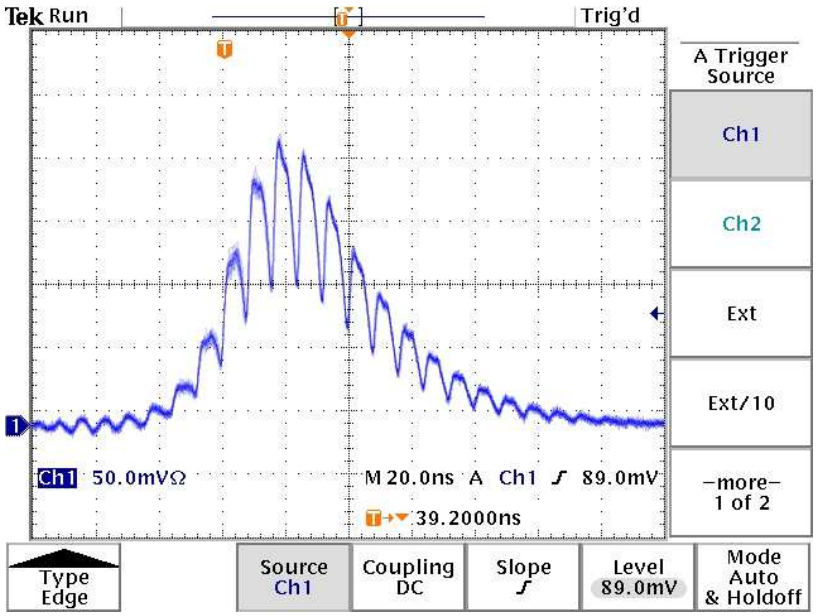

Figure H.11: Unseeded Titan pulse train.

15. On the oscilloscope monitoring the pulse train, set the voltage divisions to a small value (i.e., 50 mV) in order to capture the weak signal from the pump beam-induced lasing. If no signal is immediately visible, try decreasing the voltage divisions, increasing the time divisions (up to the period of the YLF laser, 1 ms), or lowering the trigger level on the oscilloscope. It may also be necessary to change the timing of Delay 1 on the Medox; the timing should not change by more than 10 units on the delay scale (not on the fine scale). As of the writing of this document, Delay 1 was set at 234 (rather than the 270 stated in the manual). Finally, the bleedthrough from M22 may be misaligned with the photodiode; try realigning the photodiode as in the previous step. If a signal still cannot be found, proceed to "RGA cavity free-running" (below). If a pulse train appears, proceed to "Unseeded quarter-wave operation" (page 314). The pulse train should appear similar to that in Figure H.11.

RGA cavity free-running

RGA cavity free-running is the alignment procedure used to correctly orient the polarizations of the various optics within and leading up to the RGA. Since it involves removing the Pockels cell, it should only be used: a) after replacing the RGA's Ti:sapphire crystal, b) when the RGA's output spectrum is significantly modulated and no other alignment technique has solved the problem, or c) to obtain an initial cavity oscillation when conducting a full alignment (optional).

1. Turn off the YLF laser. Turn off the high voltage on the Medox (the Pockels cell uses high voltage).

2. Remove PC21. Be careful not to turn either of the tilt adjusts, so that the Pockels cell remains in quarter-wave position.

3. Adjust M22 to center the retroreflection of the input seed beam on A5.

4. Place a quarter-wave plate in the seed beam path between Z20 and M22.

5. Turn on the high voltage. Block the beam path between P1 and P2, then turn on the YLF.

6. Proceed with steps 7 of "RGA seed input alignment" (page 305) through 15 of "Pump beam cavity lasing".

7. Place a spectrometer behind M22 to monitor the spectrum of the light that leaks through the mirror.

8. (*If necessary.*) Loosen TS23's mount in its mount assembly. Rotate the crystal mount (not the assembly) to minimize any birefringence-induced spectrum modulation. The correct spectrum should be Gaussian or nearly Gaussian. Tighten TS23's mount.

9. Remove the quarter-wave plate. Remove the spectrometer. Turn off the YLF. Turn off the high voltage.

10. Replace the Pockels cell, which should already be in quarter-wave position (i.e., where transmission of light through Z20 is maximized) from the RGA seed input alignment. Turn on the high voltage. Turn on the YLF laser. Unblock the pump beam.

11. Block the beam between Z20 and M40. Retune M22 to center the spot of light exiting the RGA on A5. Unblock the beam.

Following the cavity free-running alignment, proceed to "Unseeded quarter-wave operation".

Unseeded quarter-wave operation

At this stage, the RGA should lase when only the pump beam is applied. The purpose of unseeded quarter-wave operation is threefold: a) to obtain a modulated waveform at the proper delay, b) to obtain a smooth spectrum, and c) to further optimize the Pockels cell's orientation.

1. If the photodiode has not already been realigned to maximize signal from the bleedthrough from M22, do so now.

2. As seen in Figure H.11, the unseeded pulse train appears as a broad peak, strongly modulated by an oscillation with a period equal to the cavity length of the RGA. The leading edge of the waveform should be steep, indicating a fast gain build-up.

3. Adjust Delay 1 on the Medox to maximize the amplitude on the oscilloscope. The depth of the modulation should not change.

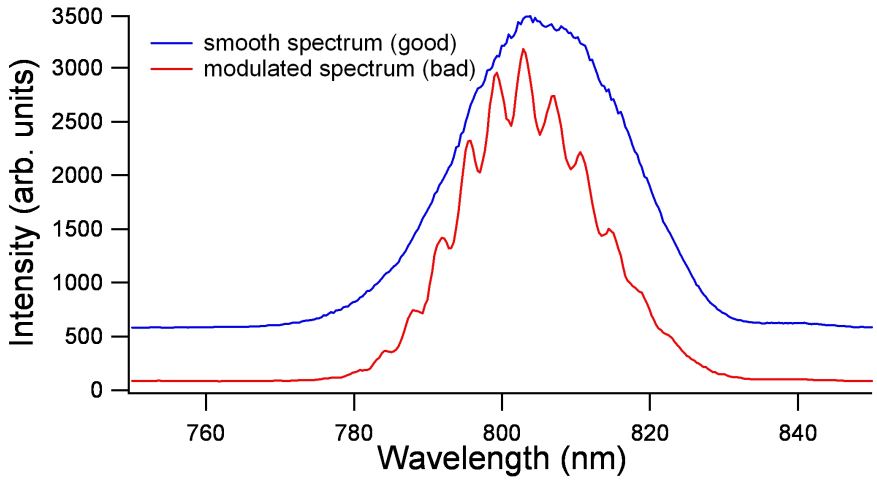

Figure H.12: RGA emission spectra. A modulated spectrum (red) indicates a misaligned Pockels cell, while a smooth spectrum (blue) indicates good alignment.

4. Reconnect Delay 2 on the Medox. Adjust Delay 2 so that the cavity dumps at, or just after, the peak of the waveform. Delay 2 is always greater than Delay 1, so if the pulse train disappears when Delay 2 is reconnected, reset Delay 2 to the same value as Delay 1, then increase Delay 2 until the pulse train appears. At the correct delay, power output as measured between TS28 and M29 is maximized.

5. Place a spectrometer to catch the bleedthrough from M26. The Pockels cell is birefringent and should produce a spectrum centered at 803 nm. Adjust the horizontal and vertical tilts of the Pockels cell until the spectrum is smooth (Figure H.12). Remove the spectrometer.

6. BURT (page 337).

7. Turn off the high voltage on the Medox. Verify that lasing in the RGA ceases (because the cavity is now blocked). No power should register on the power meter, and lasing spots should disappear from all the optics within the RGA when viewed with an IR viewer. If the cavity continues to lase, then either the

Pockels cell is not at quarter-wave position ("RGA seed input alignment", page 299), or the first step voltage setting is incorrect (the Titan manual refers to a 'Pockels cell manual' for the correction of this, but we do not appear to have this manual).

8. Turn on the high voltage on the Medox. Adjust Delay 2 to maximize power output. At this point, the Titan manual[352] states that the power coming from the RGA should be 400 - 500 mW. However, experience suggests that the true power should be *at least* 500 mW (> 450 mW as measured after TS28). If sufficient power cannot be achieved, the RGA is not sufficiently aligned - try again.

Seeded quarter-wave operation

In this section, the overlap of the seed and pump beams in the RGA is optimized.

1. Unblock the seed beam. Disconnect Delay 2.

2. Place a business card at A5. This card blocks the seed input into the RGA and the pump lasing output from the RGA, both of which appear as spots on the card. Visually overlap the two spots using M12 or M16. Remove the card.

3. Block the RGA cavity between A6 and TS23. Use whichever of M12 or M16 that was not used in the previous step to move the seed beam to the exact center of A6. Unblock the RGA cavity.

4. Repeat steps 2 and 3 to walk the seed beam into position at both locations.

5. At this point, the seed beam should overlap the lasing from the pump beam. When this occurs, the pulse train on the oscilloscope should appear similar to the one shown in Figure H.13. The seeded waveform appears 20 - 40 ns before

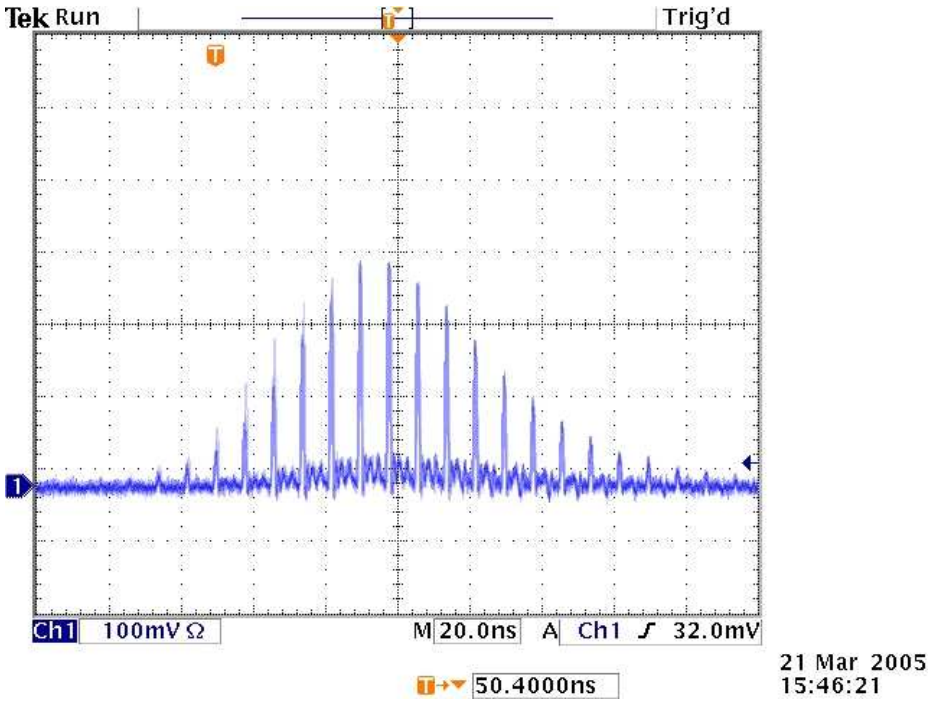

Figure H.13: Initial seeded pulse train from the RGA.

the unseeded waveform on the oscilloscope, and its amplitude should be about twice that of the unseeded waveform. Make small adjustments to M12 and M16 to maximize the amplitude of the waveform and to bring the peak amplitude left on the oscilloscope (earlier in time) as much as possible. The pulse train resulting from good alignment should appear similar to that in Figure H.14.

6. Verify that there is only one set of peaks in the pulse train. If there is more than one set, such as in Figure H.15, then Delay 1 is most likely incorrect. Adjust Delay 1 to minimize the smaller peak sets.

7. Reconnect Delay 2. Since the seeded waveform occurs before the unseeded waveform in time, decrease Delay 2 until the seeded waveform is sliced properly (at or just after the peak amplitude, Figure H.16). The power should be greater than the sliced, unseeded beam power by about the power of the seed beam. Proceed to "Pockels cell contrast ratio optimization" (below).

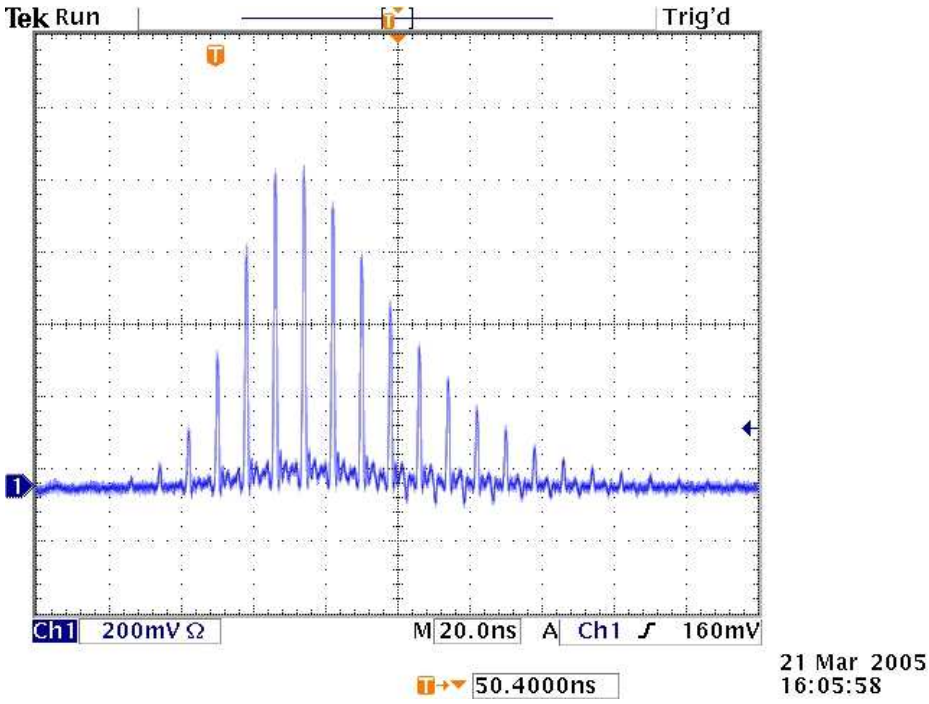

Figure H.14: Optimized seeded pulse train from the RGA. Here the peak intensity is greater and occurs earlier in time than the initial pulse train (Figure H.13).

Pockels cell contrast ratio optimization

When the RGA is running in seeded quarter-wave operation (with Delay 2 operational), the amplified output from the RGA occurs as a main peak and two satellite peaks, one before and one after the main peak. The power from the satellite peaks cannot be used by the TOPAS units, so this power is wasted. Therefore, this section details how to dump as much power into the main peak as possible, while minimizing power in the satellite peaks.

The contrast ratio between the main peak and satellite peaks can be controlled by tuning the voltage applied to the Pockels cell. Changing the voltage changes the degree of rotation of light entering and leaving the RGA. Theoretically, as long as nothing drastic has happened to the Pockels cell, the voltages set by the Quantronix technicians upon installation of the Titan are correct; thus, it should not be necessary to change these.

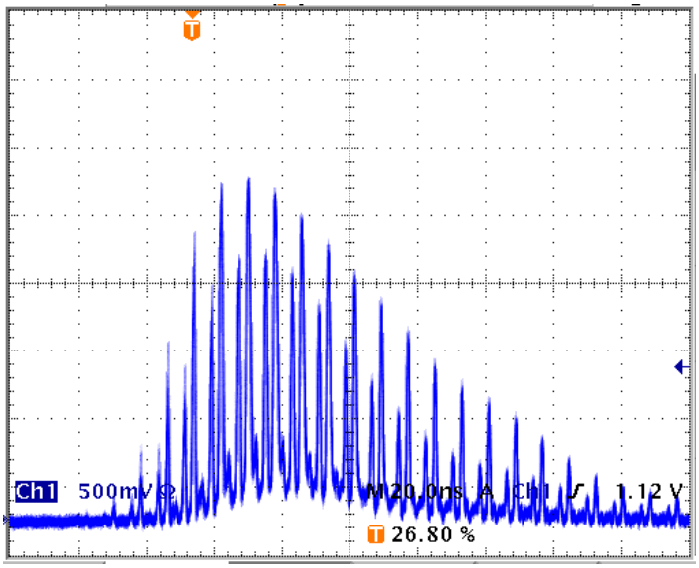

Figure H.15: Pulse train with Delay 1 improperly set. Three distinct sets of peaks are visible. Delay 1 is used to overlap the seed and pump pulses temporally within TS23. Since pulses from the YLF laser are long enough that they encompass three pulses from the Mira, each pulse from the YLF generates three peaks within the RGA - the main peak, a prepeak, and a postpeak. When Delay 1 is properly set, the overlap of seed and pump is such that the main peak is maximized, while the pre- and postpeaks are minimized (As in Figure H.14).

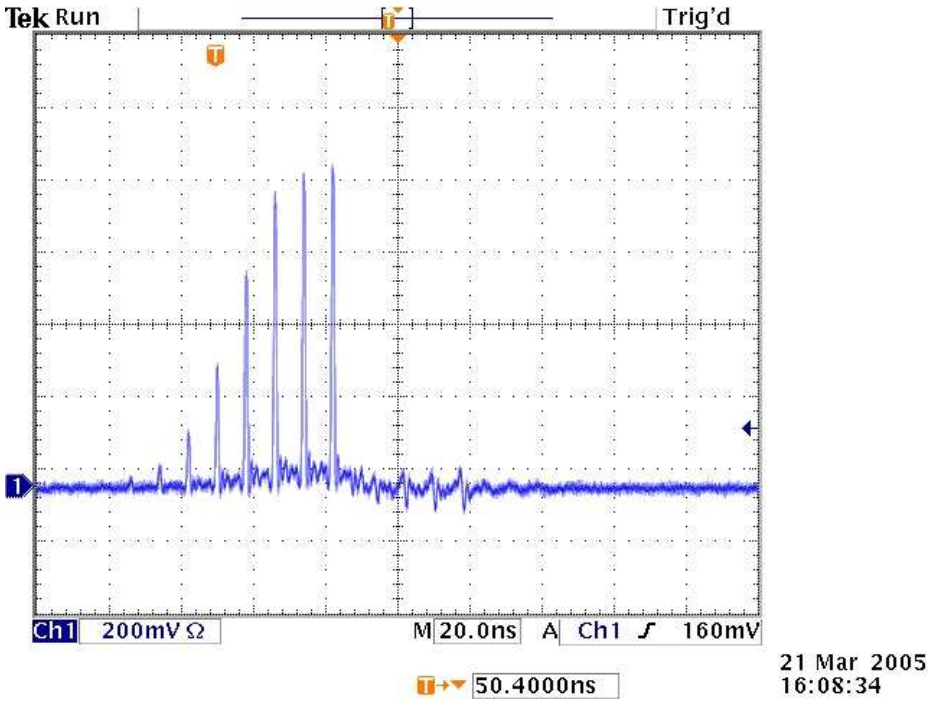

Figure H.16: Properly sliced seeded pulse train from the RGA.

More commonly, the contrast ratio is changed by tuning the position of the Pockels cell. This procedure should be used during full alignment before attempting to change the voltages, or if the Titan is already operating at full power but the TOPAS units are not generating sufficient power (when properly aligned). It is important to note, however, that tuning the Pockels cell's orientation may also change the spectrum of emitted light, as in Figure H.12, so the spectrum should be verified after tuning. A procedure for the optimization of the Pockels cell by changing its orientation follows:

1. Place a fast photodiode such that it catches the bleedthrough from M26 if conducting full alignment, or after the beamsplitter between the Titan and the TOPAS units if the Titan has measurable output. The photodiode used to monitor the pulse train in the RGA suffices for this. Place a series of strong neutral density filters or lens cleaning tissues in front of the photodiode if necessary, so that the beam does not overload the photodiode. The photodiode should not

register a voltage of greater than a few hundred millivolts. Alternately, one or more glass microscope slides can be used to deflect a small portion of the beam onto the photodiode.

2. The prepeak and postpeak are located 8.5 ns on either side of the main peak. The postpeak may be obscured in the noise following the main peak. Using PC21's horizontal and vertical adjusts, tune the Pockels cell to maximize the ratio of the main peak to the prepeak (or postpeak). Ideally, the area of the main peak should be $400 - 500$ times that of the satellite peaks; this translates to a ratio of about 100:1 in terms of peak height. The main peak and satellite peaks appear on different voltage scales when the Pockels cell is nearly aligned, so it is necessary to periodically switch scales on the oscilloscope. Figure H.17 shows photodiode readings from a Pockels cell that is very poorly aligned (H.17a) and that is aligned well (H.17b and c).

3. If a good contrast ratio cannot be obtained, try making adjustments to M24, P3 (during an initial alignment only), P7, M12, and M16 as well as the Pockels cell.

4. Replace the photodiode so that it catches the bleedthrough from M22. Verify that Delay 2 is still properly timed.

5. BURT (page 337).

6. Repeat the entire contrast ratio alignment until no further optimization of the Pockels cell and BURT mirrors can be obtained.

The preceding procedure is based on that given in the Titan manual.[352] Kozub uses an alternate procedure. When the Pockels cell is close to the proper alignment, then slight adjustments change only the intensities of the prepeak and the postpeak, while leaving the intensity of the main peak unchanged. When the Pockels cell is

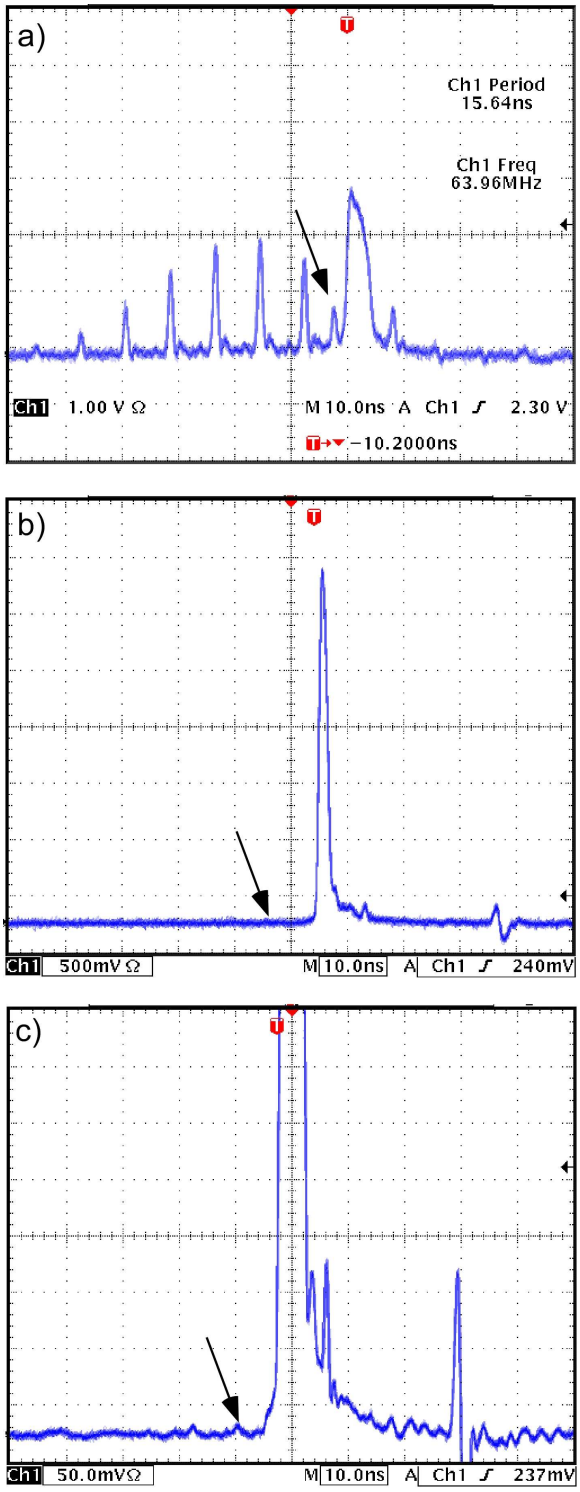

Figure H.17: Oscilloscope traces of RGA output when the Pockels cell is properly and improperly aligned. (a) The Pockels cell is so poorly aligned that leakage light from the RGA is on the scale as the dumped pulse. The prepeak is indicated by the arrow. The main peak is not Gaussian in shape because the photodiode is saturated. (b) A properly aligned Pockels cell shows only a single output peak, even when zooming in on the base of the peak (c). In (b) and (c), the prepeak is virtually gone.

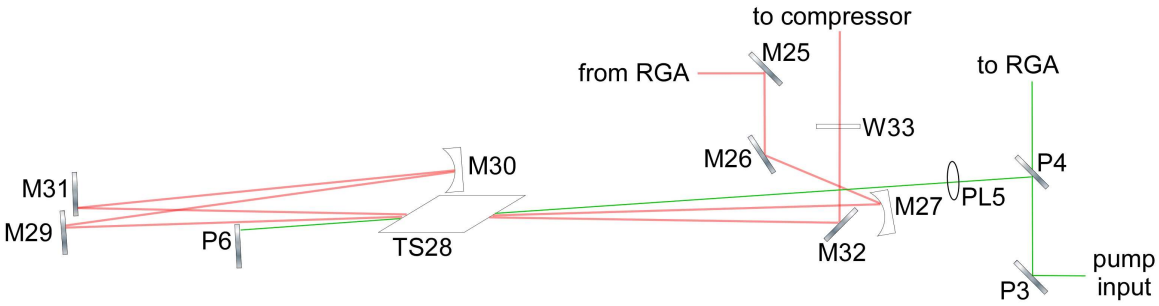

Figure H.18: Titan multipass amplifier.

properly aligned, the prepeak and postpeak are minimized; thus, the power output from the RGA is also minimized. A power meter placed after the RGA output but before the TOPAS units can thus be used to tune the Pockels cell. One must be careful when using this technique, however, as too great a change in PC21's alignment can cause clipping or RGA cavity misalignment, both of which would cause a decrease in power for the wrong reasons. A slightly safer method is to disconnect Delay 2 and to use a power meter placed between TS28 and M29 to minimize power; with Delay 2 disconnected, a well-aligned Pockels cell should nearly eliminate any power output from the RGA. Neither of these methods is as accurate as the photodiode-based procedure. As with the photodiode-based alignment, one should BURT after tuning the Pockels cell.

The power output from the RGA should be at least 450 mW as measured between TS28 and M29.

H.3.6 Multipass amplifier alignment

The multipass amplifier, shown in Figure H.18, is a much simpler system to align than the RGA. In the MPA, the output from the RGA and the majority of the light from the YLF laser make two passes each through a long, lightly doped Ti:sapphire crystal (TS28). The length and doping level allow the crystal to absorb much of the energy from the two passes of the pump without much spontaneous

fluorescence. The two passes of the beam from the RGA then stimulate coherent emission of the energy. The alignment proceeds by setting the alignment of the first pass of the pump beam, then overlapping the first pass, then the second pass, of the RGA output, followed by overlap of the second pass of the pump beam, so that all four beams overlap within the crystal, generating maximum power.

It is noted that the pump beam has only one steering optic, a beamsplitter (P4), whose transmitted light is the pump beam leading to the RGA. While it is necessary to move P4 during the course of the alignment, this slightly alters the trajectory of the pump beam into the RGA. If moved enough, the RGA ceases to operate, requiring the user to once again align the RGA. To avoid this complication, P4 should be moved in one direction at a time, periodically checking the operation of the RGA to ensure that it still operates properly and BURTing (Section H.3.8) as necessary to keep the RGA operational as P4 is moved.

WARNING: Once the MPA is operational, interruptions in the path of the seed beam through the stretcher must absolutely be avoided, as even a small interruption in the stretcher causes TS28 to burn.

1. Use a beam block (not a business card) placed in front of L33$\frac{1}{2}$ to block the path of the MPA output. Use a beam block to block the pump beam between P4 and PL5.

2. Disconnect Delay 2 and dial the YLF's lamp current to its minimum value. The Titan manual states that the Q-switch on the YLF laser should be turned off at this point, so that the YLF operates in CW mode; however, the technicians at Quantronix say NEVER to do this, as turning off the Q-switch can cause a buildup of power that can damage the optics within the YLF. It is noted that the pulse train disappears from the oscilloscope.

3. The path of the RGA-amplified seed beam in its first pass through TS28 is OI18

→ Z17 → M25 → M26 → M27 → TS28 → M29. Verify that the height of the beam is 3 inches from M26 to M29. If necessary, make vertical adjustments to M25, M26, and M27 to achieve the required height. In addition, some horizontal adjustments to these three mirrors may be necessary to roughly steer the beam through the first pass.

4. When the first pass of the MPA is properly aligned, the beam is incident on the left side of M27, passes through the (horizontal) center of the front face of TS28, narrowly misses the right (cut) edge of P6, misses M31, and hits M29. Use the horizontal adjusts of M25, M26, and M27 to walk the first pass into position.

5. Mark M29's position on the table, then remove it. Place a power meter behind the Pockels cell so that it catches the light that ordinarily would hit M29. (NOTE: Removal of M29 is necessary because the intensity of the beam between TS28 and M29 with the first passes of pump and seed aligned is sufficient to burn a power meter placed in that locale.)

6. Block the RGA beam before M25. Unblock the pump beam between P4 and PL5.

7. The path of the pump beam to the MPA's Ti:sapphire crystal is P3 → P4 → PL5 → TS28 → P6. Use P4 to center the pump beam horizontally on the front surface of TS28. The portion of the pump beam that is transmitted through TS28 should be incident on P6, a small, D-shaped mirror, near its right (cut) edge.

8. Use a beam block to block the pump beam between P4 and PL5. On the YLF controller, turn up the lamp current to its normal operating value. Since moving P4 can alter the trajectory of the pump beam in the RGA, verify that

the power from the RGA is still normal. If the RGA is still working but power has dropped, BURT (Section H.3.8). If the RGA is no longer working, repeat the RGA alignment (Section H.3.5), but only move M12, M16, M24, PC21, and P7, as no other alignment should be required. DO NOT move P3 or M22. Once the RGA is working again at optimum power, decrease the YLF's lamp to its minimum current.

9. Use P4 to adjust the height of the pump beam at TS28 to 3 inches. Since only one pump mirror (P4) is available to steer the first pass of the pump beam, it is probably not possible to maintain a height of 3 inches over the entire length of the pump beam. Instead, use the Titan alignment tool or a ruler placed first in front of, then equidistantly behind, TS28. When the beam is at 3 inches in the center of the crystal, then the difference between the true beam height and the ideal 3 inches in front of the crystal is the same as the difference in the heights behind the crystal (though opposite in sign).

10. Use P6 to visually overlap the initial pass of the pump beam through TS28 with its reflection from P6. Then change the height of the reflection from P6 so that is still passes through TS28, but is significantly removed from the first pass. Be sure to note which pass is which. (This is necessary to prevent second-pass amplification from inadvertently increasing the power of the beam when aligning the first pass.)

11. Use a beam block to block the pump beam between P4 and PL5. On the YLF controller, turn up the lamp current to its normal operating value. Since moving P4 can alter the trajectory of the pump beam in the RGA, verify that the power from the RGA is still normal. If the RGA is still working but power has dropped, BURT (Section H.3.8). If the RGA is no longer working, repeat the RGA alignment (Section H.3.5), but only move M12, M16, M24, PC21, and

P7, as no other alignment should be required. DO NOT move P3 or M22. Once the RGA is working again at optimum power, decrease the YLF's lamp current to its minimum value.

12. Use M26 and M27 to visually overlap the first-pass RGA and pump beams in TS28. Since the beams should cross in the center of the crystal, and since the crystal is not only long but also set in a larger heat sink, this is best accomplished by alternately holding a business card first at a specific distance on one side of TS28, then at the same distance on the other side, using the two mirrors to first align the beams vertically on both sides of the crystal, and then using the mirrors to make sure that the two beams are the same distance from each other on both sides of the crystal. M25 can also be used to steer the beam, if necessary.

13. Block the pump beam between P4 and PL5. Increase the YLF's lamp current to its normal operating value, and reconnect Delay 2. Unblock the pump beam. Adjust M25, M26, and M27 until the power on the power meter is maximized. A well-aligned first pass has a power of 1.9 - 2.3 W according the Titan manual. Because of the power requirements of the TOPAS units, our system needs at least 2.1 W.

14. Use the vertical adjust on P6 to align the second pass of the pump beam to the first. With the second pass of the pump, the power should increase to $\sim$2.7 W (2.6 - 2.9 W according to the manual). This power is sufficient to burn any business card placed in the beam path for more than a second, so after this point, business cards should not be used to view the beam. We recommend the use of the Mira's alignment tools, instead, as they are black matte metal. It is noted that the tool heats up rapidly, though.

15. Close the YLF shutter. Replace M29. Tune M29 to send the beam to M30.

16. Use an IR viewer to verify that the beam does not clip on M31 as it passes from TS28 to M29 or as it passes from M29 to M30. If it does clip, and if M29 cannot be tuned to eliminate clipping, then turn the YLF's lamp to its minimum value, open the YLF's shutter, and use P4 to translate the pump beam left on P6. Then go back to step 8.

17. Use the IR viewer and/or a business card to verify that the beam does not clip on TS28. Adjust M29 as necessary to eliminate clipping, making sure that it does not begin to clip on M31.

18. Adjust M30 to reflect the beam onto M31 near its left edge (as close as possible without clipping). The height of the spot should be identical to the height of the spot on M29.

19. Adjust M31 to send the beam back through TS28. This is the second pass of the seed beam.

20. Using the Titan's alignment tool and the vertical adjusts of M30 and M31, walk the second pass into vertical alignment with the first pass through TS28. Use as points of reference one place between M27 and TS28 and one place between TS28 and M29. The first pass should travel through the hole on the alignment tool, while the second hits the face of the tool (or travels through the hole as well).

21. Using the alignment tool placed first before, and then equidistantly after, TS28, visually overlap the first and second passes of the seed beam. The distance between the two passes should be the same on both sides of the crystal, though the passes should cross within TS28.

22. Verify that the second pass hits M32 without clipping. Use M32 to steer the beam through half-wave plate W33 and L33$\frac{1}{2}$ (this optic does not appear in the

Titan manual) to hit the approximate center of M34 at a height of 3 inches.

23. Remove any beam blocks (business cards, alignment tools, etc.) from the Titan. Place the Mira's alignment tool (or a beam block) in front of M35.

24. (*Optional.*) Close the YLF's shutter. Remove the center bar of the Titan's cover. The bar is attached to the ends of the Titan by four bolts, which can be removed with the aid of a socket wrench with a 1/2" socket. The bar can then be lifted out vertically. Next, remove the clear, plastic panel next to the Pockels cell that divides the Titan in half lengthwise. Only the panel next to the Pockels cell need be removed. It is secured in place by a single screw and nut attaching it to the second panel. Once the screw is removed, the panel can be lifted out carefully, so that it does not bump into M41 or any of the other optics nearby. This gives easier access to the compressor and allows the placement of a power meter in front of M35.

25. Block the pump beam between P4 and PL5. Open the YLF's shutter and increase the lamp current to its normal operating current. Verify that Delay 2 is operating, and that the RGA is properly sliced.

26. Use M34 to steer the beam to the alignment tool in front of M35.

27. Unblock the pump beam into the MPA. Look at the shape of the beam on the alignment tool in front of M36. It should be round and without structure. If structure is evident, check the *entire* Titan for signs of clipping by using a mirror to steer the beam a long distance out of the Titan and then viewing the enlarged beam with a business card. The clipping must be eliminated before proceeding.

28. Close the YLF shutter. Replace the alignment tool in front of M35 with a power meter. Open the YLF shutter.

29. Use M30 and M31 to maximize power. Make sure that steering the second pass does not cause clipping on or after M32. M32 and M34 can be used to keep the beam on the power meter. The optimized power should be > 4.2 W (the manual states $4.1 - 4.6$ W).

30. Verify that the spot on the power meter remains round and featureless. The spot is large, but not so large that it clips on L34$\frac{1}{2}$, and it should be fairly intense. If clipping is evident, or if the spot appears too diffuse, recheck the placement of M29's mount on the table, as well as the path of the beam from M29 to the power meter.

31. Close the YLF's shutter. Remove the power meter.

H.3.7 Compressor alignment

The compressor is the last portion of the Titan to be aligned, and is potentially the most dangerous. Although alignment of the compressor is not difficult, there is a significant risk of damage to the compressor gratings (and skin!) because of the power of the beam at this point. To avoid damage, the path of the beam through the compressor should never be partially blocked or inadvertently interrupted. Therefore, it is recommended that the YLF's shutter be closed whenever moving objects in and out of the compressor.

It is noted that the input path of the beam into the compressor differs significantly from the path given in the manual. Two additional optics, L33$\frac{1}{2}$ and L34$\frac{1}{2}$, are in the beam path, alignment aperture A7 is not present, and M36 is in a different location. The correct scheme is given in Figure H.19. It is also noted that the compressor outputs 70% - 90% of the power that it receives from the MPA when aligned properly. Therefore, to obtain the 3.2 W output from the Titan necessary to operate the TOPAS units, the power output from the MPA should be $4.2 - 4.6$ W, depending on the efficiency of the compressor alignment.

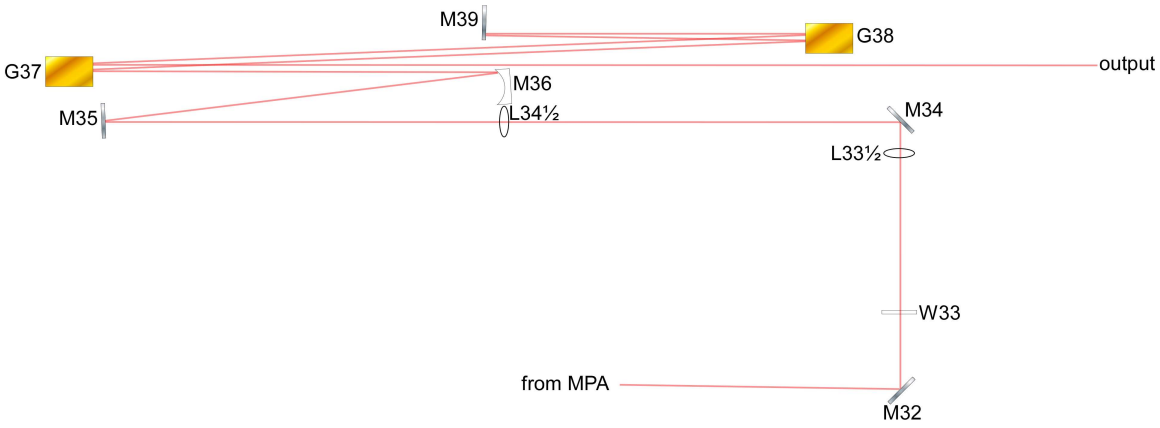

Figure H.19: Titan compressor.

WARNING: When aligning the compressor, the path of the seed beam through the stretcher must absolutely be avoided, as even a small interruption in the stretcher causes TS28 to burn.

1. Close the YLF's shutter. Place one of the Titan's alignment tools in front of M35. Place a power meter capable of measuring > 4 W at the Titan's output port to measure the output from the compressor.

2. (*Optional.*) Remove the center bar of the Titan's cover. The bar is attached to the ends of the Titan by four bolts, which can be removed with the aid of a socket wrench with a 1/2" socket. The bar can then be lifted out vertically. Next, remove the clear, plastic panel next to the Pockels cell that divides the Titan in half lengthwise. Only the panel next to the Pockels cell need be removed. It is secured in place by a single screw and nut attaching it to the second panel. Once the screw is removed, the panel can be lifted out carefully, so that it does not bump into M41 or any of the other optics nearby. This gives easier access to the compressor.

3. Open the YLF's shutter. Use M32 to steer the MPA's output to the center of M34. The height of the beam on M34 should be 3 inches.

4. Use M34 to steer the beam to M35. The height of the beam on M35 should be 4 inches. Use the alignment tool in front of M35 to achieve this.

5. Close the YLF's shutter. Move the alignment tool from before M35 to before M36. Open the shutter.

6. Use M34 to center the beam horizontally on M35. Verify that no clipping occurs. Use M35 and the alignment tool to steer the beam to the left side of M36 at a height of 4 inches. The beam should remain at a height of 4 inches throughout the remainder of the compressor.

7. Close the YLF's shutter. Remove the alignment tool. Open the shutter.

8. Verify that the beam hits very close to the left edge of M36 without clipping. The beam must be close to the left edge so that the beam output by the compressor does not clip on M36.

9. Use M36 to steer the beam to the left side of G37 so that it is centered vertically at 4 inches on the grating.

10. Contrary to the procedure outlined in the manual, DO NOT adjust either G37's or G38's tilts. The gratings should only be adjusted when their alignment had been altered, e.g., when installing new gratings. Instead, use M36 and, if necessary, M35 and M34 to send the beam from G38 to G39 (roughly 1/3" from the right edge) and thence to M39 near the left edge.

11. Adjust M39 to send the spectrum back to G38 1/4" to the left of the original spectrum. The beam should hit the left side of G38, then the right side of G37, before narrowly missing the left edge of M36 on its way out of the Titan. This should be possible by adjusting only M39. If not, make small adjustments as necessary to M36.

12. Once the beam passes out of the Titan, it passes through an alignment aperture and a collimating periscope. Make adjustments as necessary to M36 and M39 to center the beam in the alignment aperture and periscope.

13. Measure the power output from the Titan. It should be at least 3.2 W, although the TOPAS units can operate with slightly less power.

In aligning the compressor, it is very important that the output from the compressor be round and featureless with respect to both spectrum and time. The best method for measuring the pulse in time is to use a single-shot autocorrelator. The Free-Electron Laser (FEL) Center owns such an instrument; alternately, one can be built without too much difficulty. The FEL's autocorrelator is shown in Figure H.20. Essentially, a beam input exactly normal to the surface of the autocorrelator travels to a polarizer whose polarization is set 45° to the polarization of the incoming beam. The beam is thus split in two, with half transmitting to a pair of mirrors on a micrometer-driven translation stage and the other half reflected to a fixed mirror. The beams travel through the autocorrelator using a series of mirrors until both beams hit the same mirror, which reflects the beams into a mixing crystal. When aligned properly, the beams cross spatially within the crystal, while the micrometer-driven stage and mirrors act as a delay stage, allowing the beams to be aligned in time as well (in the FEL's autocorrelator, this occurs at a micrometer setting of $\sim 3 - 4.5$).

When the beams are aligned in both time and space, a bar of sum-frequency 400 nm light is generated between the two transmitted 800 nm beams; this is readily visible on a business card if the beams are not attenuated too much (Figure H.21). A thin bar of SF light perpendicular to the axis formed by the two transmitted beams (H.21b) is indicative of a properly aligned compressor. A thick bar (H.21a) is formed when the pulses from the Titan are not compressed properly, because long pulses overlap in space and time over a large region of the mixing crystal. When the compressor gratings are not perfectly parallel, the Titan outputs a beam that displays

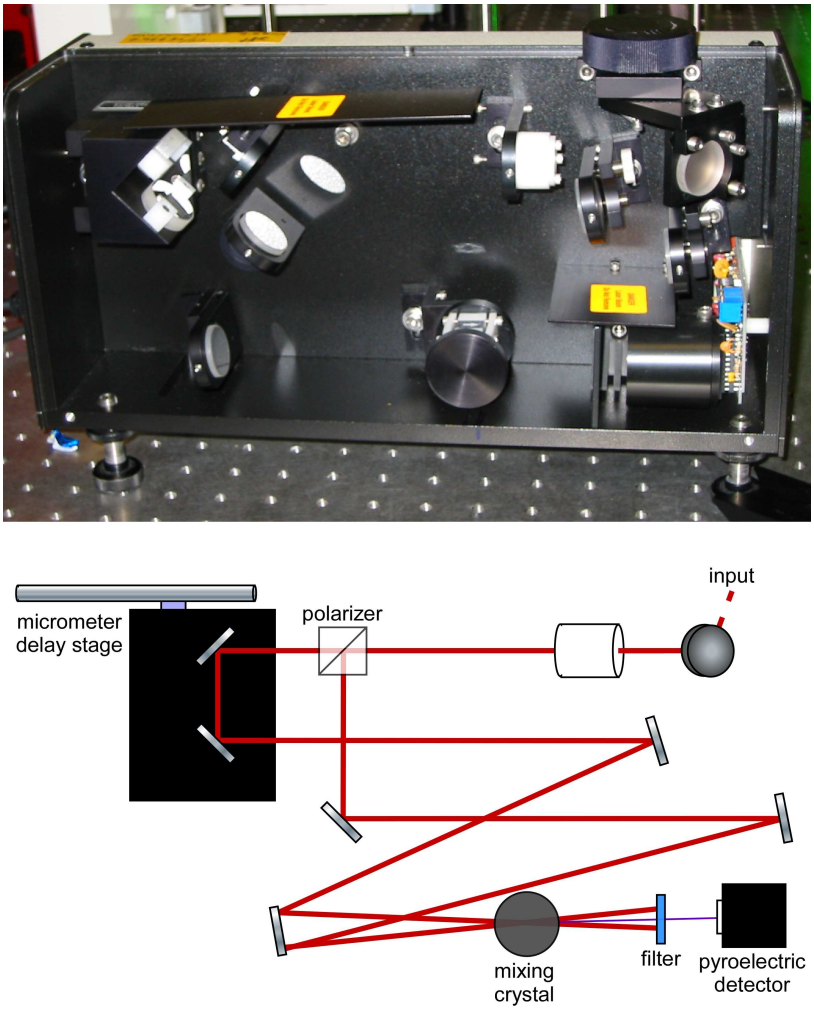

Figure H.20: Photograph (top) and schematic (bottom) of the interior of the FEL's single-shot autocorrelator.

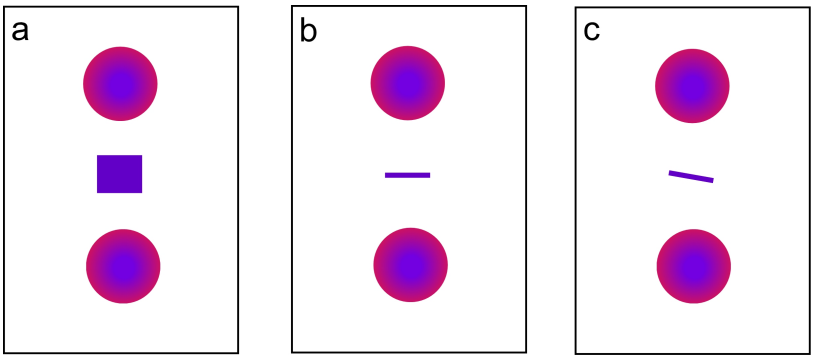

Figure H.21: Output beams from the single-shot autocorrelator, as viewed on a business card. The top and bottom circles are the transmitted beams and SH light generated in the mixing crystal. The bars in the middle are the SF light from the mixing of the two beams in the crystal. (a) Insufficient compression. (b) Proper compression. (c) Structured output from misaligned gratings.

structure in space and time; as a result, overlap of the beams in the autocorrelator's mixing crystal is not uniform, and the bar appears tilted (H.21c). In this case, the grating parallelism is not perfect; since we never corrected the grating parallelism, the reader is referred to the Titan manual[352] for this procedure.

The FEL's autocorrelator utilizes a pyroelectric detector connected to an oscilloscope to detect the intensity and location of the SF light. The oscilloscope trace (Figure H.22) gives the autocorrelated signal with a ratio of $\sim$ 1 fs autocorrelated signal per 2 μs measured on the oscilloscope. As usual, the autocorrelated signal must be divided by $\sqrt{2}$ to yield the true pulse length. The maximum compression attainable by the Titan's compressor gives a pulse whose duration is equal to the pulse length of the Mira's output, usually 100 - 120 fs (160 - 175 fs autocorrelated). If the measured pulse is longer than this, then the compression can be improved by moving G37 in the z-direction using its micrometer-driven translation stage. Although there is a dial for this stage on the exterior of the Titan's case, ours is not actually attached to the stage, so the inner dial must be used instead. It is noted that once G37 has been translated, it may be necessary to realign the compressor slightly.

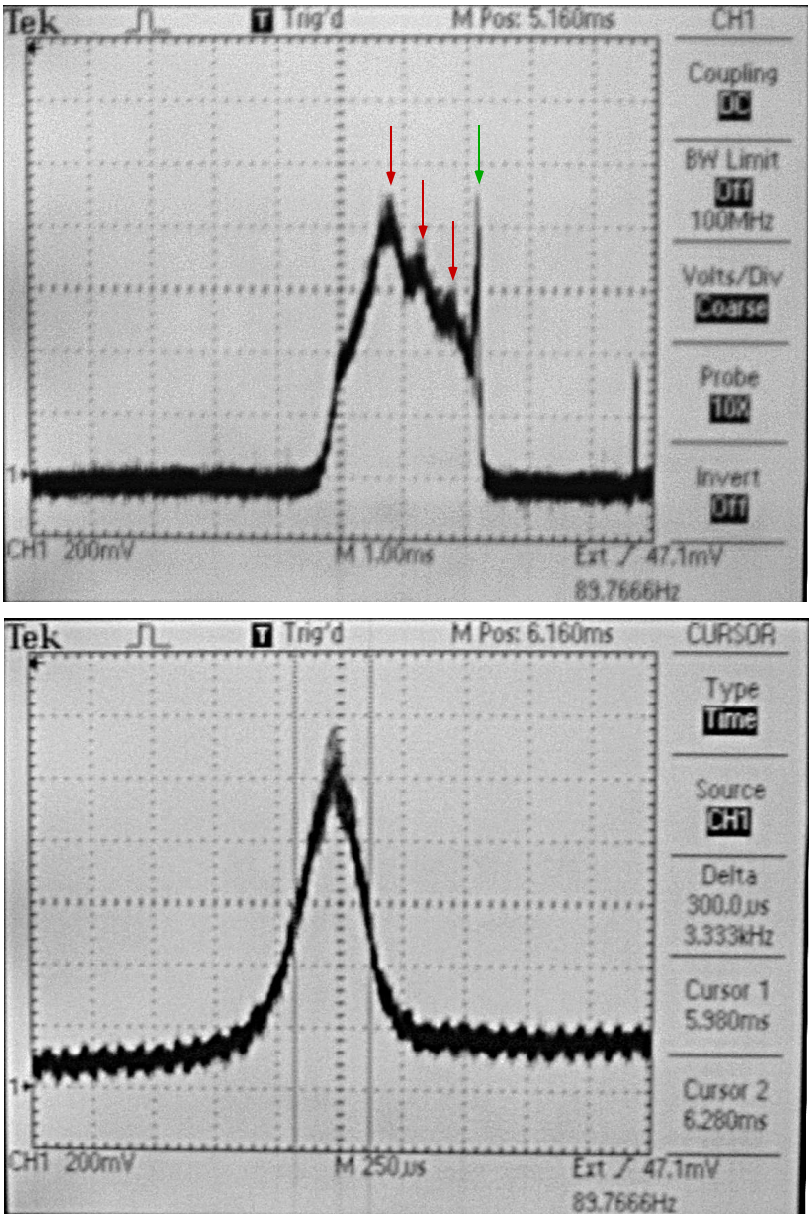

Figure H.22: Oscilloscope traces of Titan output using a single-shot autocorrelator. (Top) Autocorrelator trace of a poorly aligned compressor. The trace is very far from Gaussian, containing both regularly spaced peaks (red arrows) that may indicate a diffraction problem and a sharp spike (green arrow), indicating possible beam structure. In addition, the shape of the trace changed as the delay stage in the autocorrelator was moved, which should not occur. The length of the pulse shown here is approximately 1 ps FWHM autocorrelated ($\sim$ 700 fs true length) - the compressor is clearly not compressing sufficiently. (Bottom) After translating G37 in the z-direction, the compressor is working properly, giving a pulse length of 150 fs autocorrelated (110 fs true length), identical to the pulse duration from the Mira.

Once good compression has been achieved, the beam should be checked for spatial structure by diverting the Titan's output several meters and viewing it with a business card. The spot should be round and featureless. If it shows structure, the vertical height of the beam through the compressor may be incorrect. Make slight adjustments to M36 (and M35 and M34, as necessary), correcting the height of the return beam using M39. Kozub says that only the vertical height need be adjusted.

For the TOPAS units to operate properly, the Titan's output should have a power of 3.2 W with a pulse length of 150 fs FWHM.

H.3.8 Peaking power/build up reduction in time (BURT)

When the Titan is operating reasonably well, there are a few optics that can be tweaked to maximize performance and power without changing the path of the beam output by the Titan. The primary method of optimizing performance is BURTing, a procedure by which power from the RGA is optimized. Simply put, the purpose of BURTing is to move the buildup of power in the RGA cavity earlier in time. This reduces power loss from cavity leakage and correspondingly increases RGA output power. Figure H.23 shows which optics can be used to optimize the Titan's performance in general and to BURT. Table H.3 lists each of these optics and the effects of adjusting them. Because the BURT procedure is most commonly used and is central to good operation, we discuss it first.

BURTing is monitored through the pulse train on the oscilloscope, and, if applicable, through the use of a power meter placed appropriately. It can be performed with Delay 2 either on or off. However, it is rather easier to observe BURTing while the pulse train is sliced (i.e., Delay 2 is on). When the train is sliced, BURTing manifests as a shift in the peak intensity in the pulse train from the last peak in the sliced train to some peak before the last (Figure H.24).

To BURT, four mirrors are adjusted: M12, M16, M24, and P7. M24 aligns the

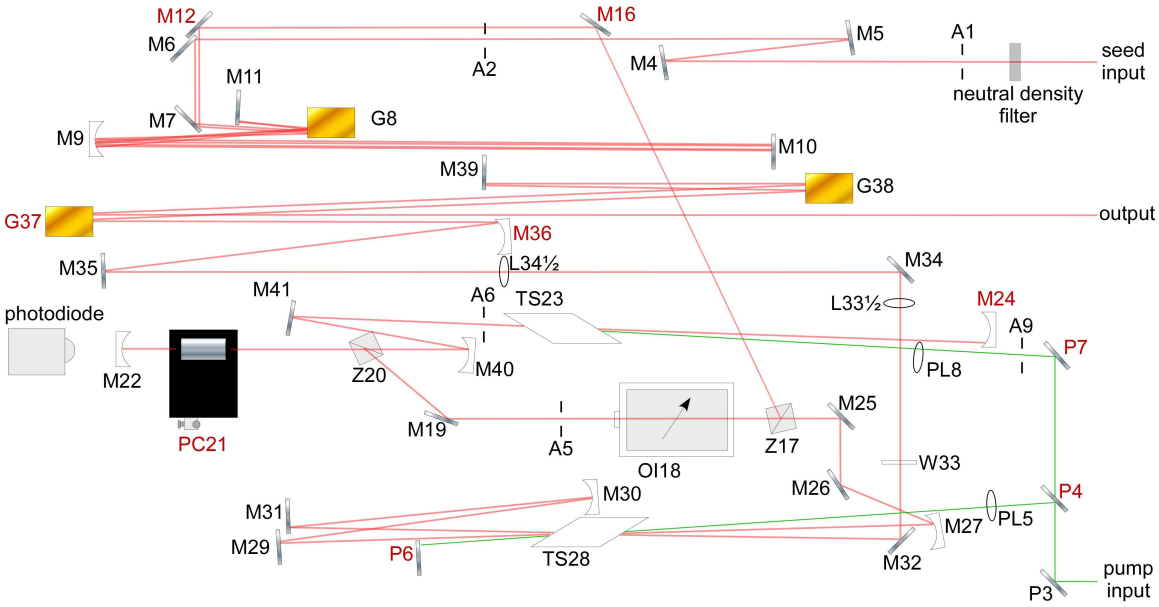

Figure H.23: Optics used to peak power and BURT. Optics labelled in red can be adjusted during Titan operation to optimize performance. Table H.3 lists the effects of adjusting each optic.

Table H.3: Optics used to peak power and BURT.

optic	effect
M12	2^{nd} iteration seed alignment in RGA (BURT)
M16	1^{st} iteration seed alignment in RGA (BURT)
PC21	RGA output peak shape (BURT)
M24	RGA cavity alignment (BURT)
P7	pump alignment in RGA (BURT)
P4	MPA alignment
P6	MPA alignment
M36	compressor output direction
G37	output pulse duration (z-translation only)

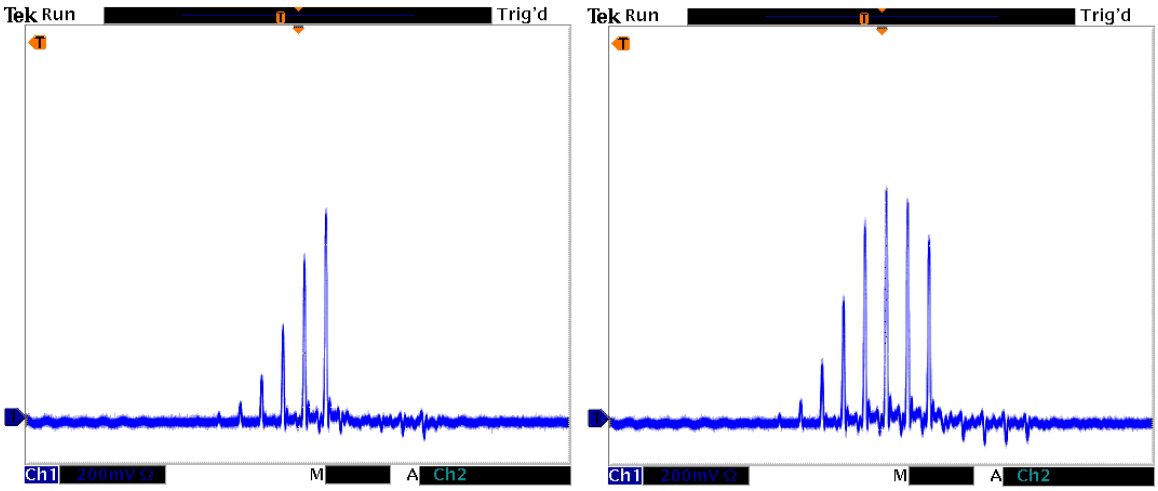

Figure H.24: Effects of BURT on the pulse train. (Left) Original pulse train. (Right) After BURTing, the peak of the pulse train has moved earlier in time.

RGA cavity and usually makes the most significant contribution to BURT, followed by P7, which is used to optimize the direction and placement of pump input into the cavity. M12 and M16 are used to obtain the best overlap of seed and pump in the cavity. When adjusting, it is best to optimize only one direction (horizontal or vertical) at a time, using all four mirrors, before repeating the process in the other direction. Generally, M24 and P7 are adjusted, using several iterations as necessary, followed by M12 and M16 to recover seed overlap. Delay 2 is moved earlier in time as necessary to keep slicing the pulse train at maximum power.

Once the four mirrors have been optimized, the Pockels cell (PC21) is adjusted to optimize the contrast ratio of the RGA output, and is outlined in the "Pockels cell contrast ratio optimization" procedure given on page 318. As tuning the Pockels cell slightly alters the path of the beam through the RGA cavity, it is sometimes necessary to perform a few iterations of contrast ratio optimization and BURT before the RGA cavity is optimized.

When the RGA has been optimized, the MPA can be optimized by making very slight adjustments to P4 and P6. A power meter placed at the Titan's output

should be used to monitor the MPA optimization. It is noted that tuning P4 changes the placement of the pump beam on P6 as well, so that the second pass of the pump beam moves out of alignment with the first pass; P6 must be adjusted to correct this. Tuning P4 also changes the placement of the beam on P7, so it is a good idea to BURT once P4 has been moved.

If TOPAS output is low because the output pulse from the Titan is not compressed sufficiently, this can be corrected by moving the z-placement of G37. However, this may change the alignment of the compressor enough that other optics must also be moved. M36 can be tuned to change the direction of the Titan output beam.

REFERENCES

[1] Swafford, L. A.; Rosenthal, S. J. Molecular- and nanomaterial-based photovoltaics. In *Molecular Nanoelectronics*; Reed, M. A.; Lee, T. K., Eds.; American Scientific Publishers: Stevenson Ranch, California, 2003.

[2] Greenham, N. C.; Peng, X.; Alivisatos, A. P. *Physical Review B* **1996,** *54,* 17628-17636.

[3] Huynh, W. U.; Dittmer, J. J.; Alivisatos, A. P. *Science* **2002,** *295,* 2425-2427.

[4] Robel, I.; Subramanian, V.; Kuno, M.; Kamat, P. V. *Journal of the American Chemical Society* **2006,** *128,* 2385-2393.

[5] Schaller, R. D.; Klimov, V. I. *Physical Review Letters* **2004,** *92,* 186601.

[6] Mueller, A. H.; Petruska, M. A.; Achermann, M.; Werder, D. J.; Akhadov, E. A.; Koleske, D. D.; Hoffbauer, M. A.; Klimov, V. I. *Nano Letters* **2005,** *5,* 1039-1044.

[7] Erwin, M. M.; Kadavanich, A. V.; McBride, J.; Kippeny, T.; Pennycook, S.; Rosenthal, S. J. *European Physical Journal D* **2001,** *16,* 275-277.

[8] Bowers, M. J.; McBride, J. R.; Rosenthal, S. J. *Journal of the American Chemical Society* **2005,** *127,* 15378-15379.

[9] Gao, M. Y.; Lesser, C.; Kirstein, S.; Mohwald, H.; Rogach, A. L.; Weller, H. *Journal of Applied Physics* **2000,** *87,* 2297-2302.

[10] Wang, L. G.; Pennycook, S. J.; Pantelides, S. T. *Physical Review Letters* **2002,** *89,* 075506.

[11] Henglein, A. *Pure and Applied Chemistry* **1984,** *56,* 1215-1224.

[12] Henglein, A. *Berichte der Bunsen-Gesellschaft-Physical Chemistry and Chemical Physics* **1997,** *101,* 1562-1572.

[13] Kho, R.; Nguyen, L.; Torres-Martinez, C. L.; Mehra, R. K. *Biochemical and Biophysical Research Communications* **2000,** *272,* 29-35.

[14] Zimmer, J. P.; Kim, S. W.; Ohnishi, S.; Tanaka, E.; Frangioni, J. V.; Bawendi, M. G. *Journal of the American Chemical Society* **2006,** *128,* 2526-2527.

[15] Bentzen, E. L.; House, F.; Utley, T. J.; Crowe, J. E.; Wright, D. W. *Nano Letters* **2005,** *5,* 591-595.

[16] Dubertret, B.; Skourides, P.; Norris, D. J.; Noireaux, V.; Brivanlou, A. H.; Libchaber, A. *Science* **2002,** *298,* 1759-1762.

[17] Gerion, D.; Parak, W. J.; Williams, S. C.; Zanchet, D.; Micheel, C. M.; Alivisatos, A. P. *Journal of the American Chemical Society* **2002,** *124,* 7070-7074.

[18] Rosenthal, S. J.; Tomlinson, I.; Adkins, E. M.; Schroeter, S.; Adams, S.; Swafford, L.; McBride, J.; Wang, Y. Q.; DeFelice, L. J.; Blakely, R. D. *Journal of the American Chemical Society* **2002,** *124,* 4586-4594.

[19] Wu, X. Y.; Liu, H. J.; Liu, J. Q.; Haley, K. N.; Treadway, J. A.; Larson, J. P.; Ge, N. F.; Peale, F.; Bruchez, M. P. *Nature Biotechnology* **2003,** *21,* 41-46.

[20] Dahan, M.; Levi, S.; Luccardini, C.; Rostaing, P.; Riveau, B.; Triller, A. *Science* **2003,** *302,* 442-445.

[21] Klein, D. L.; Roth, R.; Lim, A. K. L.; Alivisatos, A. P.; McEuen, P. L. *Nature* **1997,** *389,* 699-701.

[22] Kononkamp, R.; Hoyer, P.; Wahi, A. *Journal of Applied Physics* **1996,** *79,* 7029-7035.

[23] Vlasov, Y. A.; Yao, N.; Norris, D. J. *Advanced Materials* **1999,** *11,* 165-169.

[24] Peter, L. M.; Riley, D. J.; Tull, E. J.; Wijayantha, K. G. U. *Chemical Communications* **2002,** *2002,* 1030-1031.

[25] Qian, H. F.; Qiu, X.; Li, L.; Ren, J. C. *Journal of Physical Chemistry B* **2006,** *110,* 9034-9040.

[26] McBride, J.; Treadway, J.; Feldman, L. C.; Pennycook, S. J.; Rosenthal, S. J. *Nano Letters* **2006,** *6,* 1496-1501.

[27] Qian, H. F.; Li, L.; Ren, J. C. *Materials Research Bulletin* **2005,** *40,* 1726-1736.

[28] Zhong, X. H.; Han, M. Y.; Dong, Z. L.; White, T. J.; Knoll, W. *Journal of the American Chemical Society* **2003,** *125,* 8589-8594.

[29] Jang, E.; Jun, S.; Pu, L. **2003,** *2004,* 2964-2965.

[30] Zhong, X.; Feng, Y.; Knoll, W.; Han, M. *Journal of the American Chemical Society* **2003,** *125,* 13559-13563.

[31] Tian, Y. C.; Newton, T.; Kotov, N. A.; Guldi, D. M.; Fendler, J. H. *Journal of Physical Chemistry* **1996,** *100,* 8927-8939.

[32] Bailey, R. E.; Nie, S. *Journal of the American Chemical Society* **2003,** *125,* 7100-7106.

[33] Kuno, M.; Higginson, K. A.; Qadri, S. B.; Yousuf, M.; Lee, S. H.; Davis, B. L.; Mattoussi, H. *Journal of Physical Chemistry B* **2003,** *107,* 5758-5767.

[34] Swafford, L. A.; Weigand, L. A.; Bowers II, M. J.; McBride, J. R.; Rapaport, J. L.; Watt, T. L.; Dixit, S. K.; Feldman, L. C.; Rosenthal, S. J. *Journal of the American Chemical Society* **2006,** *128,* 12299-12306.

[35] Alivisatos, A. P. *Journal of Physical Chemistry* **1996,** *100,* 13226-13239.

[36] Wang, Z. L.; Petroski, J. M.; Green, T. C.; El-Sayed, M. A. *Journal of Physical Chemistry B* **1998,** *102,* 6145-6151.

[37] Tolbert, S. H.; Alivisatos, A. P. *Journal of Chemical Physics* **1995,** *102,* 4642-4656.

[38] Mamlui, Y. A.; Ol'khovik, L. P. *Low Temperature Physics* **2005,** *31,* 268-276.

[39] Wang, L. W.; Zunger, A. *Physical Review B* **1996,** *53,* 9579-9582.

[40] Yu, W. W.; Qu, L.; Guo, W.; Peng, X. *Chemistry of Materials* **2003,** *15,* 2854-2860.

[41] Yu, W. W.; Qu, L. H.; Guo, W. Z.; Peng, X. G. *Chemistry of Materials* **2004,** *16,* 560.

[42] Aktsipetrov, O. A.; Nikulin, A. A.; Ekimov, A. I. *JETP Letters* **1992,** *55,* 435-439.

[43] Ekimov, A. I.; Hache, F.; Schanne-Klein, M. C.; Ricard, D.; Flytzanis, C.; Kudryavtsev, I. A.; Yazeva, T. V.; Rodina, A. V.; Efros, A. L. *Journal of the Optical Society of America B* **1993,** *10,* 100-107.

[44] Alivisatos, A. P. *Science* **1996,** *271,* 933-937.

[45] Brus, L. E. *Journal of Chemical Physics* **1983,** *79,* 5566-5571.

[46] Landolt, H. *Landolt-Börnstein: Numerical Data and Functional Relationships in Science and Technology;* volume III-17b of *New Series* Springer: New York, 1982.

[47] Yoffe, A. D. *Advances in Physics* **2001,** *50,* 1-208.

[48] Kippeny, T.; Swafford, L. A.; Rosenthal, S. J. *Journal of Chemical Education* **2002,** *79,* 1094-1100.

[49] Brus, L. E. *Journal of Chemical Physics* **1984,** *80,* 4403-4409.

[50] Kuno, M.; Lee, J. K.; Dabbousi, B. O.; Mikulec, F. V.; Bawendi, M. G. *Journal of Chemical Physics* **1997,** *106,* 9869-9882.

[51] Soloviev, V. N.; Eichhöfer, A.; Fenske, D.; Banin, U. *Journal of the American Chemical Society* **2000,** *122,* 2673-2674.

[52] Murray, C. B.; Norris, D. J.; Bawendi, M. G. *Journal of the American Chemical Society* **1993,** *115,* 8706-8715.

[53] Peng, X.; Wickham, J.; Alivisatos, A. P. *Jounal of the American Chemical Society* **1998,** *120,* 5343-5344.

[54] Rogach, A. L.; Koronowski, A.; Gao, M.; Eychmüller, A.; Weller, H. *Journal of Physical Chemistry B* **1999,** *103,* 3065-3069.

[55] Woodyard, J. R.; Landis, G. A. *Solar Cells* **1991,** *31,* 297-329.

[56] Yang, J.; Banerjee, A.; Guha, S. *Applied Physics Letters* **1997,** *70,* 2975-2977.

[57] Chopra, K. L.; Das, S. R. *Thin Film Solar Cells;* Plenum Press: New York, 1983.

[58] Luque, A.; Hegedus, S., Eds.; *Handbook of Photovoltaic Science and Engineering;* John Wiley & Sons: West Sussex, England, 2003.

[59] Peternai, L.; Kovac, J.; Jakabovic, J.; Vincze, A.; Satka, A.; Gottschalch, V. *Vacuum* **2005,** *80,* 229-235.

[60] Akasaki, I.; Amano, H. *Journal of the Electrochemical Society* **1994,** *141,* 2266-2271.

[61] Kondow, M.; Kitatani, T.; Nakatsuka, S.; Larson, M. C.; Nakahara, K.; Yazawa, Y.; Okai, M.; Uomi, K. *IEEE Journal of Selected Topics in Quantum Electronics* **1997,** *3,* 719-730.

[62] Yang, X. H.; Hays, J. M.; Shan, W.; Song, J. J.; Cantwell, E. *Applied Physics Letters* **1993,** *62,* 1071-1073.

[63] Weller, D.; A, M.; Folks, L.; Best, M. E.; Lee, W.; Toney, M. F.; Schwickert, M.; Thiele, J. U.; Doerner, M. F. *IEEE Transactions on Magnetics* **2000,** *36,* 10-15.

[64] Lee, I. S.; Ryu, H.; Lee, H. J.; Lee, T. D. *Journal of Applied Physics* **1999,** *85,* 6133-6135.

[65] Végard, L. *Zeitschrift für Physik* **1921,** *5,* 17-26.

[66] Bernard, J.; Zunger, A. *Physcal Review B* **1987,** *36,* 3199-3228.

[67] Czaja, W. *Festkörperprobleme* **1971,** *11,* 65.

[68] Naumov, A.; Permogorov, S.; Reznitsky, A.; Verbin, S.; Klochikhin, A. *Journal of Crystal Growth* **1990,** *101,* 713-717.

[69] Ridley, B. K. *Quantum Processes in Semiconductors;* Clarendon: Oxford, 1982.

[70] Wu, J.; Walukiewicz, W.; Yu, K. M.; III, J. W. A.; Haller, E. E.; Miotkowski, I.; Ramdas, A. K.; Sou, C. S. I. K.; Perera, R. C. C.; Denlinger, J. D. *Physical Review B* **2003,** *67,* 035207.

[71] Walukiewicz, W.; Shan, W.; Yu, K. M.; III, J. W. A.; Haller, E. E.; Miotkowski, I.; Seong, M. J.; Alawadhi, H.; Ramdas, A. K. *Physical Review Letters* **2000,** *85,* 1552-1555.

[72] Shan, W.; Walukiewicz, W.; III, J. W. A.; Haller, E. E.; Geisz, J. F.; Friedman, D. J.; Olson, J. M.; Kurtz, S. R. *Physical Review Letters* **1999,** *82,* 1221-1224.

[73] Böer, K. W. *Survey of Semiconductor Physics: Electrons and Other Particles in Bulk Semiconductors;* Van Nostrand Reinhold: New York, 1990.

[74] Wei, S.-H.; Zhang, S. B.; Zunger, A. *Journal of Applied Physics* **2000,** *87,* 1304-1311.

[75] Goede, O.; Hennig, D.; John, L. *Physica Status Solidi B* **1979,** *96,* 671-681.

[76] McBride, J. R.; Kippeny, T. C.; Pennycook, S. J.; Rosenthal, S. J. *Nano Letters* **2004,** *4,* 1279-1283.

[77] Kippeny, T. C.; Bowers II, M. J.; Rosenthal, S. J. Unpublished data.

[78] Hines, M. A.; Guyot-Sionnest, P. *Journal of Physical Chemistry B* **1998,** *102,* 3655-3657.

[79] Peng, X.-G.; Manna, L.; Yang, W. D.; Wickham, J.; Scher, E.; Kadavanich, A.; Alivisatos, A. P. *Nature* **2000,** *404,* 59-61.

[80] Kippeny, T. C. *Exciton Dynamics in Cadmium Selenide/Zinc Selenide Core/Coreshell Nanocrystals as Affected by Surface Ligand Modification Using Femtosecond Fluorescence Upconversion,* Thesis, Vanderbilt University, 2005.

[81] Talapin, D. V.; Rogach, A. L.; Kornowski, A.; Haase, M.; Weller, H. *Nano Letters* **2001,** *1,* 207-211.

[82] Yu, W. W.; Peng, X. *Angewandte Chemie-International Edition* **2002,** *41,* 2368-2371.

[83] Taylor, J.; Kippeny, T.; Bennett, J. C.; Huang, M. B.; Feldman, L. C.; Rosenthal, S. J. *Materials Research Society Symposium Proceedings* **1999,** *536,* 413-418.

[84] Smith, M. B.; March, J. *March's Advanced Organic Chemistry: Reactions, Mechanisms, and Structure;* John Wiley & Sons: New York, Fifth ed.; 2001.

[85] Peng, Z. A.; Peng, X. G. *Journal of the American Chemical Society* **2002,** *124,* 3343-3353.

[86] Vossmeyer, T.; Katsikas, L.; Giersig, M.; Popovic, I. G.; Diesner, K.; Chemseddine, A.; Eychmüller, A.; Weller, H. *Journal of Physical Chemistry* **1994,** *98,* 7665-7673.

[87] Klimov, V. I. *Journal of Physical Chemistry B* **2000,** *104,* 6112-6123.

[88] McBride, J. R. *Atomic Level Characterization of CdSe Nanocrystal Systems Using Atomic Number Contrast Scanning Transmission Electron Microscopy and Rutherford Backscattering Spectroscopy,* Thesis, Vanderbilt University, 2005.

[89] Kadavanich, A. V. *The Structure and Morphology of Semiconductor Nanocrystals,* Thesis, University of California, Berkeley, 1997.

[90] Tolbert, S. H.; Alivisatos, A. P. *Science* **1994,** *265,* 373-376.

[91] Kadavanich, A. V.; Kippeny, T. C.; Erwin, M. M.; Pennycook, S. J.; Rosenthal, S. J. *Journal of Physical Chemistry B* **2001,** *105,* 361-369.

[92] Feldman, L. C.; Mayer, J. W. *Fundamentals of Surface and Thin Film Analysis;* North Holland-Elsevier: New York, 1986.

[93] Erwin, M. M.; McBride, J.; Kadavanich, A. V.; Rosenthal, S. J. *Thin Solid Films* **2002,** *409,* 198-205.

[94] Tesmer, J. R.; Nastasi, M.; Barbour, J. C.; Maggiore, C. J.; Mayer, J. W., Eds.; *Handbook of Modern Ion Beam Materials Analysis;* Materials Research Society: Pittsburgh, Pennsylvania, 1995.

[95] Taylor, J.; Kippeny, T.; Rosenthal, S. J. *Journal of Cluster Science* **2001,** *12,* 571-582.

[96] Bevington, P. R. *Data Reduction and Error Anaysis for the Physical Sciences;* McGraw-Hill: New York, 1969.

[97] Mayer, M. "SIMNRA User's Guide", Max-Planck-Institute für Plasmaphysik, Boltzmannstr. 2, D-85748 Garching, Germany, 1997.

[98] Peng, Z. A.; Peng, X. *Journal of the American Chemical Society* **2001,** *123,* 1389-1395.

[99] Bullen, C. R.; Mulvaney, P. *Nano Letters* **2004,** *4,* 2303-2307.

[100] Peng, Z. A.; Peng, X. *Journal of the American Chemical Society* **2001,** *123,* 183-184.

[101] Weigand, L. "Compositional and Size Control of Optical Properties of Alloyed $CdSe_xS_{1-x}$ Nanocrystals", undergraduate honors thesis, Vanderbilt University, Department of Chemistry, 2005.

[102] Peng, X.; Schlamp, M.; Kadavanich, A.; Alivisatos, A. P. *Journal of the American Chemical Society* **1997,** *119,* 7019-7029.

[103] Qu, L.; Yu, W. W.; Peng, X. *Nano Letters* **2004,** *4,* 465-469.

[104] Landes, C.; Braun, M.; Burda, C.; El-Sayed, M. A. *Nano Letters* **2001,** *1,* 667-670.

[105] Landes, C.; Braun, M.; El-Sayed, M. A. *Chemical Physics Letters* **2002,** *363,* 465-470.

[106] Chen, X.; Samia, A. C. S.; Lou, Y.; Burda, C. *Journal of the American Chemical Society* **2005,** *127,* 4372-4375.

[107] Urbieta, A.; Fernández, P.; Piqueras, J. *Journal of Applied Physics* **2004,** *96,* 2210-2213.

[108] Mohamed, M. B.; Tonti, D.; Al-Salman, A.; Chemseddine, A.; Chergui, M. *Journal of Physical Chemistry B* **2005,** *109,* 10533-10537.

[109] Li, J. J.; Yang, Y. A.; Guo, W. Z.; Keay, J. C.; Mishima, T. D.; Johnson, M. B.; Peng, X. G. *Journal of the American Chemical Society* **2003,** *125,* 12567-12575.

[110] Jasieniak, J.; Bullen, C.; vanEmbden, J.; Mulvaney, P. *Journal of Physical Chemistry B* **2005,** *109,* 20665-20668.

[111] Yu, W. W.; Wang, Y. A.; Peng, X. *Chemistry of Materials* **2003,** *15,* 4300-4308.

[112] Murray, C. B.; Kagan, C. R.; Bawendi, M. G. *Annual Review of Materials Science* **2000,** *30,* 545-610.

[113] Underwood, D. F.; Kippeny, T.; Rosenthal, S. J. *Journal of Physical Chemistry B* **2001,** *105,* 436-443.

[114] Katari, J. E. B.; Colvin, V. L.; Alivisatos, A. P. *Journal of Physical Chemistry* **1994,** *98,* 4109-4117.

[115] Shiang, J. J.; Kadavanich, A. V.; Grubbs, R. K.; Alivisatos, A. P. *Journal of Physical Chemistry* **1995,** *99,* 17417-17422.

[116] Bawendi, M. G.; Kortan, A. R.; Steigerwald, M. L.; Brus, L. E. *Journal of Chemical Physics* **1989,** *91,* 7282-7290.

[117] McGinley, C.; Riedler, M.; Moller, T.; Borchert, H.; Haubold, S.; Weller, H. *Physical Review B* **2002,** *65,* 245208.

[118] Rabani, E. *Journal of Chemical Physics* **2001,** *115,* 1493-1497.

[119] Guyot-Sionnest, P.; Wehrenberg, B.; Yu, D. *Journal of Chemical Physics* **2005,** *123,* 074709.

[120] Kalyuzhny, G.; Murray, R. W. *Journal of Physical Chemistry B* **2005,** *109,* 7012-7021.

[121] Myung, N.; Bae, Y.; Bard, A. J. *Nano Letters* **2003,** *3,* 747-749.

[122] Califano, M.; Franceschetti, A.; Zunger, A. *Nano Letters* **2005,** *5,* 2360-2364.

[123] Kumar, V.; Sharma, T. P. *Journal of Physics and Chemistry of Solids* **1998,** *59,* 1321-1325.

[124] Mane, R. S.; Lokhande, C. D. *Thin Solid Films* **1997,** *304,* 56-60.

[125] Kainthla, R. C.; Pandya, D. K.; Chopra, K. L. *Journal of the Electrochemical Society* **1982,** *129,* 99-102.

[126] Mezrag, F.; Aouina, N. Y.; Bouarissa, N. *Journal of Materials Science* **2006,** *41,* 5323-5328.

[127] Levinshtein, M.; Rumyantsev, S.; Shur, M., Eds.; *Handbook Series on Semiconductor Parameters;* volume 2 of *Ternary and Quaternary III-V Compounds* World Scientific: New Jersey, 1999.

[128] Bleuse, J.; Carayon, S.; Reiss, P. *Physica E* **2004,** *21,* 331-335.

[129] Akamatsu, K.; Tsuruoka, T.; Nawafune, H. *Journal of the American Chemical Society* **2005,** *127,* 1634-1635.

[130] Brainard, R. J.; Paulson, C. A.; Saulys, D.; Gaines, D. F.; Kuech, T. F.; Ellis, A. B. *Journal of Physical Chemistry B* **1997,** *101,* 11180-11184.

[131] Lifshitz, E.; Dag, I.; Litvin, I.; Hodes, G.; Gorer, S.; Reisfeld, R.; Minti, H. *Chemical Physics Letters* **1998,** *288,* 188-196.

[132] Guyot-Sionnest, P.; Shim, M.; Matranga, C.; Hines, M. *Physical Review B* **1999,** *60,* R2181-R2184.

[133] Hohng, S.; Ha, T. *Journal of the American Chemical Society* **2004,** *126,* 1324-1325.

[134] Flügge, S. *Practical Quantum Mechanics I;* volume 177 of *Die Grundlehren der mathematischen Wissenschaften in Einzeldarstellungen* Springer-Verlag: New York, 1971.

[135] Schooss, D.; Mews, A.; Eychmüller, A.; Weller, H. *Physical Review B* **1994,** *49,* 17072-17078.

[136] BenDaniel, D. J.; Duke, C. B. *Physical Review* **1966,** *152,* 683-692.

[137] Jordan, K. D.; Michejda, J. A.; Burrow, P. D. *Journal of the American Chemical Society* **1976,** *98,* 1295-1296.

[138] Lu, K.-T.; Eiden, G. C.; Weisshaar, J. C. *Journal of Physical Chemistry* **1992,** *96,* 9742-9748.

[139] Lowe, J. P. *Quantum Chemistry;* Academic: San Diego, 2^{nd} ed.; 1993.

[140] Efros, A. L.; Rosen, M.; Kuno, M.; Nirmal, M.; Norris, D. J.; Bawendi, M. *Physical Review B* **1996,** *54,* 4843-4856.

[141] Lide, D. R.; Frederikse, H. P. R., Eds.; *CRC Handbook of Chemistry and Physics;* CRC Press: Boca Raton, Florida, 74^{th} ed.; 1993.

[142] Hales, T. C. *Notices of the American Mathematical Society* **2000,** *47,* 440-449.

[143] Conway, J. H.; Sloane, N. J. A. *Sphere Packings, Lattices and Groups;* volume 290 of *A Series of Comprehensive Studies in Mathematics* Springer-Verlag: New York, 1999.

[144] Jaeger, H. M.; Nagel, S. R. *Science* **1992,** *255,* 1523-1531.

[145] Torquato, S.; Truskett, T. M.; Debenedetti, P. G. *Physical Review Letters* **2000,** *84,* 2064-2067.

[146] Bezdek, A.; Kuperberg, W. Packing Euclidean space with congruent cylinders and with congruent ellipsoids. In *Applied Geometry and Discrete Mathematics: The Victor Klee Festschrift*, Vol. 4; Gritzmann, P.; Sturmfels, B., Eds.; American Mathematical Society: Providence, RI, 1991.

[147] Sloane, N. J. A. *Nature* **1998,** *395,* 435-436.

[148] Donev, A.; Cisse, I.; Sachs, D.; Variano, E. A.; Stillinger, F. H.; Connelly, R.; Torquato, S.; Chaikin, P. M. *Science* **2004,** *303,* 990-993.

[149] "Annual Energy Review 1999", U. S. Department of Energy. Energy Information Administration. Office of Energy Markets and End Use. U. S. Government Printing Office: Washington, D. C., DOE/EIA-0384(99), 2000.

[150] Campbell, C. J. *Oil & Gas Journal* **1997,** *95,* 33-39.

[151] Shah, A.; Torres, P.; Tscharner, R.; Wyrsch, N.; Keppner, H. *Science* **1999,** *285,* 692-698.

[152] www.eere.energy.gov/solar/mission_vision_goals.html.

[153] Shah, A. V.; Platz, R.; Keppner, H. *Solar Energy Materials and Solar Cells* **1995,** *38,* 501-520.

[154] Fleming, G.; van Grondelle, R. *Physics Today* **1994,** *February Issue,* 48.

[155] Bergmann, R. B. *Applied Physics A* **1999,** *69,* 187-194.

[156] Zhao, J.; Wang, A.; Green, M. A. *Applied Physics Letters* **1998,** *73,* 1991-1993.

[157] Sze, S. M. *The Physics of Semiconductor Devices;* John Wiley & Sons: New York, 2^{nd} ed.; 1981.

[158] Green, M. A. *Energy Policy* **2000,** *28,* 989-998.

[159] Deckman, H. W.; Wronski, C. R.; Witzke, H.; Yablonovitch, E. *Applied Physics Letters* **1983,** *42,* 968-970.

[160] Jimenez, R.; Dikshit, S. N.; Bradforth, S. E.; Fleming, G. R. *Journal of Physical Chemistry* **1996,** *100,* 6825-6834.

[161] Hess, S.; Chachisvilis, M.; Timpmann, K.; Jones, M. R.; Fowler, G. J. S.; Hunter, C. N.; Sundstrom, V. *Proceedings of the National Academy of Sciences of the United States of America* **1995,** *92,* 12333-12337.

[162] Visscher, K.; Bergstrom, H.; Sundstrom, V.; Hunter, C.; van Grondelle, R. *Photosynthesis Research* **1989,** *22,* 211-217.

[163] Du, M.; Rosenthal, S. J.; Xie, X.; DiMagno, T. J.; Schmidt, M.; Hanson, D. K.; Schiffer, M.; Norris, J. R.; Fleming, G. R. *Proceedings of the National Academy of Sciences of the United States of America* **1992,** *89,* 8517-8521.

[164] Ke, B. *Photosynthesis: Photobiochemistry and Photobiophysics;* Kluwer Academic: Dodrecht, 2001.

[165] Zallen, R. *The Physics of Amorphous Solids;* John Wiley & Sons: New York, 1983.

[166] Hauser, J. J. *Physical Review B* **1973,** *8,* 3817-3823.

[167] Morgan, M.; Walley, P. A. *Philosophical Magazine* **1971,** *23,* 661.

[168] Sirringhaus, H.; Brown, P. J.; Friend, R. H.; Nielsen, M. M.; Bechgaard, K.; Langeveld-Voss, B. M. W.; Spiering, A. J. H.; Janssen, R. A. J.; Meijer, E. W. *Synthetic Metals* **2000,** *111,* 129-132.

[169] Assadi, A.; Svensson, C.; Willander, M.; Inganäs, O. *Applied Physics Letters* **1988,** *53,* 195-197.

[170] Paloheimo, J.; Kuivalainen, P.; Stubb, H.; Vuorimaa, E.; Ylilahti, P. *Applied Physics Letters* **1990,** *56,* 1157-1159.

[171] Muller, R. S.; Kamins, T. I. *Device Electronics for Integrated Circuits;* John Wiley & Sons: New York, 2nd ed.; 1986.

[172] Sirringhaus, H.; Brown, P. J.; Friend, R. H.; Nielsen, M. M.; Bechgaard, K.; Langeveld-Voss, W.; Spiering, A. J. H.; Janssen, R. A. J.; Meijer, E. W.; Herwig, P.; de Leeuw, D. M. *Nature* **1999,** *401,* 685-688.

[173] Forro, L.; Chauvet, O.; Emin, D.; Zuppiroli, L.; Berger, H.; Levy, F. *Journal of Applied Physics* **1994,** *75,* 633-635.

[174] Tang, H.; Prasad, K.; Sanjines, R.; Schmid, P. E.; Levy, F. *Journal of Applied Physics* **1994,** *75,* 2042-2047.

[175] Konenkamp, R. *Physical Review B* **2000,** *61,* 11057-11064.

[176] Allemand, P. M.; Koch, A.; Wudl, F.; Rubin, Y.; Diederich, F.; Alvarez, M. M.; Anz, S. J.; Whetten, R. L. *Journal of the American Chemical Society* **1991,** *113,* 1050-1051.

[177] Miller, B.; Rosamilia, J. M.; Dabbagh, G.; Tycko, R.; Haddon, R. C.; Muller, A. J.; Wilson, W.; Murphy, D. W.; Hebard, A. F. *Journal of the American Chemical Society* **1991,** *113,* 6291-6293.

[178] Ghosh, A. K.; Feng, T. *Journal of Applied Physics* **1973,** *44,* 2781-2788.

[179] Cacialli, F.; Friend, R. H.; Bouche, C. M.; Barny, P. L.; Facoetti, H.; Soyer, F.; Robin, P. *Journal of Applied Physics* **1998,** *83,* 2343-2356.

[180] Yu, G.; Zhang, C.; Heeger, A. J. *Applied Physics Letters* **1994,** *64,* 1540-1542.

[181] Seki, I.; Hayashi, N.; Oji, H.; Ito, E.; Ouchi, Y.; Ishii, H. *Thin Solid Films* **2001,** *393,* 298-303.

[182] Peisert, H.; Schwieger, T.; Knupfer, M.; Golden, M. S.; Fink, J. *Synthetic Metals* **2001,** *121,* 1435-1436.

[183] Seguy, I.; Mamy, R.; Destruel, P.; Jolinat, P.; Bock, H. *Applied Surface Science* **2001,** *174,* 310-315.

[184] Peisert, H.; Schwieger, T.; Knupfer, M.; Golden, M. S.; Fink, J. *Journal of Applied Physics* **2000,** *88,* 1535-1540.

[185] Schroeder, P. G.; Nelson, M. W.; Parkinson, B. A.; Schlaf, R. *Surface Science* **2000,** *459,* 349-364.

[186] Lane, P. A.; Rostalski, J.; Giebeler, C.; Martin, S. J.; Bradley, D. D. C.; Meissner, D. *Solar Energy Materials and Solar Cells* **2000,** *63,* 3-13.

[187] Ishii, H.; Oji, H.; Ito, E.; Hayashi, N.; Yoshimura, D.; Seki, K. *Journal of Luminescence* **2000,** *87-9,* 61-65.

[188] Brabec, C. J.; Cravino, A.; Meissner, D.; Sariciftci, N. S.; Fromherz, T.; Rispens, M. T.; Sanchez, L.; Hummelen, J. C. *Advanced Functional Materials* **2001,** *11,* 374-380.

[189] Ishii, H.; Hasegawa, S.; Yoshimura, D.; Sugiyama, K.; Narioka, S.; Sei, M.; Ouchi, Y.; Seki, K.; Harima, Y.; Yamashita, K. *Molecular Crystals and Liquid Crystals Science and Technology Section A-Molecular Crystals and Liquid Crystals* **1997,** *296,* 427-444.

[190] Ishii, H.; Sugiyama, K.; Yoshimura, D.; Ito, E.; Ouchi, Y.; Seki, K. *IEEE Journal of Selected Topics in Quantum Electronics* **1998,** *4,* 24-33.

[191] Hill, I. G.; Rajagopal, A.; Kahn, A.; Hu, Y. *Applied Physics Letters* **1998,** *73,* 662-664.

[192] Hill, I. G.; Milliron, D.; Schwartz, J.; Kahn, A. *Applied Surface Science* **2000,** *166,* 354-362.

[193] Shen, C. F.; Kahn, A.; Schwartz, J. *Journal of Applied Physics* **2001,** *90,* 6236-6342.

[194] Shen, C.; Kahn, A. *Journal of Applied Physics* **2001,** *90,* 4549-4554.

[195] Shen, C. F.; Kahn, A.; Schwartz, J. *Journal of Applied Physics* **2001,** *89,* 449-459.

[196] Shen, C.; Kahn, A. *Organic Electronics* **2001,** *2,* 89-95.

[197] Tang, C. W. *Applied Physics Letters* **1986,** *48,* 183-185.

[198] Yoshimura, D.; Ishii, H.; Ouchi, Y.; Ito, E.; Miyamae, T.; Hasegawa, S.; Okudaira, K. K.; Ueno, N.; Seki, K. *Physical Review B* **1999,** *60,* 9046-9060.

[199] Yamamoto, I.; Sakurai, Y.; Hosoi, Y.; Ishii, H.; Kajikawa, K.; Ouchi, Y.; Seki, K. *Journal of Physical Chemistry B* **2000,** *104,* 7370-7376.

[200] Narioka, S.; Ishii, H.; Yoshimura, D.; Sei, M.; Ouchi, Y.; Seki, K.; Hasegawa, S.; Miyazaki, T.; Harima, Y.; Yamashita, K. *Applied Physics Letters* **1995,** *67,* 1899-1901.

[201] Lee, S. T.; Wang, Y. M.; Hou, X. Y.; Tang, C. W. *Applied Physics Letters* **1999,** *74,* 670-672.

[202] Umbach, E.; Glockler, K.; Sokolowski, M. *Surface Science* **1998,** *404,* 20-3.

[203] Le, Q. T.; Yan, L.; Gao, Y. G.; Mason, M. G.; Giesen, D. J.; Tang, C. W. *Journal of Applied Physics* **2000,** *87,* 375-379.

[204] Park, Y.; Choong, V. E.; Hsieh, B. R.; Tang, C. W.; Wehrmeister, T.; Mullen, K.; Gao, Y. *Journal of Vacuum Science and Technology A* **1997,** *15,* 2574-2578.

[205] Park, Y.; Choong, V. E.; Hsieh, B. R.; Tang, C. W.; Gao, Y. *Physical Review Letters* **1997,** *78,* 3955-3958.

[206] Lee, S. T.; Hou, X. Y.; Mason, M. G.; Tang, C. W. *Applied Physics Letters* **1998,** *72,* 1593-1595.

[207] Hsieh, B. R.; Ettedgui, E.; Park, K. T.; Gao, Y. *Molecular Crystals and Liquid Crystals Science and Technology Section A-Molecular Crystals and Liquid Crystals* **1994,** *256,* 71-78.

[208] Ettedgui, E.; Razafitrimo, H.; Park, K. T.; Gao, Y.; Hsieh, B. R. *Surface and Interface Analysis* **1995,** *23,* 89-98.

[209] Ettedgui, E.; Razafitrimo, H.; Park, K. T.; Gao, Y.; Hsieh, B. R. *Journal of Applied Physics* **1994,** *75,* 7526-7530.

[210] Razafitrimo, H.; Park, K. T.; Ettedgui, E.; Gao, Y.; Hsieh, B. R. *Polymer International* **1995,** *36,* 147-153.

[211] Gao, Y.; Park, K. T.; Hsieh, B. R. *Journal of Applied Physics* **1993,** *73,* 7894-7899.

[212] Gao, Y.; Park, K. T.; Hsieh, B. R. *Journal of Chemical Physics* **1992,** *97,* 6991-6993.

[213] Cowley, A. M.; Sze, S. M. *Journal of Applied Physics* **1965,** *36,* 3212.

[214] Mason, M. G.; Tang, C. W.; Hung, L. S.; Raychaudhuri, P.; Madathil, J.; Giesen, D. J.; Yan, L.; Le, Q. T.; Gao, Y.; Lee, S. T.; Liao, L. S.; Cheng, L. F.; Salaneck, W. R.; dos Santos, D. A.; Bredas, J. L. *Journal of Applied Physics* **2001,** *89,* 2756-2765.

[215] Yan, L.; Watkins, N. J.; Zorba, S.; Gao, Y. L.; Tang, C. W. *Applied Physics Letters* **2001,** *79,* 4148-4150.

[216] Monch, W. *Surface Science* **1994,** *300,* 928-944.

[217] Shen, C.; Kahn, A.; Hill, I. G. Organic molecular interfaces: Investigations of electronic structure, chemistry and carrier injection properties. In *Conjugated Polymer and Molecular Interfaces: Science and Technology for Photonic and Optoelectronic Applications*; Kahn, A.; Pireaux, J.-J.; Salaneck, W. R.; Seki, K., Eds.; Marcel-Dekker: New York, 2001.

[218] Kurtin, S.; McGill, T. C.; Mead, C. A. *Physical Review Letters* **1969,** *22,* 1433-1436.

[219] Yan, L.; Mason, M. G.; Tang, C. W.; Gao, Y. L. *Applied Surface Science* **2001,** *175,* 412-418.

[220] Tran, V. H.; Massardier, V.; Guyot, A.; Nguyen, T. P. *Polymer* **1993,** *34,* 3179-3183.

[221] Nguyen, T. P.; Tran, V. H.; Massardier, V.; Guyot, A. *Synthetic Metals* **1993,** *55,* 235-240.

[222] Kera, S.; Setoyama, H.; Onoue, M.; Okudaira, K. K.; Harada, Y.; Ueno, N. *Physical Review B* **2001,** *63,* 115204.

[223] Weaver, J. H. *Journal of Physics and Chemistry of Solids* **1992,** *53,* 1433-1447.

[224] Shen, C. F.; Hill, I. G.; Kahn, A.; Schwartz, J. *Journal of the American Chemical Society* **2000,** *122,* 5391-5392.

[225] Shen, C. F.; Hill, I. G.; Kahn, A. *Advanced Materials* **1999,** *11,* 1523-1527.

[226] Curioni, A.; Andreoni, W. *Journal of the American Chemical Society* **1999,** *121,* 8216-8220.

[227] Johansson, N.; Osada, T.; Stafstrom, S.; Salaneck, W. R.; Parente, V.; dos Santos, D. A.; Crispin, X.; Bredas, J. L. *Journal of Chemical Physics* **1999,** *111,* 2157-2163.

[228] Zhang, R. Q.; Hou, X. Y.; Lee, S. T. *Applied Physics Lettes* **1999,** *74,* 1612-1614.

[229] Rajagopal, A.; Kahn, A. *Journal of Applied Physics* **1998,** *84,* 355-358.

[230] Choong, V. E.; Mason, M. G.; Tang, C. W.; Gao, Y. G. *Applied Physics Letters* **1998,** *72,* 2689-2691.

[231] Dyakonov, V.; Godovsky, D.; Parisi, J.; Brabec, C. J.; Sariciftci, N. S.; Hummelen, J. C.; Ceuster, J. D.; Goovaerts, E. *Synthetic Metals* **2001,** *121,* 1529-1532.

[232] Tang, C. W.; Albrecht, A. C. *Nature* **1975,** *254,* 507-509.

[233] Tang, C. W.; Albrecht, A. C. *Journal of Chemical Physics* **1975,** *62,* 2139-2149.

[234] Lyons, L. E.; Newman, O. M. G. *Australian Journal of Chemistry* **1971,** *24,* 13.

[235] Usov, N. N.; Bendersk, V. A. *Soviet Physics Semiconductors-USSR* **1968,** *2,* 580.

[236] Ghosh, K.; Morel, D. L.; Feng, T.; Shaw, R. F.; Rowe, C. A. *Journal of Applied Physics* **1974,** *45,* 230-236.

[237] Hall, K. J.; Bonham, J. S.; Lyons, L. E. *Australian Journal of Chemistry* **1978,** *31,* 1661-1677.

[238] Fan, F. R.; Faulkner, L. R. *Journal of Chemical Physics* **1978,** *69,* 3334-3340.

[239] Fan, F. R.; Faulkner, L. R. *Journal of Chemical Physics* **1978,** *69,* 3341-3349.

[240] Dodelet, J. P.; Pommier, H. P.; Ringuet, M. *Journal of Applied Physics* **1982,** *53,* 4270-4277.

[241] Mazur, U.; Hipps, K. W. *Journal of Physical Chemistry B* **1999,** *103,* 9721-9727.

[242] Kampas, F. J.; Gouterman, M. *Journal of Physical Chemistry* **1977,** *81,* 690-695.

[243] Gregg, B. A.; Fox, M. A.; Bard, A. J. *Journal of Physical Chemistry* **1990,** *94,* 1586-1598.

[244] Takahashi, K.; Iwanaga, T.; Yamaguchi, T.; Komura, T.; Murata, K. *Synthetic Metals* **2001,** *123,* 91-94.

[245] Quickenden, T. I.; Yim, G. K. *Solar Energy* **1977,** *19,* 283-289.

[246] Merritt, V. Y.; Hovel, H. J. *Applied Physics Letters* **1976,** *29,* 414-415.

[247] Sharma, G. D.; Saxena, D.; Roy, M. S. *Synthetic Metals* **1999,** *106,* 97-105.

[248] Ghosh, A. K.; Feng, T. *Journal of Applied Physics* **1978,** *49,* 5982-5989.

[249] Skotheim, T.; Yang, J. M.; Otvos, J.; Klein, M. P. *Journal of Chemical Physics* **1982,** *77,* 6144-6150.

[250] Skotheim, T.; Yang, J. M.; Otvos, J.; Klein, M. P. *Journal of Chemical Physics* **1982,** *77,* 6151-6161.

[251] Cao, Y.; Yu, G.; Zhang, C.; Menon, R.; Heeger, A. J. *Synthetic Metals* **1997,** *87,* 171-174.

[252] Zyung, T.; Jung, S. D. *Etri Journal* **1996,** *18,* 181-193.

[253] Lemmer, U.; Vacar, D.; Moses, D.; Heeger, A. J.; Ohnishi, T.; Noguchi, T. *Applied Physics Letters* **1996,** *8,* 3007-3009.

[254] Parker, I. D. *Journal of Applied Physics* **1994,** *75,* 1656-1666.

[255] Karg, S.; Riess, W.; Dyakonov, V.; Schwoerer, M. *Synthetic Metals* **1993,** *54,* 427-433.

[256] Ng, P. K.; Gong, X.; Chan, S. H.; Lam, L. S. M.; Chan, W. K. *Chemistry-a European Journal* **2001,** *7,* 4358-4367.

[257] Harrison, M. G.; Gruner, J.; Spencer, G. C. W. *Physical Review B* **1997,** *55,* 7831-7849.

[258] Videlot, C.; Kassmi, A. E.; Fichou, D. *Solar Energy Materials and Solar Cells* **2000,** *63,* 69-82.

[259] Yu, G.; Pakbaz, K.; Heeger, A. J. *Applied Physics Letters* **1994,** *64,* 3422-3424.

[260] Tagmouti, S.; Outzourhit, A.; Oueriagli, A.; Khaidar, M.; Elyacoubi, M.; Evrard, R.; Ameziane, E. L. *Solar Energy Materials and Solar Cells* **2002,** *71,* 9-18.

[261] Too, C. O.; Wallace, G. G.; Burrell, A. K.; Collis, G. E.; Officer, D. L.; Boge, E. W.; Brodie, S. G.; Evans, E. J. *Synthetic Metals* **2001,** *123,* 53-60.

[262] Takayama, I.; Kaneko, M.; Pandey, S. S.; Takashima, W.; Kaneto, K. *Synthetic Metals* **2001,** *121,* 1565-1566.

[263] Lee, S. B.; Yoshino, K.; Park, J. Y.; Park, Y. W. *Physical Review B* **2000,** *61,* 2151-2158.

[264] Antoniadis, H.; Hsieh, B. R.; Abkowitz, M. A.; Jenekhe, S. A.; Stolka, M. *Synthetic Metals* **1994,** *62,* 265-271.

[265] Koltun, M.; Faiman, D.; Goren, S.; Katz, E. A.; Kunoff, E.; Shames, A.; Shtutina, S.; Uzan, B. *Solar Energy Materials and Solar Cells* **1996,** *44,* 485-491.

[266] Lee, C. H.; Yu, G.; Moses, D.; Heeger, A. J.; Srdanov, V. I. *Applied Physics Letters* **1994,** *65,* 664-666.

[267] Kagan, C. R. *The Electronic and Optical Properties of Close Packed Cadmium Selenide Quantum Dot Solids,* Thesis, Massachusetts Institute of Technology, 1996.

[268] Ginger, D. S.; Greenham, N. C. *Journal of Applied Physics* **2000,** *87,* 1361-1368.

[269] Brabec, C. J.; Sariciftci, N. S.; Hummelen, J. C. *Advanced Functional Materials* **2001,** *11,* 15-26.

[270] Dyakonov, V.; Frankevich, E. *Chemical Physics* **1998,** *227,* 203-217.

[271] DeVore, H. B. *Physical Reviews* **1956,** *102,* 86-91.

[272] Desormeaux, A.; Max, J. J.; Leblanc, R. M. *Journal of Physical Chemistry* **1993,** *97,* 6670-6678.

[273] Gattinger, P.; Rengel, H.; Neher, D. *Synthetic Metals* **1996,** *83,* 245-247.

[274] Mort, J.; Okumura, K.; Machonkin, M.; Ziolo, R.; Huffman, D. R.; Ferguson, M. I. *Chemical Physics Letters* **1991,** *186,* 281-283.

[275] Riess, W.; Karg, S.; Dyakonov, V.; Meier, M.; Schwoerer, M. *Journal of Luminescence* **1994,** *60-61,* 906-911.

[276] Sicot, L.; Fiorini, C.; Lorin, A.; Raimond, P.; Sentein, C.; Nunzi, J. M. *Solar Energy Materials and Solar Cells* **2000,** *63,* 49-60.

[277] Sicot, L.; Geffroy, B.; Lorin, A.; Raimond, P.; Sentein, C.; Nunzi, J. M. *Journal of Applied Physics* **2001,** *90,* 1047-1054.

[278] Mort, J.; Mashonkin, M.; Ziolo, R.; Chen, I. *Applied Physics Letters* **1992,** *61,* 1829-1831.

[279] Nasr, C.; Hotchandani, S.; Leblanc, R. M. *Proceedings of the Indian Academy of Sciences-Chemical Sciences* **1995,** *107,* 699-708.

[280] Pan, Y. L.; Chen, L. B.; Wang, Y.; Zhao, Y. Y.; Li, F. M.; Wagiki, A.; Yamashita, M.; Tako, T. *Applied Physics Letters* **1996,** *68,* 1314-1316.

[281] Roy, M. S.; Sharma, G. D.; Gupta, S. K. *Thin Solid Films* **1997,** *310,* 279-288.

[282] Sharma, G. D.; Gupta, S. K.; Roy, M. S. *Journal of Materials Science-Materials in Electronics* **1998,** *9,* 91-97.

[283] Sariciftci, N. S.; Braun, D.; Zhang, C.; Srdanov, V. I.; Heeger, A. J.; Stucky, G.; Wudl, F. *Applied Physics Letters* **1992,** *62,* 585-587.

[284] Sharma, G. D.; Roy, M. S.; Sangodkar, S. G.; Gupta, S. K. *Synthetic Metals* **1996,** *83,* 1-6.

[285] Sharma, G. D.; Saxena, D.; Roy, M. S. *Synthetic Metals* **2001,** *124,* 399-405.

[286] Tsutsui, T.; Nakashima, T.; Fujita, Y.; Saito, S. *Synthetic Metals* **1995,** *71,* 2281-2282.

[287] Trombach, N.; Tada, H.; Hiller, S.; Schlettwein, D.; Wohrle, D. *Thin Solid Films* **2001,** *396,* 109-118.

[288] Stubinger, T.; Brutting, W. *Journal of Applied Physics* **2001,** *90,* 3632-3641.

[289] Ahn, Y. J.; Kang, G. W.; Lee, C. H. *Molecular Crystals and Liquid Crystals* **2002,** *377,* 301-304.

[290] Scher, H.; Zallen, R. *Journal of Chemical Physics* **1970,** *53,* 3759.

[291] O'Regan, B.; Grätzel, M. *Nature* **1991,** *353,* 737-740.

[292] Salafsky, J. S. *Physical Review B* **1999,** *59,* 10885-10894.

[293] Salafsky, J. S.; Lubberhuizen, W. H.; van Faassen, E.; Schropp, R. E. I. *Journal of Physical Chemistry B* **1998,** *102,* 766-769.

[294] Nazeeruddin, M. K.; Kay, A.; Rodicio, I.; Humphrey-Baker, R.; Muller, E.; Liska, P.; Vlachopoulos, N.; Grätzel, M. *Journal of the American Chemical Society* **1993,** *115,* 6382-6390.

[295] Hamer, P. J.; Pichler, K.; Harrison, M. G.; Friend, R. H.; Ratier, B.; Moliton, A.; Moratti, S. C.; Holmes, A. B. *Philosophical Magazine B* **1996,** *73,* 367-382.

[296] Shaheen, S. E.; Brabec, C. J.; Sariciftci, N. S.; Padinger, F.; Fromherz, T.; Hummelen, J. C. *Applied Physics Letters* **2001,** *78,* 841-843.

[297] Erwin, M. M. *Synthesis, characterization and design of a nanocrystal based photovoltaic device,* Thesis, Vanderbilt University, 2005.

[298] Baur, J. W.; Durstock, M. F.; Taylor, B. E.; Spry, R. J.; Relbach, S.; Chiang, L. Y. *Synthetic Metals* **2001,** *121,* 1547-1548.

[299] Gebeyehu, D.; Brabec, C. J.; Padinger, F.; Fromherz, T.; Spiekermann, S.; Vlachopoulos, N.; Kienberger, F.; Schindler, H.; Sariciftci, N. S. *Synthetic Metals* **2001,** 1549-1550.

[300] Hiramoto, M.; Fujiwara, H.; Yokoyama, M. *Journal of Applied Physics* **1992,** *72,* 3781-3787.

[301] Grätzel, M. *Pure and Applied Chemistry* **2001,** *73,* 459-467.

[302] Kubo, W.; Murakoshi, K.; Kitamura, T.; Yoshida, S.; Haruki, M.; Hanabusa, K.; Shirai, H.; Wada, Y.; Yanagida, S. *Journal of Physical Chemistry B* **2001,** *105,* 12809-12815.

[303] Finklea, O. *Semiconductor Electrodes;* Elsevier: New York, 1988 Ch. 1.

[304] Rees, E. G. *Notes on Geometry;* volume Part III Springer-Verlag: Berlin, 1988.

[305] Yang, P. D.; Zhou, D. Y.; Margolese, D. I.; Chmelka, D. F.; Stucky, G. D. *Nature* **1998,** *396,* 152-155.

[306] Yao, B. D.; Zhang, L. D. *Journal of Materials Science* **1999,** *34,* 5983-5987.

[307] "Terrestrial Photovoltaic Measurement Procedures", NASA; ERDA/NASA/1022-77/16, 1977.

[308] Murray, C. B. IBM Watson, 1999.

[309] http://www.nrel.gov/gis/images/us_csp_annual_may2004.jpg.

[310] Maxwell, E.; George, R.; Wilcox, S. A climatological solar radiation model. In *Proceedings of the 1998 Annual Conference, American Solar Energy Society*; American Solar Energy Society: Albuquerque NM, 1998.

[311] George, R.; Maxwell, E. High-resolution maps of solar collector performance using a climatological solar radiation model. In *Proceedings of the 1999 Annual Conference, American Solar Energy Society*; American Solar Energy Society: Portland, ME., 1999.

[312] Flytzanis, C.; Hutter, J. Nonlinear optics in quantum confined structures. In *Contemporary Nonlinear Optics*; Agrawal, G. P.; Boyd, R. W., Eds.; Quantum Electronics-Principles and Applications, Academic Press: New York, 1992.

[313] Kayanuma, Y. *Physical Review B* **1988,** *38,* 9797-9805.

[314] Terekhova, S. F.; Onishchenko, N. A.; Talenskii, O. N.; Pendur, S. A. *Physica Status Solidi B 131,* 207.

[315] Rajh, T.; Mićić, O. I.; Nozik, A. J. *Journal of Physical Chemistry* **1993,** *97,* 11999-12003.

[316] Leatherdale, C. A.; Woo, W.-K.; Mikulec, F. V.; Bawendi, M. G. *Journal of Physical Chemistry B* **2002,** *106,* 7619-7622.

[317] Schmelz, O.; Mews, A.; Basché, T.; Herrmann, A.; Müllen, K. *Langmuir* **2001,** *17,* 2861-2865.

[318] Striolo, A.; Ward, J.; Prausnitz, J. M.; Parak, W. J.; Zanchet, D.; Gerion, D.; Milliron, D.; Alivisatos, A. P. *Journal of Physical Chemistry B* **2002,** *106,* 5500-5505.

[319] Folden, C. "Surface Studies and Size-Independent Extinction Coefficients of CdSe Nanocrystals", Senior Thesis, Vanderbilt University, 1999.

[320] Dabbousi, B. O.; Rodriguez-Viejo, J.; Mikulec, F. V.; Heine, J. R.; Mattoussi, H.; Ober, R.; Jensen, K. F.; Bawendi, M. G. *Journal of Physical Chemistry B* **1997,** *101,* 9463-9475.

[321] Apfel, J. H.; Hadley, L. N. *Physical Review* **1955,** *100,* 1689-1691.

[322] Marka, Z.; Pasternak, R.; Rashkeev, S. N.; Jiang, Y.; Pantelides, S. T.; Tolk, N. H.; Roy, P. K.; Kozub, J. *Physical Review B* **2003,** *67,* 045302.

[323] Pankove, J. I. *Optical Processes in Semiconductors;* Dover Publications: New York, 1975.

[324] Boyd, R. W. *Nonlinear Optics;* Academic: New York, 1992.

[325] Blanton, S. A.; Leheny, R. L.; Hines, M. A.; Guyot-Sionnest, P. *Physical Review Letters* **1997,** *79,* 865-868.

[326] Jun, B.; White, Y. V.; Schrimpf, R. D.; Fleetwood, D. M.; Brunier, F.; Bresson, N.; Cristoloveanu, S.; Tolk, N. H. *Applied Physics Letters* **2004,** *85,* 3095-3097.

[327] Jun, B.; Schrimpf, R. D.; Fleetwood, D. A.; White, Y. V.; Pasternak, R.; Rashkeev, S. N.; Brunier, F.; Bresson, N.; Fouillat, M.; Cristoloveanu, S.; Tolk, N. H. *IEEE Transactions on Nuclear Science* **2004,** *51,* 3231-3237 Part 2.

[328] Wherrett, B. S. *Journal of the Optical Society of America B* **1984,** *1,* 67-72.

[329] Stryland, E. W. V.; Woodall, M. A.; Williams, W. E.; Soileau, M. J. Two- and three-photon absorption in semiconductors with subsequent absorption by photogenerated carriers. In *Laser Induced Damage in Optical Materials: 1981*, Vol. 638; Bennett, H. E.; Guenther, A. H.; Milam, D.; Newnam, B. E., Eds.; National Bureau of Standards: Boulder, 1983.

[330] Adamchuk, V. K.; Afanas'ev, V. V. *Progress in Surface Science* **1992,** *41,* 111-211.

[331] Robertson, J. *Journal of Vacuum Science & Technology B* **2000,** *18,* 1785-1791.

[332] Williams, R. *Physical Review* **1965,** *140,* A569.

[333] Afanas'ev, V. V.; Houssa, M.; Stesmans, A.; Heyns, M. M. *Applied Physics Letters* **2001,** *78,* 3073-3075.

[334] Keister, J. W.; Rowe, J. E.; Kolodziej, J. J.; Niimi, H.; Madey, T. E.; Lucovsky, G. *Journal f Vacuum Science & Technology B* **1999,** *17,* 1831-1835.

[335] Miyazaki, S.; Nishimura, H.; Fukuda, M.; Ley, L.; Ristein, J. *Applied Surface Science* **1997,** *113/114,* 585-589.

[336] Glinka, Y. D.; Shahbazyan, T. V.; Perakis, I. E.; Tolk, N. H.; Liu, X.; Sasaki, Y.; Furdyna, J. K. *Applied Physics Letters* **2002,** *81,* 3717-3719.

[337] Glinka, Y. D.; Shahbazyan, T. V.; Perakis, I. E.; Tolk, N. H.; Liu, X.; Sasaki, Y.; Furdyna, J. K. *Applied Physics Letters* **2002,** *81,* 220-222.

[338] Jiang, Y. *et al. Physica Status Solidi B* **2003,** *240,* 490-499.

[339] Sipe, J. E.; Moss, D. J.; van Driel, H. M. *Physical Review B* **1987,** *35,* 1129-1141.

[340] Fomenko, V.; Bodlaki, D.; Faler, C.; Borguet, E. *Journal of Chemical Physics* **2002,** *116,* 6745-6754.

[341] Tom, H. W. K.; Heinz, T. F.; Shen, Y. R. *Physical Review Letters* **1983,** *51,* 1983-1986.

[342] Mitchell, S. A.; Boukherroub, R.; Anderson, S. *Journal of Physical Chemistry B* **2000,** *104,* 7668-7676.

[343] Kempf, R. W.; Wilson, P. T.; Canterbury, J. D.; Mishina, E. D.; Aktsipetrov, O. A.; Downer, M. C. *Applied Physics B* **1999,** *68,* 325-332.

[344] Fomenko, V.; Hurth, C.; Ye, T.; Borguet, E. *Journal of Applied Physics* **2002,** *91,* 4394-4398.

[345] Tomlinson, I. D.; Kippeny, T.; Swafford, L.; Siddiqui, N. H.; Rosenthal, S. J. *Journal of Chemical Research* **2002,** *S,* 203-204.

[346] Kern, W.; Puotinen, D. A. *RCA Review* **1970,** *31,* 187.

[347] Hulthen, R. *Physica Scripta* **1975,** *12,* 342-344.

[348] Philipp, H. R.; Taft, E. A. *Physical Review* **1960,** *120,* 37-38.

[349] Jacobsohn, M.; Banin, U. *Journal of Physical Chemistry B* **2000,** *104,* 1-5.

[350] Eilon, M. J.; Mokari, T.; Banin, U. *Journal of Physical Chemistry B* **2001,** *105,* 12726-12731.

[351] Coherent, Coherent Laser Group, 5100 Patrick Henry Drive, Santa Clara, CA 95054 "Mira Model 900-F Laser Operator's Manual", 2003.

[352] Quantronix, 41 Research Way, East Setauket, NY 11733 "Titan User's Manual", 2003.

[353] Coherent, Coherent Laser Group, 5100 Patrick Henry Drive, Santa Clara, CA 95054 "RegA Model 9000 Laser Operator's Manual", 2003.